



Provided by the author(s) and University of Galway in accordance with publisher policies. Please cite the published version when available.

| | |
|------------------|---|
| Title | Ultra-short and short pulsed laser ablation of molybdenum bulk, thin film and heterostructure |
| Author(s) | Das Gupta, Pinaki |
| Publication Date | 2018-02-22 |
| Item record | http://hdl.handle.net/10379/7153 |

Downloaded 2024-04-25T09:29:12Z

Some rights reserved. For more information, please see the item record link above.



Ultra-short and short pulsed laser ablation of molybdenum bulk, thin film and heterostructure

by

Pinaki Das Gupta, M.Sc., M.Phil.

A thesis submitted in partial fulfilment of the
requirements for the degree of

Doctor of Philosophy



Academic supervisor: Dr. Gerard M. O'Connor

National Centre for Laser Applications

School of Physics

College of Science

National University of Ireland, Galway

February 2018

This thesis is dedicated to my parents and all my friends...

For their endless love, support and encouragement, without whom none of my success would be possible

Table of Contents

| | |
|--|-------|
| Abstract..... | v |
| Declaration..... | vii |
| Acknowledgements | viii |
| List of Figures | ix |
| List of Tables | xviii |
| 1. Chapter 1: Introduction | 1 |
| 2. Chapter 2: Literature review..... | 5 |
| 2.1. Laser fundamentals | 5 |
| 2.2. Nd:YAG laser | 7 |
| 2.3. Pulse shortening | 9 |
| 2.3.1. Q-switching | 9 |
| 2.3.2. Mode-locking | 11 |
| 2.4. Chirped pulse amplification | 11 |
| 2.5. Laser-material interaction | 14 |
| 2.5.1. Reflection of laser light by material surface | 15 |
| 2.5.2. Interaction of an ultra-short pulse laser with material | 18 |
| 2.5.3. Interaction of a short pulse laser with a material | 19 |
| 2.5.4. Laser ablation mechanism | 21 |
| 2.5.5. Laser produced plasma plume generation | 24 |
| 2.5.6. Spectral emission from the ejected species | 24 |
| 2.5.7. Threshold fluence | 25 |
| 2.6. Molybdenum and its applications | 26 |
| 2.7. Laser processing of molybdenum | 28 |
| 3. Chapter 3: Materials and methods..... | 30 |
| 3.1. Molybdenum bulk..... | 30 |
| 3.2. Thin film deposition | 30 |
| 3.2.1. Method 1: Electron beam evaporation | 31 |
| 3.2.2. Method 2: Magnetron sputtering..... | 34 |
| 3.3. Laser workstation | 36 |
| 3.3.1. Femtosecond laser system | 36 |
| 3.3.2. Nanosecond laser system | 39 |
| 3.3.3. Laser intensity profile | 41 |
| 3.3.4. Laser power control | 42 |

| | |
|--|-----|
| 3.3.5. Focussing of laser beams | 42 |
| 3.3.6. Transmission of laser pulse through galvanometer | 42 |
| 3.4. Measurement of absorbed laser fluence into the material | 43 |
| 3.4.1. Integrating sphere | 44 |
| 3.4.2. Measurement of reflected and transmitted laser beam | 45 |
| 3.4.3. Measurement of threshold fluence..... | 45 |
| 3.5. Offline characterisations..... | 47 |
| 3.5.1. Atomic force microscopy (AFM) | 47 |
| 3.5.2. Scanning electron microscopy | 49 |
| 3.5.3. Energy dispersive X-ray (EDX) analysis | 49 |
| 3.6. Development of laser workstation for online characterisations..... | 50 |
| 3.6.1. Temporal alignment..... | 50 |
| 3.6.2. Spatial alignment | 53 |
| 3.7. Numerical simulation..... | 57 |
| 3.7.1. Heat diffusion model combined with mechanical stress model | 58 |
| 3.7.2. Two temperature model combined with mechanical stress model..... | 61 |
| 3.7.3. Terminology of the stress vector | 61 |
| 3.8. Summary..... | 63 |
| 4. Chapter 4: Laser molybdenum interaction..... | 64 |
| 4.1. Interaction of bulk molybdenum with laser sources | 64 |
| 4.1.1. Measurement of absorbed laser energy using integrating sphere | 64 |
| 4.1.2. Micro-machining of bulk molybdenum by femtosecond laser..... | 65 |
| 4.1.3. Computer simulation using Finite Element Method (FEM)..... | 67 |
| 4.2. Interaction of molybdenum thin film with laser sources | 71 |
| 4.2.1. Measurement of absorbed laser energy using integrating sphere | 71 |
| 4.2.2. Micro-machining of 50 nm thin molybdenum film using femtosecond and nanosecond pulsed laser sources | 73 |
| 4.2.3. Computational simulation using finite element method (FEM)..... | 86 |
| 4.3. Chapter conclusions..... | 97 |
| (a) Interaction of bulk molybdenum with femtosecond laser..... | 98 |
| (b) Interaction of thin film with femtosecond laser | 98 |
| (c) Interaction of molybdenum thin film nanosecond laser | 100 |
| 5. Chapter 5: Real-time imaging of laser molybdenum interaction | 102 |
| Optical emission from the plasma plume..... | 103 |
| Online diagnostics:..... | 104 |
| 5.1. Spectral imaging: | 104 |

| | |
|--|-----|
| 5.1.1. Spectral imaging of ultra-short pulse laser ablation of molybdenum bulk | 108 |
| 5.1.2. Spectral imaging of ultra-short laser pulse ablation of molybdenum thin film | 111 |
| 5.2.3. Spectral imaging of short laser ablation of molybdenum thin film | 113 |
| 5.2. Plasma Imaging | 115 |
| 5.2.1. Spatial imaging of plasma plume during ablation of molybdenum bulk by ultra-short pulse laser | 116 |
| 5.2.2. Spatial imaging of plasma plume during ablation of molybdenum thin film by ultra-short pulse laser | 123 |
| 5.2.3. Spatial imaging of plasma plume during ablation of molybdenum thin film by short pulse laser | 131 |
| 5.2.4. Discussion | 137 |
| 5.3. Conclusions of the chapter | 143 |
| 6. Chapter 6: Interaction of laser pulses with molybdenum based heterostructure | 145 |
| 6.1. Reflectivity measurement by integrating sphere | 145 |
| 6.2. Processing of MAM by femtosecond (FS) laser source | 146 |
| 6.2.1. Measurement of threshold fluence | 147 |
| 6.2.2. Characterisation by scanning electron microscope (SEM) technique | 150 |
| 6.2.3. Characterisation by atomic force microscope (AFM) technique | 158 |
| 6.2.4. Energy dispersive X-ray analysis | 163 |
| 6.2.5. Numerical simulation of femtosecond laser ablation at low fluence | 165 |
| 6.3. Processing of MAM by nanosecond (NS) laser sources | 168 |
| 6.3.1. Measurement of threshold fluence | 169 |
| 6.3.2. Characterisation by scanning electron microscope (SEM) technique | 171 |
| 6.3.3. Characterisation by atomic force microscope (AFM) technique | 173 |
| 6.3.4. Energy dispersive X-ray analysis | 180 |
| 6.3.5. Numerical simulation of nanosecond laser ablation at low fluence | 182 |
| 6.4. Discussion | 184 |
| 6.4.1. Femtosecond laser ablation | 185 |
| 6.4.2. Nanosecond laser ablation | 189 |
| 6.4.3. Optimisation of molybdenum-aluminium-molybdenum sample processing by femtosecond and nanosecond laser sources | 191 |
| 6.5. Chapter conclusion | 193 |
| 7. Chapter 7: Conclusions and future work | 195 |
| 7.1. Opportunities for future work | 199 |
| A. Appendix | 201 |
| Publications and other outputs | 214 |
| Publications | 214 |

| | |
|--------------------------------|-----|
| Patent..... | 214 |
| Conference presentations | 214 |
| B. References | 215 |

Abstract

Molybdenum (Mo) provides several properties that can be useful for the advanced manufacturing industries. It has found applications in touch panel, printed circuit boards and numerous electronic components. The primary goal of this study is to understand the interaction of Mo with different types of pulsed laser sources. This thesis investigates the ultrashort and short pulse laser interaction of Mo bulk, loosely adhered single-layered Mo thin film on a BK7 glass substrate and a multi-layered thin film (Mo-Al-Mo: commercially known as 'MAM').

Micron and submicron scale ablation of Mo-based structures are performed using a femtosecond (1030, 515 and 343 nm) and a nanosecond (1064, 532 and 355 nm) laser. The ablated samples were characterised using off-line techniques such as atomic force microscopy (AFM) and scanning electron microscopy (SEM). Design and implementation of in-situ spectral and real-time spatial imaging measurement of the plasma plume were undertaken for understanding the fundamentals of the interaction of laser pulse with Mo and for the comparison between the femtosecond and nanosecond laser ablation of Mo bulk and thin film. Different Multiphysics numerical simulations, based on finite element method (FEM), were developed to understand the femtosecond and nanosecond laser-Mo interaction by the evolution of temperature and thermally induced mechanical stress in these materials.

During femtosecond laser interaction with Mo bulk, a high compressive stress is established due to the rapid thermalisation of the hot electrons. At low fluence, this high stress results in the fragmentation of the Mo bulk sample. At higher fluence melting and vaporisation of Mo is observed. The molybdenum thin film ablation process was found to be dependent on the wavelength of the incident laser, duration of the laser pulse and the substrate material. The interaction of a femtosecond laser pulse with the Mo thin film leads to a formation of a high compressive stress. Above the ablation threshold, the expansion of Mo reaches its fracture limit and it leads to the mechanical fracture and delamination of the Mo thin film. The interaction of the short laser pulses with Mo thin film results in an almost uniform temperature distribution along the depth of the Mo film. At a fluence higher than the ablation threshold, the higher expansion of glass than Mo film along the normal to surface results in the fragmentation and removal of Mo thin film with significant damage of the substrate.

The existence of non-ionized ablated/removed Mo was observed from the online diagnostics of ablation mechanism by the spectral analysis of plasma plume at high fluences. From the real-time spatial imaging, it was observed that the Green and UV laser pulses produced plasma plume possess higher velocity than that produced by the IR laser pulse. This results from the interband absorption of Green and UV laser photons by the free electrons compared with the intraband absorption of IR photons.

A different laser ablation mechanism of the multi-layered samples was recognised from the mono-layered Mo-laser interaction. In the case of femtosecond laser interaction with the MAM samples, selectively material removal was observed. Formation of novel 'nano-bump' with several nanostructures of Mo is observed at a set of low fluences. This arises from the relaxation of high

compressive stress, a reflected pressure wave from the Mo/Al interface and the higher expansion of Al than Mo. Using a single femtosecond laser pulse solid state re-crystallisation of Al layer was achieved caused by the surface diffusion of Al. In the case of nanosecond laser interaction, at low fluence, the formation of 'micro-bump' is observed. These 'micro-bumps' are initiated by the expansion of sub-surface Al layer. The high-volume expansion of Al results in a ductile deformation of solid Mo layer. When the temperature cools down, the Mo surface remains strained and does not return to its initial position leading a 'micro-bump'. It is predicted that the at higher fluence range, the ablation is almost thermal. At large value of the applied laser fluence, the thermal effect dominates and results in thermal ablation.

In summary, this thesis investigates the interaction of a laser with a loosely adhered metal layers of different crystal structure, creating a new parameter space for ultrashort and short laser thin film interaction.

Declaration

The work in this thesis is based on the research carried out at the National Centre for Laser Applications (NCLA), School of Physics, National University of Ireland, Galway. I, Pinaki Das Gupta, hereby certify that this thesis has been written by me, that it is the record of work carried out by me and that it has not been submitted in any previous application for a degree or qualification.

Pinaki Das Gupta

Galway, February 2018

Acknowledgements

I would like to begin by acknowledging my academic supervisor Dr Gerard O'Connor, for giving me this opportunity. I feel grateful for your great assiduousness in my work and challenging me throughout the whole PhD process. On a personal level, one could not ask for a better advisor than Gerard. Thank you for all the motivations and providing great ideas those have been given throughout the course of the years.

I take this opportunity to express my special thanks to Dr Nazar Farid for being my friendly project advisor. I am grateful for your creative suggestion and encouragement. Thank you, Dr Miriam Byrne and Edward Coyne for their valuable output for this thesis work.

I would also like to thank Claire Bennett, Cormac O'Brien, Danijella Rostohar and Allan Connelly for their help and expertise. Thank you, Rebecca Nolan, for introducing me to the NCLA members and helping me with all the official works. Thanks, Dr Oliver Ryan, Mr James Nallen and Mr Stuart Harries for your help with the required instrumentations. Massive thanks to everyone in M-Solv in Oxford, especially Beatriz Sanchez Garcia, Helios Chan, Camilo Prieto and Tino Sin. Also, I would like to acknowledge INSPIRE programme for the financial support.

Many thanks to Dan O'Connell and his team in Tyndall in Cork for helping me with his expertise in the fabrication of thin film. Thank you, Éadaoin Timmins, for providing me help with the SEM and EDX measurements in NCBES, NUIG.

Thank you, Dr Adam Collins, for being the most amazing office mate. I count myself lucky to have had such a great colleague and gained an even better friend. Thank you, Cormac, Natalie, Nigel, Leah and Clare for providing valuable research output, ideas and recommendations. Thank you, everyone, for helping me.

My particular thanks go to Miss Edha Jain for supporting and encouraging me during this long journey. Thank you, for your endurance. I know, words are not enough to acknowledge you.

Thank you, my friend, Tanumoy Mondol for your unconditional friendship. Thank you my wonderful housemates Shejin and Roshan. I loved the time when we cook, share food, do bowling, have ice cream, play donkey and carom. I won't forget the sleepless nights and the beautiful road trips we had. I am grateful to you guys, Vijay, Arun, Pratham, Pushpalata, Swapnil and Mangesh, for your friendly support to complete my PhD work.

I would like to thank all the staff members of Smokeys for regulating the caffeine level in my body on the everyday basis. Distinctive thanks to Boojum in Galway for feeding me the delicious Burritos and free t-shirts.

Finally, I would like to thank my parents and family for their loving support throughout these many years of my education. I love you. This work is as much yours as it is mine.

List of Figures

| | |
|---|----|
| Figure 2.1: Simplified schematic of typical laser..... | 6 |
| Figure 2.2: Energy levels of the Nd:YAG laser crystal | 7 |
| Figure 2.3: Evolution of Q-switched laser pulse, adapted from [6]..... | 10 |
| Figure 2.4: Generation of highly intense short pulse laser by CPA technique | 12 |
| Figure 2.5: Schematic of CPA technique using two pairs of gratings | 13 |
| Figure 2.6: Ray diagram of the pulse compression of a chirped pulse using a pair of grating | 13 |
| Figure 2.7: Typical laser ablation process..... | 14 |
| Figure 2.8: Different types of electronic excitations in a solid. Adapted from [29] | 17 |
| Figure 2.9: Time scale of material response by ultra-fast laser excitation..... | 22 |
| Figure 2.10: Approximate time scales of nanosecond and femtosecond and laser ablation along with various process happening during and after laser pulse is given. Adapted from [104] | 23 |
| Figure 2.11: Temperature dependent thermal conductivity of molybdenum, adapted from [29, 147]..... | 27 |
| Figure 2.12: Optical penetration depth of molybdenum and its dependence with wavelength from UV to NIR region [148] | 27 |
| Figure 2.13: Electron temperature dependence of electron-phonon coupling and electronic heat capacity of molybdenum, adapted from [150]. The dashed line represents the constant value of electron-phonon coupling constant | 28 |
| Figure 3.1: Deposition of thin film by electron beam evaporation technique..... | 32 |
| Figure 3.2: The electron beam evaporation workstation with chamber with the schematic diagram during deposition..... | 33 |
| Figure 3.3: Schematic diagram inside a magnetron sputtering | 35 |
| Figure 3.4: Production line of thin film deposition by magnetron sputtering technique | 35 |
| Figure 3.5: Interference box in front of Laser head consisting of optical layout of SHG and THG pulse generation from amplified IR laser beam | 37 |
| Figure 3.6: Femtosecond laser workstation for micro processing of samples | 39 |
| Figure 3.7: HIPPO (nanosecond) workstation for material processing attached with frequency doubling module..... | 40 |
| Figure 3.8: Spatial profile of IR FS laser beam (1030 nm) at very low intensity | 41 |
| Figure 3.9: Schematic diagram of using integrating sphere (a) and the workstation development for measurement of reflectivity and transitivity using integrating sphere..... | 44 |
| Figure 3.10: Integrating sphere base | 45 |
| Figure 3.11: Spectral profile of Gaussian beam and its relationship with different laser fluence | 46 |
| Figure 3.12: The atomic force microscopy setup is enclosed in an anti-vibration chamber in order to preclude any external vibration..... | 48 |
| Figure 3.13: Scanning electron microscope system (a) and the available setup (b) with energy dispersive X-ray facility used for characterisation (Hitachi S-4700)..... | 49 |
| Figure 3.14: External triggering of femtosecond laser using a pulse generator..... | 50 |
| Figure 3.15: Relationship between pulse picker and laser pulse, Laser pulse (green) was detected after 1.036 μ s from the rising edge of MON PP pulse picker signal (yellow)..... | 51 |
| Figure 3.16: Relationship between external gate signal, external trigger signal and the laser output for the HIPPO nanosecond laser system (HIPPO Manual)..... | 52 |

| | |
|--|----|
| Figure 3.17: Quantum efficiency of different photocathodes available for ICCD device, adapted from [190]..... | 54 |
| Figure 3.18: Spatial diagram for real-time plasma imaging measurement | 54 |
| Figure 3.19: Optical arrangement for Laser-induced breakdown spectroscopy (a) with the propagation of light inside the spectrometer (b) | 56 |
| Figure 3.20: Spectral measurement of real-time spectral imaging of ablated particles. The light path to spectrometer are indicated in the figure. | 57 |
| Figure 3.21: Approximated effective lattice heat capacity of molybdenum (a) and aluminium (b) used for computational simulation | 59 |
| Figure 3.22: Temperature dependent thermal conductivity of (a) molybdenum and (b) aluminium used for simulation | 60 |
| Figure 3.23: Components of the stress tensor along X, Y and Z direction on 50 nm molybdenum thin film | 62 |
| Figure 3.24: (a) Two-dimensional experimental condition of the laser-molybdenum interaction and (b) conventional notation of the stress vector in two dimensions (X, Z) for the numerical simulation of the molybdenum thin film of thickness 50 nm..... | 63 |
| Figure 4.1: Image of damage craters on molybdenum by 1030 nm femtosecond laser at different average energies (applied) as viewed by an optical microscope (Olympus BX60M). Values of the applied pulse energy are listed. | 66 |
| Figure 4.2: Measurement of single pulse (a) applied and (b) absorbed threshold fluence of molybdenum by 1030 nm, 515 nm and 343 nm femtosecond laser. The intercept of the linear fit at $Y = 0$ determines the peak value of the threshold fluence | 67 |
| Figure 4.3: Two temperature modelling of 500 fs (at FWHM) IR laser pulse using finite element method and evolution of electron and lattice temperature at a fluence of 0.3 Jcm^{-2} (absorbed) temperature in the bulk molybdenum. The electron-phonon coupling constant used for this simulation is $13.6 \times 10^{16} \text{ Wm}^{-1}\text{K}^{-1}$ | 68 |
| Figure 4.4: Prediction of melting and evaporation threshold fluence for bulk molybdenum, when exposed to a single 1030 nm femtosecond laser pulse..... | 69 |
| Figure 4.5: Variation of r.m.s. roughness of molybdenum craters with peak laser fluence (absorbed)..... | 70 |
| Figure 4.6: Temporal behaviour of lattice temperature of bulk molybdenum under the influence of Gaussian shaped nanosecond laser of fluence 0.2, 0.5, 1.0 and 1.5 Jcm^{-2} (absorbed). T_m and T_v are the melting and evaporation temperature of molybdenum, respectively. | 71 |
| Figure 4.7: Removal of the molybdenum film from the glass substrate, as observed from the optical microscope image, Optical microscope image reveals an increase of crater diameter with higher absorbed 1030 nm femtosecond laser fluence | 73 |
| Figure 4.8: Estimation of threshold fluence (absorbed) of molybdenum thin film using 1030 nm, 515 nm and 343 nm femtosecond laser sources. The extrapolate values provide the peak value of absorbed threshold fluence | 74 |
| Figure 4.9: (a) Fragmentation of the molybdenum thin film surrounding the ablated crater (peak value of absorbed fluence: 0.3 Jcm^{-2}) and (b) electrostatic charging in glass during the interaction of high energy electron beam with non-conductive glass substrate is also evident; the peak value of the absorbed fluence is 0.1 Jcm^{-2} | 75 |
| Figure 4.10: (a) Delamination of molybdenum film as a result of interaction with 500 femtoseconds laser source of wavelength of 1030 nm and (b) molybdenum surface at a fluence | |

| | |
|--|----|
| of 0.1 Jcm ⁻² . A thin layer of gold was coated on the laser processed molybdenum thin film to avoid the charging | 76 |
| Figure 4.11: SEM images of single pulse IR FS processed molybdenum film on glass substrate at different peak absorbed fluences | 77 |
| Figure 4.12: Strained molybdenum film after incidence of 1030 nm femtosecond laser just about the ablation threshold | 78 |
| Figure 4.13: Femtosecond laser processed molybdenum thin film using 515 and 343 nm wavelength at different peak absorbed fluences..... | 78 |
| Figure 4.14: (a) 1030 nm femtosecond laser produced damage on 50 nm molybdenum film at an absorbed fluence of 0.1 Jcm ⁻² . (b) The extraction of the profile from AFM image indicates that substrate surface below the film is damage free except for contamination by particulate. The dashed line indicates the position where the profile extraction of the crater was measured..... | 79 |
| Figure 4.15: Profile extraction from AFM image reveals femtosecond laser processing of molybdenum film results damage free substrate. The dashed line on the AFM images corresponds the line from where the surface profile was extracted | 80 |
| Figure 4.16: Removal of molybdenum film at low fluence (Femtosecond, 515 nm, Peak value of the absorbed fluence: 0.028 Jcm ⁻²)..... | 81 |
| Figure 4.17: Optical microscope image of molybdenum thin film using single pulse 1064 nm nanosecond laser by varying energy of laser pulse | 81 |
| Figure 4.18: Estimation of the threshold fluence (absorbed) of molybdenum thin film by 1064 nm, 532 nm and 355 nm nanosecond laser sources. The insert presents the extrapolation of the linear fit at Y=0, and corresponds the value of ablation threshold at three different wavelengths | 82 |
| Figure 4.19: SEM images of single pulse nanosecond laser (wavelength 1064 nm) processed molybdenum film on glass substrate at different fluences. The peak value of the absorbed fluences are indicated with each crater..... | 83 |
| Figure 4.20: Selective removal of molybdenum film a low fluence, just above peak absorbed ablation threshold. Presents fracture in molybdenum thin film. A small increase of the fluence leads to removal of molybdenum thin film from the glass substrate | 84 |
| Figure 4.21: (a) Atomic force microscope image shows complete film removal during by nanosecond laser (wavelength: 1064 nm, peak fluence 0.1 Jcm ⁻²) ablation with (b) the profile extraction of the AFM image corresponds significant damage in the substrate. Evidence for glass damage was observed in centre of the crater..... | 84 |
| Figure 4.22: AFM microscopy images at different absorbed fluences. Profile extraction from AFM image reveals femtosecond laser processing of molybdenum film results complete film removal with significant damage on the substrate. The dashed line on the AFM images corresponds the line from where the surface profile was extracted | 85 |
| Figure 4.23: Transient temperature increase of electronic and lattice subsystem with a normalised laser intensity in a thin film. The peak absorbed fluence was chosen to be was 0.1 Jcm ⁻² and the electron-phonon coupling coefficient selected from [150] | 86 |
| Figure 4.24: The variation in the peak temperature of the lattice for different depths in the molybdenum thin film and near surface region of the glass substrate at different times after the peak pulse (peak absorbed fluence 0.1 Jcm ⁻²) was applied to the materials | 87 |
| Figure 4.25: Transient expansion of compressive stress (σ_{xx}) at the film surface | 88 |

| | |
|---|-----|
| Figure 4.26: Compressive stress (σ_{XX}) at different depth from molybdenum film surface to the molybdenum-substrate interface. The insert shows the Cartesian coordinate system and the direction of the different stress components..... | 89 |
| Figure 4.27: Transient nature of the peak orthogonal stress (σ_{ZZ}) the magnitude of the lateral compressive stress (σ_{XX}) at the thin film-glass interface..... | 90 |
| Figure 4.28: The increase of the temperature of electronic (blue line) and lattice (black line) subsystem with a normalised arbitrary laser intensity (red line). The peak value of the laser pulse intensity was taken at 0.5 picoseconds from an arbitrary reference. A temperature independent value of the electron-phonon coupling constant was used for the simulation..... | 92 |
| Figure 4.29: Thermal response of lattice temperature at the surface of the molybdenum thin film ($Z=0$) after incident of nanosecond laser of absorbed fluence 0.1 and 0.05 Jcm^{-2} . The peak temperature of the lattice occurs in the film 4 ns after the laser pulse. The peak temperature of the lattice does not exceed the melting temperature of molybdenum. | 93 |
| Figure 4.30: The variation in the peak temperature of the lattice for different depths in the molybdenum thin film and near surface region of the glass substrate at different time after the peak pulse was applied to the materials at a reference time of 20 ns duration | 94 |
| Figure 4.31: Magnitude of the compressive stress (σ_{XX}) at the film surface and interface during nanosecond laser ablation..... | 95 |
| Figure 4.32: Transient behaviour of expansion stress (σ_{ZZ}) and strain (ϵ_{ZZ}) at molybdenum film and the interface during nanosecond laser ablation. The peak tensile stress was observed 4 ns prior to the peak vertical strain..... | 96 |
| Figure 5.1: Wavelength-dependent intensity response calibration of Andor iStar ICCD and spectrometer, (a) standard and observed intensity of standard light source was used to determine response curve (b) of the spectrometer and Andor iStar ICCD. | 107 |
| Figure 5.2: Laser-induced breakdown spectroscopy (LIBS) intensities of 1030 nm femtosecond laser ablated molybdenum bulk sample at different absorbed fluences..... | 108 |
| Figure 5.3: Peak LIBS intensity for the six major molybdenum peaks (550.65, 553.31, 557.04, 563.23, 568.91 and 575.14 nm) as a function of absorbed fluence by 1030 nm femtosecond laser. The peak intensity is found the increase with increase peak absorbed fluence | 110 |
| Figure 5.4: Laser-induced breakdown spectroscopy (LIBS) intensities of 1030 nm femtosecond laser ablated 50 nm molybdenum thin film at various absorbed fluences | 111 |
| Figure 5.5: Laser-induced breakdown spectroscopy (LIBS) intensities of 1064 nm nanosecond laser abated 50 nm molybdenum thin film at various absorbed fluences | 113 |
| Figure 5.6: Time-resolved plasma plume generated from the molybdenum bulk samples after the interaction of 1030 nm femtosecond laser pulse at fluences (absorbed) 1, 1.5 and 2 Jcm^{-2} . The MCP gain used for this study was 170. | 117 |
| Figure 5.7: Time-resolved plasma plume generated from the molybdenum bulk samples after the interaction of 515 nm femtosecond laser pulse at fluences (absorbed) 1, 1.5 and 2 Jcm^{-2} ; the MCP gain value used for this study was 100..... | 118 |
| Figure 5.8: Time-resolved plasma plume generated from the molybdenum bulk samples after the interaction of 343 nm femtosecond laser pulse at fluences (absorbed) 1, 1.5 and 2 Jcm^{-2} ; the MCP gain value used for this study was 220..... | 118 |
| Figure 5.9: Vertical intensity distribution of the emission from the plasma plume, through the centre of the plasma ($X=0$, $Y=0$), after the interaction of molybdenum bulk with the femtosecond laser pulse of wavelength of (a) 1030 nm (b) 515 nm and (c) 343 nm using an absorbed fluence of 1 Jcm^{-2} | 119 |

| | |
|---|-----|
| Figure 5.10: Vertical distance travelled plasma front at 1, 1.5 and 2.0 Jcm ⁻² produced by 1030 nm femtosecond laser. | 120 |
| Figure 5.11: Spatial distribution of ejected elements at long delay for a peak absorbed fluence of 1 Jcm ⁻² using wavelength of 1030 nm. The surface of the sample is represented by the black dotted line. Reflection of the plume from the surface of the target resulted in the presence of a light signal was detected at the images below the surface of the target. | 122 |
| Figure 5.12: Time-resolved plasma plume generated from the 50 nm thin molybdenum thin film after the interaction of 1030 nm femtosecond laser pulse at peak fluences (absorbed) of 1.0, 1.5 and 2.0 Jcm ⁻² . The MCP gain used for this study is 220. | 123 |
| Figure 5.13: Time-resolved plasma plume generated from the 50 nm thin molybdenum thin film after the interaction of 1030 nm femtosecond laser pulse at peak fluences (absorbed) of 0.5, 1.0 and 1.5 Jcm ⁻² . The MCP gain used for this study is 200. | 124 |
| Figure 5.14: Vertical intensity distribution of the emission from the plasma plume, through the centre of the plasma (X=0, Y=0), after the interaction of molybdenum thin film with the femtosecond laser pulse of wavelength of (a) 1030 nm and (b) 515 nm using an absorbed fluence of 1 Jcm ⁻² | 125 |
| Figure 5.15: Vertical intensity distribution of the emission from the plasma plume, through the centre of the plasma (X=0, Y=0), after the interaction of molybdenum thin film with the femtosecond laser pulse of wavelength of (a) 1030 nm and (b) 515 nm using an absorbed fluence of 2 Jcm ⁻² | 126 |
| Figure 5.16 Propagation of plasma front at various absorbed fluencies values using 1030 laser wavelength..... | 127 |
| Figure 5.17: Propagation of delaminated film edge at various absorbed fluencies values using 1030 laser wavelength..... | 127 |
| Figure 5.18: Spatial image (a) and intensity profile (b) of the plasma plume at a time delay of 300 ns for 1030 nm femtosecond laser fluence of 0.5, 1, 1.5 and 2 Jcm ⁻² | 130 |
| Figure 5.19: Expansion of 1030 nm single pulse femtosecond laser (absorbed fluence 1 Jcm ⁻²) produced Molybdenum thin film plume at delay of 200, 500 and 1000 ns. The gate width was kept at 100 ns. The black dotted line represents the top surface of the thin film. | 131 |
| Figure 5.20: Expansion of 1064 nm nanosecond laser produced plasma plume on molybdenum thin film at absorbed fluence of 1.0, 1.5 and 2.0 Jcm ⁻² | 132 |
| Figure 5.21: Expansion of 532 nm nanosecond laser produced plasma plume on molybdenum thin film at absorbed fluence of 1.0, 1.5 and 2.0 Jcm ⁻² | 133 |
| Figure 5.22: Expansion of 355 nm nanosecond laser produced plasma plume on molybdenum thin film at absorbed fluence of 1.0, 1.5 and 2.0 Jcm ⁻² | 133 |
| Figure 5.23: Distance travelled by the faster moving part of the plasma plume using the interaction of nanosecond laser (wavelength: 1064 nm) with molybdenum thin film samples at 0.5, 1, 1.5, and 2 Jcm ⁻² fluence values..... | 134 |
| Figure 5.24: Plasma plume imaging of molybdenum film on glass at various gate width (exposure time) at a fluence of 0.1 Jcm ⁻² using 1064 nm nanosecond laser, indicates removal of film..... | 136 |
| Figure 5.25: Expansion of 1064 nm single pulse nanosecond laser (absorbed fluence 0.5 Jcm ⁻²) produced Molybdenum thin film plume at delay of 200, 500 and 1000 ns..... | 137 |
| Figure 5.26: Estimated number of electron emitted per unit area per unit time from molybdenum with corresponding electron temperature..... | 140 |

| | |
|--|-----|
| Figure 5.27: Numerical simulation predicts increase of absorbed fluence leads to increase of peak temperature of electron. At a particular fluence, 515 nm laser produced electron becomes hotter than electrons generated by 1030 nm laser pulse..... | 141 |
| Figure 5.28: Electronic band structure of bcc molybdenum crystal, adapted from [248]. The insert shows the possibility of interband absorption during interaction of Green and UV laser photon with molybdenum sample, adapted from [248]. | 142 |
| Figure 6.1: Optical microscope images of different craters on MAM surface at different absorbed fluences using 1030, 515 and 343 nm single pulse femtosecond laser..... | 146 |
| Figure 6.2: Nomenclature of different diameters created on multi-layered MAM surface at (a) low (0.29 Jcm^{-2}) and (b) high (3.77 Jcm^{-2}) fluence, wavelength 1030 nm, as observed by the optical microscope..... | 147 |
| Figure 6.3: Optical microscope image of crater on MAM surface after irradiation of 515 nm femtosecond laser of fluence 6.6 Jcm^{-2} , numerical aperture (NA) of the focusing lens: 0.13. ... | 147 |
| Figure 6.4: Understanding of different fluence regimes associated with the various diameters on MAM surface by a spatially Gaussian femtosecond laser source. | 148 |
| Figure 6.5: The relationship between the squared diameter and logarithmic fluence to determine different threshold fluence associated with the square diameters D1, D2 and D3, for a femtosecond laser of a wavelength at 1030, 515 and 343 nm. | 149 |
| Figure 6.6: Scanning electron microscope images of a 1030 nm laser created craters at different peak absorbed fluences, indicated with each image. The spot radius of the laser beam (peak intensity of laser beam drops to $1/e^2$ times) is $26.55 \mu\text{m}$ | 151 |
| Figure 6.7: Scanning electron microscope images of a 515 nm laser created craters at different peak absorbed fluences, indicated with each image. A fixed lens (NA: 0.13) was used to achieve smaller spot size and thus higher fluence to get D4 on the MAM surface. The spot radius of the galvanometer and fixed lens are 22.08 and $8.2 \mu\text{m}$, respectively..... | 152 |
| Figure 6.8: Scanning electron microscope images of 343 nm laser created craters at different peak absorbed fluences, indicated with each image. The spot radius of the laser beam (peak intensity of laser beam drops to $1/e^2$ times) is $16.96 \mu\text{m}$ | 153 |
| Figure 6.9: Structural difference of fluence regimes among $F < F^{D1}$, $F^{D1} < F < F^{D2}$ and $F^{D1} < F < F^{D2}$ for 1030, 515 and 343 nm laser wavelength, respectively. Corresponding peak fluence for b, d and f are 2.49 , 0.93 and 1.23 Jcm^{-2} | 154 |
| Figure 6.10: Optical changes between the fluence regime $F < F^{D1}$ and $F^{D1} < F < F^{D2}$, where F^{D1} and F^{D2} present laser exposed, and unexposed laser treated the area, respectively..... | 155 |
| Figure 6.11: Several nano-cracks was observed at the centre of the region defined by the peak fluence $F^{D2} < F < F^{D3}$ for (a) 1030, (b) 515 and (c) 343 nm laser wavelength at fluence value of 0.29 , 0.56 and 0.22 Jcm^{-2} , respectively. | 155 |
| Figure 6.12: Structural modification of MAM layer at a region defined by $F^{D2} < F < F^{D3}$ from $F^{D1} < F < F^{D2}$ by 1030 (a), 515 and 343 nm femtosecond laser ablation at 1.98 , 1.59 and 1.23 Jcm^{-2} , respectively. | 156 |
| Figure 6.13: Delamination of molybdenum layer at the edge of the fluence regime defined by, $F^{D3} < F$ during femtosecond laser ablation using 1030, 515 and 343 nm wavelength. | 156 |
| Figure 6.14: Increase in grain size of the layer at the peak fluence $F^{D3} < F < F^{D4}$ with increasing laser (515 nm) fluence. The value of absorbed fluence associated with images a, b, c and d are 0.64 , 0.81 , 1.39 and 1.98 Jcm^{-2} | 157 |
| Figure 6.15: Several nano-cracks at the centre of fluence regime $F > F^{D4}$ for 343 nm femtosecond laser, with a delamination of another layer. | 158 |

| | |
|---|-----|
| Figure 6.16: Atomic for microscope (AFM) images of 1030 nm femtosecond laser induced craters with a corresponding surface profile at different fluences, showing the maximum depth. Radius of the laser beam was set at $29.06 \pm 0.002 \mu\text{m}$ | 159 |
| Figure 6.17: Atomic for microscope (AFM) images of 515 nm femtosecond laser induced craters with a corresponding surface profile at different fluences, showing the maximum depth. The beam radius of the 515 nm laser spot at the surface of MAM is $22.08 \pm 0.001 \mu\text{m}$ | 160 |
| Figure 6.18: Atomic for microscope (AFM) images of 343 nm femtosecond laser induced craters with a corresponding surface profile at different fluences, showing the maximum depth. The beam radius of the 343 nm laser spot at the surface of MAM is $16.96 \pm 0.005 \mu\text{m}$ | 161 |
| Figure 6.19: Electron microscope image presents ablated craters at three peak fluences, and the elemental analysis was carried out at different fluence regimes | 163 |
| Figure 6.20: Cartesian geometry used for the simulation of temperature evolution in MAM during femtosecond laser ablation. The incident laser beam diameter was set at $2 \mu\text{m}$ | 166 |
| Figure 6.21: Two temperature modelling of femtosecond laser interaction (FWHM 500 fs, wavelength 1030 nm) with MAM sample at the peak absorbed fluence of (a) 0.068 and (b) 0.133 Jcm^{-2} . The black and blue line indicate the time dependent electronic and lattice temperature, respectively. The red line indicates normalised intensity of the laser beam. | 166 |
| Figure 6.22: Transient behaviour of the lattice temperature at different depths of the MAM sample indicate the temperature of the molybdenum does not exceed the melting temperature, while solid to liquid phase change take place at the aluminium layer after the interaction with femtosecond laser at the peak absorbed fluence of (a) 0.068 and (b) 0.133 Jcm^{-2} | 167 |
| Figure 6.23: Optical microscope images of different craters on MAM surface at different absorbed fluences using 1064, 532 and 355 nm single pulse nanosecond laser. | 168 |
| Figure 6.24: Nomenclatures of different diameters created on multi-layered MAM surface at (a) low (0.35 Jcm^{-2}) and (b) high (1.46 Jcm^{-2}) fluence, wavelength 1064 nm | 169 |
| Figure 6.25: Relationship between squared diameter and logarithmic fluence to determine different threshold fluence associated with the square diameters D1, D2 and D3, for a nanosecond laser of a wavelength at 1064, 532 and 355 nm. | 170 |
| Figure 6.26: Scanning electron microscope images of a 1064 nm nanosecond laser created craters at different absorbed peak fluences, indicated with each image. The spot radius of the laser beam is $19.96 \pm 0.002 \mu\text{m}$ | 172 |
| Figure 6.27: Scanning electron microscope images of a 532 nm nanosecond laser created craters at different absorbed peak fluences, indicated with each image. The spot radius of the laser beam is $16.49 \pm 0.004 \mu\text{m}$ | 172 |
| Figure 6.28: Scanning electron microscope images of a 355 nm nanosecond laser created craters at different absorbed peak fluences, indicated with each image. The spot radius of the laser beam is $21.01 \pm 0.001 \mu\text{m}$ | 173 |
| Figure 6.29: Atomic for microscope (AFM) images of 1064 nm nanosecond laser induced craters with a corresponding surface profile at different peak fluences, showing the maximum depth. The spot radius of the 1064 laser beam at the sample surface was set at $19.27 \mu\text{m}$ | 174 |
| Figure 6.30: Atomic for microscope (AFM) images of 532 nm nanosecond laser induced craters with a corresponding surface profile at different peak fluences, showing the maximum depth. The spot radius of the 532 laser beam at the sample surface was set at $20.22 \mu\text{m}$ | 175 |
| Figure 6.31: Atomic for microscope (AFM) images of 355 nm nanosecond laser induced craters with a corresponding surface profile at different peak fluences, showing the maximum depth. The spot radius of the 355 laser beam at the sample surface was set at $21.10 \mu\text{m}$ | 176 |

| | |
|---|-----|
| Figure 6.32: Surface of MAM without any interaction with the laser beam, showing grain structure on MAM surface using (a) SEM and (b) AFM techniques | 177 |
| Figure 6.33: Change in surface morphology at the ‘micro-bump’ with increasing laser fluence. Figure (a), (b) and (c) represent crater with peak absorbed fluences of (a) 0.317, (b) 0.337 and (c) 0.357 Jcm ⁻² , respectively. | 178 |
| Figure 6.34: Formation of micro bumps on the surface of MAM surface and the difference in surface morphology between two fluence regimes, $F^{D1} < F < F^{D2}$ and $F^{D2} < F < F^{D3}$, wavelength 355 nm. | 178 |
| Figure 6.35: Permanent deformation of the surface of MAM with the initiation of fracture from the centre of the crater. The craters correspond to the peak absorbed fluences of 0.482, 0.505 and 0.536 Jcm ⁻² | 178 |
| Figure 6.36: Different surface structures on MAM surface after irradiation of a nanosecond laser pulse indicating different ablation phenomena and the surface profile across these craters present a change in height between sample surfaces. | 179 |
| Figure 6.37: Atomic force micrograph of ablated crater at peak fluence of 0.63 Jcm ⁻² (a), the close-up inspection (b) shows significant substrate damage at the core of the crater, wavelength 532 nm | 180 |
| Figure 6.38: Electron microscope image presents ablated craters at four peak fluences, and the elemental analysis were carried out at different fluence regimes, wavelength 532 nm | 180 |
| Figure 6.39: The transient peak lattice temperature on the surface $Z = 0$ and $Z = -40$ nm, resulted from the interaction of nanosecond laser (wavelength 1064 nm, pulse width 9 ns) of the fluences of (a) 0.155 and (b) 0.309 Jcm ⁻² . At the fluence 0.155 Jcm ⁻² , the peak temperature of aluminium layer just exceeds the melting temperature..... | 182 |
| Figure 6.40: Peak temperature at different time delays as a function of the depth of the multi-layered MAM film at the peak fluences of (a) 0.155 and (b) 0.309 Jcm ⁻² . Nanosecond laser pulse of wavelength of 1064 nm and pulse width of 9 ns was used as a source. | 183 |
| Figure 6.41: Thermally induced strain (ϵ_{zz}) at different layers of the MAM sample at the peak fluence of (a) 0.155 and (b) 0.309 Jcm ⁻² . First (40 nm), second (430 nm), third (30 nm) and fourth (34 nm) layers correspond molybdenum, aluminium, molybdenum and ITO film, respectively and presented in the Figure 6.20. | 184 |
| Figure 6.42: Cross-section of the MAM sample indicate the source of the induced pressure due to the thermal expansion of different layers at the peak fluence of (a) 0.155 and (b) 0.309 Jcm ⁻² | 184 |
| Figure 6.43: Predicted early removal mechanism of molybdenum thin film from aluminium layer | 187 |
| Figure 6.44: Delamination mechanism of molybdenum from the aluminium layer. The separation between molybdenum and aluminium results is less conduction of thermal energy from molybdenum to aluminium..... | 187 |
| Figure 7.1: A summary of laser molybdenum processing..... | 199 |
| Figure 7.2: Scanning electron microscopy image of a crater on the surface of MAM, produced by a 515 nm femtosecond laser pulse at a fluence of 0.56 Jcm ⁻² . The right image shows the magnified view of the centre of the crater shows several nanostructures on the MAM surface | 200 |
| Figure A.1: Dependence of peak femtosecond LIBS intensity of molybdenum thin film centred at 550.65, 553.31, 557.04, 563.23, 568.81 and 575.14 nm by different fluences. | 201 |
| Figure A.2: Dependence of peak nanosecond LIBS intensity of molybdenum thin film centred at 550.65, 553.31, 557.04, 563.32 and 575.14 nm by different fluences..... | 201 |

| | |
|--|-----|
| Figure A.3: Vertical distance travelled by 515 nm produced plasma plume front at 1, 1.5 and 2.0 Jcm ⁻² | 202 |
| Figure A.4: Vertical distance travelled by 343 nm, femtosecond laser produced plasma plume front at specific fluences | 202 |
| Figure A.5: Propagation of 515 nm femtosecond laser produced plasma front of molybdenum thin film at different fluence values | 203 |
| Figure A.6: Propagation of delaminated film edge at different peak absorbed fluence (0.25, 0.5 and 1 Jcm ⁻²) values using 515 nm laser wavelength | 203 |
| Figure A.7: Distance travelled by the faster moving part of the plasma plume using the interaction of nanosecond laser (wavelength: 532 nm) with molybdenum thin film samples at 0.5, 1, 1.5, and 2 Jcm ⁻² fluence values | 204 |
| Figure A.8: Distance travelled by the faster moving part of the plasma plume using the interaction of nanosecond laser (wavelength: 355 nm) with molybdenum thin film at 0.5, 1, 1.5, and 2 Jcm ⁻² fluence values | 204 |

List of Tables

| | |
|--|-----|
| Table 2.1: Various parameters of an Nd:YAG laser system..... | 8 |
| Table 2.2: Different laser ablation mechanisms [29] | 14 |
| Table 2.3: Different physical and chemical properties of molybdenum [29, 143-145]..... | 26 |
| Table 3.1: Thickness and sheet resistance of the multilayered heterostructure | 36 |
| Table 3.2: Technical specifications of Amplitude systems S-Pulse HP femtosecond laser..... | 38 |
| Table 3.3: Technical specifications of nanosecond HIPPO laser system..... | 40 |
| Table 3.4: Transmission (%) of laser pulse through the beam delivery system..... | 43 |
| Table 3.5: Different features of the cantilever probe used in AFM measurements [142] | 48 |
| Table 3.6: Thermal parameters for heat diffusion model | 58 |
| Table 3.7: COMSOL coefficients for material processing for stress/strain simulation..... | 60 |
| Table 4.1: Reflectivity measurement of bulk molybdenum by integrating sphere | 64 |
| Table 4.2: Optical penetration depth of different laser wavelengths in molybdenum [55, 202].. | 65 |
| Table 4.3: Reflected and transmitted fraction of incident femtosecond and nanosecond laser by 50 nm thick molybdenum thin film on BK7 optical glass substrate | 72 |
| Table 4.4: Fraction of incident laser light absorbed by molybdenum film of thickness 50 nm.... | 72 |
| Table 4.5: Absorbed threshold fluence at different femtosecond laser wavelength | 74 |
| Table 4.6: Absorbed threshold fluence at different nanosecond laser wavelength..... | 82 |
| Table 4.7: Comparison of the inner diameter on the glass substrate measured by an optical microscope with the numerically estimated diameter where the temperature of glass reaches its melting temperature..... | 97 |
| Table 5.1: Term designation and energy of the upper and lower electronic levels with transition probability of neutral molybdenum (Mo I) atom [6]..... | 103 |
| Table 5.2: Term designation and energy of the upper and lower electronic levels with transition probability of singly ionised molybdenum atom (Mo II) | 104 |
| Table 5.3: Variation of the background intensity, FWHM, area and the height of the Lorentzian curve centred at a wavelength of 550.65 nm (interaction of molybdenum bulk with ultra-short pulsed laser) | 109 |
| Table 5.4: Variation of the background intensity, height, FWHM and area under the fitted Lorentzian curve centred at 550.65 nm at different peak fluences (interaction of molybdenum thin film with ultra-short pulsed laser)..... | 112 |
| Table 5.5: Variation of the background intensity, height, FWHM and area under the fitted Lorentzian curve centred at 550.65 nm at different peak fluences (interaction of molybdenum thin film with short pulsed laser) | 114 |
| Table 5.6: Estimated ‘stopping distance’, ‘average velocity’ and ‘deceleration coefficient’ of the faster-moving plasma plume front of bulk molybdenum after exposure of 1030, 515 and 343 nm femtosecond laser at the fluence of 2, 1.5 and 1 Jcm ⁻² | 121 |
| Table 5.7: The stopping distance, average velocity and the deceleration coefficients of fast components of the plasma plume produced by the interaction of molybdenum thin film with femtosecond laser of wavelength of 1030, 515 nm at different peak absorbed fluences | 128 |
| Table 5.8: The stopping distance, average velocity and the deceleration coefficients of slow components femtosecond laser produced plasma using wavelength of the 1030, 515 nm at different peak value of absorbed fluences..... | 129 |

| | |
|---|-----|
| Table 5.9: The stopping distance, average velocity and the deceleration coefficients of fast components of the 1064, 532 and 355 nm plasma plume at different fluences (absorbed). | 135 |
| Table 6.1: Reflectivity (R) of multi-layered MAM under femtosecond and nanosecond laser pulse using an integrating sphere..... | 145 |
| Table 6.2: The estimated threshold fluence required to produce the diameters D1, D2 and D3 by femtosecond laser ablation using 1030, 515 and 343 nm wavelength. | 150 |
| Table 6.3: Atomic percentage of detected elements at different femtosecond fluence regimes using EDX technique..... | 165 |
| Table 6.4: Estimated threshold fluence require to get the diameters D1 and D2 by nanosecond laser ablation using 1064, 532 and 355 nm wavelength | 171 |
| Table 6.5: Atomic percentage of detected elements at different nanosecond fluence regimes using EDX technique..... | 181 |
| Table 6.6: Preferred parameters to process molybdenum-aluminium-molybdenum sample by femtosecond and nanosecond laser sources | 191 |
| Table 6.7: Comparison of cost of a G10 sheet processed by femtosecond and nanosecond laser pulses..... | 192 |
| Table A.1: Variation of the background intensity, FWHM, area and the height of the Lorentzian curve centred at a wavelength of 553.31 nm (interaction of molybdenum bulk with ultra-short pulsed laser) | 205 |
| Table A.2: Variation of the background intensity, FWHM, area and the height of the Lorentzian curve centred at a wavelength of 557.04 nm (interaction of molybdenum bulk with ultra-short pulsed laser) | 205 |
| Table A.3: Variation of the background intensity, FWHM, area and the height of the Lorentzian curve centred at a wavelength of 563.23 nm (interaction of molybdenum bulk with ultra-short pulsed laser) | 206 |
| Table A.4: Variation of the background intensity, FWHM, area and the height of the Lorentzian curve centred at a wavelength of 568.91 nm (interaction of molybdenum bulk with ultra-short pulsed laser) | 207 |
| Table A.5: Variation of the background intensity, FWHM, area and the height of the Lorentzian curve centred at a wavelength of 575.14 nm (interaction of molybdenum bulk with ultra-short pulsed laser) | 207 |
| Table A.6: Variation of the background intensity, height, FWHM and area under the fitted Lorentzian curve centred at 553.31 nm at different peak fluences (interaction of molybdenum thin film with ultra-short pulsed laser)..... | 208 |
| Table A.7: Variation of the background intensity, height, FWHM and area under the fitted Lorentzian curve centred at 557.04 nm at different peak fluences (interaction of molybdenum thin film with ultra-short pulsed laser)..... | 209 |
| Table A.8: Variation of the background intensity, height, FWHM and area under the fitted Lorentzian curve centred at 563.23 nm at different peak fluences (interaction of molybdenum thin film with ultra-short pulsed laser)..... | 209 |
| Table A.9: Variation of the background intensity, height, FWHM and area under the fitted Lorentzian curve centred at 568.91 nm at different peak fluences (interaction of molybdenum thin film with ultra-short pulsed laser)..... | 210 |
| Table A.10: Variation of the background intensity, height, FWHM and area under the fitted Lorentzian curve centred at 575.14 nm at different peak fluences (interaction of molybdenum thin film with ultra-short pulsed laser)..... | 210 |

| | |
|--|-----|
| Table A.11: Variation of the background intensity, height, FWHM and area under the fitted Lorentzian curve centred at 553.31 nm at different peak fluences (interaction of molybdenum thin film with short pulsed laser) | 211 |
| Table A.12: Variation of the background intensity, height, FWHM and area under the fitted Lorentzian curve centred at 557.04 nm at different peak fluences (interaction of molybdenum thin film with short pulsed laser) | 212 |
| Table A.13: Variation of the background intensity, height, FWHM and area under the fitted Lorentzian curve centred at 563.23 nm at different peak fluences (interaction of molybdenum thin film with short pulsed laser) | 212 |
| Table A.14: Variation of the background intensity, height, FWHM and area under the fitted Lorentzian curve centred at 568.91 nm at different peak fluences (interaction of molybdenum thin film with short pulsed laser) | 213 |
| Table A.15: Variation of the background intensity, height, FWHM and area under the fitted Lorentzian curve centred at 575.14 nm at different peak fluences (interaction of molybdenum thin film with short pulsed laser) | 213 |

Chapter 1: Introduction

LASER (acronym of ‘Light amplification by stimulated emission of radiation’) is a powerful source of light that has extraordinary properties which are not found in the conventional light sources. It is the device that generates and amplifies electromagnetic radiation, wavelength ranging from the near infrared (NIR) region up through the visible region (VIS) and extending to the ultraviolet (UV) and recently even to the X-ray region [1].

Because of the uniqueness of the laser sources, soon after the discovery, it is being used for countless applications such as in defence, medical, astronomy, optical fibre communication, seismography, power engineering, spectroscopy, data storage, holography, chemistry, scientific research e.g. nuclear fusion, spectroscopy and material processing. New fields are opened in science and technology. Lasers are used as a versatile tool to study the physics of the interaction of light with matter. It is also a valuable instrument for spectroscopic analysis, such as Raman, atomic, LIBS (laser induced breakdown spectroscopy).

The laser material processing is one of the most important industries to have developed following the invention of the laser. It offers many advantages over more traditional materials processing techniques. It is a non-contact tool in which the optical energy is delivered to the target material, where it can be converted into photothermal, photochemical and photomechanical energy. Depending on the type of laser-material interaction, material removal may occur by melting and subsequent melt ejection, by direct vaporisation, by the breaking of chemical bonds, or by the mechanical interactions by which the material disintegrates due to the stress involved with rapid heating and expansion. On the other hand, traditional machining processes rely on mechanical stresses induced by the tools to break the bonds between the constituent elements or molecules of the material. Laser material processing can be applied to any material that can appropriately absorb the laser irradiation; traditional machining process requires suitable tools for the material with different levels of hardness and abrasiveness. It is difficult to machine hard or brittle materials such as ceramics using traditional methods whereas the laser is a good choice for such applications.

Although the laser micromachining is widely employed in the manufacturing industry nowadays, a full understanding of various phenomena involved in the laser micromachining is still a matter of trials and speculations. The micromachining of different materials is essential in today’s advanced manufacturing, of, e.g., touch panels, printed circuit boards and electronic components. It is imperative to recognise the physics of laser material interaction to achieve a clean, damage free and economically efficient processing to meet industrial demands. The interaction of laser pulse with materials enables us to explore various physical process involved. Experiments reveal that proper selection of laser parameters such as pulse duration, polarisation, fluence, repetition rate, etc., as well as other parameters such as ambient pressure, which are all critical to produce desired results. The dissertation attempts are to investigate the short and ultra-short laser ablation phenomena and to increase the efficiency of laser structuring of molybdenum materials.

Molybdenum (Mo) is an attractive material because of its half-filled d-band electronic configuration ($[\text{Kr}] 5s^1 4d^5$). Because of its half field electronic configuration, it is very stable

material. As molybdenum has high melting (2887 K) and evaporation (4913 K) temperatures; it is used as a thermal shock resistant layer. Molybdenum is also used in missile, aircraft, and filament materials and as the electrodes (anode) in electrically heated glass furnaces. Because of the high reflectivity, it is used as a thin film mirror. Molybdenum is of huge interest to photovoltaics as it is used as a back contact for various solar cells such as CIGS, CZTS and CdTe. Molybdenum-based compounds such as molybdenum disulphide (MoS_2) and molybdenum diselenide (MoSe_2) are promising for solar energy conversion as they have band gaps falling in the visible or near infrared regime.

Similar to the heavy material tungsten (W), molybdenum is a hard and brittle material, and it is comparatively difficult to process by a laser compared with other metals, such as gold, copper, aluminium, etc. It is important to select specific laser parameters to process molybdenum thin film for an efficient micro-machining. Laser processing of molybdenum, commonly known as P1 scribing, is essential to create a monolithically interconnected integrated device in photovoltaic applications. Molybdenum has a growing interest in touch panel devices, where molybdenum is served as a thermally resistant layer. Precision processing of molybdenum is required to achieve desirable printable electronic circuit fabrication. An efficient processing of molybdenum based devices calls for an in-depth understanding of the interaction of laser with molybdenum.

The motivation for this study is to understand the various process involved in the interaction of laser with molybdenum, to micro-structure of a multilayered thin film assembly for touch panel applications.

The main aspiration of this dissertation is to investigate the ablation of a molybdenum based multilayered film of relevance of industry and to find a proper parameter for the efficient and selective removal of different layers. Following steps were carried out to understand the various physical process involved in laser processing of molybdenum based thin film.

Firstly, micro-structuring of bulk molybdenum was conducted by a femtosecond laser at three different wavelengths. The absorbed threshold fluence required to structure molybdenum bulk was calculated after interaction of femtosecond laser with various fluences. Micro-structuring of molybdenum bulk was performed at different fluences, and structured molybdenum was investigated using offline and online characterisation tools. The offline characterisation tool included optical and electron microscopy techniques. On the other hand, the characterisations by online technique include real-time spectral and spatial plasma imaging. Finally, the interaction of ultra-short pulse (500 fs) with molybdenum was investigated by a numerical simulation based on a finite element method (FEM). The numerical method was solved for different fluences, and the increase of the lattice temperature was investigated. The investigation brings the different process involved in the ablation process. The further investigation is based on structuring of a very thin molybdenum film by a short (fundamental 9 ns) and an ultrashort (fundamental 500 fs) laser pulses.

The second part of this dissertation is to investigate the physics of interaction of a thin molybdenum film with short and ultrashort pulsed laser in order to understand the ablation mechanism and find out the effect of the interaction. The interaction of nanosecond and femtosecond laser with molybdenum thin film resulted in complete removal of a loosely adhered

molybdenum layer on BK7 glass substrate. The offline characterisation of the removed surfaces on molybdenum thin film was investigated using an optical microscope, scanning electron microscopy (SEM) and atomic force microscopy (AFM) methods. Real-time measurements were carried out using on-line characterisation methods such as spectral and plasma imaging and various physical associated properties. The nanosecond and femtosecond ablation process of a molybdenum film at low fluence was understood numerically using finite element method (FEM).

The final part of this thesis is to investigate the ablation mechanism of a molybdenum based multilayered structure which is an important material for the industrial application (touch panel). Selective laser ablation was observed, and different threshold fluences were measured for the nanosecond and femtosecond laser interaction with the multilayered film. Various offline characterisation such as SEM, AFM and EDX reveals different novel and exciting features on the MAM surface. Finally, the different ablation process was understood by simple numerical solutions using finite element method technique. It was concluded that the nanosecond laser processing of MAM is a thermally activated process, whereas femtosecond laser ablation is a stress governed phenomenon. It was also concluded that the complete removal of MAM is easy to achieve with the nanosecond laser, but it provides thermal damage at the substrate. It is possible to remove different sub-layers of molybdenum selectively by femtosecond laser interaction. Also, a comparatively higher fluence is required to remove the multilayered film from the substrate. A simple numerical solution based on two temperature and mechanical stress model were developed to understand the femtosecond laser ablation phenomena. Further investigation of the various process involved in the ablation process of the multilayered structure is needed.

The novel findings/contributions of this dissertation are listed below,

1. Comparison of the single pulse femtosecond interaction of bulk molybdenum bulk and thin film by the offline characterisation tool.
2. Comparison of femtosecond and nanosecond laser ablation of 50 nm thick molybdenum thin film on a dielectric (BK7 glass) substrate.
3. Evaluation of the wavelength dependence of single pulsed laser ablation phenomena.
4. Numerical simulation confirming the ablation phenomena at low fluence leads to delamination due to induced stress.
5. The real-time imaging of the femtosecond and nanosecond ablation of bulk and 50 nm thin molybdenum in real time at atmospheric pressure by a femtosecond and a nanosecond laser at various fluence, and different parameters were estimated.
6. Femtosecond and nanosecond laser performed micro-structuring of a multilayered film at IR, green and UV wavelength and selective ablation was observed.
7. The creation of novel micro & nano structures on MAM at low fluences is due to comparatively higher expansion of aluminium than molybdenum.
8. The formation of an aluminium microprotrusion is most likely due to a photo-thermal subsurface expansion of the aluminium layer.

9. The generation of stress by a photomechanical mechanism gives rise to mechanical fracture of molybdenum layer.

Thesis structure:

The structure of this thesis is presented as follows,

Chapter 2 provides an introduction to laser fundamentals, followed by production of short and ultra-short pulse relevant background information on selective processing, thin film micro-processing and laser conservation. A literature review of ultra-short pulse laser technology and its application to microfabrication is included. Ultra-short pulse laser ablation mechanisms, related experiments and results are analysed.

Chapter 3 provides a description of the laser processing workstation and characterisation equipment with the methodology used to implement and analyse the experiments described in this thesis. Various parameters of the materials utilised in the study are provided. Numerical models employed in the simulations are also discussed. Details of the materials used in testing are also provided with different parameters.

Chapter 4 presents the structuring of bulk molybdenum by a 500 fs femtosecond laser at three different wavelengths. Numerical simulation based on two temperature model was carried out to investigate the physical process and factors for ablation process. Interaction of 50 nm thick molybdenum film with a femtosecond and a nanosecond (9 ns, fundamental) laser were carried out, and the results provide evidence of selective ablation with delamination effect. Numerical simulation provides an investigation into the factors governing selective processing by femtosecond and nanosecond laser. Effects of absorption, the variation of the absorbed fluence of molybdenum bulk and molybdenum thin film were investigated using various offline characterisation tools and factors like reflectivity, and ablation threshold were measured.

In **chapter 5**, real-time observation of the ablation of molybdenum bulk and thin film by femtosecond and nanosecond laser are presented. Spatial and spectral imaging of molybdenum was carried out at different fluences are represented. Parameters such as plasma lifetime, average velocity and deceleration coefficient are calculated and presented.

In **chapter 6** ablation of a multilayered thin film by a femtosecond and a nanosecond laser was studied. Micro-structuring of the multilayered film was performed at IR, green and UV wavelength at different wavelengths at a range of fluence. SEM and AFM microscopy of the ablated craters are presented at the EDX analysis is presented to detect ablated layers. Through these case studies, the usefulness of selective processing techniques of the multilayered film, advantages and limitations are identified.

Chapter 6 concludes this thesis, providing a summary of its findings and achievements. Suggestions are provided for future research directions based on the work presented herein.

Chapter 2: Literature Review

This chapter presents relevant background to short pulse and ultra-short pulse laser processing of molybdenum materials. Brief reviews of laser science, various laser-material interaction mechanisms and the micro-processing of materials by pulsed laser sources currently available in the literature are presented. The background necessary for an understanding of laser micro-processing of molybdenum bulk and thin films is presented. In addition, a review of the state of the art is conducted on the processing of multi-layered thin films for industrial applications.

As this thesis focusses on the processing of the molybdenum by different laser sources, a general overview of interaction of laser with materials is required. To understand the micro-processing of molybdenum-based structures by various laser sources, the following sections are covered in the literature review section.

1. This chapter begins with the generation of the coherent light pulse from a laser system; particularly a four-level emission mechanism is discussed. The laser pulse from the four-level system is used in the current experiments.
2. In the next segment, two techniques of shortening of a laser pulse are discussed, termed as Q-switching and mode locking. These approaches are used to create a compressed a laser pulse inside a laser cavity. Further amplification and shortening of a laser pulse by chirped pulse amplification (CPA) technique, operates outside of the laser cavity, is presented in the next section.
3. A general introduction to the laser material interaction involving various associated processes is discussed in the next section. This addresses the excitation of a material (metal, semiconductor and dielectric) by linear and non-linear absorption process during the interaction of laser pulse. In particular, an in-depth review of the interaction of an ultrashort and short laser pulse within a material is discussed.
4. The ablation/removal of a material by means of thermal, photochemical and photomechanical mechanisms.
5. Other relevant processes, e.g. plasma formation, spectral emission and plasma shielding is discussed.
6. The final segment of this chapter emphasises the laser processing of molybdenum with different findings achieved by other researchers. Also, various properties and applications of molybdenum are discussed herein.

2.1. Laser fundamentals

A short description of laser fundamental is discussed in this section. Laser sources are devices that generate and amplify coherent radiation at wavelengths from infrared (IR) to ultraviolet (UV) regions of the electromagnetic (EM) spectrum. The output of laser beam is directional and monochromatic. The physics underlying stimulated emission were first hypothesised by Einstein in 1917 [2, 3], however, it was confirmed in 1928 by Landenberg [4]. Theodore Harold Maiman demonstrated the first laser at the Hughes Research Laboratory in 1960 [5]; the lasing medium

was a ruby crystal and it produced a laser pulse at a wavelength of 694.3 nm, pumped by xenon flash discharge.

A laser consists of three primary system components, e.g. pumping system, an active medium and a resonator consisting one or two mirrors. The pumping system is required to achieve population inversion in an active medium; this population inversion acts as an amplifying mechanism. To effectively extend the length of the amplifier, the active medium is placed inside of a resonator which introduces a suitable positive feedback; feedback is achieved by two highly reflective mirrors reflecting the light through the active medium. The electromagnetic wave (EM) wave generated by spontaneous or stimulated emission is amplified on each passage through active material. If one of the mirrors is partially transparent, an output beam is emitted from the resonator. Figure 2.1 shows a simplified schematic of a typical laser system.

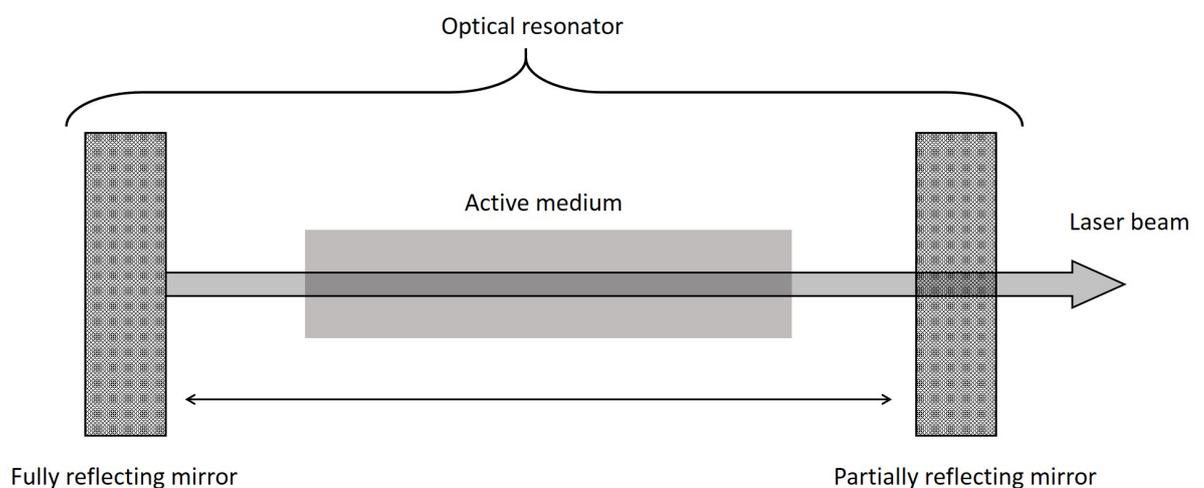


Figure 2.1: Simplified schematic of typical laser

There are three phases of matter used as laser sources according to the physical state of the active medium, these are solid-state, liquid or gases. Lasers are termed as being infrared (IR), visible (VIS), ultraviolet (UV) or X-ray depending on its emitted wavelength. Lasers are termed as continuous or pulsed, if the laser beam is emitted in the form of a continuous wave or as a temporal pulse of light lasting a specific time duration, respectively. In general, the peak and the average powers of continuous wave lasers are the same and lies between a few milliwatts to several megawatts. In pulsed laser sources, high peak powers can be achieved when the pulse is on up to values of petawatts (PW). For pulsed lasers, the pulse duration can vary widely from the milliseconds to femtoseconds. Repetitively pulsed lasers offer high repetition rates from kilohertz to several megahertz.

As the primary focus of the study is to investigate how the molybdenum material is modified by solid state lasers, the development of these specific laser tools will be discussed. In commercial high power solid state laser system, the most conventional active medium used are Nd^{3+} doped medium, such as Nd:YVO₄ and Nd:YAG. The laser having Nd^{3+} doped yttrium matrix as an active medium is known as Nd:YAG laser and thus the emission process from this laser is discussed in the next section.

2.2. Nd:YAG laser

Nd:YAG laser is a solid-state laser (SSL) that utilises a gain medium made from a garnet doped with a rare earth or transition metal ions (for example neodymium-doped yttrium aluminium garnet, simply known as Nd³⁺:YAG) [6]. When the neodymium ion (Nd³⁺) doped with host material yttrium aluminium garnet (Y₃Al₅O₁₂) the strongest emission at a wavelength of 1.064 μm. Nd³⁺ also lases at 0.94 μm and at 1.32 μm from the same upper laser level as the 1.064 μm transition, although these transitions have lower gain.

A simplified energy level diagram of a Nd:YAG solid-state laser is shown in Figure 2.2. Nd³⁺YAG laser incorporates a four-level system and it has small pumping threshold when compared with other solid state lasers such as Ruby laser [7, 8]. The typical parameters for Nd:YAG lasers are listed in Table 2.1.

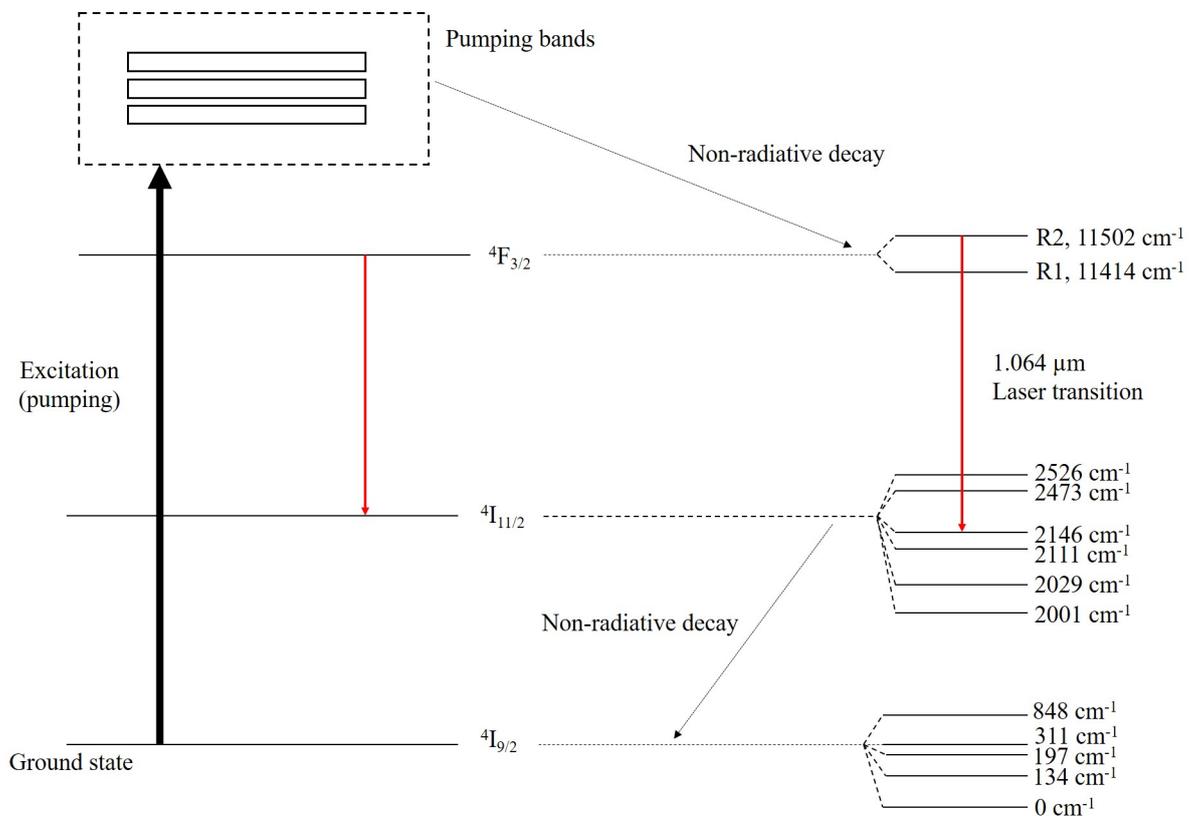


Figure 2.2: Energy levels of the Nd:YAG laser crystal

The gain medium is pumped using flash lamps, laser diodes or other lasers. The population inversion is accumulated over the time duration, during the active period of the pumping cycle. The emission occurs when stimulated emission exceeds a specific threshold and when is permitted to occur. The gain line width is typically narrow, approximately 0.45 nm, which is homogeneously broadened by thermally activated lattice vibrations in the YAG matrix.

Table 2.1: Various parameters of an Nd:YAG laser system

| <i>Property</i> | <i>Value</i> | <i>Unit</i> |
|--|--|----------------------------------|
| <i>Chemical formula</i> | Nd ³⁺ :Y ₃ Al ₅ O ₁₂ | |
| <i>Crystal structure</i> | Cubic | |
| <i>Mass density</i> | 4.56 | gcm ⁻³ |
| <i>Young's modulus</i> | 280 | GPa |
| <i>Tensile strength</i> | 200 | MPa |
| <i>Melting temperature</i> | 1970 | °C |
| <i>Thermal conductivity</i> | 10-14 | Wm ⁻¹ K ⁻¹ |
| <i>Thermal expansion coefficient</i> | $7 - 8 \times 10^{-6}$ | K ⁻¹ |
| <i>Emission cross-section at 1064 nm</i> | 28×10^{-20} | cm ² |
| <i>Gain bandwidth</i> | 0.45 | nm |

Excited electrons quickly drop from the pumping bands to ⁴F_{3/2} level, where the electrons remain for a relatively long time. This level is split into two components, which are referred to as R1 and R2. The energy level of R2 is approximately 0.011 eV above than R1. Because these levels are closely coupled, their relative populations are related by a Boltzmann factor. The most probable lasing transition is to the ⁴I_{11/2} state, where a photon at 1064 nm is emitted. Electrons in that state in turn quickly relax to the ground state, so its population remains low. Hence, it is easy to build a population inversion. At room temperature, the emission cross section of this transition is high, so its lasing threshold is low. While there are competing transitions for the same upper state, most notably at 1319, 1338, and 946 nm, all have lower gain and a higher threshold value than the favoured 1064 nm transition.

The current study was undertaken using a Neodymium-doped yttrium orthovanadate (Nd:YVO₄) laser instead of Nd:YAG laser. The Nd:YVO₄ laser/crystal is similar to the Nd:YAG laser but it offers some advantages; such as:

1. It has a lower dependency on pump wavelength and temperature control of a diode laser.
2. It has a wider spectral absorption band compared with Nd:YAG laser.
3. It has a higher slope efficiency than Nd:YAG laser.
4. It has lower the lasing threshold of Nd:YVO₄ than Nd:YAG.
5. The emission output from the Nd:YVO₄ laser is single-longitudinal mode and linearly polarised.
6. Nd:YVO₄ laser has more compact design than Nd:YAG. etc.

In general, the Nd:YAG and Nd:YVO₄ laser both can operate in continuous and pulsed mode. Laser emission by the pulse mode is more preferable than the continuous mode for the scientific

and industrial applications. Micro-machining of materials requires shortening (compression) of these laser pulses as the reduction of the laser pulse that offers more extreme intense phonon density and shorter temporal duration.

2.3. Pulse shortening

Shortening of the laser pulse is required in the fields of digital communications, precision machining and for use as diagnostics (pump & probe) of ultrafast chemical processes. This also allows processing of material without causing significant heating and thus damage of material. For short and ultra-short laser pulse generation two key techniques of Q-switching and mode locking are used.

2.3.1. Q-switching

The Q-switching technique is used in the nanosecond laser system to produce short laser pulses from an otherwise CW (continuous wave) source for our study. The Q-switching, also known as Q-spoiling [9], is a technique used in many types of commercial solid state lasers to obtain a high energetic short pulsed output by modulating the Q-factor (quality factor) of the laser resonator. The Q-factor is a measure of the damping strength of the laser resonator [10, 11]. An abrupt increase of the Q-factor of a laser resonator results in an intense laser pulse generates [6].

In general, pumping in a laser system begins when the optical pump source is activated. The population inversion eventually reaches a steady state value with proper matching of pumping and decay rates. The laser beam intensity begins to grow during this period until it reaches a saturation intensity value [6]. If the gain is high enough to overcome cavity losses, the extraction of energy starts from the cavity.

The population inversion is decreased during the process of stimulated emission as the laser beam intensity increases. The inversion density reaches a lower steady state value such that the reduced gain equals the losses in the cavity. In most solid-state lasers, the upper-level lifetime is significantly longer than the time required for population inversion to reach the steady state equilibrium value inside the cavity. For this kind of laser, the laser output reaches a saturation intensity long before the maximum population inversion is achieved and thus, the laser operates with a lower gain [12].

A higher gain and energy output is possible if the solid-state gain media were pumped for a duration without the optical feedback in the cavity in place. The ability to suddenly switch the optical feedback of the cavity back in place is known as ‘Q-switching’ as the cavity is rapidly changed between a high and low state where ‘Q’ represents the ratio between energy stored and to the energy dissipated within the cavity.

This technique allows generating laser pulses with a duration comparable to photon delay time (time scale) and high peak power (~MW). Figure 2.3 represents the summarised evolution process of Q-switched laser pulse [12, 13].

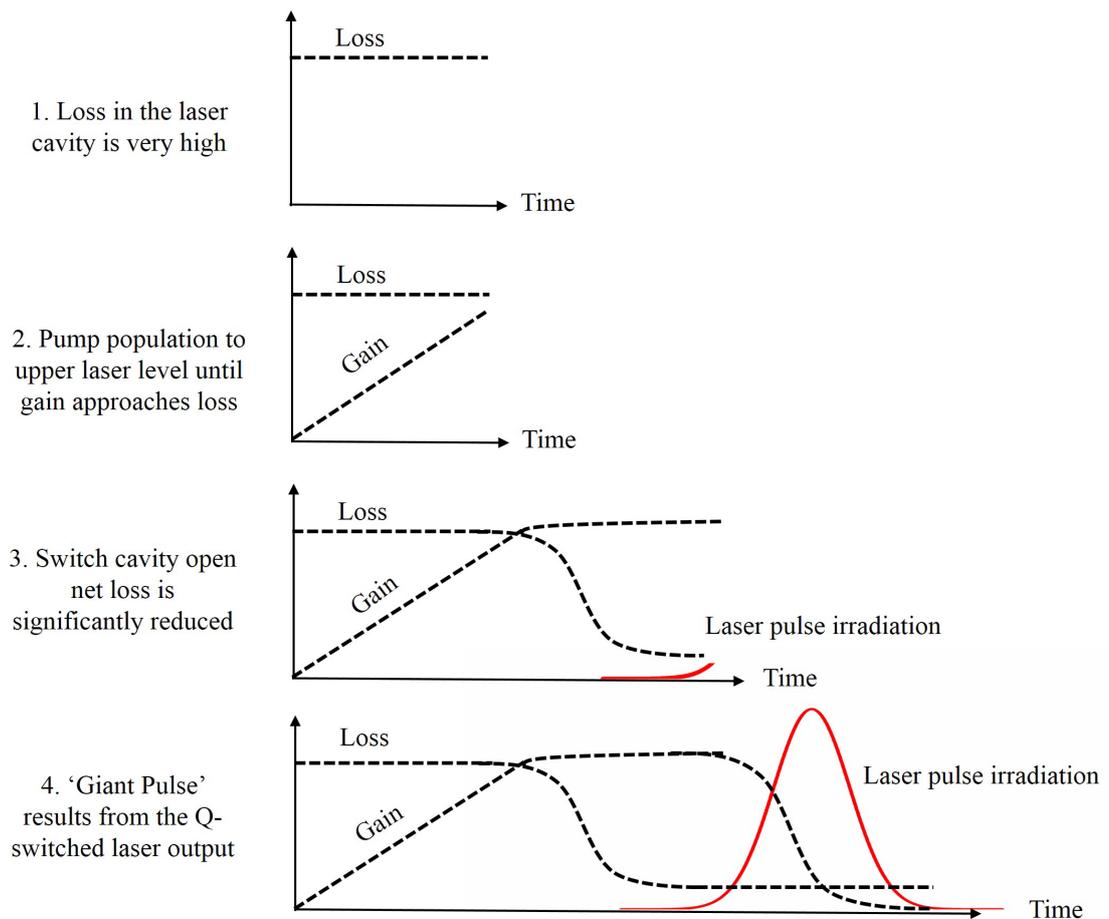


Figure 2.3: Evolution of Q-switched laser pulse, adapted from [6]

Initially, the cavity loss in the laser cavity is set at some arbitrarily high value by not allowing the spontaneously emitted photons to oscillate between the mirrors. Simultaneously, the laser pumping builds the population inversion over some period of time to a value larger than that achieved by normal circumstance; this results in a higher population inversion at the upper level. The cavity loss is then suddenly lowered by allowing photons to oscillate inside the cavity. The reflected photons from the mirrors trigger a large number of stimulated emission and produce a rapidly rising and intense burst (giant pulse).

Four requirements must be satisfied to produce high inversion population density required for Q-switching,

1. The lifetime of upper laser level needs to be longer than the time required for cavity re-alignment.
2. The duration of pumping must be longer than the upper state population build-up time and at least as long as the lifetime of the upper-level.
3. Initial cavity losses must be higher than pumping gain and
4. The cavity loss must be reduced almost instantaneously during high Q time.

Different methods for producing Q-switching within a laser cavity include rotating prisms, electro-optic and acoustic-optic shutter, pocket cells or Kerr cell or using a saturable absorber. Q-switched pulses are limited to generate minimum pulse durations of few nanoseconds. Further reduction of

pulse width requires other technique e.g. mode locking and CPA techniques and described in the following section.

2.3.2. Mode-locking

The mode locking is discussed as it was used to generate an ultra-short laser pulse from the femtosecond laser system. Mode-locking allows optical pulses as short as 5 femtosecond to be generated [14, 15].

When modes of electromagnetic waves of different frequencies but with random phases are added together, they produce a randomly distributed, average output of both the electric field and the intensity in the time domain. Mode-locking is achieved by combining a number of distinct in phase longitudinal modes of laser pulses, all having slightly different frequencies. When all the same frequencies (modes) are added in phase, they combine to produce a total amplitude field and intensity output that has a characteristic repetitively pulsed nature. Hence, achieving such phasing or mode-locking has become a powerful method for generating ultra-short pulses. The greater the frequency separation between these modes, the shorter the achievable pulse duration [16].

The methods of mode locking can be divided into two categories, active mode-locking and passive mode-locking. In active mode locking, the mode-locking element is driven by external sources [17]. Active mode locking can be induced by an amplitude modulator (AM mode locking) [17, 18], a phase modulator (FM mode locking) [19] or by the periodic modulation [20] of laser gain at a repetition rate equal to the fundamental cavity frequency. For a pulsed and high gain laser, mode locking is achieved by Pockel cell amplitude modulators. For a CW-pumped and generally low gain laser, the amplitude mode locking is achieved by an acoustic-optic modulator.

There are four major types of passive mode locking e.g. fast saturable absorber mode locking [21], slow saturable absorber mode locking, Kerr-lens mode locking [22] and additive pulse mode locking [23]. Saturable absorber uses the saturation properties of a suitable absorber e.g. semiconductor or a dye molecule. Mode locking using slow saturable absorber exploit the dynamic saturation of the gain medium. Self-focussing property of a transparent nonlinear material is used in Kerr-lens mode locking. Additive pulse mode locking exploits the self-phase modulation induced in a suitable nonlinear optical element.

The minimum pulse width of a mode-locked laser is determined by the gain bandwidth of the pulse. To generate an even shorter pulse, the bandwidth is increased beyond its original width, associated with the mode-locked laser pulse. This technique is known as chirped pulse amplification (CPA).

2.4. Chirped pulse amplification

The *Chirped Pulse Amplification* (CPA) technique is used in the current study, where amplification of a low intense femtosecond laser pulse is performed to generate a highly intense femtosecond laser.

The introduction of chirped pulse amplification played a revolutionary role to generate ultrashort laser pulse of high peak power. This was done by the amplification of very short (femtosecond) laser pulse energies previously available from long-pulse lasers [24-26]. In CPA technique, stretching of an ultra-short laser pulse is first conducted followed by its amplification in to a gain

medium. Following the amplification, the amplified laser beam is again re-compressed (Figure 2.4).

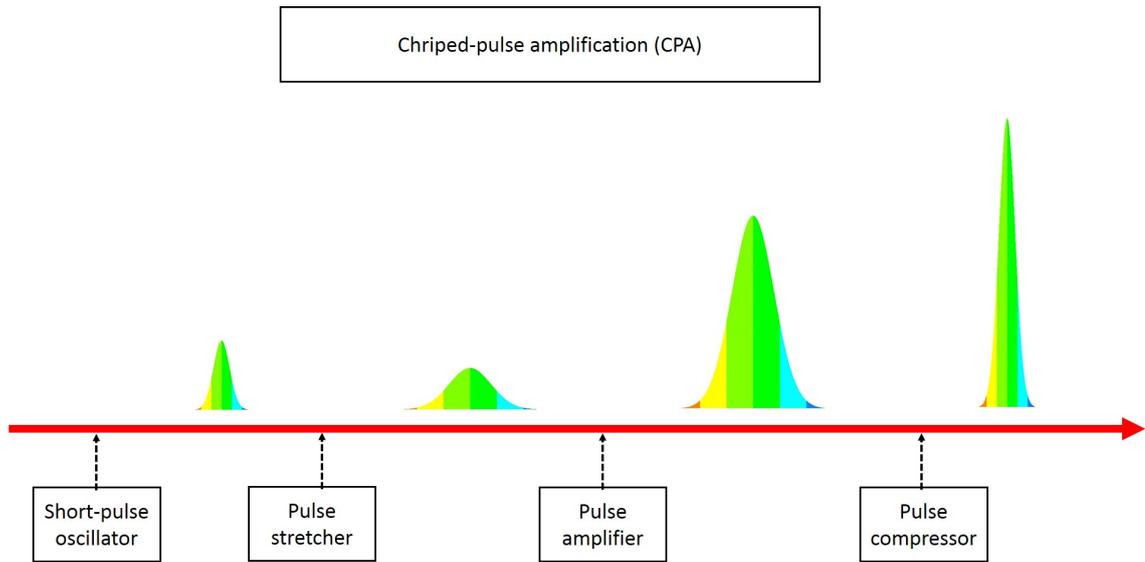


Figure 2.4: Generation of highly intense short pulse laser by CPA technique

A pair of grating or prism are used for the temporal stretching of seed laser pulse. These pair are organised in such a way that the high-wavelength component of the laser pulse travels a shorter distance than the low-wavelength component. After the laser pulse travel through the grating pair, the high frequency component lags behind the low frequency component of the laser pulse i.e., the laser pulse becomes positively chirped. The pulse width of the original laser beam can be increased by a factor of 10^3 to 10^5 by the positive chirping mechanism. Then a gain medium is used to amplify the stretched and less intense laser pulse. During the amplification process, the intensity of the laser pulse is amplified by a large amount (10^6 times or even more). In the end, the positively chirped and sufficiently amplified laser pulse is recompressed back to the shorter pulse width using the pair of grating or prism. In this case, the laser pulse become is negatively stretched. The compression of the laser pulse enables to increase higher peak power of laser pulse [27, 28].

The ultra-short pulse duration can be achieved only if the coherent light consists of a range of wavelengths which are carefully and orderly synthesised such as the pulses produced by mode-locked lasers. The stretcher operates by introducing large, well-characterised dispersion, i.e. time delay of different spectral components of the ultra-short pulse to produce a long, chirped optical pulse. During positive dispersion, the time to travel of lower wavelength (higher frequencies) component of the laser light is more than the components of laser light with higher wavelengths (lower frequencies). The compressor operates on the same principle, with a dispersion that closely matches that produced by the stretcher, but opposite in sign i.e., in this case, the negative dispersion is used. Thus, the ultra-short pulse initially generated in a mode-locked laser first undergoes stretching in the pulse stretcher (to ps-ns durations), amplification factor to high energies in the laser amplifier, followed by compression close to its original pulse duration in the pulse compressor. The CPA phenomena are illustrated in Figure 2.5,

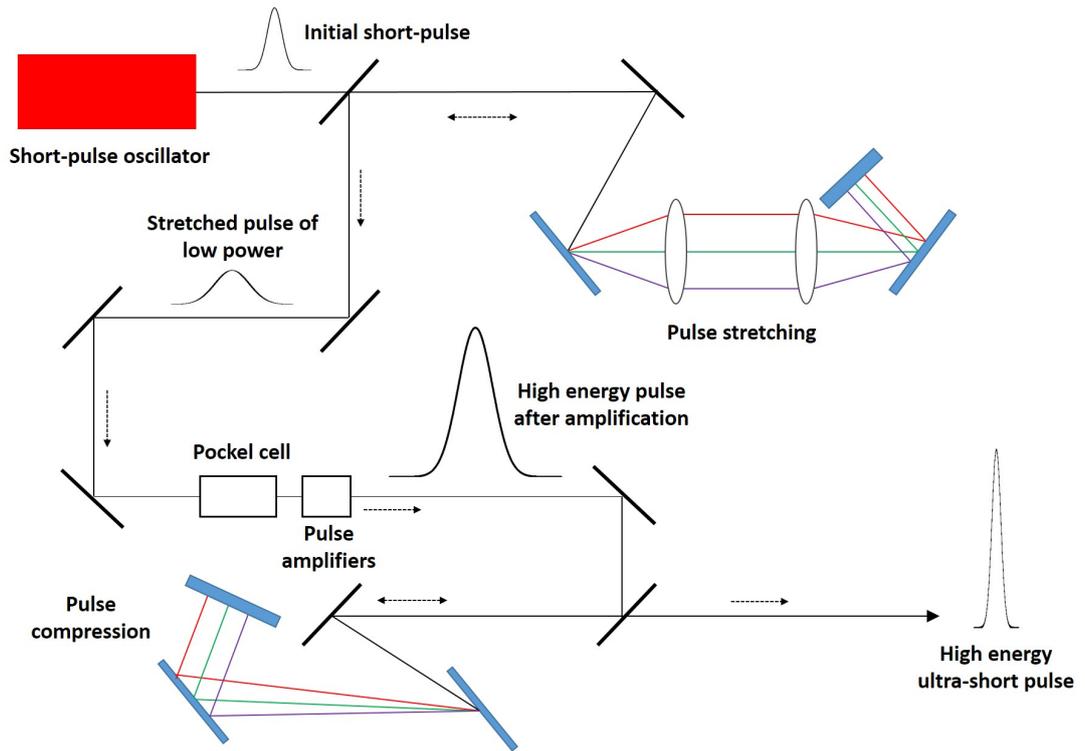


Figure 2.5: Schematic of CPA technique using two pairs of gratings

In general, the compressors and stretchers can be designed by several ways. A grating-based stretchers and compressors is widely used in today's advanced ultrashort laser system. Also, sometimes, as dispersive elements, a pair of prism is used as a substitute of gratings. Moderate stretching and compression ratios can be achieved with prism-based devices, optical fibres and Bragg gratings implemented either in bulk materials or fibres. Finally, relatively small stretching and compression ratios can be achieved using the natural dispersion of bulk material or specially designed reflective dielectric stacks (chirped mirrors). Figure 2.6 represents pulse compression made with a pair of gratings,

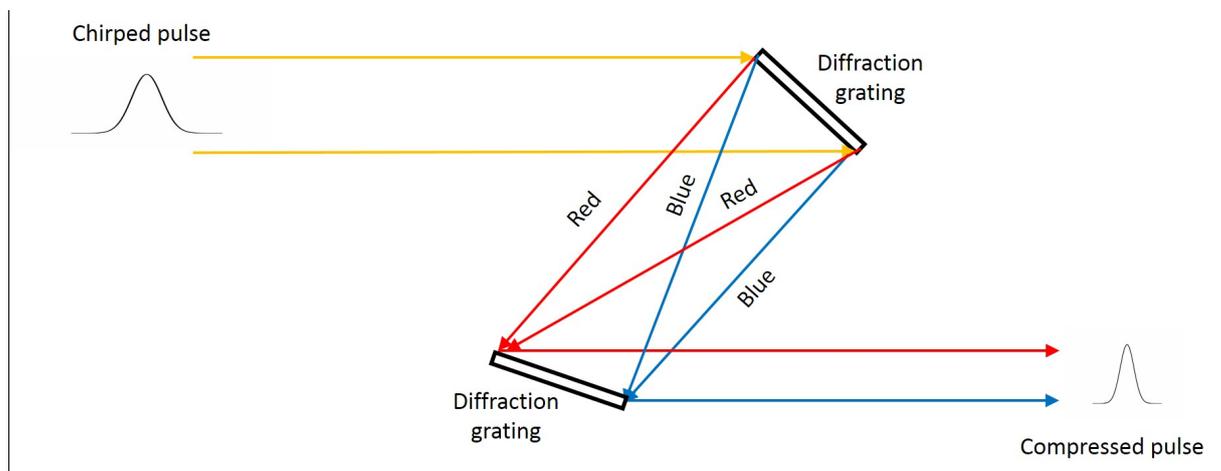


Figure 2.6: Ray diagram of the pulse compression of a chirped pulse using a pair of grating

These three techniques were used in our study to produce ultrashort and short laser pulses. As these pulses are used to process materials (molybdenum), a literature review of the laser-material interaction is needed.

2.5. Laser-material interaction

Pulsed lasers are used in a variety of different industrial and scientific fields because of the fact that they are useful as intense, readily manipulated energy sources. They are applied in a wide variety of situations in which their interactions with matter are of great importance. Most of the laser processing is performed by infrared laser light sources [29]. In metal, laser energy excites free electrons [30], in insulator the energy is absorbed by vibrational energy levels [29, 31]. Both kinds of excitation can be observed in the case of semiconductors [32-34]. In case of metals, the excitation of free electrons depends upon several factors including temporal duration of laser source [35], incident laser intensity [36], wavelength [37] etc. In general, the excitation energy is dissipated into heat energy within a time frame that is small compared to any change in another physical process. The different process associated with the laser processing is shown in Figure 2.7.

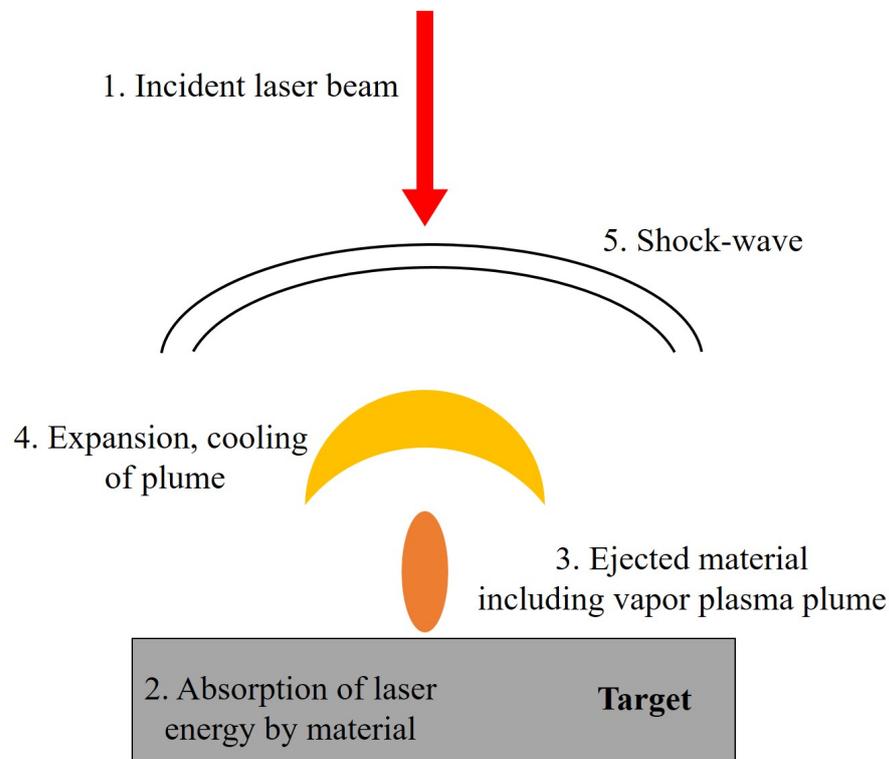


Figure 2.7: Typical laser ablation process

Table 2.2 lists some of the mechanisms associated with laser ablation process with a progressive time scale, the individual processes are dependent on laser and material parameters.

Table 2.2: Different laser ablation mechanisms [29]

| | |
|----|---|
| 1. | Propagation of laser beam through the ambient |
| 2. | Reflection of laser light (time dependent) at the surface of the material |
| 3. | Absorption of photon energy by material (single or multi-photon) |

-
4. Thermodynamic response of the material (time dependent). This includes the phase change of the material
-
5. Electron and ion emission and plasma ignition
-
6. Evolution of stress wave that originates from the interaction zone
-
8. Plasma shielding (laser-plasma interaction) if the incident laser pulse is still ON.
-
9. Hydrodynamic expansion of the vapour plume
-

2.5.1. Reflection of laser light by material surface

A general balance of the incident energy can be used to account for energy absorption by the material, by considering reflection at the surface, transmission through the material and optical emission (blackbody emission) from the surface. For an optically thick body, the transmission of laser light can be ignored. Thus, the optical laser energy is divided into two components, the reflected and absorbed laser energy. Under an ambient atmosphere or vacuum, the reflected energy (at normal incidence) from an incident laser pulse depends upon reflectivity (R) of the material which is essentially calculated from the Fresnel's relation shown in the following formula,

$$R = \frac{(\tilde{n} - 1)^2}{(\tilde{n} + 1)^2} \quad (1)$$

where, \tilde{n} is known as the complex index of refraction. In real material the complex refractive index is expressed by [38],

$$\tilde{n} = n + i\kappa \quad (2)$$

where, n is known as real part of refractive index that is determined by Snell's law and κ is called the extinction coefficient of the material.

Substituting \tilde{n} in the equation 1, we get,

$$R = \frac{\{(n - 1)^2 + \kappa^2\}^2}{\{(n + 1)^2 + \kappa^2\}^2} \quad (3)$$

The reflectivity and absorption of light by the material depend on the laser beam's frequency/wavelength and the material's properties. For simplicity, in our study, it was assumed that the reflectivity is intensity independent which is an approximation from the pump-probe experiments [39, 40].

The reflectivity can be affected by the surface roughness (Ra). An increase of surface roughness results presence of macro, micron and nano-structures at the surface and these can enhance the absorption at the surface and thus the reflectivity reduces [41-43].

A general equation for the laser source term ($S(t, r, z)$) for a pulse with Gaussian shapes in the radial and temporal domain (r, t) can be described as [44, 45]

$$S(t, r, z) = \frac{2F_{app}\alpha(\lambda)}{\sqrt{\pi/\ln 2} t_p} (1 - R(\lambda)) \exp\left\{-\frac{2r^2}{\omega_0^2} - 4\ln 2 \left(\frac{t - \tau}{t_p}\right)^2\right\} \exp(-\alpha(\lambda)z) \quad (4)$$

where, t is the time (s), r is the radial parameter (m), z is the depth of the material (m), F_{app} is the applied laser fluence in Jm^{-2} , t_p is the pulse duration at FWHM of the laser beam, ω_0 is the laser beam radius at the surface of the material (m), λ represents wavelength of the laser beam, $\alpha(\lambda)$ is the wavelength dependent absorption coefficient (m^{-1}) and $R(\lambda)$ is the reflection coefficient of the material respectively. Here, τ is the arbitrary time reference in seconds.

a. Linear absorption of radiation by material

When the light is incident on an absorptive material, the energy will be absorbed by a thin layer of the material. As the light passes into the material, the irradiance (Wm^{-2}) of the laser pulse decreases exponentially with distance. The decay of irradiance depends on upon the absorption coefficient of the material, $\alpha(\lambda)$, and the depth to which the light has progressed through the material. This decay of light irradiance is described by the simple Beer Lamberts' law given below, [46]

$$I(z) = I_0 \exp(-\alpha(\lambda)z) \quad (5)$$

Where, I_0 and $I(z)$ are the impinging and transmitted intensity in Wm^{-2} , respectively and z is the distance in meter (m) the light needs to travel. $\alpha(\lambda)$ is known as the absorption coefficient in m^{-1} and is a wavelength dependent parameter. The absorption properties by a material depends upon optical properties and electronic structure of material. It is possible to estimate the penetration depth (d) within the material using a simple equation, given by,

$$d = 1/\alpha(\lambda) \quad (5)$$

The absorption coefficient ($\alpha(\lambda)$) is large for metals (α), thus the light is approximately absorbed within a depth of 10-20 nm [29].

The light-matter interaction begins with the absorption. When the laser light interacts with a material, excitation of electrons takes place by absorption of photons. In metals, the absorption of a laser photon energy takes place by free electrons in the conduction band. Fermi level lies inside the partially filled conduction band which allows the absorption of low to moderate energy photons (typically IR photons) via intraband transitions [47-49]. In the case of non-metals (semiconductors and insulators), the Fermi energy is in between the valence band and the conduction band, and the electronic absorption of photon energy take place via interband transitions. Mostly, the probability of the linear absorption from the valence band to conduction band is almost insignificant for photons have energy less than the band gap energy of the material. The presence of defect states within the energy gap can lead to single photon linear absorption [50]. The energy level of the electrons in defect sites has intermediate energy which allows excitation of electrons into the conduction band.

Although the equation 5 holds for moderate to low intensities, at extremely high intensities nonlinear effects becomes important and the light is absorbed more quickly than linear absorption via multi-photon absorption [43]. This is not generally important in molybdenum.

b. Nonlinear absorption

Nonlinear absorption is of great importance in the processing of semiconductors and wide band gap insulators during the incidence of ultra-short laser pulses [43, 51-54]. At high intensities, the absorption deviates from Beer-Lamberts' law and more intense absorption takes place by nonlinear absorption process. Various non-linear absorption process includes impact ionisation, avalanche ionisation and, multiphoton ionisation.

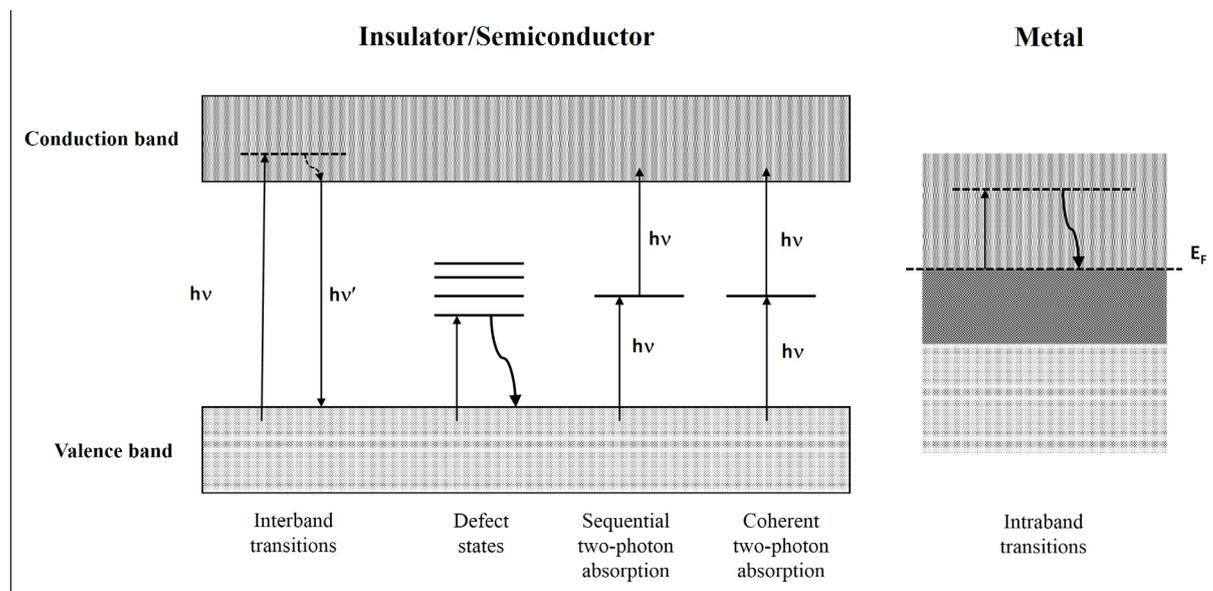


Figure 2.8: Different types of electronic excitations in a solid. Adapted from [29]

The excitation of electrons by the absorption of photon energy by the materials (metals, semiconductors and insulators) are illustrated in the Figure 2.8, and it can take place with the help of the both linear and non-linear processes. In the case of pure semiconductors and insulators, interband and intraband transition are observed. Linear absorption/transition is observed if the single photon energy exceeds the band gap of the semiconductor and insulator. Various nonlinear absorption e.g. coherent and sequential absorption take place at comparatively high intensity and indicate nonlinear absorption process. In case of metals, the valence and conduction bands overlap with each other. Thus, the energy levels are closely packed in metals, the free electrons easily absorb the incident laser energy, if allowed, and excites to higher energy states. Thus, the intraband transitions are most likely observed in case of metals [55-57].

Generally, the linear absorption is dependent on the properties of a material. When the laser intensity increases further and reaches a sufficient value, nonlinear absorption process could occur, and the absorption depends on upon the pulse intensity (photon density) and several material properties. The photon density depends upon the temporal nature of the laser pulse and it increases with reducing pulse width. The pulse width dependency on the laser processing of molybdenum

is studied in this dissertation and the following two sections presents the literature review of ultrashort and short laser pulse interaction with solids.

2.5.2. Interaction of an ultra-short pulse laser with material

When the laser pulse intensity reaches above 10^{15} Wcm^{-2} , the electron density reaches a critical value during ionisation by femtosecond laser pulse [58]. After the critical density is reached, the laser energy is mainly absorbed by inverse Bremsstrahlung method [59, 60]. Since the pulse length of the laser is considerably shorter than the thermalisation time, the removal of material is not fully dependent on a phase change of the material.

In metals, once the laser energy is incident on the metal surface, the photon energy is absorbed by free carriers in the conduction band via inverse bremsstrahlung process [61]. The electrons gain kinetic energy during absorption of photon. Since the electrons within the electronic subsystem have a low heat capacity (C_e), the electron temperatures rise to tens of thousands of degrees Kelvin very quickly due to electron-electron collisions [62]. At this point lattice remains cold (near ambient temperature). This results in a highly extreme temperature difference between the electrons and the lattice [35, 63]. Thermal energy is exchanged between from the electron to the lattice sub-systems to rebalance the equilibrium. The transfer of thermal heat energy can be described by electron-phonon coupling factor. The greater the value of electron-phonon coupling factor, the greater the rate of heat transfer between the electrons and the lattice and hence faster the thermalisation between the electronic and lattice subsystems. The time taken to reach this electron-lattice equilibrium varies depending on the material, but it is typically of the order of from one to tens of picoseconds.

Two temperature model

Ultra-short excitation of metals can often be described by two temperature model (TTM), where it is assumed that the laser excitation takes place via a rapid local thermalisation among the electrons followed by transfer of thermal energy to the lattice system, respectively [64]. Anisimov *et al.* proposed a two-step model to describe the transfer of energy between the electrons and lattice for metals; using the assumption that electron and phonon energy transfer can be described using Fourier's law [65]. Qiu and Tien later derived this model from the Boltzmann energy transport equation [66].

Assuming a uniform fluence across the irradiated area, the consideration of temperature change is only necessary in the z plane. The two-temperature model (TTM) can be described using two partial differential equations [44, 65, 67]

$$C_e(T_e) \frac{\partial T_e}{\partial t} = \nabla[K_e(T_e)\nabla T_e] - G(T_e)(T_e - T_l) + S(r, t) \quad (6)$$

$$C_l(T_l) \frac{\partial T_l}{\partial t} = \nabla[K_l(T_l)\nabla T_l] + G(T_e)(T_e - T_l) \quad (7)$$

The subscripts (e , l) refer to the electronic and lattice subsystems, respectively. C_i ($\text{Jm}^{-3}\text{K}^{-1}$) and K_i ($\text{Wm}^{-1}\text{K}^{-1}$) are the heat capacities and heat conductivities per unit volume. G ($\text{Wm}^{-3}\text{K}^{-2}$), temperature dependent parameter accounts for the coupling between hot electron and cold lattice

system and known as electron-phonon coupling factor [44, 65, 68]. $S(r, t)$ is the source term in Wm^{-3} .

Both electron and lattice temperature, T_e and T_l are functions of space and time and their evolution are governed by the above two equations. Within this model, the electron heat capacity, thermal conductivity, and electron-phonon coupling parameters are all temperature dependent variables.

The electron heat capacity depends on electron temperature. For metal samples, it can be written as follows [44, 69],

$$C_e = \frac{\pi^2 n_e}{2} \left(\frac{k_B T_e}{\varepsilon_F} \right) k_B \quad (8)$$

Here n_e is the density of free electrons ($\#/m^3$), k_B is the Boltzmann constant and ε_F is the Fermi energy. Only electrons below Fermi energy are excited [67] and the electron heat capacity is approximated to be linearly dependent on electron temperature and is represented as, $C_e = A_e T_e$, where the parameter A_e is termed as the electron heat capacity constant [70].

One of the assumptions made in the model used in this project is that the metal properties remain constant throughout the irradiation process. However, it has been found that this model works reasonably well for low fluence regimes.

Different theoretical investigations have been performed to describe the exchange of energy through electron-phonon collision using free electron gas model [71], Migdal-Eliashberg theory [72], Bardeen-Cooper-Schrieffer theory [73, 74]. The energy exchange rate can be expressed in terms of electron relaxation time. When the electron and lattice temperatures are much higher than the Debye temperature and $T_e \gg T_l$, the electron phonon coupling constant is described as,

$$G(T_e) = \frac{\pi^2 m_e C_s^2 n_e}{6 \tau(T_e) T_e} \quad (9)$$

where m_e is the effective electron mass (kg), C_s represents the velocity of sound in the medium (ms^{-1}) and $\tau(T_e)$ is the electron relaxation time (s), defined as the time required to establish an equilibrium between electron and phonon temperature [75].

2.5.3. Interaction of a short pulse laser with a material

It is assumed that during the short pulse laser interaction with the material, the electron and lattice temperature are assumed to be equal during short pulse laser interaction with a material. The main source of energy losses is the heat conduction into the solid target and reflection of laser from plasma. The heat penetration depth is approximated from the formula [76],

$$L_{th} = (2D\tau_L)^{1/2} \quad (10)$$

where, D refers the diffusion coefficient in m^2s^{-1} and τ_L is the pulse duration of laser (at FWHM) in seconds [76].

As the temperature rises, the kinetic energy of the atoms can overcome their binding energy, which results in a phase transition from a solid to a molten state in the first instance. This energy required to overcome the binding energy is known as latent heat of fusion. If the temperature of the molten region is increased further, evaporation of the atoms away from the molten material can take place. This heating of a material can be described for long heat sources, such as nanosecond laser pulses, using the Fourier heat equation [77]

$$\left[c_p \rho + L_m \rho \delta(T - T_m) + L_v \rho \delta(T - T_v) \right] \frac{\partial T(x, y, x, t)}{\partial t} - \nabla[K \nabla T] = S \quad (11)$$

where, c_p is the heat conductivity at constant pressure ($Jkg^{-1}K^{-1}$), ρ is the mass density (kgm^{-3}), K is the thermal conductivity ($Wm^{-1}K^{-1}$), L_m and L_v are the latent heat (Jkg^{-1}) of melting and vaporisation, and T_m is melting temperature and T_v is vaporisation temperature. ‘ S ’ is defined as laser source term (Wm^{-3}). The term, $L_{m,v} \rho \delta(T - T_{m,v})$ is the parameter used to simulate the increase in heat capacity as the material undergoes a phase change due to melting and vaporisation at temperatures T_m and T_v , respectively.

Analytical solutions to the heat equation can be found using methods of integral transformations and Greens function [78], however, finite element methods can also be used to directly solve the equation [79]. For a set of laser parameters, the temperature of the material depends on the optical absorption properties of the material and the transport of heat away from the excitation region.

The absorption of the laser energy by the solid material results in an increase of temperature and the material undergoes a transition to the molten phase, if the temperature exceeds the melting temperature. The increase of the temperature in the material can result in ablation with or without surface melting. In the case of an interaction with a short (\sim few nanosecond) laser pulse, there is enough time for a temperature wave to propagate into the material and thus it can create a relatively large layer of molten material. Therefore, even at low laser intensities, it is possible to remove the target material in both vapour and liquid phases if the vaporisation process creates a recoil pressure that can expel this liquid. Ablation of the molten particle from the molten phase can take place if the recoil pressure exceeds the surface tension forces [80]. Evaporation depends on the vapour pressure and can be represented by the Clausius Clapeyron equation [81, 82]

$$p_r = p_0 \exp \left[\frac{L_v(T - T_v)}{R_g T T_v} \right] \quad (12)$$

where, p_0 is the atmospheric pressure (pa), L_v is the latent heat of vaporisation (Jkg^{-1}) and R_g is the gas constant ($Jkg^{-1}K^{-1}$). Due to experimental functions, values of p_r are in general only relevant as $T \rightarrow T_v$, where, T_v is the vaporisation temperature. The rate of atomic flux away from the surface can be taken from the Hertz Knudsen equation [81].

$$J_i = \frac{p_r(T)}{(2\pi m_i k_B T)^{1/2}} \quad (13)$$

where, J_i is the atomic flux (species/cm²), m_i is the mass of the species leaving the surface (kg), and k_B is the Boltzmann's constant.

Removal of material during ultrashort and short pulse laser interaction process from surfaces is known as ablation. If the photon energy is high enough, it is observed that single atoms, molecules, clusters or fragments desorb from the substrate's surface. The next section will emphasise the different laser ablation mechanisms. The removal mechanisms are important to understand the interaction of laser pulses with the material of interest of the present study.

2.5.4. Laser ablation mechanism

The mechanism of material ejection depends upon the chemical and mechanical properties of the material such as melting and vaporisation temperature, electronic structure and, also, on the laser properties such as laser pulse duration, wavelength and fluence.

Although ablation mechanisms are typically complex with many contributing factors, three types of ablation processes are mainly used to describe material ejection; these photophysical processes are known as photothermal, photochemical, and photomechanical ablation mechanisms.

2.5.4.1. Photothermal ablation process

The photothermal process describes ablation mechanisms resulting from a temperature increase of a material following the absorption of the laser radiation. During the photothermal ablation process, the absorbed and thermalised photon energy ultimately excites vibrations within the molecule resulting heat energy [83, 84]. With purely thermal ablation process, the absorbed laser energy is treated simply as a heat source. Thermal ablation mechanisms are usually observed for ultra-short pulses with low fluence [37]. The ablation of the material corresponds to an evaporation rather than an explosion of a volume of material at the surface.

2.5.4.2. Photochemical (photolytic) process

Photochemical ablation, sometimes called photolysis, describes when the absorption of laser energy results in direct bond-breaking between atoms. The overall thermalisation of excitation energy is slow compared to the chemical relaxation time. This condition frequently holds where photoelectron transfer has taken place and is followed by chemisorption or desorption of the species on the solid surface. It also occurs when chemical reactions of excited molecules take place for photomechanical desorption of species from the surface [29]. With purely photochemical processes, the temperature of the system remains almost unchanged under laser light irradiation [29].

2.4.4.3. Photo-physical ablation process

The photothermal and photochemical process is considered as the limiting case of the photophysical mechanism. If both thermal and photochemical process directly contribute to the overall processing rate, the ablation is termed as photophysical ablation [29]. Figure 2.9 illustrate the photophysical ablation process on ultra-short timescales. The interactions is initiated in a non-thermal process following which thermal processes can develop which can induce phase changes [37].

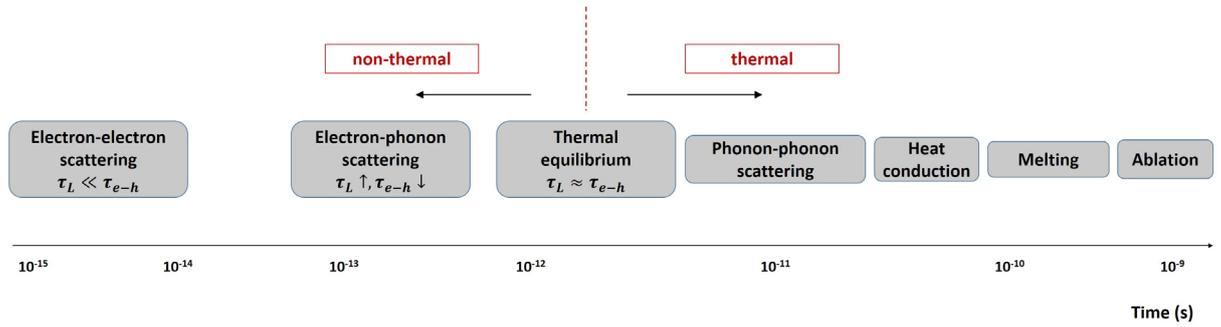


Figure 2.9: Time scale of material response by ultra-fast laser excitation

Different photo-physical ablation mechanisms have been observed for metal such as thermal vaporisation [85] and Coulomb explosion [86].

Thermal vaporisation is considered to be strong ablation phenomena and is observed at pulse intensities significantly higher than the ablation/damage threshold fluence [87, 88]. In thermal vaporisation, the transfer of the laser energy to the lattice via the electrons results in an electron-phonon collision. The electron-phonon collisions increase the local temperature of the lattice. The increase of temperature of material results in phase transitions from the solid phase to a gas phase with or without melting [89-91]. When the surface region is heated very quickly and the temperature exceeds the boiling point of the material, it is said to become superheated. The superheated material remains in a metastable state when the temperature exceeds its thermodynamic stability [37]. If the liquid reaches the spinodal limit, the liquid becomes highly unstable. At this spinodal limit or point, the liquid decomposes spontaneously into a phase, in which the liquid and vapour phases coexist. In some cases, the spinodal limit is not reached due to the onset of homogeneous nucleation of vapour bubbles. In this case, vapour bubbles are spontaneously created throughout the liquid, without requiring nucleation sites. These bubbles grow from this homogenous nucleation events and reach critical sizes whereby the material is classed as a liquid-gas mixture and the expansion proceeds in an explosive way. This leads to the rapid transition from a metastable superheated liquid into a mixture of vapour and liquid droplets and is described as a phase explosion [92, 93]. It is found that the emitted species are likely to have similar kinetic energy with a temperature being near to the vaporisation point [87]. After thermalisation of the laser energy, the remaining non-vaporised material is left in a fluid with a density approximately equivalent to a solid. The hot fluid is carried away by hydrodynamic flow and the high temperature is equilibrated as a result [94]. The ablated area is found to be non-smooth and ablation depth achieved using single pulse is on the order of micrometre or less in depth. In the case of metals, the thermal evaporation is mainly responsible for ablation [95].

Coulomb Explosion, often termed as a gentle ablation phenomenon, occurs before the thermalisation of hot electrons with the lattice. Coulomb explosion is an ablation mechanism commonly observed for dielectrics and some semiconductors [96, 97], but is insignificant in bulk metals. Some studies assume that Coulomb explosion does not occur with metals due to their high electron mobility and effective electron screening because of positive charges [95, 98]. However, there are a few studies that provide evidence to the contrary [99-101]. The ejection of hot electrons via photoemission or thermionic emission occurs on very short time-scales and results in unshielded positively charged ions within the lattice. The excited electrons which have escape

from the bulk material, forms a strong electric field which attempts to pull out the remaining ions from within the impacted area. Also, the repulsive forces established between these positively charged constituents also significantly contribute to ion ejection. When the force exceeds the lattice binding energy, the material explosively breaks up [102]. Characteristic evidence of the Coulomb explosion ablation mechanism is that there are two distinct velocity regimes for electrons: prompt (energy order of eV) and slow electrons (energy of meV) [95] which are trapped by positive ions. Other evidence includes a smooth surface that remains following the explosion of material during this mechanism [103]. It is observed that during Coulomb explosion, ions of different materials are ejected with the same momentum. Although, majority of ions is faster than thermal vaporisation. Unlike thermal vaporisation process, the ablated area is found to be smooth and ablation depth lies within few nanometre range.

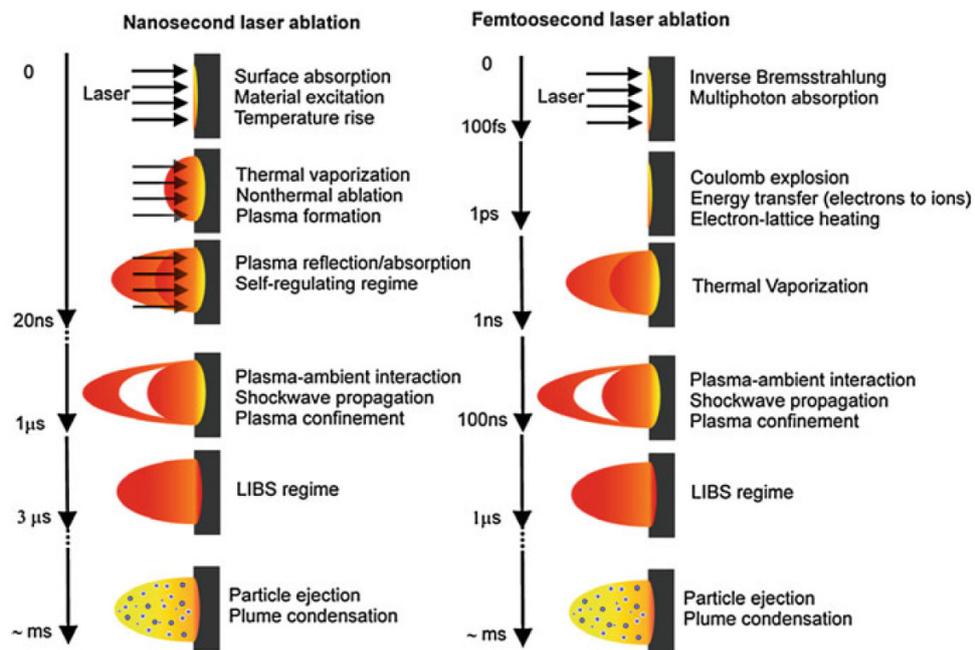


Figure 2.10: Approximate time scales of nanosecond and femtosecond laser ablation along with various processes happening during and after laser pulse is given. Adapted from [104]

2.4.4.4. Photo-mechanical ablation mechanism

Of particular importance to this study is photomechanical ablation. The photo-mechanical ablation occurs due to the build-up of mechanical stress in a material following laser absorption. The build-up of stress/strain in a material can occur from the thermal or the non-thermal effects [105]. The removal mechanism is typically photomechanical when the relaxation time of the material is shorter than the pulse duration. Different kinds of photo-mechanical ablation include delamination, spallation and fragmentation.

a. Delamination

Delamination is often observed for thin films. A steep temperature rise is established during the laser heating of a thin film and it leads to an expansion of the thin film away from the substrate. Due to this fast expansion of the thin film, a mechanical stress is established in the film, which ultimately causes the film to fracture. This expansion away from the substrate intensifies when the substrate has a lower thermal expansion coefficient than the thin film material. This build-up

stress is a function of the delaminated area and depends on upon laser fluence, incidence angle and number of pulses [106]. In particular, the delamination is important for the present study in the case of the interaction of laser with molybdenum thin film.

b. Spallation

Spallation has an important effect on the processing of thin molybdenum film with ultrashort laser pulses. The absorption of a short laser pulse induces initial stress confinement because of the inability of expanding the lattice during laser heating time. This results in a compressive stress pulse that propagates from the surface to the film-substrate interface before reflecting and becoming a tensile wave [107]. The compressive stress is generated since the temperature of a thin film material rises quicker than the time required for the expansion. The amplitude of the tensile wave is dependent on the absorbed fluence; the material mechanically spallates and if the amplitude of the tensile wave exceeds the tensile strength of the material [108]. This mechanism is typically termed as spallation. The tensile wave must be generated prior to phase changes occurring in the material [109]. Both front and rear surface spallation are possible during short pulse laser ablation of a thin film. Rear-surface spallation occurs when the separation is initiated from the interface of a film, whereas front side spallation is observed when the compressive stress initiated at the surface of a film reflects from the sub-surface interface which leads to the material to fracture and eject in terms of cold fragments [110].

c. Fragmentation

Typically, fragmentation takes place at the energies higher than that required for spallation mechanism. Stress builds up in the material due to a constant expansion. The internal stress is converted to strain before becoming a supercritical fluid, which fragments into liquid drops. During this fragmentation, the strain energy in the material is converted into surface energy for the liquid fragments. Excess elastic energy stored in the target can exceed the surface energy of the target, in which case the excess elastic stress is converted to surface energy during the formation of the fragments [37, 100].

2.5.5. Laser produced plasma plume generation

It is found that during laser ablation, electrons, ions, atoms, excited neutral particles are ejected from a target material. The charged particles such as electrons, ions are collectively known as plasma. This excited phase and others such as clusters are termed as a plume. The ejection of the plasma components typically occurs up to tens of picoseconds [60] after the incidence of ultrashort laser pulse followed by the emission of nanoparticles occurring after several hundred nanoseconds. The exacting time-scale on which the electrons, atomic and ionic mass is ejected is highly dependent on the mechanism for ablation and the properties of laser and the target material.

The initial velocity of species ejected from a surface is typically of the order of 1 to 10 km/s [111]. It is also observed that the velocity of the front edge of the plasma plume varies with applied laser fluence [112]. In case of molybdenum, for fluence between 0.5 to 2 Jcm⁻², the velocity of the front edge of the plasma plume varies between 3 to 7 kms⁻¹.

2.5.6. Spectral emission from the ejected species

The Laser-produced plasma is a rich source of electrons, ions, neutrals, and excited particles. The spectral emission from these components take place in the visible, ultraviolet (UV), extreme UV

(EUV), and X-ray regions of the electromagnetic spectrum [113, 114]. This laser produced plasma plume typically expands adiabatically in vacuum. A modification of the entire process of plasma generation and hydrodynamic expansion takes place at atmospheric pressure. The pressure of an ambient gas greatly influences the expansion features. It also affects the cooling, and characteristic parameters (electron density, temperature) of the plume [115] and the laser-plasma coupling.

The interaction of a nanosecond and femtosecond laser ablation plume with an ambient gas has been studied extensively in the past [116-122]. Compared with vacuum, the interaction of the laser-produced plasma with a background gas is complicated because of the involvement of several new processes, such as a reduction in ablation, formation of shock waves and clustering, plume splitting and sharpening, deceleration and confinement of ablated species, thermalisation of the ablated species, diffusion, etc. [123-127]. Background pressure levels also play an important role on the morphology of the laser irradiated region and the evolution of laser produced plasma [128].

In the case of nanosecond laser ablation phenomena, and the nature and pressure of ambient gas have a definite role in controlling the shielding effect of the laser produced plasma [128, 129]. The dependence of the emitted plasma plume on background pressure is extremely complicated because of the coupling of laser with plasma. It was observed by several researchers that the excitation temperature of the plasma plume has a strong dependence on nature and pressure of the ambient gas [118, 121]. The plasma emission intensity and the plasma lifetime decreases with the reduction with the ambient pressure due to a decrease in collisional excitons [121].

2.5.7. Threshold fluence

Ablation by laser pulse is observed when the laser fluence (Jcm^{-2}) is higher than a certain value at a given pulse width and laser wavelength. Theoretically, it is defined as *'the laser fluence at which lattice instabilities of such magnitude are induced that the system is irreversibly damaged and at least a monolayer of material is removed'* [130]. The damage threshold is determined using various techniques including, visual inspection using an optical or an electron microscope [131, 132], ablation depth measurement [132, 133], plasma radiation monitoring [134] etc. It is noted that experimentally it is measured as the minimum fluence required to create a damage on a material.

The ablation threshold depends on different optical and thermal properties of material. Ristau et al [135], Akhar et al [136] and Lange et al [137] showed that the threshold fluence for ablation is proportional to the melting temperature of the material and some other material constants such as density, specific heat and thermal conductivity. Neglecting reflectivity and transmissivity, it is found that ablation threshold depends on thermal diffusion length and optical penetration depth. Ablation is driven by the energy density of a material which is determined by the thermal diffusivity. Below the thermal diffusion length and above optical absorption depth the threshold fluence is found to increase linearly with film thickness [138]. Above the thermal diffusion length, independency of threshold fluence with respect to film thickness has found [85]. It was found that the threshold fluence also depends on amorphous and crystalline nature of metal [139, 140]. Moreover, substrate [37, 85, 141] and impurity [142] dependence of threshold fluence was also found.

2.6. Molybdenum and its applications

The strength and stability at high temperature make molybdenum as the prominent choice for many industrial applications. Different properties of molybdenum are listed in the Table 2.3.

Table 2.3: Different physical and chemical properties of molybdenum [29, 143-145]

| <i>Property</i> | <i>Value</i> | <i>Unit</i> |
|--|--------------------------|-----------------------------------|
| <i>Melting temperature (T_m)</i> | 2887 | K |
| <i>Vaporisation temperature (T_b)</i> | 5442 | K |
| <i>Melting enthalpy (ΔH_m)</i> | 0.288×10^{-6} | Jkg ⁻¹ |
| <i>Vaporisation enthalpy (ΔH_v)</i> | 6.23×10^{-6} | Jkg ⁻¹ |
| <i>Density (ρ)</i> | 10.2×10^3 | kgm ⁻³ |
| <i>Specific heat at constant pressure (c_p)</i> | 0.26 | Jkg ⁻¹ K ⁻¹ |
| <i>Thermal conductivity (k_l) (@ 300 K)</i> | 138 | Wm ⁻¹ K ⁻¹ |
| <i>Debye temperature (θ_D)</i> | 399 | K |
| <i>Lattice heat capacity (C_l)</i> | 2.8×10^6 | Jm ⁻³ K ⁻¹ |
| <i>Electron-phonon coupling constant (G)</i> | 13×10^{16} [67] | Wm ⁻³ K ⁻¹ |
| <i>Electron specific heat constant (A_e)</i> | 211 [145] | Jm ⁻³ K ⁻² |

Molybdenum is very attractive in industrial and daily uses [146] because of the following properties,

1. Reasonably good thermal conductivity
2. High electrical conductivity
3. Low thermal expansion coefficient
4. High resistance to prevent corrosion caused by molten metals
5. Thermal shock resistance
6. Compatibility with most glass compositions
7. High stiffness coefficients (Young modulus: 317 MPa)

It was found an increase of temperature causes a change in thermal conductivity. Figure 2.11 shows temperature-dependent thermal conductivity in Wm⁻¹K⁻¹ of high purity molybdenum. At low temperature, the values are considered to be accurate within $\pm 10\%$, $\pm 4\%$ at melting temperature. The thermal conductivity at temperatures near and below melting temperature is highly sensitive to small physical and chemical variations among different specimens. It is found that the thermal conductivity value differs almost $\pm 15\%$ once the temperature of molybdenum approaches to its melting point [147].

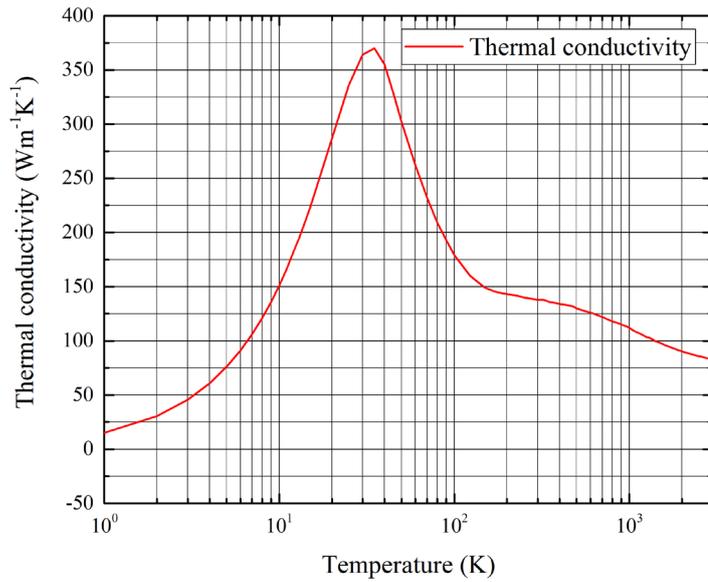


Figure 2.11: Temperature dependent thermal conductivity of molybdenum, adapted from [29, 147]

Figure 2.12 presents optical penetration depth of molybdenum covering a range from ultraviolet to near infrared. The optical penetration depth of molybdenum is found to decrease with wavelength in the visible range.

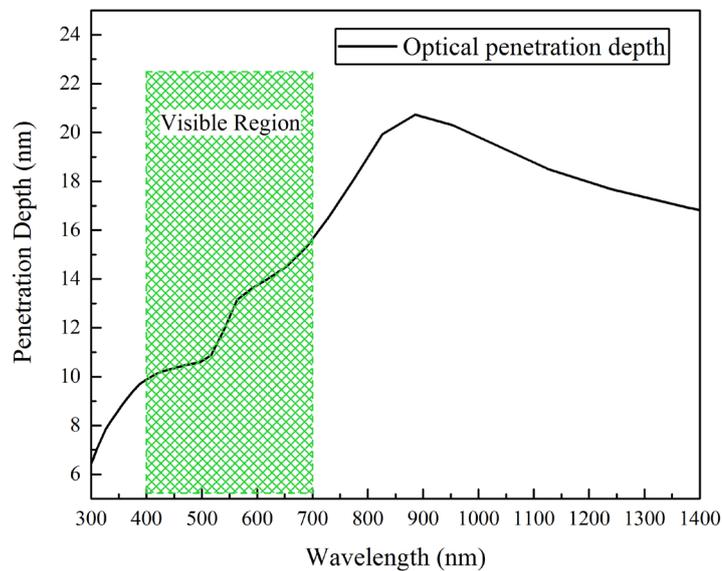


Figure 2.12: Optical penetration depth of molybdenum and its dependence with wavelength from UV to NIR region [148]

The electron-phonon coupling constant of molybdenum is assumed to be $13 \times 10^{16} \text{ Wm}^{-3}\text{K}^{-1}$ in most of the computational and theoretical studies of short pulse laser interaction at low laser intensity [149]. Zhigilei et al analysed temperature dependence of electron heat capacity and electron-phonon coupling factor for molybdenum at high electron temperature using density

functional theory (DFT) considering electron DOS effects [150]. The increase of electron-phonon coupling shows faster energy transfer from hot electrons to the cold lattice which results in thermal energy confinement in a smaller surface region of the irradiated target. This generates greater thermo-elastic stress, reduction of threshold fluence and less changes in the time scales of laser-induced phase transformations [70, 151]. Figure 2.13 the temperature dependency of electron-phonon coupling constant (G) and electron heat capacity (C_e) at high electron temperatures,

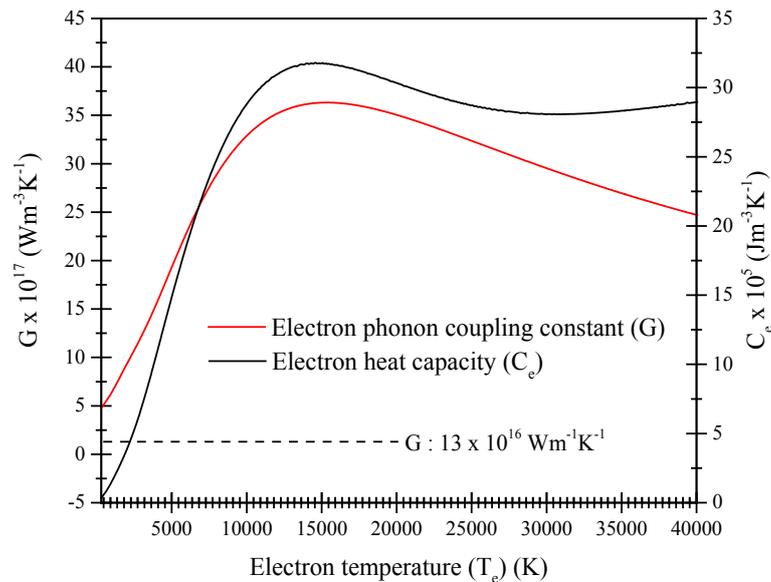


Figure 2.13: Electron temperature dependence of electron-phonon coupling and electronic heat capacity of molybdenum, adapted from [150]. The dashed line represents the constant value of electron-phonon coupling constant

Because of its high melting point and low reactivity, molybdenum is used in nuclear energy applications, missile and aircraft parts. Molybdenum thin film is used as a suitable back contact for $\text{CuIn}_{1-x}\text{Ga}_x\text{Se}_{2-y}\text{S}_y$ (CIGS), CuInSe_2 and cadmium telluride (CdTe) thin film solar cells [152-156]. Ablation of molybdenum is interesting because of its partially filled d-band electronic configuration ($[\text{kr}]4d^55s^1$) which makes molybdenum stable and inertness material.

2.7. Laser processing of molybdenum

Laser ablation of molybdenum thin film on a glass substrate is a special interest of study because these films served as a back contact for CIGS-based solar cells. For the monolithic interconnection, molybdenum need to be structured and galvanically separated from glass substrate [143, 155, 157, 158].

Patterning of molybdenum by pulsed laser sources has been investigated by several groups. Currently, in industrial uses of molybdenum, the thin film is structured using nanosecond laser pulses [159]. Structuring molybdenum with short-pulse lasers can lead to pronounced thermal effects, such as micro-cracks and burrs at the ablation edges [160]. Hermann et al showed that during P1 scribing of CIS-based solar cells using a nanosecond laser results in residues of molybdenum on the wall of ablation channel which transforms the solar cell into an ohmic resistance [143]. It is found that high-quality and damage free structuring on molybdenum is

possible using ultra-short laser pulse for industrial applications [143]. Thermal effects can be significantly reduced by ultra-short laser ablation [35, 43, 161-166]. Femtosecond laser ablation of thick molybdenum thin films has been studied intensively by several groups. Reduced heat loss due to small heat diffusion length associated with ultra-short laser pulses leads to lesser threshold fluence of molybdenum film [143, 167]. Ablation of molybdenum film on transparent glass substrates is possible from both the front and rear sides [168-171]. In the case of the front-side ablation, otherwise termed as “direct laser ablation,” the laser energy is first absorbed by molybdenum and subsequent energy (heat) transport, melting, and evaporation follows directly. While in the case of backside ablation (so-called laser-induced indirect ablation) laser energy propagates through the substrate and then is absorbed by molybdenum located near to the substrate interface.

Zoppel et al. used a direct laser ablation method for selective ablation of molybdenum thin film for the structuring thin-film solar cells. Complete removal of a 500 nm thick molybdenum film from a glass substrate was observed by 800 nJ femtosecond pulses at a scan speed of 1 mms^{-1} at an ablation fluence of 0.7 Jcm^{-2} [157]. Different thresholds, e.g., damage threshold, lift-off threshold, and melting threshold of 360 nm thick molybdenum film on glass, were determined by Bartl et al. using 5 picoseconds duration laser pulse and was estimated to be 0.15 Jcm^{-2} applied via an indirect laser ablation method. A lift-off process of a molybdenum thin film was observed at a fluence value of $0.28 - 0.03 \text{ Jcm}^{-2}$ and a molten layer of molybdenum was found at a fluence value greater than the fluence of 0.62 Jcm^{-2} by indirect laser ablation [168]. Selective structuring of 50 nm molybdenum films using a 10 picoseconds, 1064 nm laser, from the substrate side, was carried out by Heise et al. at an applied fluence value 1 Jcm^{-2} for a lift-off process [160, 169]. It is also found that the ablation threshold of 500 nm molybdenum films on glass from the back side is almost 10 times lower over the front-side ablation threshold value [160]. Complete removal of molybdenum film from the glass is possible at a fluence much less than the fluence required for thermodynamic heating, melting, and vaporisation of molybdenum [160, 169]. The fragmentation of material occurs when the stress exceeds a critical value; in the case of molybdenum, this occurs at laser fluences close to the damage threshold fluence [172]. The nature of the stress depends on the thermal expansion properties of the film and substrate. Computational simulations carried out by Zhigilei et al. on photomechanical spallation and stress confinement [173-176] found that ultrafast heating of electrons [173, 174] and electron-phonon coupling give rise to photomechanical spallation and is attributed to the interaction of an incoming compressive wave with a free surface [174].

In this thesis, interaction of short and ultrashort laser pulses with molybdenum-based samples were performed which presents a greater clarity of laser molybdenum interaction.

Chapter 3: Materials and methods

This chapter describes the materials and methods used for micro-machining and the different techniques used to characterise them. The first and second sections (section 3.1 and 3.2) of this chapter elaborates on the molybdenum bulk samples, the fabrication of single and multi-layered thin films by various deposition techniques and the experimental works were performed with those materials. In the third section (section 3.3), specifications of ultrashort and short laser sources are discussed followed by the development of the laser processing workstation on these samples. Mathematical calculations to determine reflectivity, threshold fluence are discussed in the following section (section 3.4). The section 3.5 emphasis in the offline characterisation methods to study the micro-machined damage on the samples. Section 3.6 discusses the temporal and spatial alignments required to develop workstations for the real-time characterisation during the ablation process. Different computational models by finite element method (FEM) used to simulate the interaction are discussed in the final section (section 3.7) of this chapter.

An overview of this chapter is presented as follows:

1. Deposition of thin films by physical vapour deposition technique (electron beam deposition and sputtering method).
2. Measurement of reflectivity and transmissivity of the samples to be examined; this was used to determine the absorbed energy deposited in the material by laser sources.
3. Micro-structuring of the samples using ultrashort and short pulsed laser sources.
4. Offline characterisations by scanning electron microscopy, atomic force microscopy, and energy dispersive X-ray analysis techniques.
5. Real-time imaging of the femtosecond and nanosecond ablation phenomena to understand the mechanism of laser interaction with materials.
6. Finally, numerical simulations were carried out to understand the ablation mechanism.

3.1. Molybdenum bulk

Commercially available bulk molybdenum (purity 99.9 %) from Goodfellow® (MO000330) was used for the experimental works. The dimension of the samples is 25 mm x 25 mm and the thickness of those samples are 250 μm .

3.2. Thin film deposition

Thin films are deposited on a substrate by thermal evaporation, chemical decomposition or the evaporation of source materials by the irradiation of energetic species or photons. The crystal phase and orientation of the films are governed by deposition conditions.

Thin film deposition process can be categorised by two types, mainly

1. Physical vapour deposition (PVD) and
2. Chemical vapour deposition (CVD)

Physical vapour deposition (PVD) technique is widely used for deposition of metallic elements. It usually takes place at a pressure less than atmospheric pressure [177]. Some of the PVD techniques are named as thermal deposition [177], electron beam evaporation [178], pulsed laser deposition

(PLD) [179], cathodic arc deposition [177], sputtering [180]. Each process has some advantages and disadvantages. Metal thin film deposition are typically performed by sputtering or electron-beam physical vapour deposition technique.

3.2.1. Method 1: Electron beam evaporation

In our present work, electron beam evaporation method was used over sputtering because of the following facts,

1. Electron-beam vaporisation processes offers structural and morphological control of the films.
2. The deposition rate can vary and can be as low as 1 nm per minute.
3. The material utilisation efficiency is high relative to other methods such as sputtering.
4. Electron beam evaporation is much more cost effective than sputtering technique.
5. E-beam evaporation process offers good electronic and optical quality thin films for solar cell applications.

An electron beam evaporation chamber consists of three main sub-systems, given by

1. An electron beam source to vaporise material.
2. A magnetic field to rotate the path of electron beam towards the ingot where the depositing material is placed
3. A vacuum deposition chamber to increase the mean free path of vaporised species.

A schematic diagram of an electron beam evaporator is presented in Figure 3.1. Different compartments are labelled 1 to 6. The crucible (1) is known as target holder; it is made of a material with a high melting temperature. This crucible holds the coating materials (2) used for deposition. A tungsten coil is used to produce high energy electron beam (3). The path of the electron beam is deflected by a magnetic field (4) and the high energy electron beam is focussed on the target (2) where the molybdenum is kept. The high energy electron beam increases the temperature of molybdenum beyond its melting and vaporisation temperature. The vaporised material (5) is deposited on a substrate (6) which is rotated constantly during deposition. This vaporisation process takes place in high vacuum to allow deposited particles/vapour to reach the substrate without reacting with other species in the ambient. This reduces the probability of incorporating of impurities of residual gases in materials.

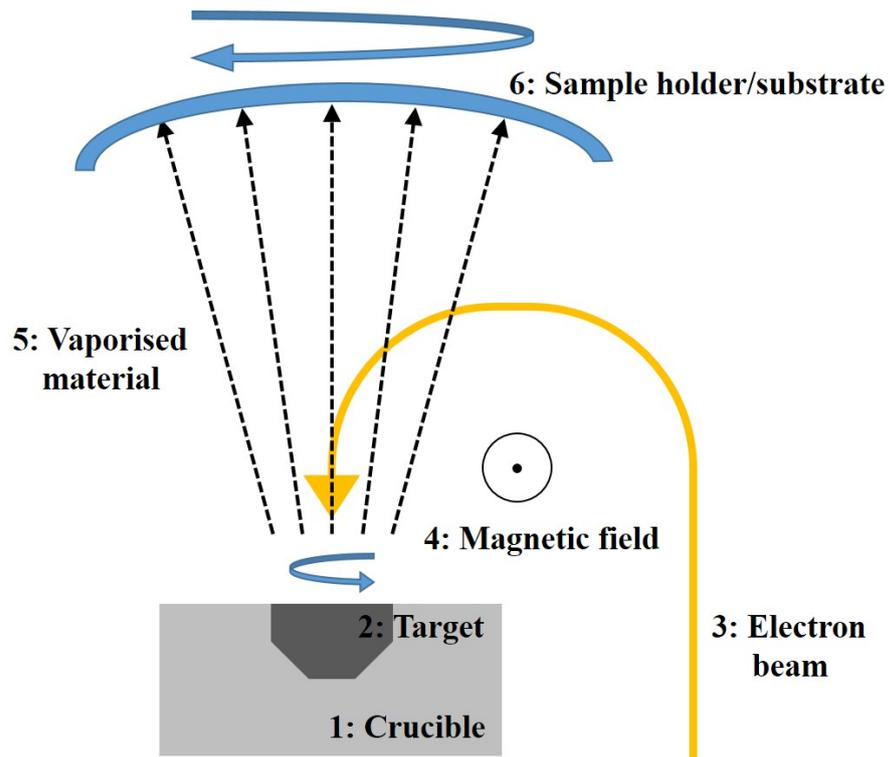


Figure 3.1: Deposition of thin film by electron beam evaporation technique

3.2.1.1. Sample preparation

There are two different assumptions taken during thin film deposition by electron beam evaporation:

1. There are no dust particle/impurities left on the deposition chamber
2. Deposited films will be uniform irrespective of its thickness

The first issue was to blow air to clear the substrate wafers prior to molybdenum film deposition. The wafers were then cleaned using a jet of de-ionised water to remove any debris. These wafers were then passed to the Central Fabrication Facility (Tyndall, Cork) with the e-beam evaporator (Temescal FC 2000) which is operated in a clean room. The electron beam deposition chamber consists of two vacuum pumps, rotary and ion pump. The initial deposition pressure was set at of 6×10^{-7} Torr which was measured by an ion gauge. The working instrument with the system map for electron beam evaporation is shown in the Figure 3.2,



Figure 3.2: The electron beam evaporation workstation with chamber with the schematic diagram during deposition

A test silicon wafer was placed in the system alongside the substrates during deposition. This enabled the film thickness to be verified using a surface profilometer at the time of fabrication. An ion etch of the substrate surface was carried out for 20 seconds prior to molybdenum deposition. To achieve the ion etch of the surface, Argon gas was circulated around the chamber for several minutes, before the tungsten filament was switched on causing ionisation of the gas and producing an Argon Ion (Ar^+) beam that plasma etched the substrate surface.

The electron beam was subsequently focused into the crucible containing a piece of molybdenum (~ 150 g) and scanned over its surface. The deposition rate was set to 3 nm / min with an error of ± 1 nm / min. The deposition chamber temperature was pre-set to 20°C , but could be varied from $25\text{-}70^{\circ}\text{C}$ during film coating. Time for deposition of molybdenum was set to achieve thickness of 50 nm. Once the thickness reached the desired value, an internal shutter was used to stop evaporation and further deposition of molybdenum on substrate. Figure 3.2(b) shows the front panel of the deposition chamber.

3.2.1.2. Substrate cooling

After deposition of thin films, the temperature of the deposition was decreased gradually in order to achieve high quality of film with minimal cracking.

3.2.1.3. Dicing

A thin flexible polymer (photoresist) was deposited on top of a molybdenum layer in order to prevent any damage on film. These were placed in the High Precision Wafer Dicer (Disco HiTec 3350). Each wafer was diced into chips of (0.7×0.7) cm^2 squares. After dicing the diced wafers

were immersed in a beaker consisting of acetone. This beaker was placed in an ultrasound bath for 10 minutes and the temperature was raised to 53°C (boiling point of acetone: 56°C) to dissolve carbon residues. After that, they were rinsed in isopropyl alcohol (IPA).

3.2.2. Method 2: Magnetron sputtering

A separate process was used for the deposition of the molybdenum-aluminium-molybdenum (MAM) samples. These were commercial samples produced Aimcore (Hsinchu, Taiwan) using the magnetron sputtering technique.

Sputtering is a physical deposition method (PVD) to coat high-quality metal, semiconductor and dielectric elements having high melting temperature on a substrate. In the basic sputtering process, a target material acts as a cathode. The chamber body or the substrate plate is either grounded or positively charged. A controlled inert gas (typically Argon, known as sputtering gas) is injected into a low pressure chamber (background pressure $\sim 10^{-4}$ Torr) chamber. A negative electrical potential is applied to the target material to be sputtered. This electrical potential caused the free electron to be accelerated away from the cathode. The gas atoms loose electrons and become ionised when these highly energised electrons collide with them. The positively ionised gas atoms are then accelerated towards the negatively charged cathode and the bombardment dislocate/eject neutral particles, such as atoms, molecules and clusters from the target material by momentum transfer. The sputtered elements are then passed through the deposition chamber and become incident on the substrate and adhered to it as a coated layer [181, 182]. Also, the positively charged ions recombine with the free electrons present in deposition chamber and causes plasma glow. It is possible to control several variables such as film thickness, grain structure, uniformity, adhesion strength within the process.

An energy source is required to generate and maintain the plasma. This is typically done by a DC source or a RF source. If the plasma generation is undertaken in a magnetic field, the sputtering process is termed as ‘magnetron sputtering’. In the conventional magnetron sputtering, one pole of the magnetic field is positioned at the central axis of the cathode and another pole is formed around the outer edge of the target. A periodic magnetic field is used to generate in the cathode (Figure 3.3).

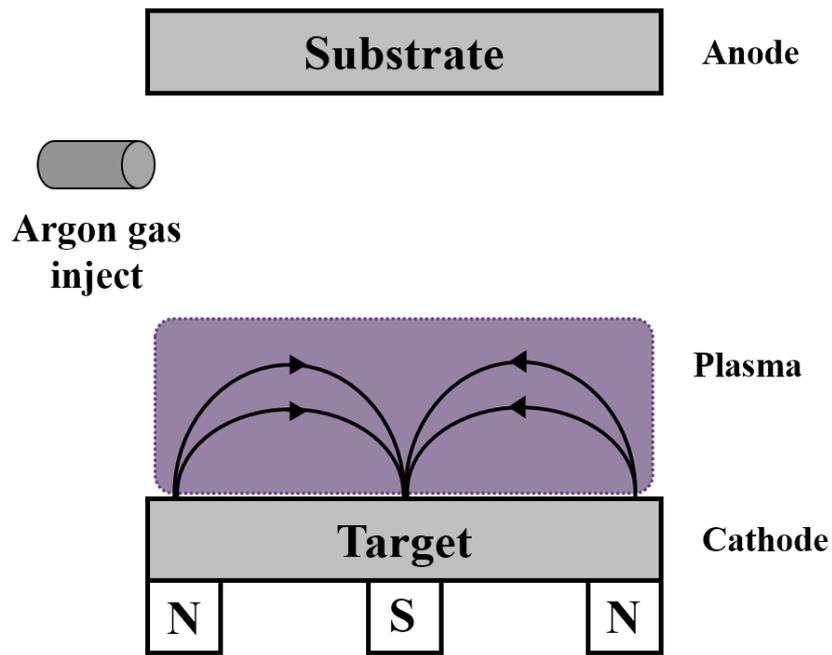


Figure 3.3: Schematic diagram inside a magnetron sputtering

In the magnetron sputtering chamber, the free electron moving in the deposition chamber can be trapped by the magnetic field near the target. The argon gas atoms are then collide with these and become positively ionised by leaving an outer cell electron. The positively ionised argon is then directed towards the negatively charged target. The impact of Ar^+ with the target material (molybdenum, aluminium and ITO) leads to removal of neutral elements from the target. The ejected electrons from argon also become trapped by the magnetic field, which will produce more Ar^+ ion, which in turn ejects more particles from the target. The trapping of electrons along the circuitous path in the magnetic field enhances the probability of ionisation of the neutral argon gas by electron-atom collisions. The increased ionisation efficiency by strong electric (DC or RF) and magnetic field can also be used to confine the plasma particles close to the surface of the sputtered target. This, in turn, leads to an increase of the bombardment probability by argon ions with the target and a higher sputtering rate. The dense plasma typically extends 60 mm from the surface of the target. The ejected elements consisting of atoms, molecules and clusters are then directed towards the substrate and condense as a thin film. The production line for the thin film coating is illustrated in the Figure 3.4,

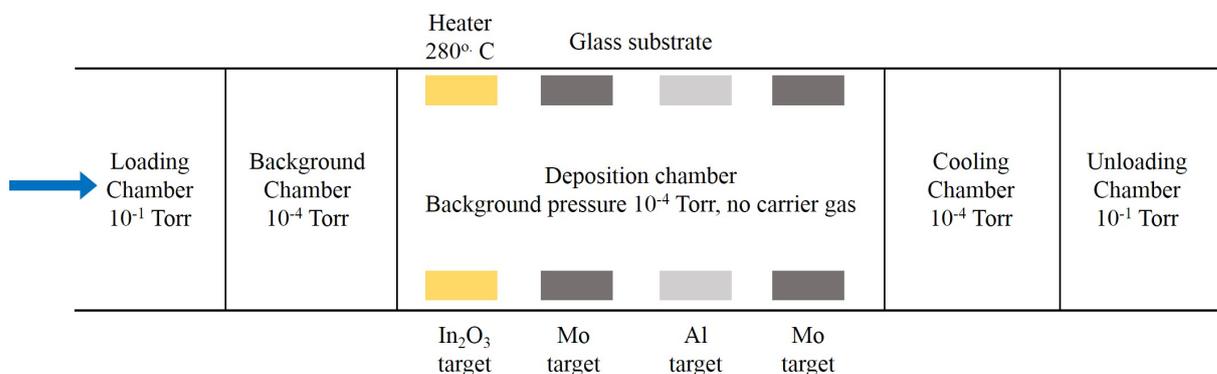


Figure 3.4: Production line of thin film deposition by magnetron sputtering technique

In the case of the heterostructure deposition on the glass substrate (0.7 mm), ITO, molybdenum, aluminium and molybdenum was deposited in different deposition chambers. The background pressure inside the deposition chambers was kept at 10^{-4} Torr. In the first deposition chamber, a layer of ITO (thickness 34 nm) was coated on the glass substrate. In the next chamber, a 30 nm thick molybdenum (Mo) layer was deposited on the ITO coated glass substrate. In the third deposition chamber 430 nm thick aluminium layer was deposited on Mo/ITO/glass substrate. Finally, 40 nm thin molybdenum layer was deposited on the Al/Mo/ITO/glass structure. The complete heterostructure was then cooled down to the room temperature without changing the background pressure. The thickness and the sheet resistance of the different layers are Table 3.1.

Table 3.1: Thickness and sheet resistance of the multilayered heterostructure

| <i>Layer</i> | <i>Coating</i> | <i>Thickness (nm)</i> | <i>Sheet resistance (Ωsq^{-1})</i> |
|----------------|----------------|-----------------------|---|
| <i>Layer 1</i> | Molybdenum | 40 ± 10 | ≤ 0.1 |
| <i>Layer 2</i> | Aluminium | 430 ± 50 | ≤ 0.1 |
| <i>Layer 3</i> | Molybdenum | 30 ± 10 | ≤ 0.1 |
| <i>Layer 4</i> | ITO | 34 ± 5 | 50 ± 10 |

3.3. Laser workstation

Two separate laser workstations were used to structure the materials (molybdenum bulk, thin film and multilayered film). The description of both the laser systems is discussed in this section.

3.3.1. Femtosecond laser system

Ultra-short laser processing of a material of interest was performed using Amplitude Systems S-Pulse HP laser system. It enables the delivery of high energy femtosecond pulses at high repetition rate (0.001-300 kHz). The laser head of S-Pulse high power system consists of a pumping medium, a mode locked oscillator, followed by optics for pulse stretching, then pulse amplification, pulse compression and finally pulse modulation by a pulse picker.

The femtosecond laser used in this study has ytterbium doped crystalline material (Yb:KYW crystal) as an active laser medium. Ytterbium belongs to rare earth family and it exhibits strong absorption bands in near infrared (typically 940-980 nm). Thus, the active medium of the S-Pulse femtosecond laser system is achieved using direct, continuous wave laser, diode pumping. The fluorescence spectral bandwidth is large enough to sustain ultra-short duration. Irradiation of the active medium by a diode laser takes place inside a Fabry–Perot cavity. The strong optical absorption, combined with a long lifetime of the upper transition on Yb results in a population inversion in the crystal. The generation of ultra-short laser pulses is controlled by mode locking which occurs when the phase of adjacent longitudinal modes is in phase relative to each other. The mode locked laser oscillator head emits a weakly powered pulse (≈ 20 nJ), 250 femtosecond pulses, with a repetition rate of 30 MHz, at a wavelength of 1030 nm.

Chirped pulse amplification technique is used to achieve efficient amplification of mode locked ultra-short pulses using a pair of reflective diffraction gratings (chapter 2, section 2.4). Firstly, the femtosecond laser pulse was temporally stretched in order to reduce laser pulse intensity and peak power. The low-intensity pulse was amplified safely after stretching. Once the pulse is stretched, the beam in the Amplitude system is put through an electro-optic shutter (in our case Pockel cell) which acts like a Brewster window. The crystal becomes birefringent when an electric field is applied across the crystal. When the voltage is turned on, the shutter rotates the plane of polarisation by 45° and the stretched beam passes through the cell. Soon after, the laser beam reflects from mirror and experiences additional 45° plane of polarisation rotation as a result of which the Pockel cell rejects the reflected beam. When the voltage is turned off, the polarisation is no longer rotated and the reflected laser beam returns to the amplifier to be further amplified in the gain medium [6]. The technique used for amplification of laser pulse is known as regenerative amplification. The pulse is kept in the resonator until the amplified energy reaches a maximum value and then extracted through the resonator using a Faraday rotator.

The stretched, high-intensity laser pulse is then compressed, using a pair of diffractive gratings, using the reverse process to the pulse stretching gratings. The pulse compressor reduces the duration of amplified pulse towards its initial value (~ 500 fs). The compressed ultra-short pulses are directed to a pulse picker modulator that controls emitted repetition frequency range (0.001 to 300 kHz). This modulator is an acousto-optic device that controls frequency of a laser frequency by generating an acousto-optic effect in the Amplitude systems. It consists of a transparent crystal attached with a piezoelectric transducer (LiNbO_3).

After emission from the femtosecond laser head, the pulse goes through an interface box, as seen Figure 3.5,

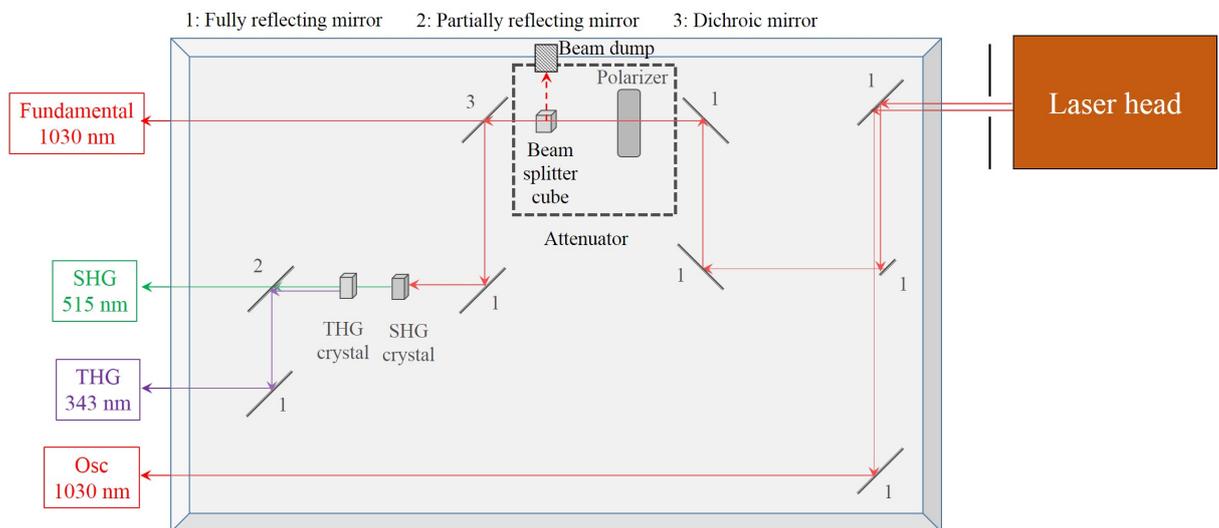


Figure 3.5: Interference box in front of Laser head consisting of optical layout of SHG and THG pulse generation from amplified IR laser beam

The emitted laser beam from the fundamental laser beam enters an interface box shown in the Figure 3.5. The fundamental laser beam goes through a motorised attenuator which consists of a polariser (half-wave plate) and a beam splitter cube. Vertical component of the polarised beam goes straight through the beam splitter cube and horizontally polarised component is extracted and

dumped to a beam bump. This attenuator provides the ability to change peak power of the fundamental beam. One part of a fundamental beam is taken through a partially reflecting mirror (50-50) for the purpose of material processing. Another component of the fundamental IR beam is used to generate higher frequency harmonics using a process known as high-harmonic generation. The IR laser pulse passes through a lithium triborate (LiB_3O_5) crystal for second harmonic generation (wavelength 515 nm), and barium borate (BaB_2O_4) for third harmonic generation (wavelength 343 nm) [183]. The fundamental wave generates a nonlinear polarisation that oscillates at twice of the fundamental frequency and therefore has half the incident wavelength [38, 184]. Frequency tripling takes place when the second harmonic waves (515 nm) combines with the fundamental wave (1030 nm) producing a third harmonic (343 nm) wave. This harmonic generation results in a lowering of the overall efficiency of the output power. The output power of 515 nm and 343 nm laser drops to 50 % and 33 % respectively. The sensitivity of the harmonic generation depends upon the nonlinear response of the LiB_3O_5 and BaB_2O_4 crystals to the incident power density. Thus, the spatial profile of 515 nm and 343 nm laser pulse slightly differs from the profile of the 1030 nm beam after passing through second and third harmonic crystals. The technical specifications of S-Pulse Amplitude femtosecond laser system are tabulated in the Table 3.5.

Table 3.2: Technical specifications of Amplitude systems S-Pulse HP femtosecond laser

| <i>Parameters</i> | <i>Value</i> | <i>Unit</i> |
|--|--|---------------|
| <i>Laser wavelength</i> | 1030 (Fundamental) 515 (SHG) 343 (THG) | nm |
| <i>Pulse duration</i> | ~500 | fs |
| <i>Power</i> | 0.4-4 | watt |
| <i>Energy</i> | 40-1000 | μJ |
| <i>Repetition rate</i> | 0.001-300 | kHz |
| <i>Spatial mode</i> | TEM ₀₀ | |
| <i>Beam quality (M^2)</i> | < 1.2 | |
| <i>Pulse to pulse stability</i> | 0.5% RMS | |

After passing through various mirrors the laser beams are focussed through a telecentric lens (F-Theta) attached with a Galvanometer scanning system (SCANLAB, hurrySCAN II). The laser beam is then focussed on the surface of a material which is placed on a computer controlled XYZ stage (Aerotech 3200). The schematic of femtosecond laser beam delivery of system along with the workstation is shown in Figure 3.6.

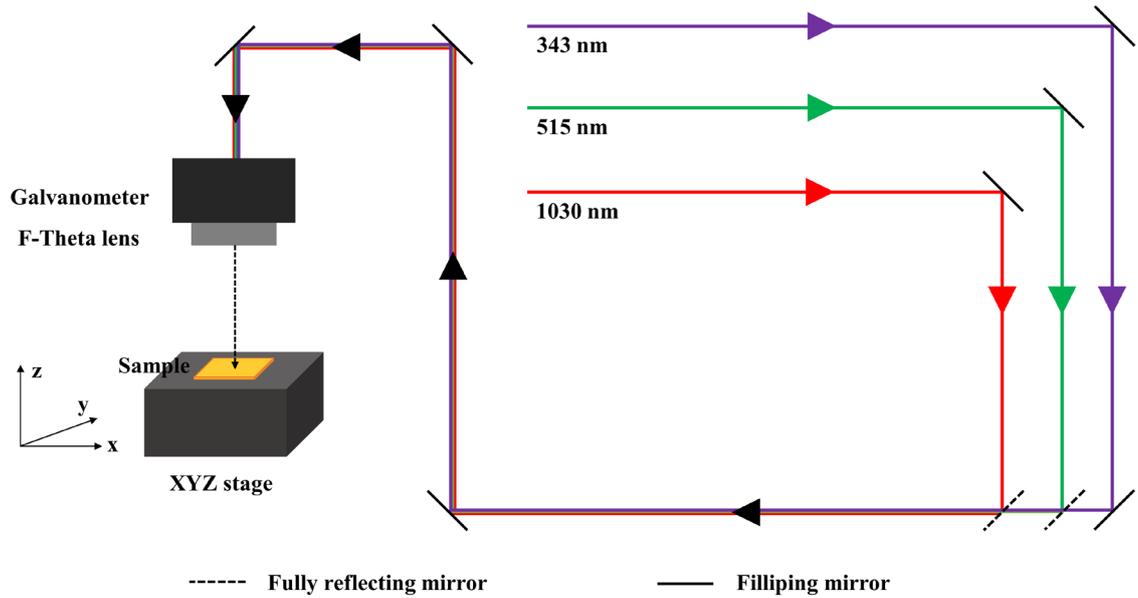


Figure 3.6: Femtosecond laser workstation for micro processing of samples

3.3.2. Nanosecond laser system

A spectra-physics high peak power oscillator (HIPPO) laser system is used to generate nanosecond pulses. The material YVO_4 (Vanadate) doped with Nd is used as the active medium of HIPPO laser system (chapter 2, section 2.2). Vanadate provides high gain and high laser power is achieved at high repetition rate values. Two high-power, thermally stabilised, Spectra-Physics ‘FCbar’ diode lasers operating at a wavelength of 808 nm, are fibre delivered to pump the $Nd:YVO_4$ active medium in the laser head. The pump beams are absorbed by the active medium and generates a wavelength of 1064 nm (Figure 2.2).

Two acousto-optic Q-switches are placed inside the laser cavity to amplify the laser beam. The acousto-optic shutter acts like a shutter which consists of a quartz crystal installed inside laser cavity. The optical surface of the crystal has low loss anti-reflection coating. A piezoelectric transducer is attached with the quartz crystal. The transducer produces strong acoustic waves which propagate through the crystal while RF signal of the transducer is turned on. The RF signal produces an effective diffraction grating. That is when the RF signal is activated during the time that the amplifier is being pumped, the laser beam is deflected out and losses in the cavity increases. Once the RF signal is turned off, the laser beam passes through crystal, reflects back and Q-switch pulse develops inside the cavity. The portion of the emitted laser light (1064 nm) energy comes out from the cavity through a partially reflecting mirror.

In order to generate 532 nm and 355 nm laser pulses, harmonic doubler and tripler modules can be attached to the main laser head. The laser operates with a TEM_{00} output spatial intensity. The acousto-optic Q-switch enables to vary the laser repetition rate from 30-300 kHz. The laser power must be optimised for each wavelength in use. The specifications of the nanosecond laser is tabulated in the table below [149].

Table 3.3: Technical specifications of nanosecond HIPPO laser system

| Parameters | Value | | | Unit |
|--|-------------------|-------------------|-------------------|-------------|
| <i>Wavelength</i> | 1064 | 532 | 355 | nm |
| <i>Pulse width</i> | 9 ns @ 50 kHz | 12 ns @50 kHz | 20 ns @50 kHz | ns |
| <i>Repetition Rate</i> | 15-300 | | | kHz |
| <i>Average power output</i> | 17 W @50 kHz | 11 W @50 kHz | 5 W @50 kHz | Watt |
| <i>Spatial mode</i> | TEM ₀₀ | TEM ₀₀ | TEM ₀₀ | |
| <i>Beam quality (M^2)</i> | < 1.2 | < 1.3 | < 1.3 | |
| <i>Raw beam diameter (at waist)</i> | 0.6 | 1 | 1 | mm |
| <i>Pulse to pulse stability</i> | < 2% at 50 kHz | < 5% at 50 kHz | <5% at 50 kHz | RMS |
| <i>Beam ellipticity</i> | < 10% | | | |
| <i>Polarisation</i> | Vertical | Horizontal | Vertical | |

The optical setup for the HIPPO laser is shown in the Figure 3.7. After passing through a polarising half wave plate and beam splitting cube, the laser beam is transferred through galvanometer system attached with a telocentric F-theta lens converging lens. The laser beam is focused in the sample surface of interest through the converging lens at a distance of 100 mm from the optic axis of the lens. The sample is placed on the top of a manually controlled XYZ stage.

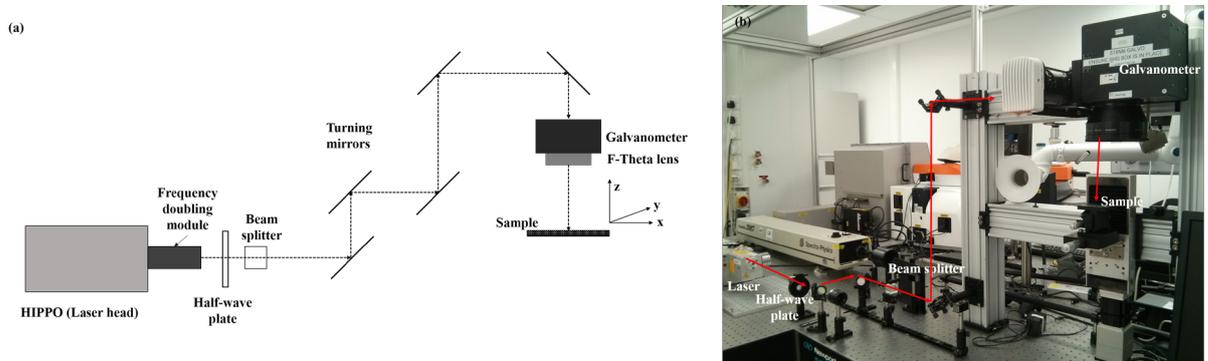


Figure 3.7: HIPPO (nanosecond) workstation for material processing attached with frequency doubling module

3.3.3. Laser intensity profile

The spatial distribution of both femtosecond and nanosecond laser beams are Gaussian in nature. This Gaussian profile corresponds to theoretical TEM_{00} mode. The ‘beam quality factor, (M^2 value) of an ideal Gaussian beam is 1, but it fluctuates with the different laser sources. For the real Gaussian beam, the M-square value is close to unity [184]. The irradiance distribution intensity in the TEM_{00} Gaussian mode is given in equation (1)

$$I(r) = I_0 \exp\left(\frac{-2r^2}{\omega(z)^2}\right) \quad (14)$$

where, r is the radial coordinate, $I(r)$ is the laser beam intensity in (Wm^{-2}), $\omega(z)$ is known as the beam radius and where the peak intensity level (I_0) of the laser beam drops to $1/e^2$ times.

When the Gaussian beam propagates in free space the beam converges to its narrowest value of ω_0 along the beam axis and is called the beam waist radius. $\omega(z)$ and ω_0 are related by the following formula,

$$\omega(z) = \omega_0 \sqrt{1 + \left(\frac{\lambda z}{\pi \omega_0^2}\right)^2} \quad (15)$$

where, λ is the wavelength of the laser beam and z is the distance from the focus. The total power is determined by integrating the spatial intensity profile,

$$P(t) = 2\pi \int_0^\infty I(r, t) r dr = \frac{\pi \omega(z)^2 I_0(t)}{2} \quad (16)$$

The beam radius for the Gaussian intensity profile, ω_0 , was determined as the radius where the intensity is equal to $1/e^2$ at the peak [185]. The unfocused beam diameter was measured using a beam profiler (Beamstar) with attenuators used to reduce the laser intensity. An example of the beam profile imaged is shown in Figure 3.8 which shows the spatial profile of a raw 1030 nm femtosecond beam with power distribution.

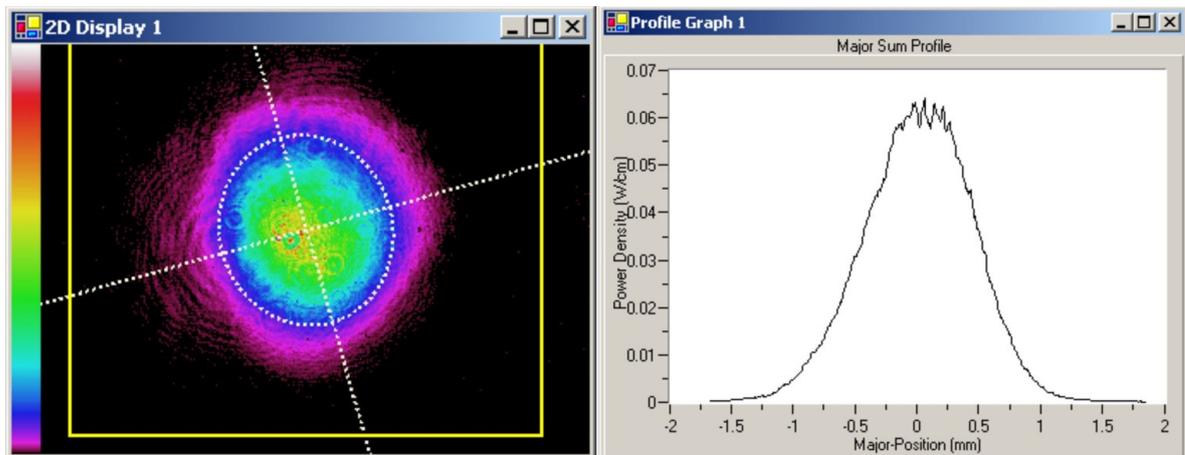


Figure 3.8: Spatial profile of IR FS laser beam (1030 nm) at very low intensity

3.3.4. Laser power control

The laser power of femtosecond and nanosecond systems were regulated by external attenuator setup. The external attenuator consists of a zero-order half wave plate and a beam splitter cube. In the case of the nanosecond laser source, the diode current can be maintained at a consistent level in order to keep low pulse to pulse instability. Three different combinations of half wave plate and beam splitter were used for the wavelengths of 1064 nm, 532 nm and 355 nm, respectively. The damage threshold of these half wave plate and beam splitting cube were higher than 10 Jcm^{-2} . The laser power of the femtosecond laser beam is controlled through an external attenuator, placed before the harmonic generation box (Figure 3.5). The orientation of the THG and SHG crystals was optimised in order to achieve 343 or 515 nm laser wavelengths. This is achieved by placing a power meter at the harmonic box exit aperture and adjusting the fine screws on the THG and SHG crystals, until maximum power is achieved at the desired wavelength. The power used was measured just before the beam reaches the galvanometer scanning system, this allows the various energy losses to be taken into account because of the reflecting mirrors. The power was measured using a thermal head (Ophir).

The pulse energy (E_p) of a single pulse was determined using the relation between the laser output power (P) and the operating laser frequency (Q), given below,

$$E_p = \frac{P}{Q} \quad (17)$$

3.3.5. Focussing of laser beams

To focus laser beams, various galvanometer systems (hurrySCAN[®] II 14, Scanlab[®]) and an F-Theta telecentric lenses (F-Theta Ronar, Qioptiq[®], focal length 100 mm) were used. The galvanometer is controlled using “Winlase[®]” (Lanmark controls) laser marking software. The Winlase software is connected to the laser control head through cable to an RC232 card. This card provides an electrical signal to the internal gate which controls shutter. In the femtosecond laser set up system, the sample height and position were adjusted using a computer driven XYZ stage (Aerotech Inc, Npaq). In case of nanosecond laser processing, the position of the sample at the focal point is controlled using a simple XYZ mechanical manual stage.

3.3.6. Transmission of laser pulse through galvanometer

Transmission of the laser pulse through the galvanometer lens was estimated by measuring the laser power before and after galvanometer setup. Table 3.4 shows the power measured by the power meter before the galvanometer and the transmitted power from the galvanometer lens measured before the femtosecond laser pulse incident on the sample surface. Finally, the transmission through the galvanometer lens was determined after taking average of five different measurements.

Table 3.4: Transmission (%) of laser pulse through the beam delivery system

| <i>Wavelength (nm)</i> | <i>Power (milli watt)</i> | | <i>Transmission (%)</i> |
|------------------------|---------------------------|--------------------|-------------------------|
| | Before Galvanometer | After Galvanometer | |
| 1030 | 100 | 98 | 98 |
| | 200 | 197 | 98.5 |
| | 300 | 293 | 97.67 |
| | 400 | 392 | 98 |
| | 500 | 490 | 98 |
| 515 | 100 | 98 | 98 |
| | 200 | 198 | 99 |
| | 300 | 296 | 98.67 |
| | 400 | 395 | 98.75 |
| | 500 | 494 | 98.8 |
| 343 | 100 | 99 | 99 |
| | 200 | 198 | 99 |
| | 300 | 296 | 98.67 |
| | 400 | 397 | 99.25 |
| | 500 | 493 | 98.6 |

The table indicates transmission of 98.03 (1030 nm), 98.64 (515 nm) and 98.9% (343 nm) laser beam takes place through the galvanometer lenses, respectively. Thus, minimal absorption of laser wavelengths (1030: 1.97, 515: 1.36 and 343: 1.1%) observed by the galvanometer lens.

Similar to the femtosecond case, transmission of nanosecond laser pulse through the galvanometer lens was measured. It was calculated that at the wavelengths of 1061, 532 and 355 nm wavelengths 96.26, 97.61 and 98.15 laser pulse transmit through the galvanometer lens, respectively.

3.4. Measurement of absorbed laser fluence into the material

The response of the material to an incident laser beam was discussed in the previous chapter (chapter 2, section 2.5). The incident laser light on a material can be reflected at the air-material interface, absorbed through the depth of the material and transmitted through the rear surface of the material. The scattering component is small due to strong absorption in thin films. Transmission through the material to the outer surface is also considered but is small. The absorbed portion of laser light is determined by subtracting the transmitted and reflected portions from the applied laser fluence. In this section, the method for measuring the reflectance and transmittance using integrating sphere is presented.

3.4.1. Integrating sphere

The reflectivity measurement was performed using an integrating sphere. The schematic diagram of the integrating sphere is shown in the Figure 3.9 (a). This is a hollow sphere of diameter (100 mm) coated with highly reflecting barium sulphate (BaSO_4) from inside. It has three ports among which the entrance port allows the laser light to enter the sphere. The bottom port is a sample holder, on which a sample is mounted at an angle of 8° . The angle of the sample is oriented so that reflected light does not travel back again through the entrance port at the top of the sphere. The port on the side of the integrating sphere has a photodiode, which detects the diffusely scattered light around the integrating sphere. A baffle was placed inside the integrating sphere to ensure that there is no reflected laser light directly incident to the detector. A photo of the integrating sphere setup is shown in Figure 3.9.

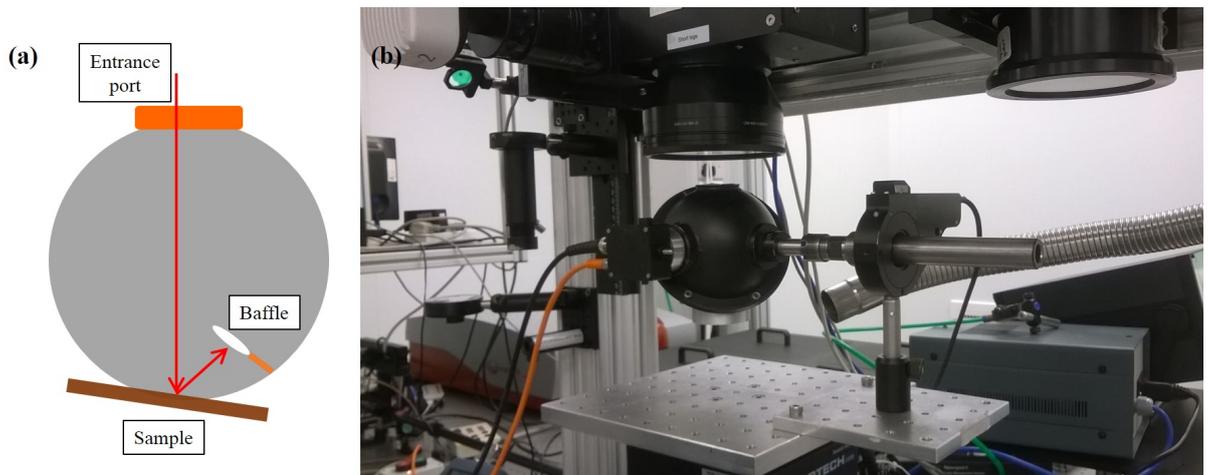


Figure 3.9: Schematic diagram of using integrating sphere (a) and the workstation development for measurement of reflectivity and transitivity using integrating sphere

The sample holder consists of a small hole in the base to prevent multiple reflection inside the sample and transmitted light does not reflect back into the sphere. A sample is placed on the top of the hole and fixed by a clip. Figure 3.10 shows the sample holder used to account for reflectivity measurement using the integrating sphere. Highly reflecting barium sulphate (BaSO_4) was used as a reference material which is the same as for the reflective coating on the inside of the sphere.



Figure 3.10: Integrating sphere base

When light is incident on a sample, the light is partially reflected, and the reflected light undergoes multiple reflection inside the sphere. The intensity of reflected beam reaches to a steady state within a few nanoseconds [186]. The total reflected radiation is collected and integrated by the sphere and is determined by a signal which is detected by a suitable photodiode (PDA10A-EC, silicon amplified detector). The photodetector was connected with a digital oscilloscope (Tektronix TDS 5054B) via a 50 Ω resistor.

3.4.2. Measurement of reflected and transmitted laser beam

For reflected and transmittance measurement a laser beam of suitable fluence was selected which is less than the ablative threshold fluence of BaSO₄ and the sample. As the photodiode is very sensitive to the light intensity care was taken to ensure that the reflected or transmitted laser light does not damage the sensor of the photodiode.

In case of reflectivity measurement, the laser was first focused on BaSO₄. A single laser pulse was focussed on the BaSO₄ powder. The focussed laser pulse reflected from the BaSO₄ was detected by the photodiode which generates an electrical signal. The electrical signal was displayed by the oscilloscope in terms of a voltage signal. After that the laser beam was focused on the sample. Using the same manner, the reflected signal was detected. The relative reflectivity was measured by dividing the reflected signal from the sample by the reflected signal from the BaSO₄.

Transmissivity measurement of the sample was implemented as follows. First, laser was focused on highly reflecting BaSO₄ sample and the reflected light intensity was measured by the photodiode. Next, a sample was placed on top of the entrance port. At this situation, only the laser transmitted from the sample incident on the BaSO₄ powder and reflects from it. This reflected light from the BaSO₄ was also measured by the photodiode. The ratio of these two signals provides the transmissivity of the sample under examination.

3.4.3. Measurement of threshold fluence

Determination of focused laser beam diameter is necessary prior to measure threshold fluence. The laser beams were focused on the material using a converging lens (section 3.2.1 and 3.2.2). It

was found that the spatial profile remains same after going through a converging lens [185]. If a Gaussian laser beam, with sufficient fluence, is focused on a material surface, the functional dependence of a crater diameter (D) determined by an optical microscope and pulse energy (E_p), is given by [187],

$$D^2 = 2\omega_0^2(\ln E_p - \ln E_{th}) \quad (18)$$

where, ω_0 is the half the beam waist (beam radius) and E_{th} is the threshold energy in Joule. The beam radius is obtained from the slope of the plot between logarithmic E_p against D^2 .

The value of, ω_0 is used to determine the peak fluence value, F_0 using the equation,

$$F_0 = \frac{2E_p}{\pi\omega_0^2} \quad (19)$$

The value of F_0 was used to determine the threshold fluence using Liu's method [187].

As the peak applied fluence is decreased, the minimum applied fluence required to visibly damage the surface, is generally referred to as the damage threshold fluence. This minimum energy density is typically found by plotting D^2 versus the natural logarithm of the peak fluence $\ln(F_0)$, and extrapolating the curve to 0.

$$D^2 = 2\omega_0^2 \ln(F_0) - 2\omega_0^2 \ln(F_{th}) \quad (20)$$

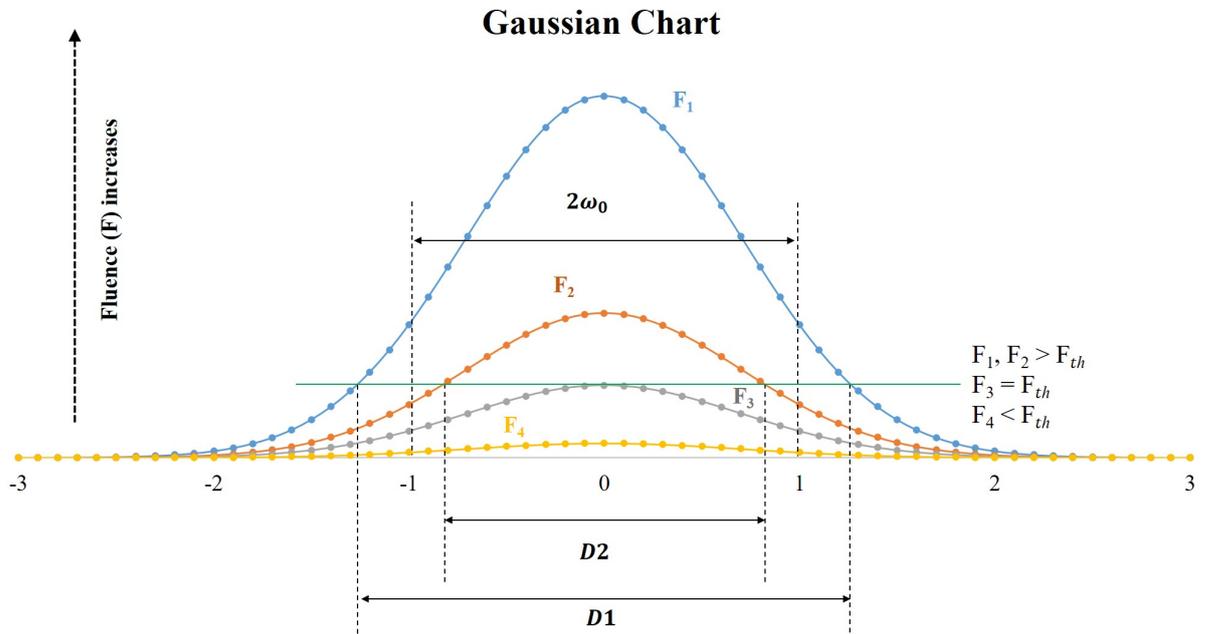


Figure 3.11: Spectral profile of Gaussian beam and its relationship with different laser fluence

Figure 3.11 shows the Gaussian profile of difference fluence value with beam waist ($2\omega_0$). F_{th} correspond the threshold fluence of laser beam. Below the threshold fluence (F_{th}), the laser is unable to create any visible damage in the material. The increase of the fluence above material threshold value creates damage on the sample surface, defined by diameters D_2 and D_1 . It is also

seen that that the diameter of the damaged area on the material surface can be higher or lower than the beam waist diameter ($2\omega_0$).

Using the amount of absorbed fraction of the incident laser light energy, absorbed threshold fluence (F_{abs}) were measured,

$$F_{abs} = (1 - R - T)F \quad (21)$$

where, R and T are the reflectivity and transmissivity, respectively, and F is the applied laser fluence on the sample surface.

Micromachining of molybdenum bulk, thin film and multilayered film assembly was performed using the Amplitude systems S-Pulse femtosecond laser and the Spectra Physics HIPPO nanosecond laser at various absorbed fluences. The next section will describe the different characterisation methods used to understand the ablation mechanism. Offline characterisation was used to study ablated/processed material surface after interaction laser pulse with different materials. While, online characterisation was used to investigate real-time measurement during femtosecond and nanosecond laser ablation.

3.5. Offline characterisations

The femtosecond and nanosecond processed samples were investigated using Atomic Force Microscope (AFM), Scanning Electron Microscope (SEM) and Energy Dispersive X-ray (EDX) techniques. The working principle of these instruments and the offline characterisation of a bulk molybdenum, single layer thin film of molybdenum and multilayered assembly on molybdenum-aluminium-molybdenum-ITO-glass is discussed in this section.

3.5.1. Atomic force microscopy (AFM)

Atomic force microscopy system is a type of scanning probe microscopy (SPM) system. The atomic force microscopy (Agilent 5500) was used to probe local properties of the laser exposed and unexposed samples. This technique was used to determine the surface topography, surface profile, roughness of the laser patterned features on a sample surface. The instrumental setup in atomic force microscopy system is shown in Figure 3.12.

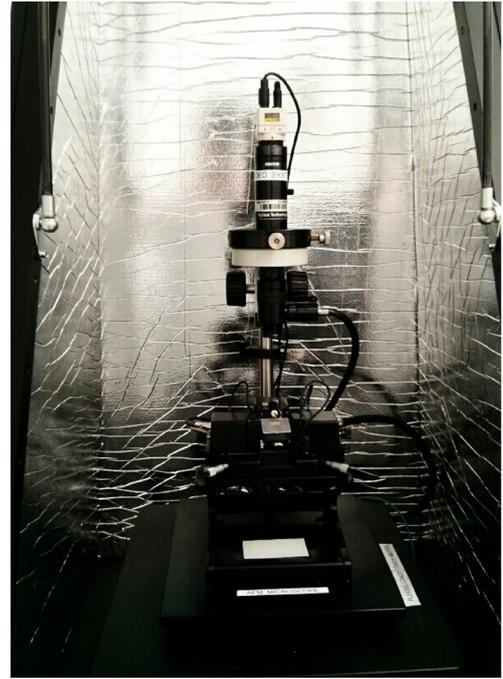
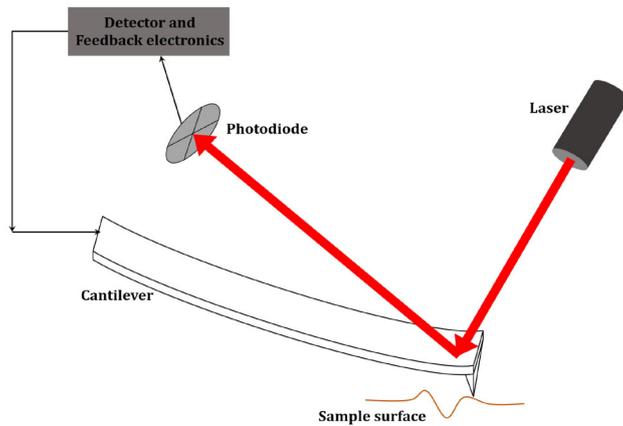


Figure 3.12: The atomic force microscopy setup is enclosed in an anti-vibration chamber in order to preclude any external vibration

Three main components of atomic force microscope system are a laser source, a sharp AFM cantilever probe and a photodiode. Usually, AFM operates in three modes e.g. contact mode, tapping mode and non-contact mode, among which contact mode was used for our study. The AFM cantilever probe used in the study are Nanosensors PointProbe Plus (PPP-CONTR) operated in contact mode and are of highly doped silicon [188]. The technical specifications of the probe are given in the following table,

Table 3.5: Different features of the cantilever probe used in AFM measurements [142]

| <i>Feature</i> | <i>Value</i> |
|--------------------------------|----------------------------|
| <i>Tip radius of curvature</i> | < 10 nm |
| <i>Tip height</i> | 10-15 μm |
| <i>Thickness</i> | 1-3 μm |
| <i>Mean width</i> | 42.5- 57.5 μm |
| <i>Length</i> | 440-460 μm |
| <i>Force constant</i> | 0.03-0.77 Nm^{-1} |
| <i>Resonance frequency</i> | 6-21 kHz |

Approaching the tip towards the sample leads to an increase of attractive and then repulsive forces between the probe and the surface. In the present study, the AFM was operated in the contact mode. The net attraction and repulsion between the tip and surface is zero when the system is

operated in the contact mode. The AFM scan of a sample was performed over an area of $100 \mu\text{m}^2$ or less. The AFM tip experiences a change in surface topography as it travels across the sample which results deflection of the cantilever in order to keep constant force between sample and probe. A position sensitive photodiode measures deflection of the reflected laser beam caused by deflection of the cantilever. A three-dimensional topographic image is generated when the tip of the cantilever moved across the surface [189].

3.5.2. Scanning electron microscopy

The Scanning Electron Microscope (SEM) was used to produce high-resolution image the samples after femtosecond and nanosecond laser ablation. In this study, scanning electron microscopy of samples was performed using Hitachi S-4700 scanning electron microscope operates in high vacuum (10^{-5} to 10^{-6} Torr) using rotary and ion pump. It has a cold cathode field emission electron gun, made of mono-crystalline tungsten which provides stable beam of electrons of adjustable energy. It consists of two condensers and one objective electromagnetic lens which are used to focus the highly energised electrons on an electrically grounded specimen of interest. Hitachi SEM has two photodetectors to detect secondary and backscattered electrons. Required sample size for SEM imaging is limited to 25 mm diameter. Molybdenum-based samples were fixed on the sample holder (stub) using a double sided conducting carbon adhesive tape. In the present work, for imaging purpose primary electron accelerating voltage was varied from 5 keV to 15 keV. Also, the samples were placed normal to focused electron beam or kept an angle of 30° , depending upon the requirement.

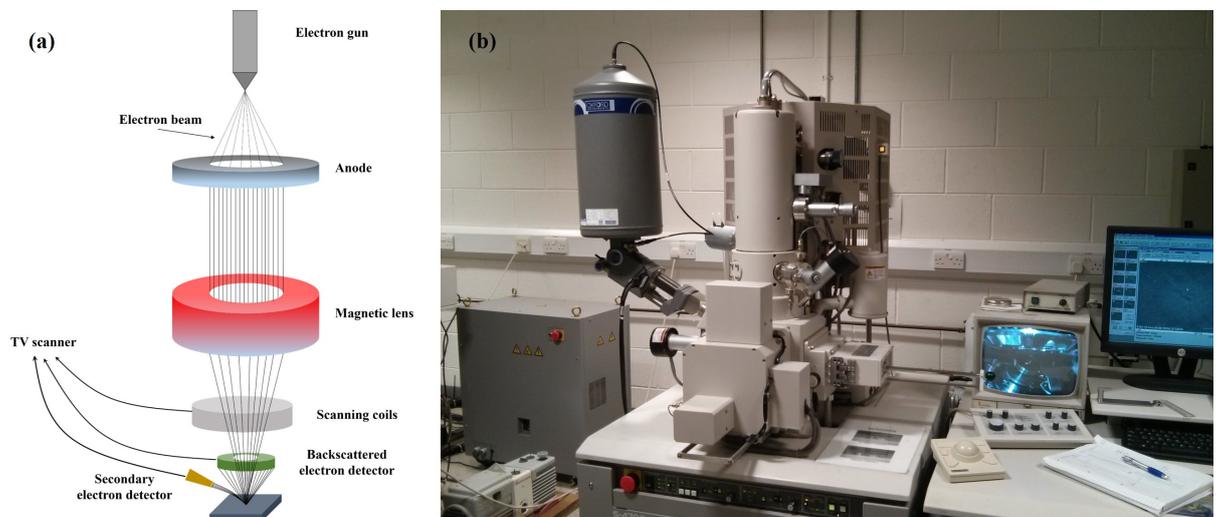


Figure 3.13: Scanning electron microscope system (a) and the available setup (b) with energy dispersive X-ray facility used for characterisation (Hitachi S-4700)

3.5.3. Energy dispersive X-ray (EDX) analysis

The electron dispersive X-ray analysis (EDX) measurement was integrated with Hitachi S-4700 scanning electron microscope system for the elemental analysis of laser processed materials. This technique (Bruker AXS, Quantax 4010) is integrated with scanning electron microscope system. Figure 3.13 shows scanning electron microscope system embedded with elemental analysis of materials.

3.6. Development of laser workstation for online characterisations

The development of new workstation for real-time imaging required both temporal and spatial alignment of observations of the laser material interaction. The generation of single laser pulse at a fixed reference time was required for temporal analysis of laser pulse interactions. In many laser material processing applications using galvanometer systems, a variable asynchronous timing exists between the rising edge of the external gate and the output laser pulse; this is not useful in real time measurements. To allow a fixed timing between laser gate signal and the emitted laser pulse, the laser pulses were therefore triggered externally which allowed a fixed temporal reference between applied gate signal and laser output pulse to be obtained. Thus, any observations of the laser material interactions could then be precisely timed from the gate signal. A new beam delivery system was designed and developed using free space optics for this purpose. This section describes the temporal and spatial alignment of both femtosecond and nanosecond laser systems, used separately, for separate real-time observations. Two types of observations were used. The first concerned spatial monitoring of the laser plasma plume. The second concerned spectral characterisation of the light emitted from this spatial plume.

3.6.1. Temporal alignment

3.6.1.1. Femtosecond laser system

It is possible to generate a single laser pulse by applying an external signal to the pulse picker signal and by triggering femtosecond laser externally.

A Stanford pulse generator (DG535 Stanford Research Systems) was used to obtain a single femtosecond laser pulse. The Generation of a single femtosecond laser pulse from a beam with repetition rate, 5 kHz, from the laser head is illustrated in Figure 3.14.

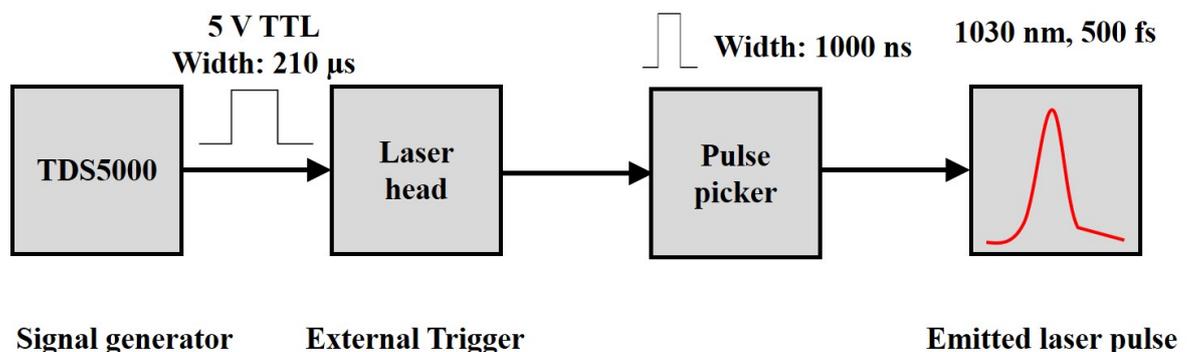


Figure 3.14: External triggering of femtosecond laser using a pulse generator

The repetition rate of the laser pulse is controlled by the Amplitude software by changing the amplifier frequency. This amplifier frequency determines the repetition rate of the output laser pulse. The amplifier is placed between the pulse stretcher and compressor and it consists of a laser cavity, Pockels cells and Faraday rotator. The amplification of the stretched laser pulse was achieved by several passes through the amplifier. The Pockels cell contains an electro-optic crystal (barium borate). Linear changes in the birefringence of this crystal take place when an external voltage is applied to it. A laser pulse transmits through when a voltage is applied on it. After the amplification, the amplified laser pulse is then compressed and passed through a pulse picker (PP) (discussed in the section 3.2.1). It is an acousto-optic modulator used to pick pulses by controlling

the frequency, power and spatial direction of laser beam by beams of acousto-optic effect. The pulse picker (PP) transmit laser pulses at its oscillation frequency and the laser pulses are emitted from the external shutter. The repetition rate of the amplified pulse can be varied after the pulse goes through the pulse picker by selecting pulse picker oscillation frequency. When the frequency of the amplifier and pulse picker matches, all laser pulses transmit through the external shutter. When the pulse picker frequency is half of the amplifier frequency, the output laser pulses have the repetition equal to the pulse picker frequency. Thus, the pulse picker (PP) controls the repetition rate of the emitted laser pulse from the interface box.

Using the external pulse generator, a 5 V TTL signal of pulse width 210 μs was given to the Pockels cells in the amplifier. The width of the pulse (pulse ON time) must be greater than the time period associated with the pulse picker frequency set in the software. Arrival time of the laser pulse at the sample surface was detected using a photodiode (PDA50B, Thorlabs). The external TTL signal supplied to the amplifier, pulse picker signal (MON PP) and the photodiode signal was monitored using a digital oscilloscope (Tektronix TDS5000) in order to understand the temporal relationship among them. The time between the rising edge of the pulse picker pulse and the single femtosecond laser pulse detection is shown in the Figure 3.15 for 1030 nm wavelength,



Figure 3.15: Relationship between pulse picker and laser pulse, Laser pulse (green) was detected after 1.036 μs from the rising edge of MON PP pulse picker signal (yellow)

The 1 μs wide pulse picker signal (MON PP) was monitored using the oscilloscope; an output is shown in the Figure 3.15. One laser pulse signal was detected at the sample surface at a time delay of 1.036 μs from the rising edge of the pulse picker.

The pulse picker (MON PP) signal was used to trigger the camera and the spectrometer for the real-time spatial and spectral measurements.

3.6.1.2. Nanosecond laser system

The triggering of the nanosecond laser is different than the femtosecond laser as it is Q-switched and has no pulse picker. Temporal alignment of the nanosecond laser system was performed by providing two separate TTL signals to the laser system via an external 26 pin connection. The rising edge of the gate signal (Pin 17) triggers laser pump diode current to drop to a standby current level and it stays constant at this low level for a pre-defined suppress time followed by which the current goes high. Again, during the time when the diode current stays high, a laser pulse is detected created when an external continuous TTL signal is applied separately to laser Q-switch using Pin 21. Hence by applying the controlled signals to pins 17 and 21 of the 26-pin connector, the output of the Q-switched laser can be timed. The external control of Q-switch allows the laser pulse emission to be precisely controlled. The external triggering of HIPPO laser is shown in the Figure 3.16.

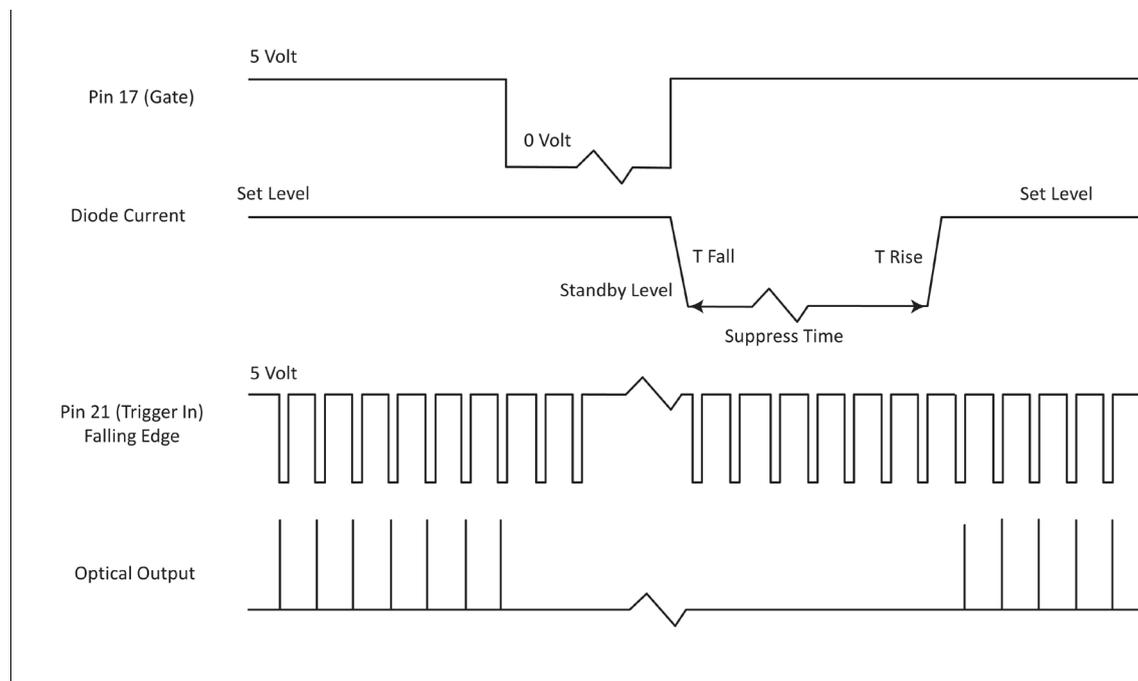


Figure 3.16: Relationship between external gate signal, external trigger signal and the laser output for the HIPPO nanosecond laser system (HIPPO Manual)

In practical terms, a Stanford research systems pulse generator (DG535) was used to produce a single TTL signal. This TTL signal was used for two purposes; one to gate the laser head using Pin 17 and the second to trigger another function generator (DS345). The DS345 function generator was used to generate a continuous TTL frequency 30 kHz, synchronised with gate signal, to Pin 21. This continuous TTL signal triggers the Q-switch signal of the laser system and the laser pulse is emitted. The suppression time and standby laser diode current were set to be 260 μ s and 18 A, respectively, using the internal laser system software. To achieve a single laser pulse, the gate signal provided to Pin 17 was controlled and set at 333 μ s. The time between the rising edge of the external gate and the laser pulse output was then determined to be 304.86 μ s using a digital

oscilloscope (Tektronix TDS5000). The rising edge of the gate signal was taken as the absolute timing reference for producing single nanosecond laser pulse.

3.6.2. Spatial alignment

Free space optics were used to perform the real-time observations. Both femtosecond and nanosecond laser beams were focussed using Thorlabs 5X microscope objectives depending on applied laser wavelength. To prevent any high laser power damage to the optics, the damage threshold of microscope objectives was chosen to be greater than 10 Jcm^{-2} . Two different setups were developed for real-time plasma imaging and laser induced breakdown spectroscopy (LIBS). For both setups, the samples were positioned using a computerised translational XYZ stage using Thorlabs APT software. Plasma imaging and LIBS were performed using two models of intensified CCD (ICCD, Andor). In the following subsection, the working principle of ICCD and spectral alignment for plasma imaging and spectral imaging performed in the current study will be elaborated.

3.6.2.1. Intensified charge coupled device (ICCD)

The ICCD provided two major advantages over simple CCD; these are higher image sensitivity with ultrafast shuttering. An ICCD device is a CCD camera equipped with an image intensifier plate. Three major elements of an image intensifier are a photocathode, a micro channel plate (MCP) and finally an output phosphor screen. The image intensifier consists of an evacuated tube on which a photocathode is located on the inner surface of the front window. When a photon is projected on a photocathode and image is focussed. The photocathode absorbs the incident photon and leads to the formation of a photoelectron. The photocathode is made of gallium arsenide (GaAs). The photoelectron is drawn across a small gap towards micro channel plate by applying an electric field of the order of 150-200 V. The MCP consists of a thin disk of honeycombed glass channels coated with resistive coating. A high electric potential is applied on the MCP so that photoelectron will cascade down the channel and produce secondary electrons which results an electron number amplification factor which can be greater than 10^4 . This gain can be varied by changing the voltage across the MCP. The electron cloud is accelerated across a small gap by a potential of several keV and finally strikes a phosphor coating on the inside of a fibre optic window. The phosphor converts the incident electron pattern into visible light which is then detected by the CCD.

The shutter speed of the ICCD camera depends upon the voltage switching time of the photocathode. If the voltage of the photocathode relative to the MCP is positive, photoelectrons are unable to reach the MCP. The ICCD has an inbuilt digital delay generator (DDG) which determines when the voltage is applied across the photocathode and the MCP. This inbuilt DDG can control the intensifier tube for gating by an internal or external trigger pulse. Based upon the requirement, a delay can be introduced of a gate pulse of definite width. Using the DDG, the gate pulse width can be resolved to 25 picoseconds and thus effective exposure time.

The quantum efficiency (QE) of the photocathode of the ICCD is shown in the Figure 3.17.

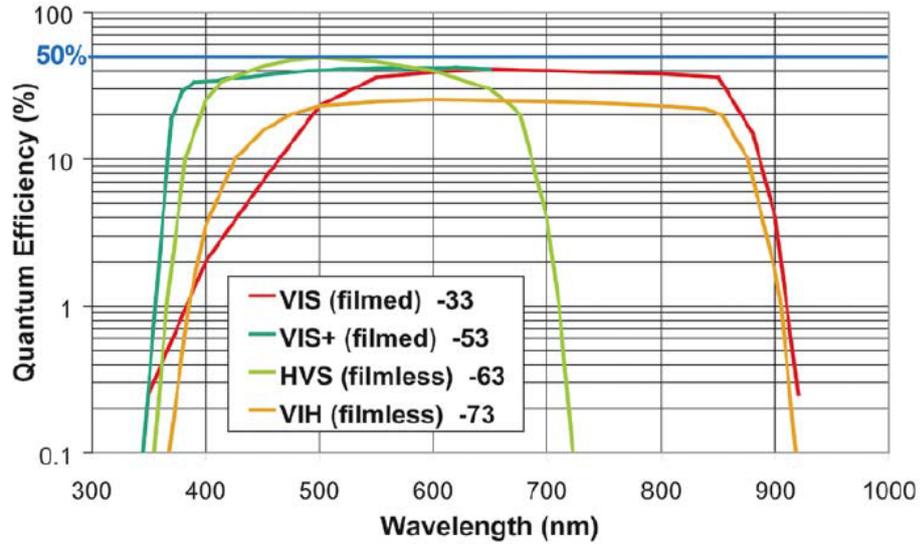


Figure 3.17: Quantum efficiency of different photocathodes available for ICCD device, adapted from [190]

A protective ion barrier film is required to be positioned over the input of the MCP to prevent the positive ion feedback damage. The film, or barrier, prevents ions coming back and damaging the photocathode but it has a detrimental effect on the overall QE of the image intensifier. However, the filmless image intensifiers offer a much higher quantum efficiency (almost 50 %) than the image intensifier without film. In the present work, to achieve higher quantum efficiency, VIH (filmless)-73 (without ion barrier film) photocathode was used. This VIH photodiode provides maximum quantum efficiency at visible region [190].

3.6.2.2. Plasma Imaging

Figure 3.18 presents a schematic for the optics used in the real-time plasma imaging study. After passing through microscope objective the plasma emission becomes parallel and it is allowed to travel through a series of lens combinations to magnify the beam. The magnified beam is finally focussed on the plane of ICCD photocathode and forms an inverted image of plasma plume.

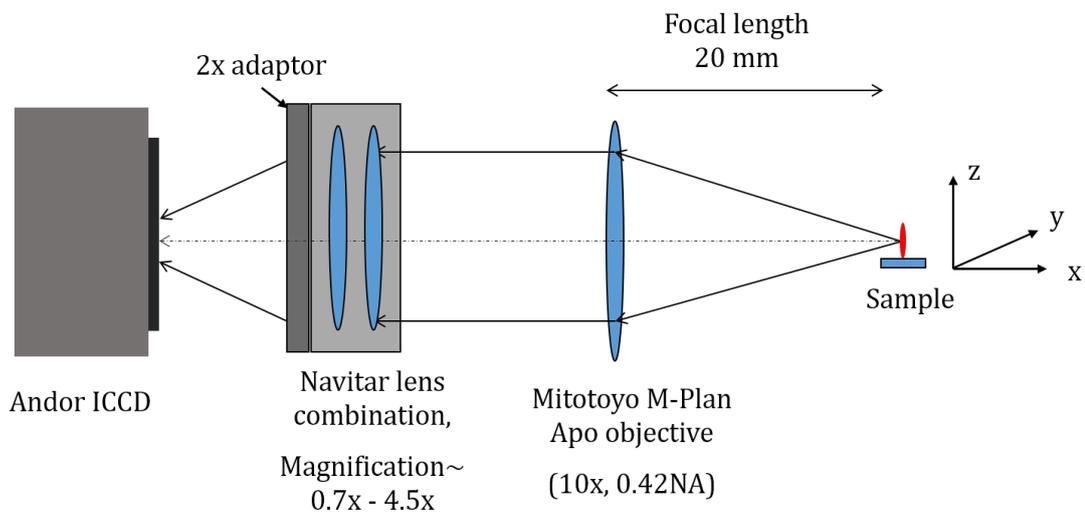


Figure 3.18: Spatial diagram for real-time plasma imaging measurement

In the present work, a microscope objective (Mitutoyo M-Plan Apo objective) of magnification 10x was used to collimate the plasma plume. The microscope objective has a focal length of 200 mm, working distance of 20 mm and a numerical aperture (NA) of 0.42. The microscope objective was connected to a Navitar zoom lens with variable magnification and a 2x adapter. The 2x adaptor was further connected with a C-mount coupler which can be attached with Andor i-star 734 ICCD detector. The magnification on the Navitar lens were varied from 0.7x to 4.5x.

The Andor camera was triggered using the rising edge pulse picker signal achieved from external triggering of S-Pulse femtosecond laser described previously. Real-time plasma imaging was executed by varying gate delay from in-built delay setting of the ICCD camera software. The variable gate delay was used for plasma imaging at different times over a range from 0 ns to 200 ns.

ICCD triggering during nanosecond ablation process was performed using rising edge of the external gate signal (Pin 17), which is defined as the absolute zero of whole timing process. Thus, the gate rising signal was used to synchronise Q-switch signal, laser output and ICCD camera.

3.6.2.3. Spectral imaging

Laser-induced breakdown spectroscopy required to resolve using a spectrometer attached before the ICCD camera. Figure 3.19 (a) shows the spatial diagram for laser-induced breakdown spectroscopy. The plasma plume is collected and focussed on the spectrograph entrance port. The spectral content of the electromagnetic radiation is measured using an ICCD camera interns of relative intensity of each wavelength.

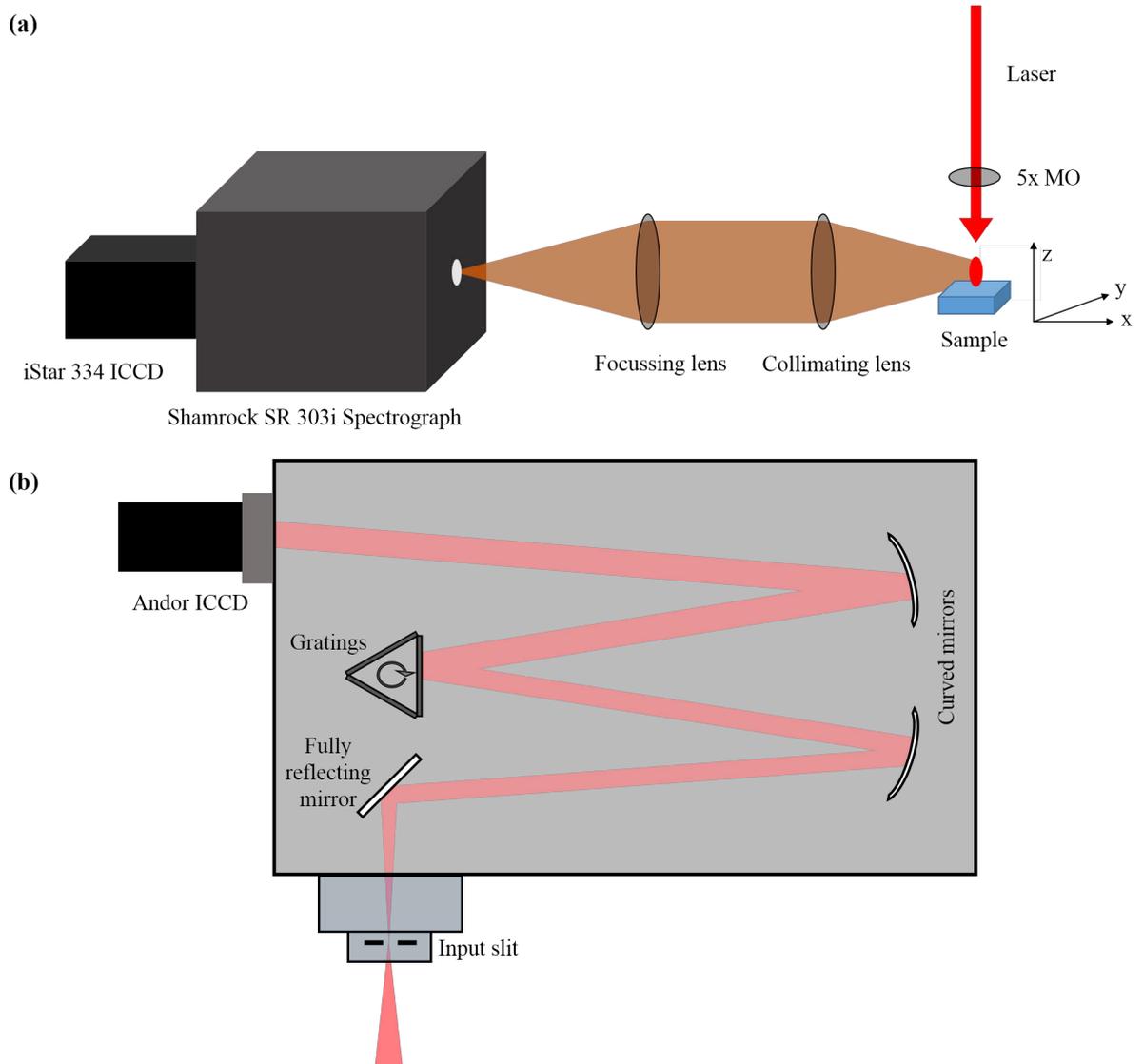


Figure 3.19: Optical arrangement for Laser-induced breakdown spectroscopy (a) with the propagation of light inside the spectrometer (b)

The laser produced plasma plume was collimated using an UV silica Plano-convex lens of focal length 200.7 mm and then focussed on a variable spectrometer aperture using a 100-mm lens. After multiple reflections, the emitted light is allowed to be incident on a rotational grating turret. The reflecting angle of different spectral components of the reflected light depends upon the groove density of a grating. Two different gratings were used in the present work these had 300 lines/mm and 1200 lines/mm. Gratings of 300 lines/mm and 1200 lines/mm provides a resolution of 0.43 and 0.10 nm and band pass of 297 and 67 nm, respectively. Both gratings have blaze wavelength at 500 nm. Spectrally resolved light is then focussed using a concave mirror of focal length 303 mm on an Andor iStar 334 ICCD. Figure 3.19 shows the optics inside the spectrometer. The mirrors of the spectrometer are coated with silver in order to get maximum efficiency. In order to achieve best resolution, the input slit width (aperture) was varied in software. The temperature inside the ICCD was fixed at -40°C to reduce noise and dark current. The spectral arrangement for time-resolved spectrometry is shown in the Figure 3.20.

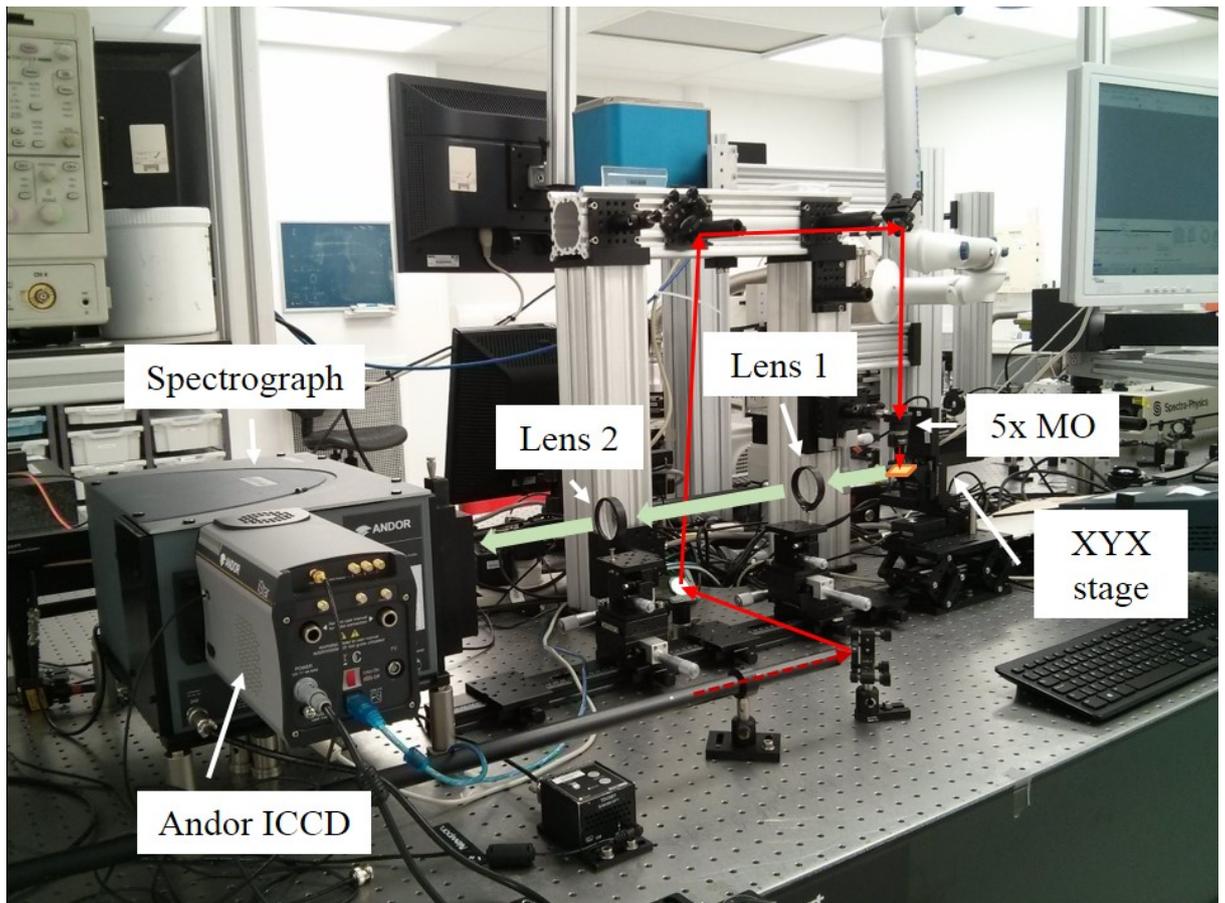


Figure 3.20: Spectral measurement of real-time spectral imaging of ablated particles. The light path to spectrometer are indicated in the figure.

3.7. Numerical simulation

The absorption of the laser energy by the material with associated physical response was modelled using the finite element method (FEM). The finite element method allows complicated differential equations to be solved numerically. Thermal response of a material was examined using COMSOL Multiphysics[®] software. In particular, two different two-dimensional (2D) models were designed and solved for the femtosecond and the nanosecond laser material interactions. A two-temperature model combined with mechanical stress was solved for the femtosecond laser ablation on bulk, thin film and multi-layered molybdenum heterostructure (MAM). The nanosecond laser material interactions were examined using a thermal diffusion model combined with thermal induced mechanical stress. The temporal and spatial Gaussian-shaped laser beam used in the simulations were described in the previous chapter (section 2.5.1).

The laser processing of different bulk, thin film and molybdenum heterostructure were carried out using a sample size of $\sim 1 \times 1 \text{ mm}^2$. The simulation by COMSOL requires the formation of a mesh structure throughout the material geometry. The mesh size of the simulation is determined by the convergence of the model towards the same solution. To accurately investigate how the energy propagates through the material requires a small mesh size, with a high density of nodes, in the depth direction and particularly at the material interfaces. As a consequence, the simulation runs for several hours. In order to work under reasonable computational limitations, the computational model was scaled with the experimental reality. Computationally the beam diameter was

normalised to 2 μm and the lateral length of the sample was taken to be 30 μm . The depth was determined by the thickness of the film and the length over which the substrate material can be affected. Although beam and sample size were normalised in order to decrease simulation time, the required fluence was kept constant by changing input laser energy and adjusting the spot-size accordingly.

3.7.1. Heat diffusion model combined with mechanical stress model

A simple heat diffusion model was used to study thermal response of a material after the deposition of single nanosecond laser pulse. The heat equation was solved using a time dependent solver in COMSOL. The time dependent heat source term was used and this is described in the equation 4 (Chapter 2). The solution was solved from 0 ns to 100 ns with a time interval of 0.5 ns. The peak of the laser pulse was at 20 ns. The initial temperature of the ambient (T_a) and material, both in thermal equilibrium, was taken to be 300 K. The material properties, such as reflectivity, absorption coefficient are assumed to be temperature independent. Other parameters such as heat capacity at constant pressure, thermal conductivity were taken as temperature dependent variables. To describe temperature dependence of thermal conductivity and heat capacity, an approximate nonlinear function was formulated. The absorption coefficient is calculated experimentally, with the results presented in chapters 4 and 6. Different material parameters used for COMSOL simulation of bulk and thin film molybdenum on BK7 glass and molybdenum based multilayered films are tabulated in the Table 3.6 .

Table 3.6: Thermal parameters for heat diffusion model

| <i>Parameters</i> | <i>Molybdenum</i> | <i>Aluminium</i> | <i>ITO</i> | <i>Glass (BK7)</i> |
|---|-------------------|------------------|------------|--------------------|
| <i>Melting temperature (K)</i> | 2896 [191, 192] | 933 [29, 192] | 1900 [193] | 830 |
| <i>Vaporisation temperature (K)</i> | 4912 [191, 192] | 2730 [29] | 3000 [194] | |
| <i>Heat capacity at constant pressure 300 K ($\text{JKg}^{-1}\text{K}^{-1}$)</i> | 250 [191, 192] | 901 [192] | 340 [195] | |
| <i>Thermal conductivity @ 300 K ($\text{Wm}^{-1}\text{K}^{-1}$)</i> | 138 [45, 67] | 237 [29] | 10 [196] | 1.1 [197] |
| <i>Density (kgm^{-3})</i> | 10200 [45, 191] | 2690 [192] | 2220 [198] | |
| <i>Melting enthalpy ($\text{kJ}^{-1}\text{kg}^{-1}$)</i> | 389 [191, 192] | 400 [29] | | |
| <i>Evaporation enthalpy ($\text{kJ}^{-1}\text{kg}^{-1}$)</i> | 6250 [191, 192] | 10750 [29] | | |

In order to incorporate latent heat of fusion and vaporisation, a parameter for an effective lattice heat capacity was used according to Sotrop et al. Here the latent heats associated with the phase changes are approximated using a Gaussian function, given by [191],

$$C_l = a + \Delta H_m b e^{-\frac{1}{2}\left(\frac{T-T_m}{\Delta T}\right)^2} + \Delta H_v c e^{-\frac{1}{2}\left(\frac{T-T_v}{\Delta T}\right)^2} \quad (22)$$

where, T_m and T_v are the melting and vaporisation temperature of the corresponding material, ΔH_m and ΔH_v are the enthalpies for melting and vaporisation in Jkg^{-1} , a ($\text{Jkg}^{-1}\text{K}^{-1}$) is the lattice heat capacity at room temperature, and b (K^{-1}) and c (K^{-1}) are the normalisation factor for Gaussian function ($\frac{1}{\Delta\sqrt{2\pi}}$) of melting and vaporisation. Δ , is estimated to be 50 K to ensure a smooth transition between phases.

Figure 3.21 shows the approximated effective heat capacity of molybdenum and aluminium with increase of lattice temperature using equation (22)

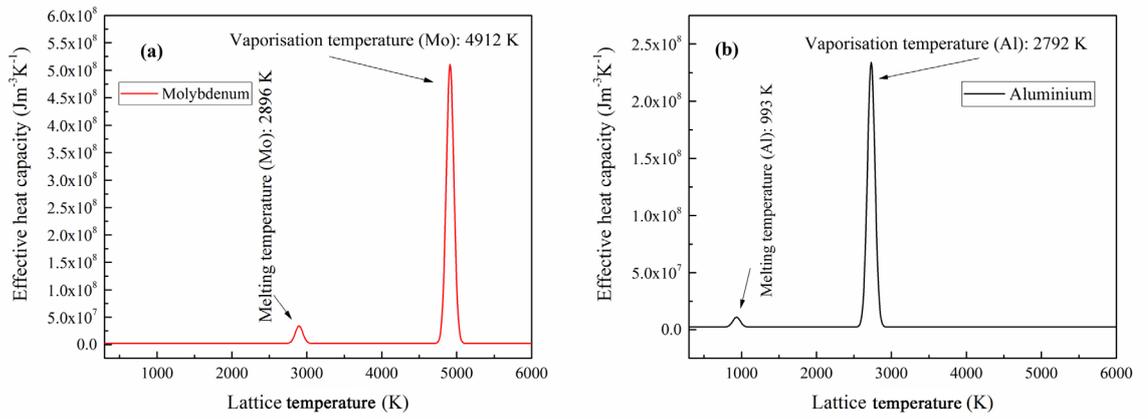


Figure 3.21: Approximated effective lattice heat capacity of molybdenum (a) and aluminium (b) used for computational simulation

The variation of the thermal conductivity with the lattice temperature was also considered in the simulation. The thermal conductivity of molybdenum and aluminium lattice is shown in the Figure 3.22.

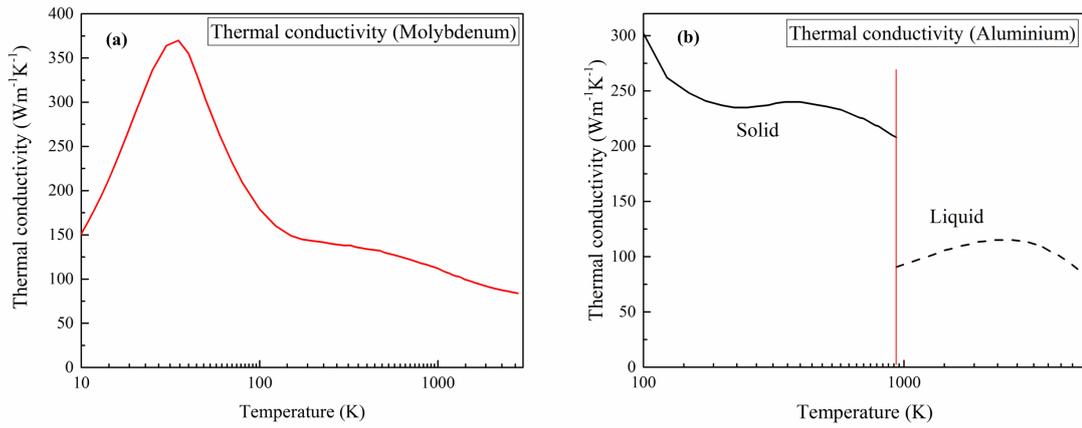


Figure 3.22: Temperature dependent thermal conductivity of (a) molybdenum and (b) aluminium used for simulation

When materials experience heating, material expansion can take place, which can lead to an associated strain and stress in the material. The thermal stress module of COMSOL allows the effect of increasing temperature, material expansion and therefore the stress/strain at different layer interfaces to be estimated. The temperature obtained from the simple heat diffusion model was used to calculate the thermal expansion by solving the thermally induced mechanical stress. Typical values of the mechanical properties of the thin film and substrate materials are estimated and listed below in Table 3.7.

Table 3.7: COMSOL coefficients for material processing for stress/strain simulation

| Parameters | Molybdenum | Aluminium | ITO | Glass (BK7) |
|---|----------------------------|---------------------------|----------------------------|---------------------------------|
| <i>Young's modulus (Nm⁻²)</i> | 321×10^9 [191] | 69×10^9 [199] | 190×10^9 [194] | 82×10^9 [167, 200] |
| <i>Poisson's ratio (unit less)</i> | 0.31 [191] | 0.33 [199] | 0.35 [194] | 0.22 [167, 200] |
| <i>Thermal expansion coefficient (K⁻¹)</i> | 4.8×10^6 [191] | 23×10^6 [199] | 8.5×10^6 [194] | 8.6×10^6 [167, 200] |

The heat diffusion model was simulated the nanosecond laser of wavelength of 1064 nm and the pulse duration of 9 ns (at FWHM).

The values for the absorption coefficients were taken from the literature [148] and the reflectivity and transmissivity values were obtained from the measurements using integrating sphere (section 3.4.1).

To avoid this complexity of the reflection, in case of multi-layered film, it was assumed that the reflection takes place at the top surface only. A simple mathematical calculation was conducted to understand the laser beam propagation inside molybdenum, using Beer's formula. It was estimated

that, the peak intensity of the laser pulse decreases to 12.5, 2.5 and 0.9% after the beam travels 40 nm through the molybdenum, for 1030, 515 and 343 nm wavelengths respectively. A small fraction (1030 nm: 0.63%, 515 nm: 0.2% and 343 nm: 0.06%) of this remaining light penetrates through to the underneath aluminium layer. The rest is reflected from the Mo/Al interface, as determined by the Fresnel equation and determined to be 11.88, 2.3 and 0.84% for the incident wavelengths of 1030, 515 and 343 nm, respectively. The reflected light from the Mo/Al interface travels back and forth between the air/Mo layer interface and the Mo/Al layer interface. Thus, it is a good approximation to consider complete absorption of laser within the top molybdenum layer.

3.7.2. Two temperature model combined with mechanical stress model

In the femtosecond case, both electronic and lattice systems were considered separately. To estimate the temperature of electronic and lattice subsystem, the two temperature model was used by solving two partial differential equations described in the chapter 2 (section 2.5.2). The source term is estimated using equation 4. The estimated optical properties such as material reflectivity and absorption coefficient are more complex for femtosecond material interactions; in this simple experimental study, the lattice values are taken to be the same as those used in the nanosecond heat diffusion model. The electron heat capacity and electron–phonon coupling constant coefficients were approximated as described in the previous chapter (section 2.6). A mechanical stress model was linked with the two temperature model where it was assumed that the lattice temperature is responsible for any stress inside a material. In case of the multi-layered heterostructure (Mo-Al-Mo-ITO), the third (Mo) and fourth (ITO) layer with the substrate was treated as a simple thermally connected layer, as electric diffusion length is much smaller than the depth of these layers (section 3.3.2).

3.7.3. Terminology of the stress vector

In general, a mechanical stress tensor (σ) in three-dimensional coordinate system (X, Y, Z) is written as follows,

$$\sigma = \begin{bmatrix} \sigma_{XX} & \sigma_{XY} & \sigma_{XZ} \\ \sigma_{YX} & \sigma_{YY} & \sigma_{YZ} \\ \sigma_{ZX} & \sigma_{ZY} & \sigma_{ZZ} \end{bmatrix} \quad (23)$$

The direction and of the different components of the stress tensor is interpreted as follows,

The stress components acting in X direction on a plane XY, YZ and ZX are termed as σ_{XZ} , σ_{XX} and σ_{XY} , respectively,

Stress acting in Y direction on a plane XY, YZ and ZX are termed as σ_{YZ} , σ_{YX} and σ_{YY} , respectively,

And, the stress acting in Z direction on a plane XY, YZ and ZX are termed as σ_{ZZ} , σ_{ZX} and σ_{ZY} , respectively,

The three-dimensional mechanical stress tensor is shown in the Figure 3.23.

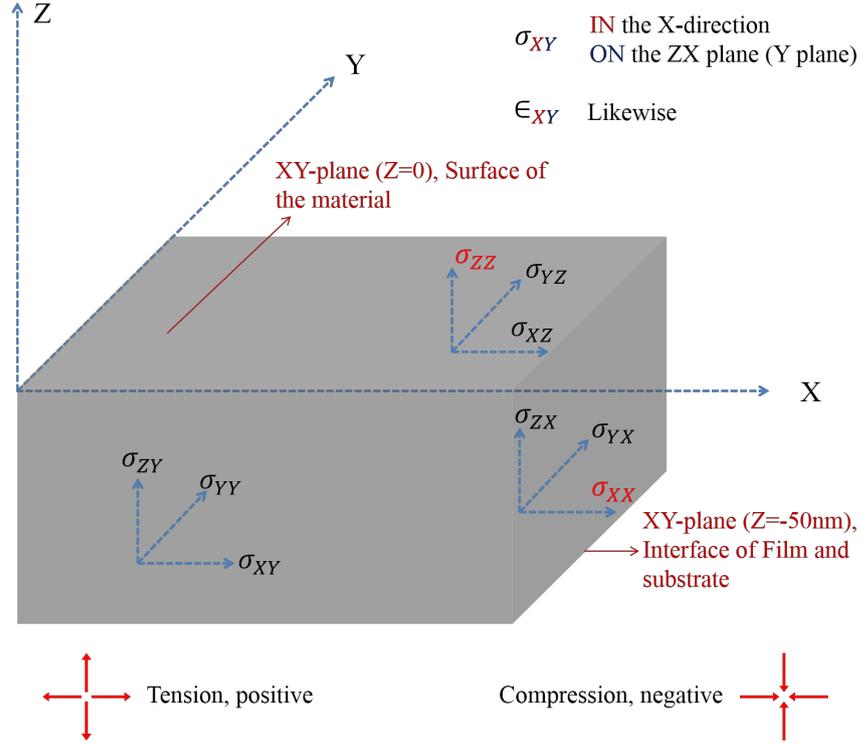


Figure 3.23: Components of the stress tensor along X, Y and Z direction on 50 nm molybdenum thin film

The quantities σ_{XX} , σ_{YY} and σ_{ZZ} are termed as the tensile tensor and σ_{XY} , σ_{YX} , σ_{YZ} , σ_{ZY} , σ_{ZX} and σ_{XZ} are known as the shear tensor. Taking into account the axial symmetry, the nine components of the stress tensors reduces to 6 quantities as,

$$\sigma_{XY} = \sigma_{YX}, \sigma_{YZ} = \sigma_{ZY} \text{ and } \sigma_{ZX} = \sigma_{XZ}$$

The stress tensor reduces to,

$$\sigma = \begin{bmatrix} \sigma_{XX} & \sigma_{YX} & \sigma_{XZ} \\ \sigma_{YX} & \sigma_{YY} & \sigma_{ZY} \\ \sigma_{XZ} & \sigma_{ZY} & \sigma_{ZZ} \end{bmatrix} \quad (24)$$

In the present work, the three-dimensional axis system is reduced to a two-dimensional axis system (X, Z) in the COMSOL model. Where, X corresponds to the axis related to the lateral direction of the sample, and Z is known as the depth of the sample. Thus, the stress tensor components σ_{YY} , σ_{YX} , σ_{YZ} were set to zero. The three-dimensional stress matrix reduces to

$$\sigma = \begin{bmatrix} \sigma_{XX} & \sigma_{XZ} \\ \sigma_{XZ} & \sigma_{ZZ} \end{bmatrix} = \begin{bmatrix} \sigma_{XX} & \sigma_{XZ} \\ \sigma_{XZ} & \sigma_{ZZ} \end{bmatrix} \quad (25)$$

The stress σ_{XX} and σ_{ZZ} are the tensile stress and the direction of these stress are along the X and Z axis, respectively and on the Z= constant and X= constant plane, respectively. σ_{XZ} is termed as the shear stress. The axis system used for numerical analysis and the two-dimensional stress tensor are illustrated in the Figure 3.24.

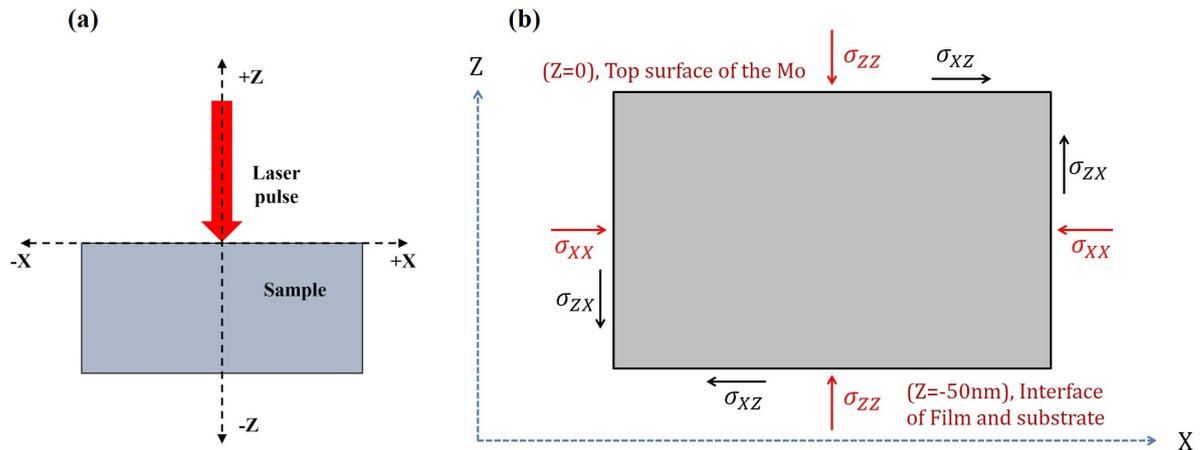


Figure 3.24: (a) Two-dimensional experimental condition of the laser-molybdenum interaction and (b) conventional notation of the stress vector in two dimensions (X, Z) for the numerical simulation of the molybdenum thin film of thickness 50 nm

3.8. Summary

In this chapter, an in-depth summary of the materials, used equipment and characterisation methods are presented. Firstly, this Chapter provides a methodology of single-layered and multilayered film deposition. The laser system, optical setup and the method of micromachining by short and ultrashort laser pulses are presented in the next section. Next section describes various offline and online characterisation methods used to study the laser material interaction. Separate workstations for real-time observation of femtosecond and nanosecond ablation was designed and developed to understand laser-material interaction. The final section of this chapter provides the method of numerical simulation to understand the ablation phenomena by short and ultrashort laser pulses. These methods will be used to examine ablation of molybdenum bulk, single and multilayered thin film in the next three result chapters.

Chapter 4: Laser-Molybdenum interaction

In this chapter, single pulse ultra-short (500 femtosecond at FWHM, 1030 nm) and short (9 nanosecond at FWHM, 1064 nm) pulsed laser ablation on molybdenum bulk and the thin film is investigated. To measure the laser fluence absorbed by the material, reflectivity and transmissivity of molybdenum bulk and thin films at the incident laser wavelength and for specific pulse durations are investigated. The absorbed laser energy is used to measure the ablative threshold fluence. The ablation mechanism is understood by investigating a two temperature (TTM) model for the femtosecond laser processes. A heat diffusion model is used for nanosecond laser material interactions. The transient behaviour of temperature and the thermally induced mechanical stress and strain is considered. The ablation of bulk molybdenum, studied experimentally and investigated by FEM simulations, is presented in first section of this chapter. Patterning of molybdenum thin films by femtosecond and nanosecond laser pulses is then reported. Finally, the thermal and mechanical properties of 50 nm molybdenum film were investigated using computational simulations.

4.1. Interaction of bulk molybdenum with laser sources

Laser processing of bulk molybdenum samples (section 3.1) using single pulse ultra-short and short pulse laser is described in this section. The dimension of the molybdenum sheet measured using a Vernier callipers was 1 cm x 1 cm and the thickness measured by a micrometre screw gauge was (0.50 ± 0.001) mm. The roughness of molybdenum samples was found to be (0.5 ± 0.03) μm by white light interferometry.

A detail analysis of laser-molybdenum interaction requires the measurement of the absorbed laser energy by a sample, and in order to do that, the reflectivity and transmissivity were measured by an integrating sphere (section 3.3.1, chapter 3).

4.1.1. Measurement of absorbed laser energy using integrating sphere

Prior to laser processing, the reflectivity (R) was measured for the bulk molybdenum sample using integrating sphere. No transmission of laser light was observed through the bulk sample. Table 4.1 shows the reflectivity of bulk molybdenum, measured by the integrating sphere.

Table 4.1: Reflectivity measurement of bulk molybdenum by integrating sphere

| <i>Pulse regime</i> | <i>IR</i> | <i>Green</i> | <i>UV</i> |
|---------------------|-------------------------------|------------------------------|------------------------------|
| <i>Femtosecond</i> | (0.65 ± 0.01) @1030 nm | (0.55 ± 0.02) @515 nm | (0.54 ± 0.04) @343 nm |
| <i>Nanosecond</i> | (0.69 ± 0.03) @1064 nm | (0.58 ± 0.05) @532 nm | (0.54 ± 0.02) @355 nm |

The measured reflectivity value of molybdenum using femtosecond and nanosecond laser are shown in the Table 4.1. The calculated values are close to the values obtained from the literature

[148]. Reflectivity measurement using IR wavelength (1030 and 1064 nm) was found higher than the green (515 and 532 nm) and UV (343 and 355 nm) wavelengths. These are average values. The effect of pulse duration was not considered.

The transmissivity (T_r) was assumed to be negligible irrespective of laser wavelength and pulse durations used in this study. The estimated penetration depth ($l_\alpha = 1/\alpha$) of various laser pulses used in this study are given in the Table 4.2. Here α (in m^{-1}) is the optical absorption coefficient of the material that varies with wavelength and pulse duration of the electromagnetic wave. The values of the optical penetration depth were obtained from the literature [55, 201]. Negligible amount of transmission is estimated through molybdenum of thickness of 500 μm .

Table 4.2: Optical penetration depth of different laser wavelengths in molybdenum [55, 202]

| <i>Laser wavelength (λ) (nm)</i> | <i>Optical penetration depth (l_α) (nm)</i> |
|--|--|
| <i>1064</i> | <i>19.23</i> |
| <i>1030</i> | <i>19.34</i> |
| <i>532</i> | <i>11.56</i> |
| <i>515</i> | <i>10.83</i> |
| <i>355</i> | <i>8.85</i> |
| <i>343</i> | <i>8.47</i> |

4.1.2. Micro-machining of bulk molybdenum by femtosecond laser

The laser material interaction of bulk molybdenum was investigated using wavelengths of 1030 nm, 515 nm and 343 nm, with a 500-femtosecond laser pulse, at different applied fluences. The optical micrograph (OM) presented in Figure 4.1; shows images of the craters generated in the bulk molybdenum sample after irradiation by a single femtosecond laser pulse with different applied pulse energies (applied). The values indicated refer to the energy of the laser pulse.

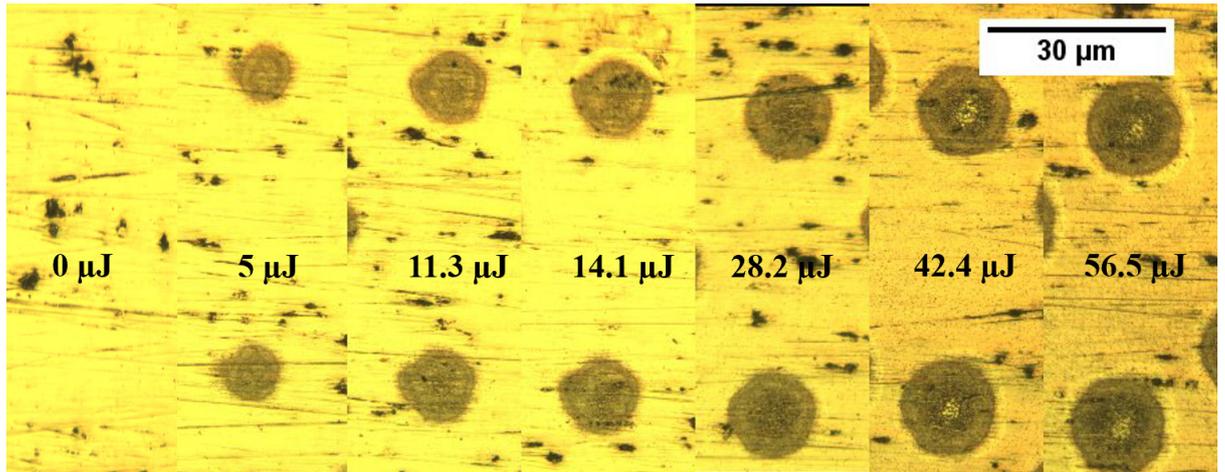


Figure 4.1: Image of damage craters on molybdenum by 1030 nm femtosecond laser at different average energies (applied) as viewed by an optical microscope (Olympus BX60M). Values of the applied pulse energy are listed.

The roughness of the bulk molybdenum sample is evident from the Figure 4.1. The pits present in the bulk molybdenum originate from the localised corrosion of the metal surface and are not due to the laser irradiation. The diameter of the craters increases with increasing applied pulse energy. Craters are approximately circular ($\frac{r_x}{r_y} \approx 1.0 \pm 0.1$). Here r_x and r_y are the radius of crater along X and Y direction.

The threshold fluence was calculated using Liu's method (section 3.4.3 in chapter 3); this involves plotting a graph of squared diameter (D) of and the logarithmic fluence. A linear fit between the natural logarithm of fluence and the squared diameter is shown in the Figure 4.2. The ablation threshold in terms of the applied fluence were obtained from extrapolating the linear fit (Figure 4.2(a)) to $D^2 = 0$ was calculated to be (0.45 ± 0.01) , (0.36 ± 0.02) , (0.27 ± 0.01) Jcm^{-2} for 1030 nm, 515 nm and 343 nm wavelengths, respectively. The peak value of the absorbed threshold fluence obtained from extrapolating the graphs (Figure 4.2(b)) are, (0.16 ± 0.01) , (0.17 ± 0.02) and (0.12 ± 0.12) Jcm^{-2} for 1030 nm, 515 nm and 343 nm wavelengths, respectively. It is found that the applied threshold fluence is wavelength dependent and it increases with increasing laser wavelength. Figure 4.2(b) reveals that when the applied energy is corrected for reflectivity, the ablation threshold in terms of the absorbed fluence for wavelengths 1030 nm and 515 nm threshold fluence are almost similar, whereas the 343 nm absorbed threshold fluence is less.

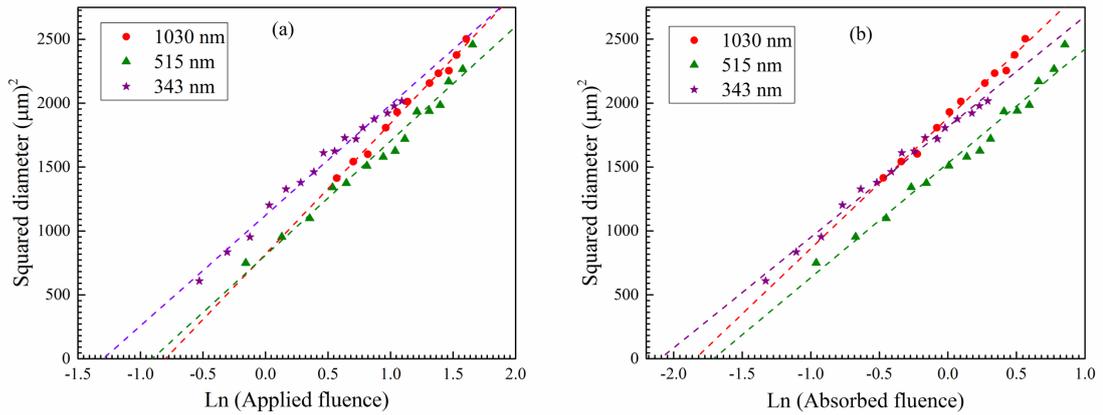


Figure 4.2: Measurement of single pulse (a) applied and (b) absorbed threshold fluence of molybdenum by 1030 nm, 515 nm and 343 nm femtosecond laser. The intercept of the linear fit at $Y = 0$ determines the peak value of the threshold fluence

4.1.3. Computer simulation using Finite Element Method (FEM)

4.1.3.1. Interaction of molybdenum bulk with ultra-short pulse laser

The time-dependent temperatures of the electronic (T_e) (blue line) and lattice (T_l) (black line) subsystem at an absorbed peak fluence of 0.3 Jcm^{-2} using 1030 nm laser wavelength are presented in Figure 4.2. The temporal profile of the laser beam is also shown in Figure 4.3 (red line). The value, 0.3 Jcm^{-2} was chosen because this fluence is greater than the ablation threshold value for all three wavelengths. An electron-phonon coupling ($13.6 \times 10^{16} \text{ Wm}^{-1}\text{K}^{-1}$) constant independent of the temperature of the electronic subsystem was used for the simulation. The model predicts that the increase of electron temperature is almost instantaneous with laser pulse, while the lattice temperature increases more slowly. At later times, greater than $4 \times 10^{-11} \text{ s}$, the electron and lattice temperature reaches thermal equilibrium. Peak electron and lattice temperatures were estimated on the molybdenum surface ($X=0, Y=0, Z=0$) for a range of femtosecond laser pulses using absorbed fluences of 0.5, 0.4, 0.3, 0.25, 0.2, 0.15 and 0.1 Jcm^{-2} .

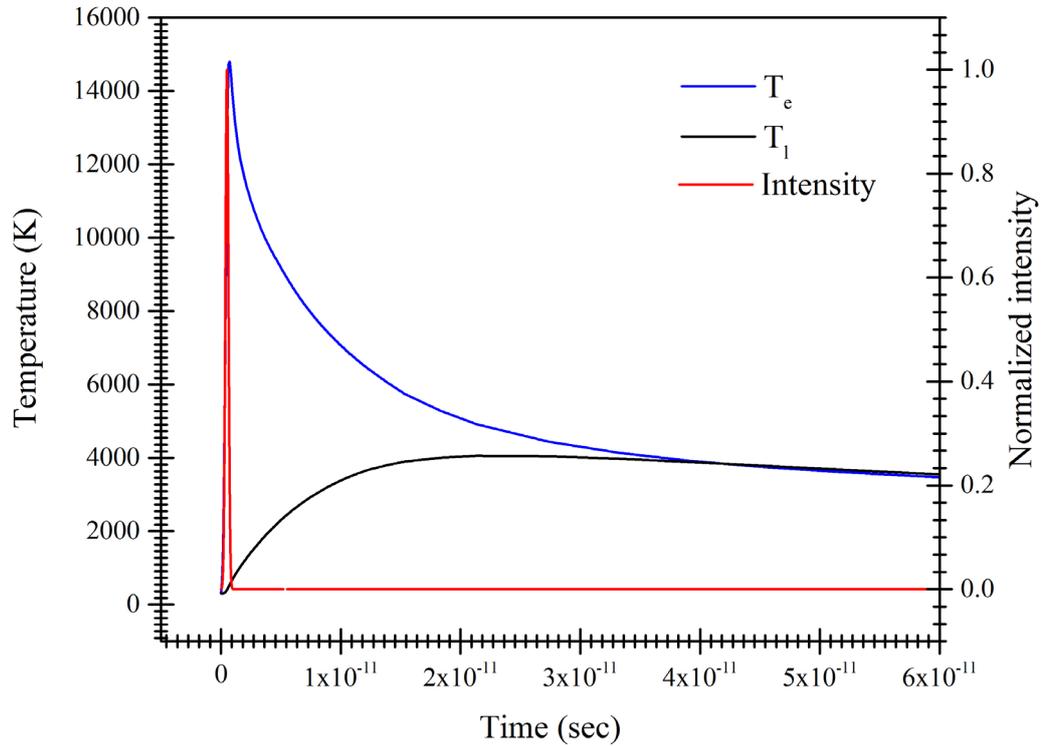


Figure 4.3: Two temperature modelling of 500 fs (at FWHM) IR laser pulse using finite element method and evolution of electron and lattice temperature at a fluence of 0.3 Jcm^{-2} (absorbed) temperature in the bulk molybdenum. The electron-phonon coupling constant used for this simulation is $13.6 \times 10^{16} \text{ Wm}^{-1}\text{K}^{-1}$

Estimate of threshold fluence

The lattice temperature was estimated at different peak absorbed fluences of 0.5, 0.3, 0.25, 0.2, 0.15 and 0.1 Jcm^{-2} and the variation of peak lattice temperature with these laser fluence is presented in the Figure 4.4. Peak temperature at different fluences were fitted to a linear model. It was found that the temperature of the molybdenum lattice reached its melting temperature (2896 K) at an absorbed peak fluence of 0.205 Jcm^{-2} . An increase of the absorbed peak laser fluence above the ablation threshold leads to an increase peak temperature beyond the melting temperature. When the peak lattice temperature exceeds the vaporisation temperature of molybdenum (4912 K), at a fluence of 0.39 Jcm^{-2} , evaporation of molybdenum is predicted; the absorbed peak laser fluence in this regime for bulk molybdenum can be nominally related to the threshold fluence for ablation.

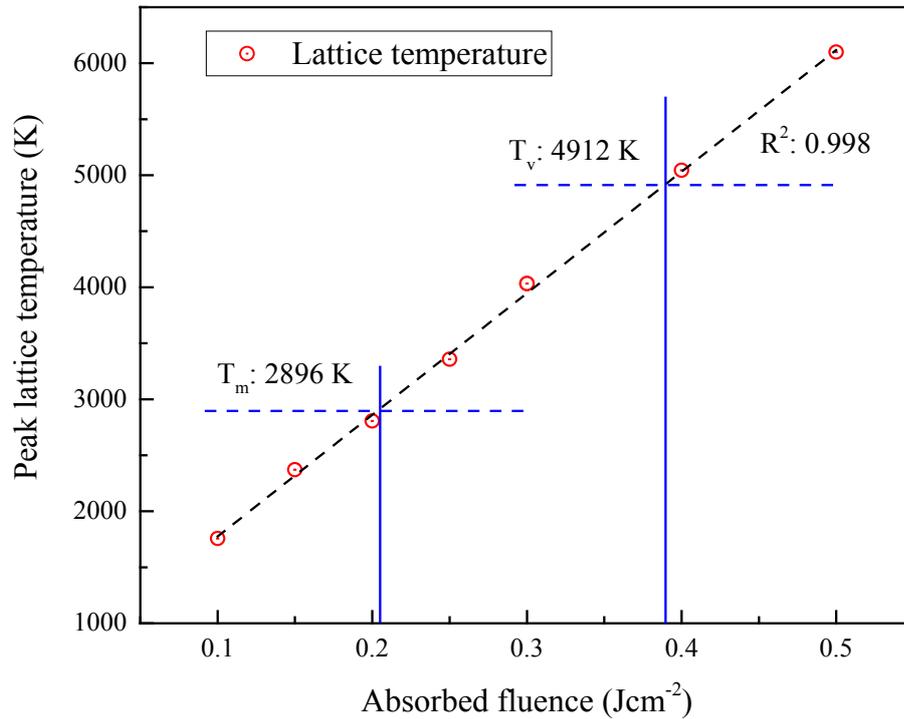


Figure 4.4: Prediction of melting and evaporation threshold fluence for bulk molybdenum, when exposed to a single 1030 nm femtosecond laser pulse

It is predicted from the numerical simulations presented in Figure 4.4 that the peak lattice temperature exceeds the melting temperature for molybdenum at fluences of 0.25, 0.3, 0.4 and 0.5 Jcm⁻² while at the fluence value of 0.1, 0.15 and 0.2 Jcm⁻², the lattice temperature remains below molybdenum melting temperature (2896 K).

A difference between the experimental (0.16 Jcm⁻²) and predicted numerical (0.205 Jcm⁻²) threshold fluences is therefore observed. The origin of this discrepancy can be due to the simplicity of the model. The sudden thermalisation of hot electrons to the lattice can result in high compressive stresses. Relaxation of the compressive stress results in the spallation and fracture of the heated molybdenum layer at absorbed fluences less than the values predicted by traditional melting and evaporative phase changes alone [174].

Variation of crater roughness with laser fluence

The RMS roughness of the femtosecond laser processed molybdenum bulk was measured in the case of IR (1030 nm) wavelength. The roughness of molybdenum bulk samples was measured using a white light interferometer at an area of 1 μm x 1 μm. In the case of measuring the roughness of ablated craters, the roughness was measured at the centre of the ablated crater at an area of 1

$\mu\text{m} \times 1\mu\text{m}$. Figure 4.5 presents the variation of roughness with peak absorbed laser fluence. Each RMS roughness value of a crater is an average of 10 individual measurements.

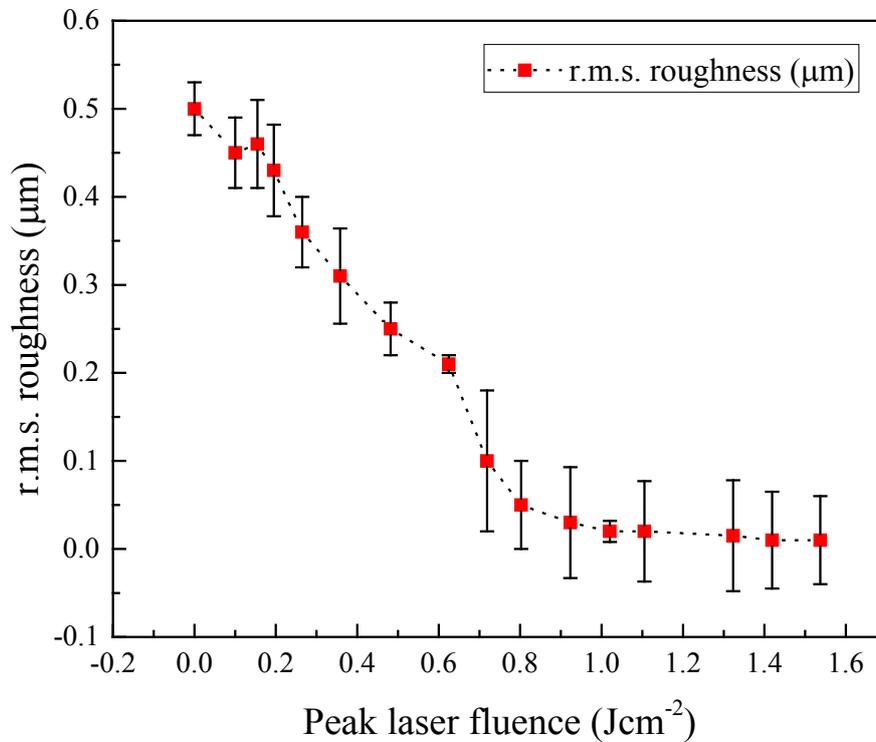


Figure 4.5: Variation of r.m.s. roughness of molybdenum craters with peak laser fluence (absorbed)

The RMS roughness values are found to decrease with increasing peak fluence. At higher fluence, a saturation in the roughness of the craters is observed. An increase of fluence results in an increase of induced temperature in molybdenum surface. At the fluence higher than melting threshold, the molybdenum undergoes through the molten phase. Eventually, resolidification of the molten molybdenum take place and thus, the roughness of the crater decreases.

At very high laser fluence, the molten molybdenum may reflow into the molybdenum crater; which leads to a saturation of roughness inside molybdenum crater.

4.1.3.2. Interaction of bulk molybdenum with short pulse laser

Experimental work on bulk molybdenum samples was only performed using femtosecond laser pulses. Nanosecond trials were conducted using low fluences in a regime where the anticipated plume interactions were small. These investigations are incomplete and not included in the thesis.

Modelling of a nanosecond laser bulk molybdenum interaction was considered in terms of a simpler heat diffusion approach using absorbed fluence values of 1.5, 1.0, 0.5 and 0.2 Jcm^{-2} . The peak lattice temperature was estimated at these fluences. It is found that the peak temperature decreases with decreasing incident laser fluence. Figure 4.6 shows the temporal profile of transient lattice heat at different absorbed laser fluence.

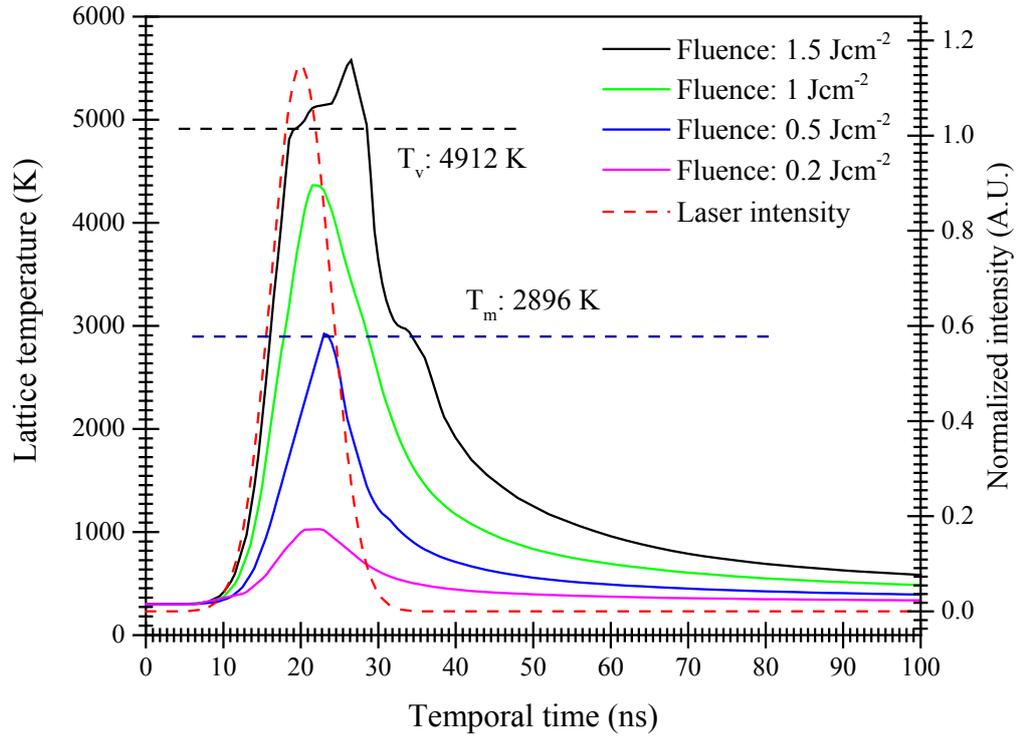


Figure 4.6: Temporal behaviour of lattice temperature of bulk molybdenum under the influence of Gaussian shaped nanosecond laser of fluence 0.2, 0.5, 1.0 and 1.5 Jcm^{-2} (absorbed). T_m and T_v are the melting and evaporation temperature of molybdenum, respectively.

It was found from the Figure 4.6 that the peak temperature of molybdenum was achieved within few nanoseconds after the maximum laser pulse intensity. At the peak absorbed fluence of 1.5 and 1.0 Jcm^{-2} , the lattice temperature reaches beyond the melting temperature of molybdenum enabling the potential for melt driven ablation. It is estimated that the melting threshold fluence of molybdenum using a 1064 nm nanosecond laser pulse is 0.5 Jcm^{-2} as the peak temperature just reaches to the melting temperature of molybdenum (2896 K). Below this threshold fluence, the peak lattice temperature reaches temperatures below that required for the onset of melting temperature and no ablation is expected.

4.2. Interaction of molybdenum thin film with laser sources

Single, ultra-short and short, pulsed laser interactions with very thin (50 nm) molybdenum film are presented in this section. In the first subsection, the absorbed fraction of laser energy by thin molybdenum is determined using an integrating sphere. Laser wavelength, pulse duration and the amount of laser energy was varied to achieve different craters on the film surface. The craters were examined using scanning electron microscopy and atomic force microscopy techniques. Finally, numerical simulations were performed in the final subsection to understand the ablation/removal mechanism by the laser pulses.

4.2.1. Measurement of absorbed laser energy using integrating sphere

Table 4.3 presents an average reflected (R) and transmitted (T_r) fraction of the incident laser energy. It was found that the amount of reflected and transmitted light decreases with lower

wavelength. Simple mathematical calculation suggests that less than 7.09%, 0.82% and 0.26% of the absorbed laser energy is transmitted through to the substrate (BK7 optical glass) for wavelengths 1030 nm, 515 nm and 343 nm respectively [148]. The attenuation of the laser energy in the molybdenum thin film suggested that a negligible amount of laser energy is reflected from the molybdenum-substrate interface. The measurements presented in Table 4.3 indicate a small difference of reflectivity and transmissivity of molybdenum thin film between femtosecond and nanosecond laser pulses.

Table 4.3: Reflected and transmitted fraction of incident femtosecond and nanosecond laser by 50 nm thick molybdenum thin film on BK7 optical glass substrate

| <i>Pulse regime</i> | <i>Wavelength (nm)</i> | <i>Reflectivity (R)</i> | <i>Transmissivity (T_r)</i> |
|----------------------------|-------------------------------|--------------------------------|--|
| <i>Nanosecond</i> | 1064 | 0.69 | 0.08 |
| | 532 | 0.581 | 0.027 |
| | 355 | 0.543 | 0.017 |
| <i>Femtosecond</i> | 1030 | 0.603 | 0.079 |
| | 515 | 0.516 | 0.041 |
| | 343 | 0.515 | 0.027 |

The different values of reflected and transmitted part of the laser light is indicated in Table 4.3, while the absorbed light (A) is calculated from the following formula,

$$A = 1 - R - T_r \quad (26)$$

Table 4.4 presents the absorbed part of laser energy by 50 nm thin molybdenum film using femtosecond and nanosecond laser pulses at IR, Green and UV wavelengths.

Table 4.4: Fraction of incident laser light absorbed by molybdenum film of thickness 50 nm

| <i>Pulse Regime</i> | <i>(1 - R - T_r)</i> | | |
|----------------------------|---------------------------------------|-------------------------|-------------------------|
| | <i>IR</i> | <i>Green</i> | <i>UV</i> |
| <i>Femtosecond</i> | 0.31 ± 0.01 (1030 nm) | 0.44 ± 0.01 (515 nm) | 0.45 ± 0.01 (343 nm) |
| <i>Nanosecond</i> | 0.23 ± 0.01 (1064 nm) | 0.39 ± 0.01 (532 nm) | 0.44 ± 0.01 (355 nm) |

4.2.2. Micro-machining of 50 nm thin molybdenum film using femtosecond and nanosecond pulsed laser sources

4.2.2.1. Femtosecond laser processing

Figure 4.7 presents an optical microscope image of the crater created in molybdenum thin film after the interaction with 1030 nm femtosecond laser pulse at different absorbed peak fluences. The first key observation of femtosecond laser processing of molybdenum thin film shows delamination of molybdenum film from the substrate [105, 106]. Several particles were observed under the optical microscope.

The absorbed peak threshold fluence of molybdenum thin film was calculated using Liu's method by varying laser pulse energy as described previously (section 3.4.3). At each specific energy value, three different diameters were measured, and an average value was determined. Although, the laser produced craters which were not perfectly circular, an approximate diameter was used; this was obtained by picking three points along a circumference of the delaminated damaged/undamaged interface. At these peak fluences, the energies absorbed by the molybdenum film are insufficient to account for any of melting or evaporative phase changes within the thin film. Hence the removal of the molybdenum thin film is attributed to other ablative mechanisms.

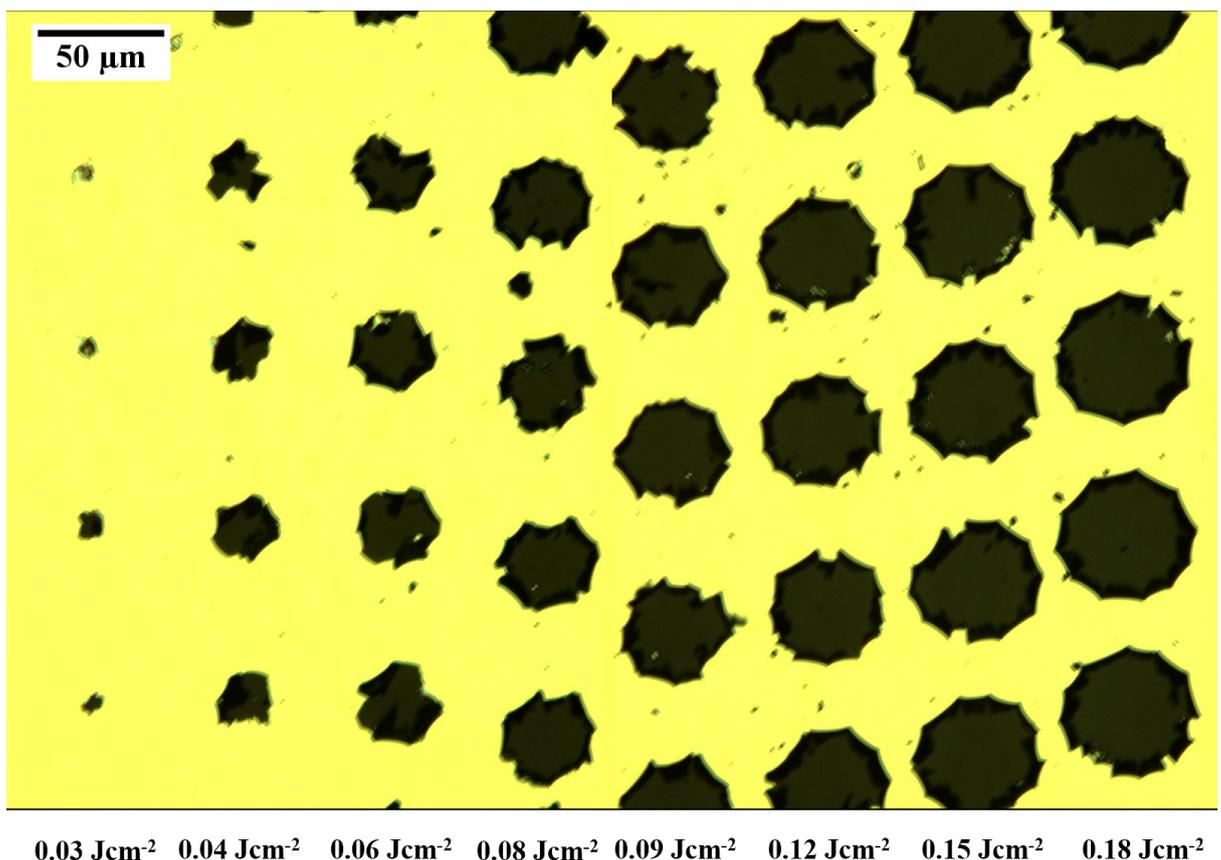


Figure 4.7: Removal of the molybdenum film from the glass substrate, as observed from the optical microscope image, Optical microscope image reveals an increase of crater diameter with higher absorbed 1030 nm femtosecond laser fluence

Measurement of absorbed threshold fluence was performed by plotting a graph between the diameter squared and the natural logarithm of the absorbed fluence (section 3.4.3), shown in the Figure 4.8. The threshold fluence was calculated and it was found that the absorbed threshold

fluence for thin films is small compared with bulk molybdenum but also varies with laser wavelength. It was found that the calculated threshold fluence is much smaller than the predicted fluence required for melting or vaporisation of molybdenum and thus the threshold value is termed as the ablation threshold. The calculated ablation threshold fluences are listed in the Table 4.5.

Table 4.5: Absorbed threshold fluence at different femtosecond laser wavelength

| <i>Wavelength (nm)</i> | <i>Threshold fluence (absorbed) (Jcm⁻²)</i> |
|----------------------------|--|
| 1030 | 0.018 ± 0.001 |
| 515 | 0.021 ± 0.007 |
| 343 | 0.016 ± 0.001 |

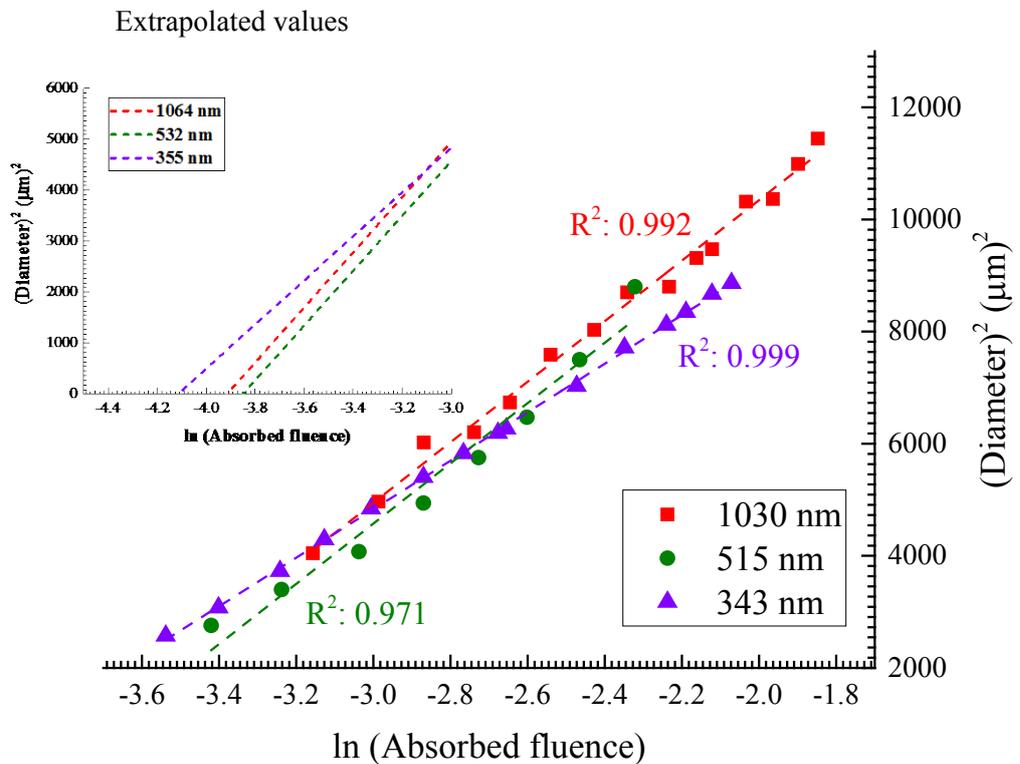


Figure 4.8: Estimation of threshold fluence (absorbed) of molybdenum thin film using 1030 nm, 515 nm and 343 nm femtosecond laser sources. The extrapolate values provide the peak value of absorbed threshold fluence

Red, green and violet points in Figure 4.8 present the diameters produced by 1030 nm, 515 nm and 343 nm femtosecond laser at different peak fluences. The slope of the lines fitted to the data points determine the beam size (radius) at the surface of thin molybdenum film. The different values of beam diameter calculated from the Figure 4.7 are $50.79 \pm 1.56 \mu\text{m}$ (1030 nm), $51.84 \pm 1.84 \mu\text{m}$ (515 nm) and $46.51 \pm 2.56 \mu\text{m}$ (343 nm). The R^2 values of each linear fit confirms the quality of the linear fitting. While, initial observations indicate that the molybdenum thin film is

loosely adhered to the glass substrate, the threshold fluence required to remove the molybdenum film from the glass substrate is also correspondingly small when compared with bulk values.

Figure 4.9 shows the scanning electron microscope image of a crater created on the thin molybdenum film using 515 nm laser wavelength at peak absorbed fluence of 0.1 Jcm^{-2} . Several loosely bounded fragmented film (particles) are observed surrounding the craters (Figure 4.9(a)). Figure 4.9(b) presents the SEM image of uncoated laser processed molybdenum film using 1030 nm femtosecond laser pulse. Electrostatic charging was observed at the substrate using SEM measurements.

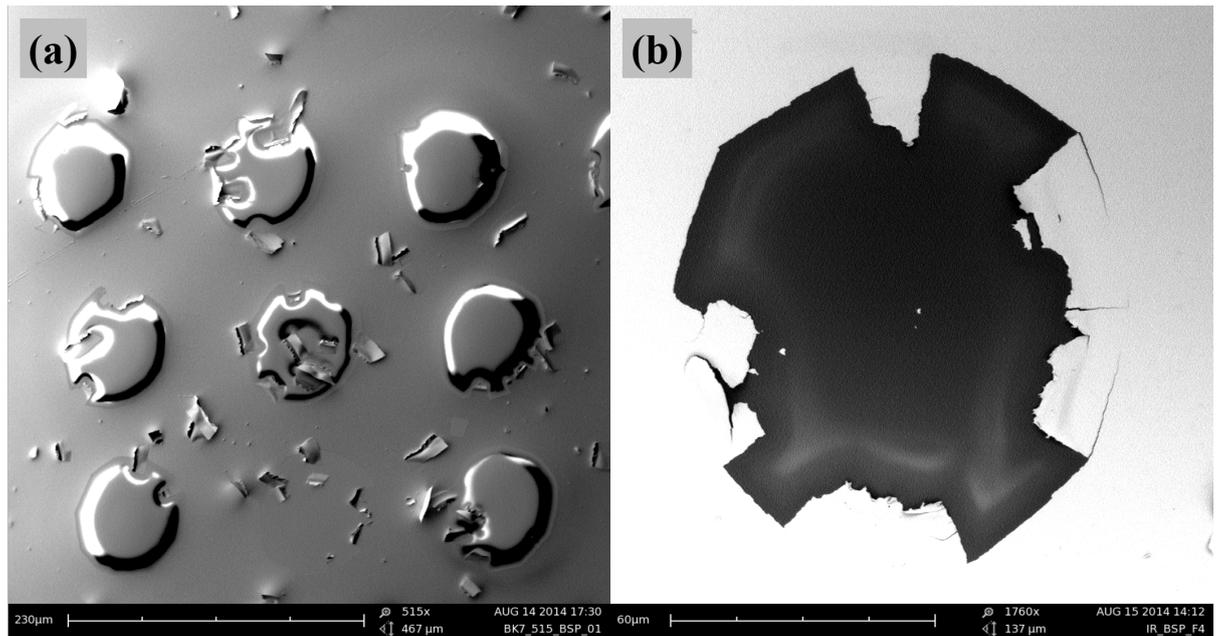


Figure 4.9: (a) Fragmentation of the molybdenum thin film surrounding the ablated crater (peak value of absorbed fluence: 0.3 Jcm^{-2}) and (b) electrostatic charging in glass during the interaction of high energy electron beam with non-conductive glass substrate is also evident; the peak value of the absorbed fluence is 0.1 Jcm^{-2}

In order to overcome this charging effect, a very thin layer of gold was sputtered prior to capture image using SEM.

The delamination of the molybdenum film was also observed from these subsequent SEM measurements. This occurred at different fluences (Figure 4.10(a)). The peak values of the absorbed fluences are indicated. Figure 4.10(b) shows the expanded view of a crater at a peak fluence of 0.1 Jcm^{-2} by 1030 nm femtosecond laser interaction with molybdenum thin film. Evidence of fragmentation of the thin film is also observed at lower magnification. The density of these fragmented particles increases with increasing laser fluence. A deformed and delaminated film is also extensively observed throughout the laser processed thin films.

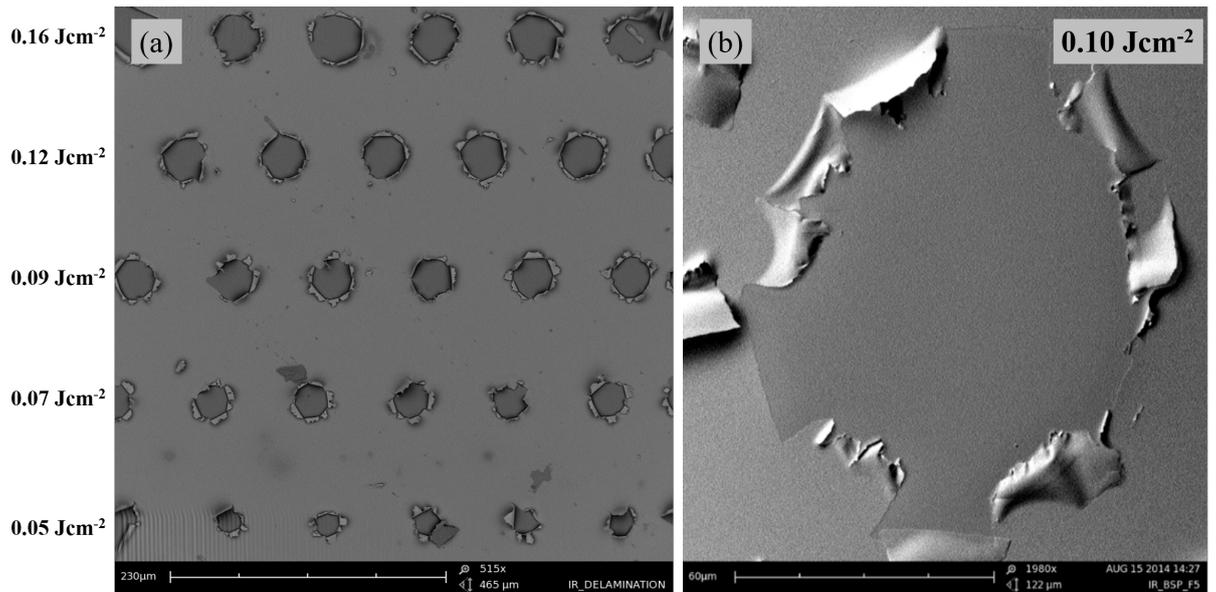


Figure 4.10: (a) Delamination of molybdenum film as a result of interaction with 500 femtoseconds laser source of wavelength of 1030 nm and (b) molybdenum surface at a fluence of 0.1 Jcm⁻². A thin layer of gold was coated on the laser processed molybdenum thin film to avoid the charging

Figure 4.11 shows higher magnification scanning electron microscope images on molybdenum film surface at nine different fluences using 1030 nm femtosecond laser wavelength. The result clearly shows an increase of the crater diameter with laser fluences. Several cracks on the molybdenum film was observed at the boundaries between the removed and non-removed molybdenum film surface, particularly at lower fluences. This effect is less noticeable with increasing laser fluence, presumably because the mechanical stress which gives to such cracks leads is released by creation of fragmented particles.

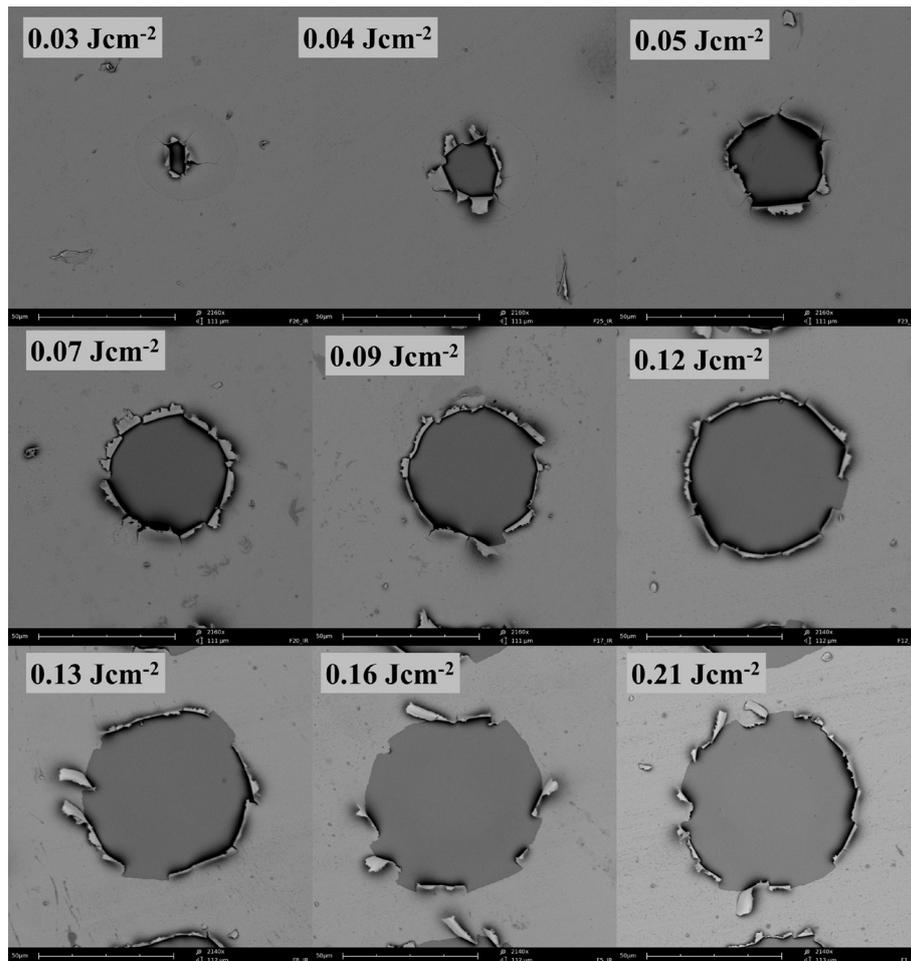


Figure 4.11: SEM images of single pulse IR FS processed molybdenum film on glass substrate at different peak absorbed fluences

The scanning electron microscope images indicate that delamination with complete removal of the molybdenum film from the substrate in the region of the crater is the cause of material removal. The samples shown in Figure 4.10 and Figure 4.11 were cleaned gently with a compressed air duster prior to examination; this removed the excess particulates from the surrounding region which otherwise may cause damage to the SEM tool. This light cleaning does not impact the crater or the proposed hypothesis for how the thin film delaminates from the surface.

The onset of delamination was clearly observed at a fluence just above the ablation threshold of molybdenum film. Figure 4.12 shows the SEM images at fluences of 0.03 and 0.025 Jcm⁻². It was also found that the delaminated edge surfaces are very loosely adhered to the substrate and thus these physically formed edges fall back to the substrate surface when the applied energy is removed.

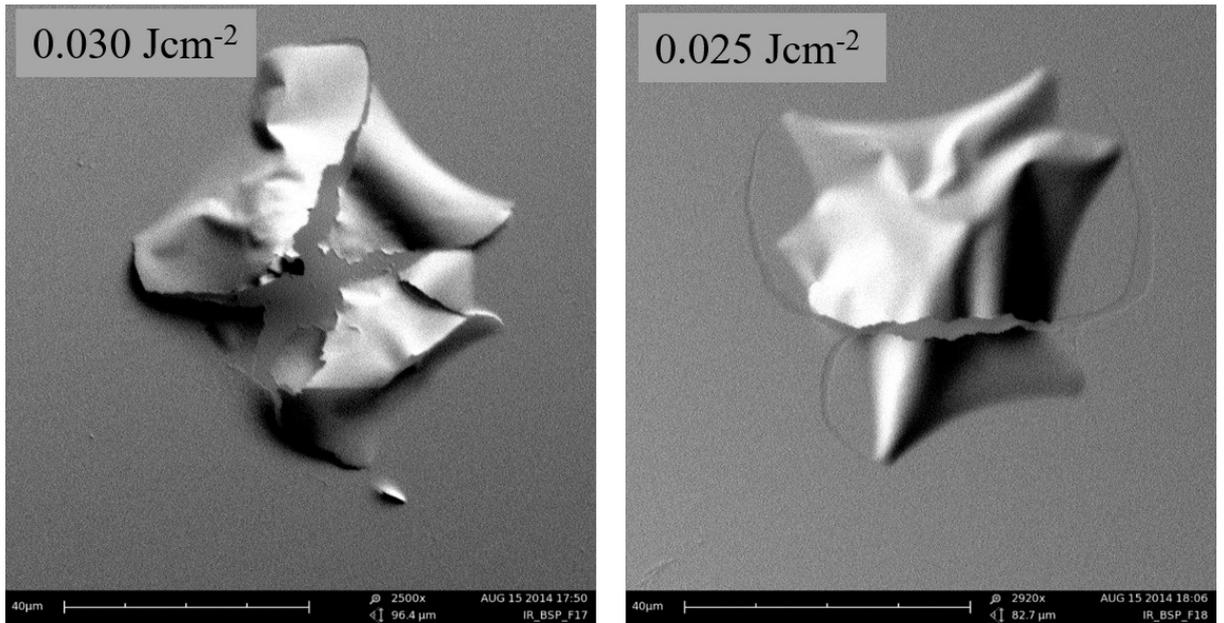


Figure 4.12: Strained molybdenum film after incidence of 1030 nm femtosecond laser just about the ablation threshold

There was no consistent pattern for how the molybdenum film broke up. This is probably due to non-uniformity of molybdenum film on glass substrate (1 ± 0.3 nm) or due to the presence of other defects in the glass substrate. A similar delamination effect was observed during 515 nm and 343 nm femtosecond laser interaction with molybdenum thin film. The craters produced by single pulse femtosecond laser molybdenum interactions at wavelengths of 515 nm and 343 nm are shown in Figure 4.13.

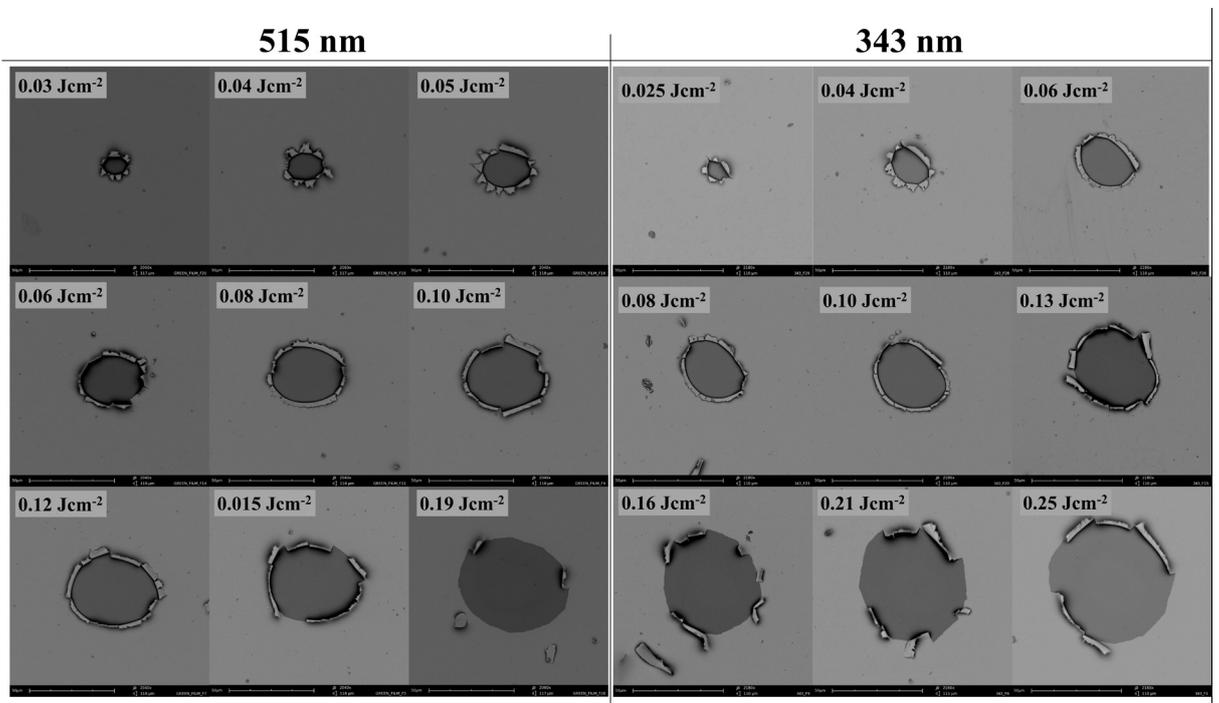


Figure 4.13: Femtosecond laser processed molybdenum thin film using 515 and 343 nm wavelength at different peak absorbed fluences

Figure 4.14(a) presents an atomic force microscope image (AFM) of a crater attained at a fluence of 0.1 Jcm^{-2} using a femtosecond laser at a wavelength of 1030 nm. The AFM technique does not provide the usual clarity because of the loosely adhered film and particulate associated with the ablation mechanism. On close inspection of the AFM image, a distortion or noise is observed in the form of horizontal lines. Many particles are also observed at the centre of the crater; which results from the fragmentation of the molybdenum film. A representative profile of the craters is shown in Figure 4.14(b). It was observed from the AFM analysis that no film was left in the centre of the crater. Several unwanted peaks were also noticed at the centre of the crater. It was concluded that these peaks are formed due to the deposition of the fragmented molybdenum film on the surface of the film and the substrate.

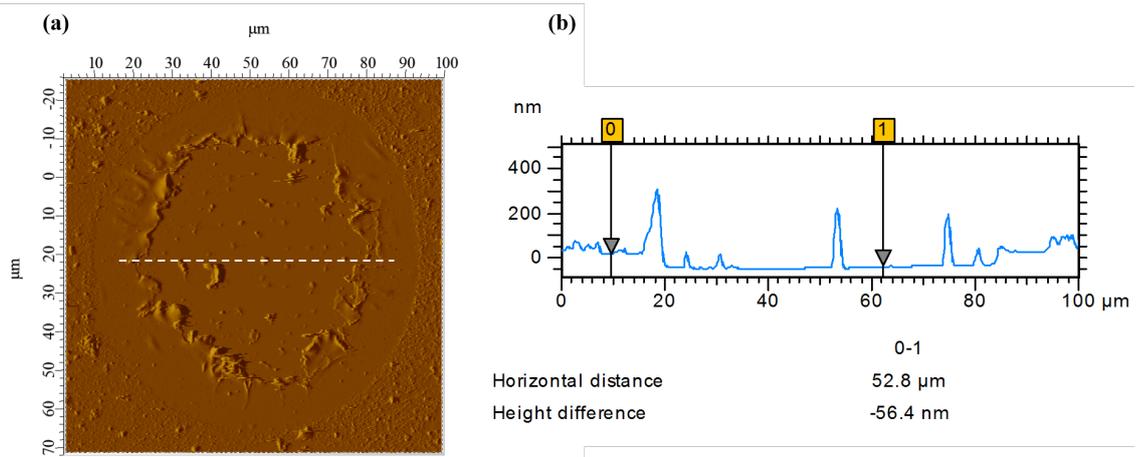


Figure 4.14: (a) 1030 nm femtosecond laser produced damage on 50 nm molybdenum film at an absorbed fluence of 0.1 Jcm^{-2} . (b) The extraction of the profile from AFM image indicates that substrate surface below the film is damage free except for contamination by particulate. The dashed line indicates the position where the profile extraction of the crater was measured

In order to overcome the noise, the AFM analysis of the damaged molybdenum film were performed again after applying the compressed air to the surface to gently remove loosely adhered particles. The AFM images post air cleaning are shown in Figure 4.15. AFM analysis was carried out at different absorbed fluences. At low fluence, a clean ablation with minimal substrate damage was observed. An increase of laser fluence results in an increase of fragmented particles. At high fluence, many small particles were observed surroundings the ablated craters. The extracted surface profile from the AFM images indicates almost clean ablation with minimal substrate damage and thin film distortion. It was found that the depth in the extracted profile is almost constant ($\sim 50 \text{ nm}$) and indicates a delamination process. No trace of molybdenum was also observed by the energy dispersive X-ray measurement.

The Figure 4.15 presents surface profile of laser processed molybdenum film at fluence 0.1, 0.07 and 0.04 Jcm^{-2} . The corresponding surface profile presents the constructed depth on the film surface and results in almost a constant value (50 nm) indicating a clear delamination effect.

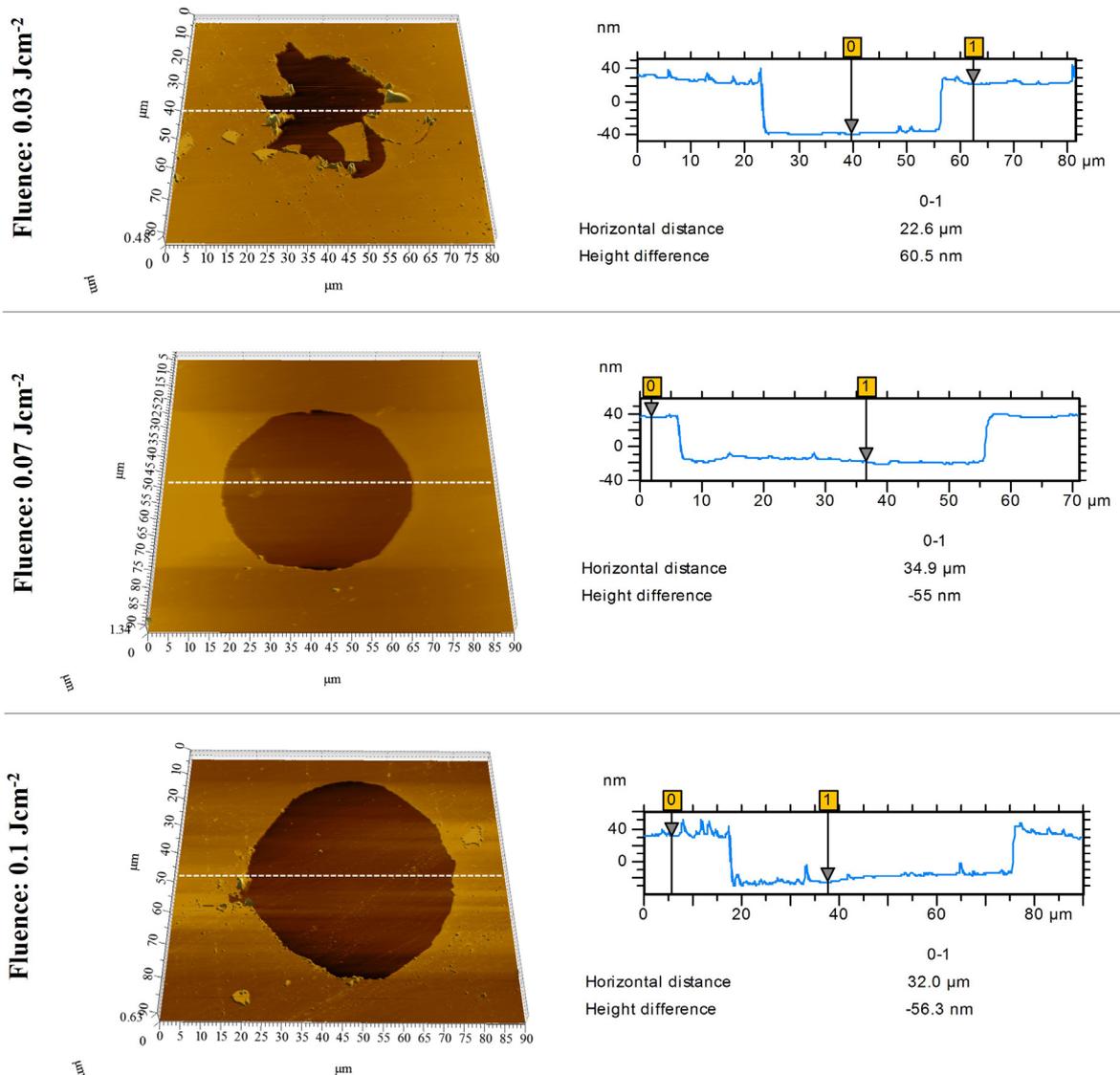


Figure 4.15: Profile extraction from AFM image reveals femtosecond laser processing of molybdenum film results damage free substrate. The dashed line on the AFM images corresponds the line from where the surface profile was extracted

The roughness of the ablated/removed area of the crater was found to be 2.81 ± 0.01 , 3.07 ± 0.05 and 4.41 ± 0.07 nm, respectively.

Figure 4.16 presents an AFM image of the crater on the surface of the molybdenum thin film, at a peak absorbed fluence 0.028 Jcm^{-2} . This peak fluence is just above the absorbed ablation threshold fluence of the molybdenum film (0.018 Jcm^{-2}) using a femtosecond laser of wavelength of 1030 nm. Some fragmented particles were noticed in the AFM image; this indicates the fragmentation of molybdenum film from the BK7 substrate.

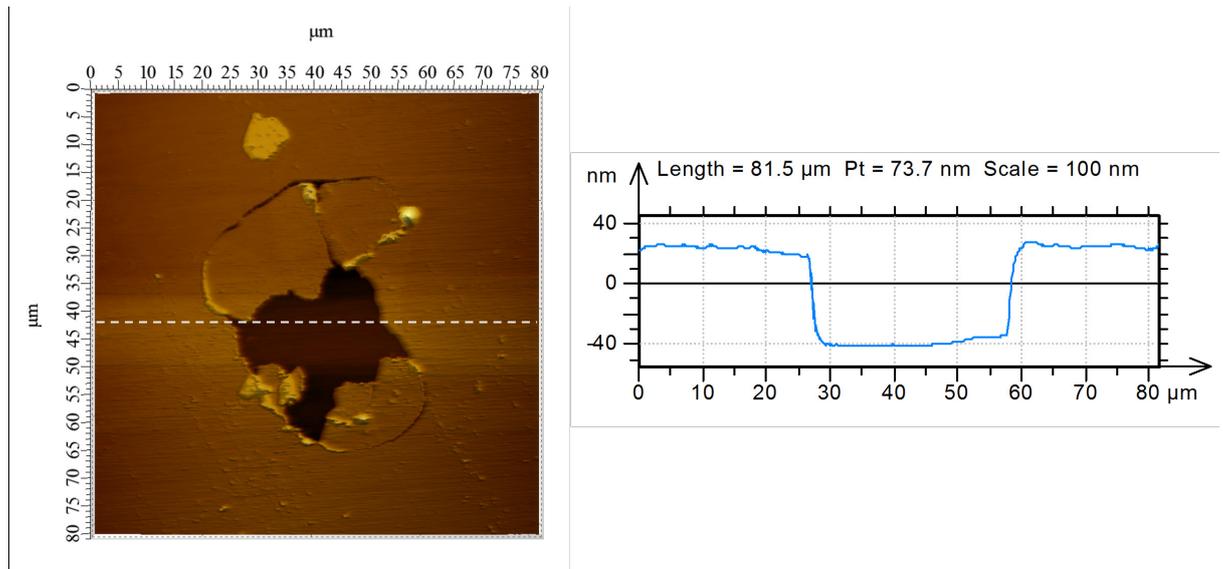


Figure 4.16: Removal of molybdenum film at low fluence (Femtosecond, 515 nm, Peak value of the absorbed fluence: 0.028 Jcm^{-2})

A clear indication of the fracture of the molybdenum film is observed from the Figure 4.16. The nature of the fracture in the molybdenum thin film appears to be brittle, presumably. After removal of the fractured molybdenum thin film, the fragmented films are re-deposited on the crater. The removed area was found to be reasonably smooth (roughness: $1.66 \pm 0.03 \text{ nm}$) and the measured depth was approximately equal to the total thickness of the molybdenum film.

4.2.2.2. Nanosecond laser processing

Figure 4.17 shows an optical microscope image of the craters produced using nanosecond laser pulse of wavelength of 1064 nm at different absorbed energies for the thin molybdenum film. In all cases material removal is observed. Two fluence regimes were observed on the ablated crater. At higher fluence, the inner circle becomes more prominent. It was presumed that the inner circle is caused due to the damage in the glass substrate. Initial observation indicates that formation of several fragmented particles surrounding the ablated craters. It was estimated that the average size of the fragmented particles are larger than $5 \mu\text{m}$. It was also noticed that the fragmented particles are loosely adhered with the surfaces of the molybdenum thin film and the craters.

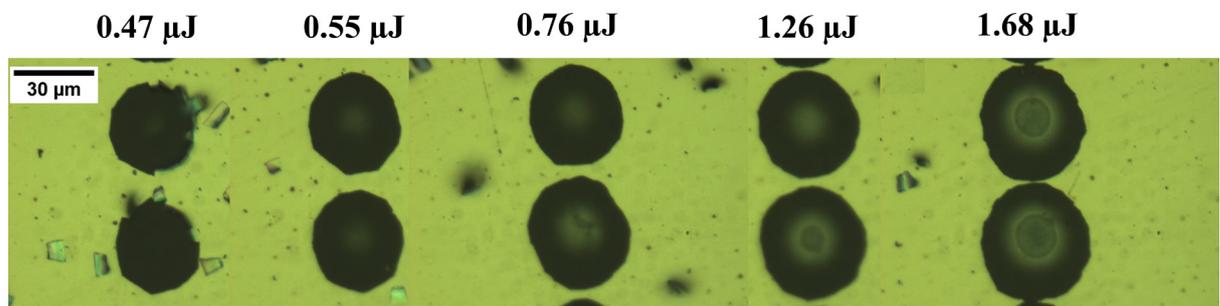


Figure 4.17: Optical microscope image of molybdenum thin film using single pulse 1064 nm nanosecond laser by varying energy of laser pulse

The peak value of the absorbed threshold fluence was calculated using Liu's method and the Figure 4.18 presents squared diameter vs natural logarithm of absorbed fluence. The extrapolated linear fit was used to determine the ablation threshold fluence.

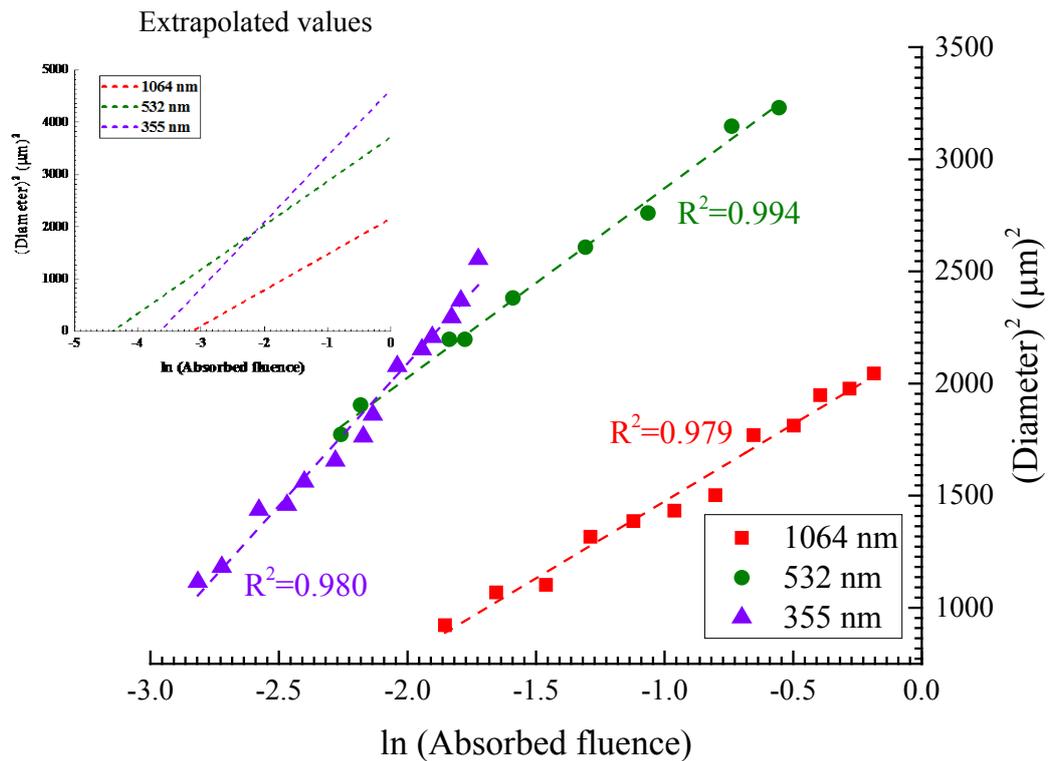


Figure 4.18: Estimation of the threshold fluence (absorbed) of molybdenum thin film by 1064 nm, 532 nm and 355 nm nanosecond laser sources. The insert presents the extrapolation of the linear fit at $Y=0$, and corresponds the value of ablation threshold at three different wavelengths

The linear fit for each data set is good ($R^2 > 0.97$). The estimated threshold fluence values are listed in the Table 4.6,

Table 4.6: Absorbed threshold fluence at different nanosecond laser wavelength

| <i>Wavelength (nm)</i> | <i>Threshold fluence (absorbed) (Jcm⁻²)</i> |
|----------------------------|--|
| 1064 | 0.043 ± 0.003 |
| 532 | 0.012 ± 0.006 |
| 355 | 0.026 ± 0.001 |

The ablation threshold fluence for the molybdenum film was smallest for the interaction of nanosecond laser using a wavelength of 532 nm. The threshold fluence required to damage the molybdenum thin film using 355 nm wavelength is almost half of 1064 nm threshold fluence.

The scanning electron microscopy images of the craters on the molybdenum thin film by different fluences are shown Figure 4.19. The glass damage is increasingly observed with increasing peak fluence of the laser pulse using nanosecond laser wavelength of 1064 nm. Re-deposited fragmented particles were also observed on the craters. The craters were created on the

molybdenum film using 1064 nm nanosecond laser pulse at different fluences. Similar to the femtosecond case, several fragmented particles were observed from the SEM image.

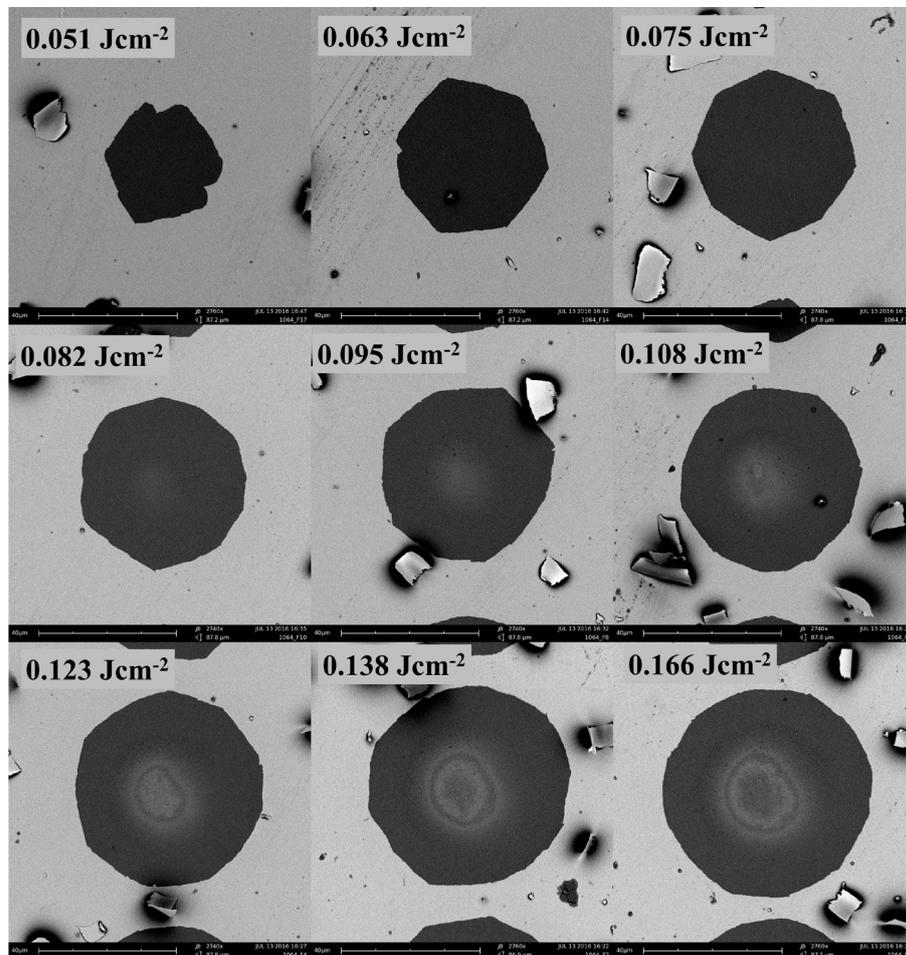


Figure 4.19: SEM images of single pulse nanosecond laser (wavelength 1064 nm) processed molybdenum film on glass substrate at different fluences. The peak value of the absorbed fluences are indicated with each crater.

Unlike the femtosecond laser ablation, it was observed that the edge of the craters produced by nanosecond laser are comparatively sharp. Two diameters are observed from the SEM images. The outer diameter defines the threshold limit for the complete removal of molybdenum thin film from the glass substrate. The inner diameter is presumably because of the substrate (glass) damage. The inner diameter becomes clear with increasing laser fluence. The diameter of both the craters increases with increasing absorbed laser fluence.

Figure 4.20 presents the scanning electron microscope images of the crater on the molybdenum thin film at the peak absorbed fluences of 0.046 and 0.048 Jcm⁻² using nanosecond laser of wavelength of 1064 nm. Both the fluences are just above the ablation threshold of molybdenum thin film using a wavelength of 1064 nm. Both the images indicate complete film removal from the substrate by fragmentation.

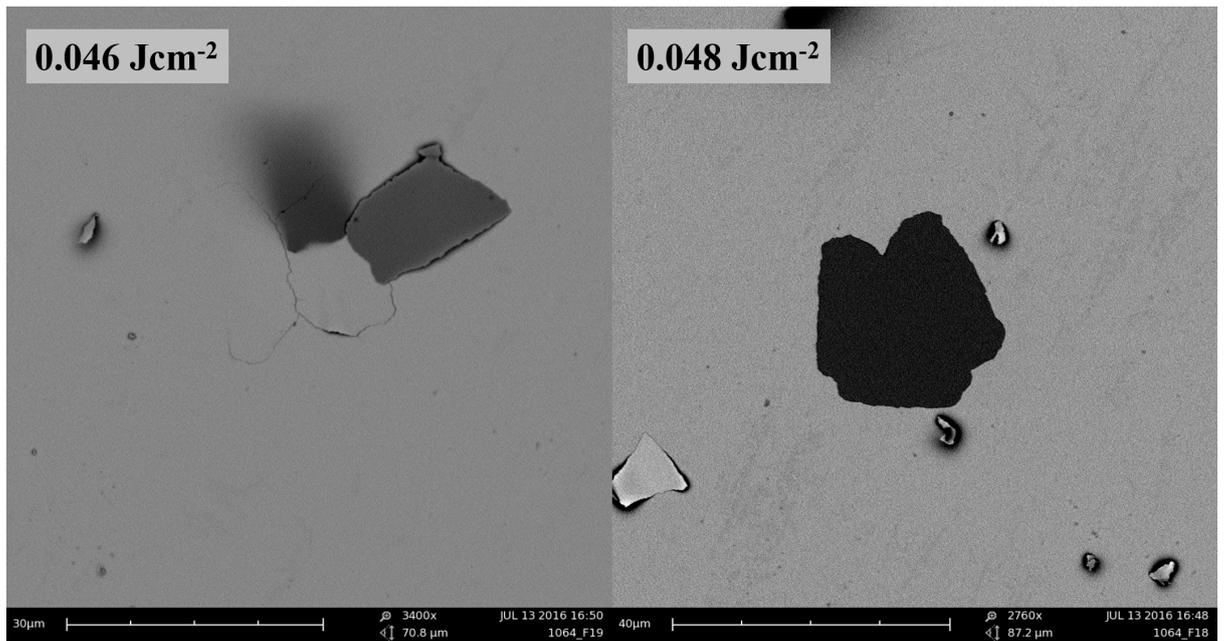


Figure 4.20: Selective removal of molybdenum film a low fluence, just above peak absorbed ablation threshold. Presents fracture in molybdenum thin film. A small increase of the fluence leads to removal of molybdenum thin film from the glass substrate

An atomic force microscope image of a nanosecond produced crater is shown in the Figure 4.21. This indicates the complete removal of molybdenum film with a significant substrate damage. Figure 4.21(a) corresponds to AFM image of surface morphology of 1064 nm nanosecond laser created molybdenum crater at a fluence of 0.1 Jcm^{-2} . The surface profile across the crater is shown in the Figure 4.21(b) and the noise at the centre of the profile indicates damage to the substrate. The full and the expanded profile across the centre part of the crater indicates ablation of the substrate with the molybdenum film.

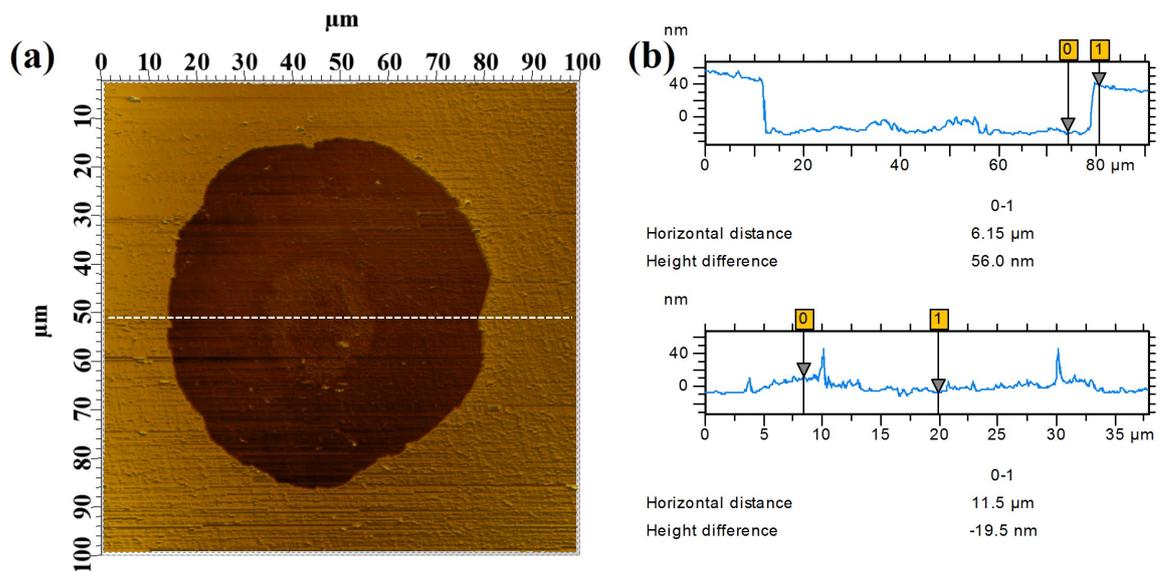


Figure 4.21: (a) Atomic force microscope image shows complete film removal during by nanosecond laser (wavelength: 1064 nm, peak fluence 0.1 Jcm^{-2}) ablation with (b) the profile extraction of the AFM image corresponds significant damage in the substrate. Evidence for glass damage was observed in centre of the crater

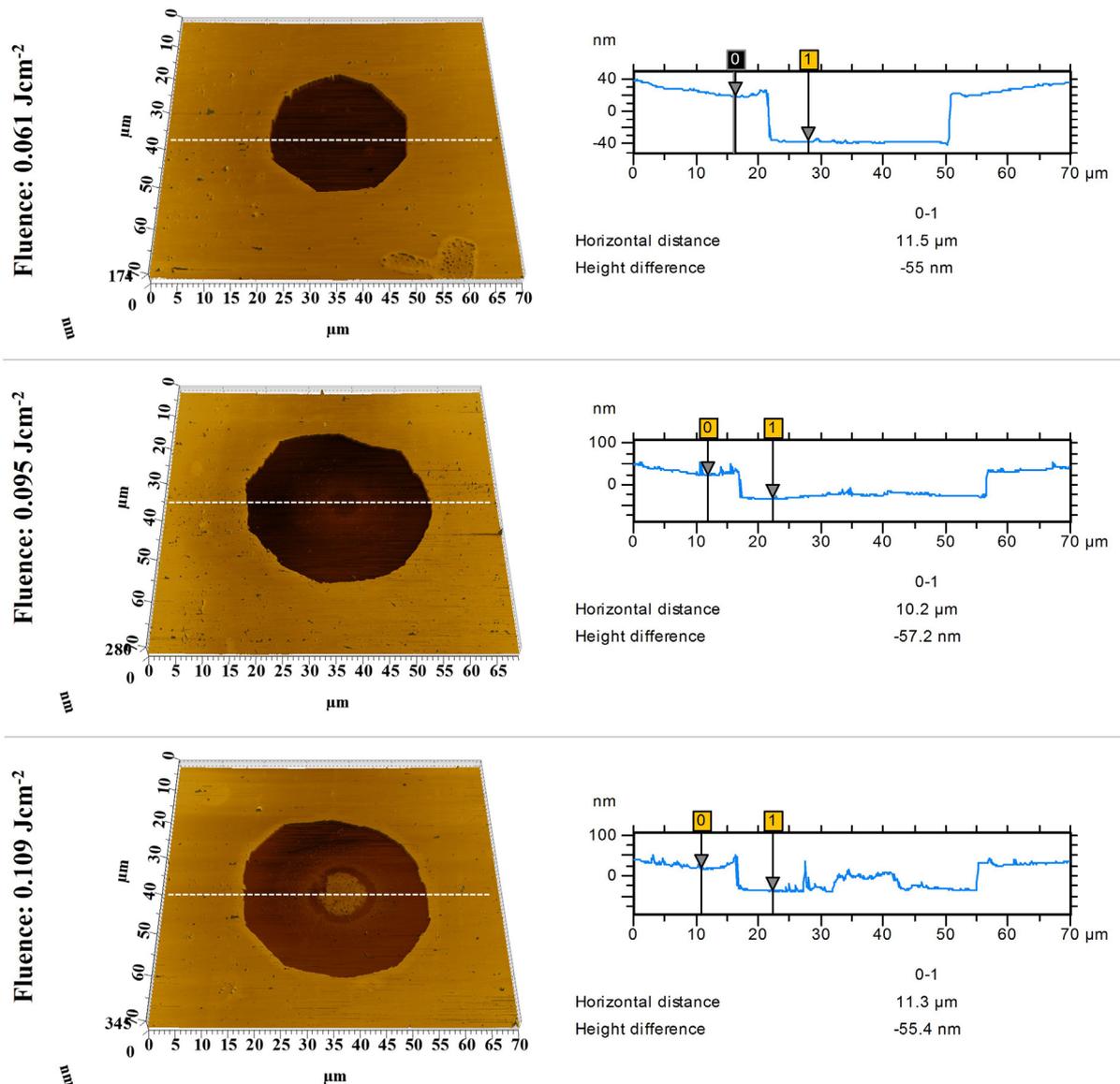


Figure 4.22: AFM microscopy images at different absorbed fluences. Profile extraction from AFM image reveals femtosecond laser processing of molybdenum film results complete film removal with significant damage on the substrate. The dashed line on the AFM images corresponds the line from where the surface profile was extracted

The AFM images in Figure 4.22 indicates a variation of the peak depth of the craters with the absorbed peak fluence. The profile measurements indicate a sampled height difference of 55.0, 57.2 and 55.4 nm for the peak fluences of 0.061, 0.095 and 0.109 Jcm⁻², respectively. Thus, complete removal of molybdenum film takes place at all the fluences. Thermal damage of the glass substrate was found to increase with increasing laser fluence. The RMS roughness of the molybdenum film at the centre of the crater was calculated to be 3.81 ± 0.04 , 5.73 ± 0.08 and 13.5 ± 0.2 nm for above fluences. The damage on the substrate suggests that the glass undergoes to the melting phase from its initial solid phase. Similar to femtosecond case, at the ablation track molybdenum was not detected by energy dispersive X-ray measurement.

4.2.3. Computational simulation using finite element method (FEM)

4.2.3.1. Interaction of thin molybdenum film with ultra-short pulse laser using combined two temperature model with mechanical stress model

To understand femtosecond laser ablation phenomena of a molybdenum thin film, two temperature modelling (TTM) was performed. A mechanical model was integrated with the simple TTM to understand evolution of stress and strain inside the molybdenum film. The coordinate system used for the numerical simulation is indicated in the section 3.7.3.

Initially, an electron-phonon coupling constant and an electron heat capacity (Figure 2.13), depend upon the temperature of the electronic subsystem, were used to study the femtosecond laser interaction with molybdenum thin film [150].

Figure 4.23 presents the transient temporal profile of localised electron and lattice temperatures with the incident laser wavelength (solid red line) at a fluence of 0.1 Jcm^{-2} . The simulation relates to when the laser pulse peaks at $t = 0.5$ picoseconds from an arbitrary time (t_0) and has a pulse width (FWHM) of 500 femtoseconds. The model predicts that the electron temperature (square dotted line) increases rapidly with the incident laser beam and reaches several thousands of Kelvin. After this peak, the electronic temperature decays slowly over a time scale of several picoseconds.

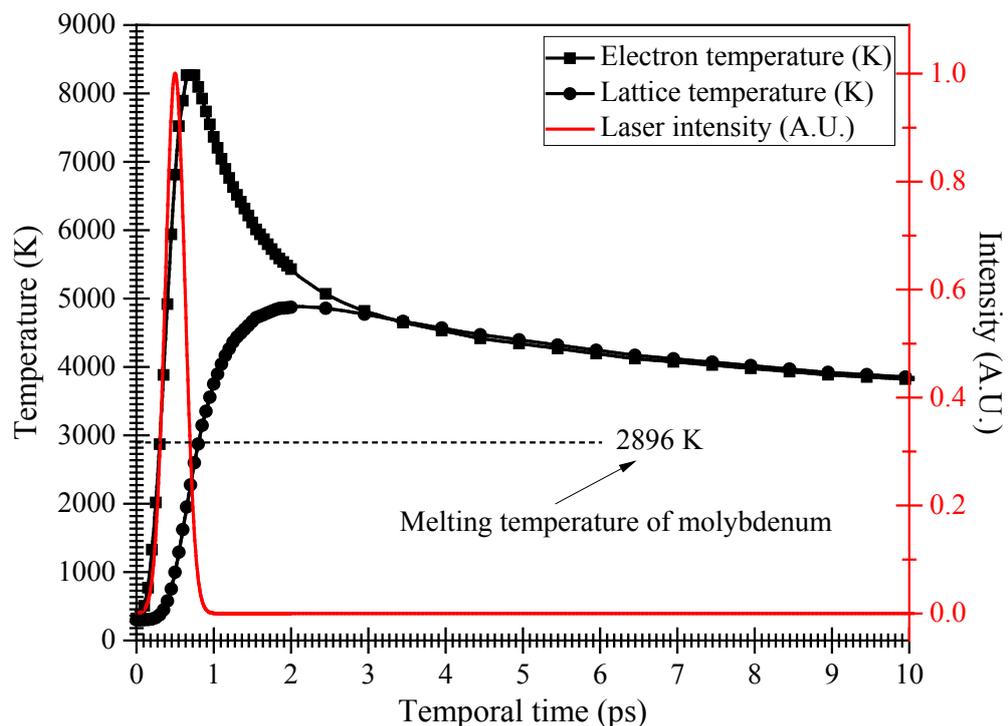


Figure 4.23: Transient temperature increase of electronic and lattice subsystem with a normalised laser intensity in a thin film. The peak absorbed fluence was chosen to be was 0.1 Jcm^{-2} and the electron-phonon coupling coefficient selected from [150]

The hot electrons diffuse into the slightly colder parts of the molybdenum film due to the temperature gradient. The electron and lattice temperature reach an equilibrium after ~ 3

picoseconds which is determined by the electron-phonon coupling constant discussed in the theory chapter (section 2.6).

The lattice temperature (circular dotted line) increases at a slower rate compared with the electron temperature. The numerical simulation suggests that the peak temperature of the lattice reaches to 4560 K at 1.93 picoseconds. The lattice temperature reaches a value above the melting temperature of the molybdenum (2896 K) at a time 0.8 picoseconds from the arbitrary reference time t_0 . This is contrary to our experimental observations where no molten phase was observed.

The distribution of the lattice temperature along the depth of the molybdenum film and the glass substrate is shown in the Figure 4.24. A rapid decay of the lattice temperature was observed at the centre of the laser pulse, from the surface of the molybdenum thin film ($Z = 0$) towards the molybdenum-glass interface ($Z = -50$ nm).

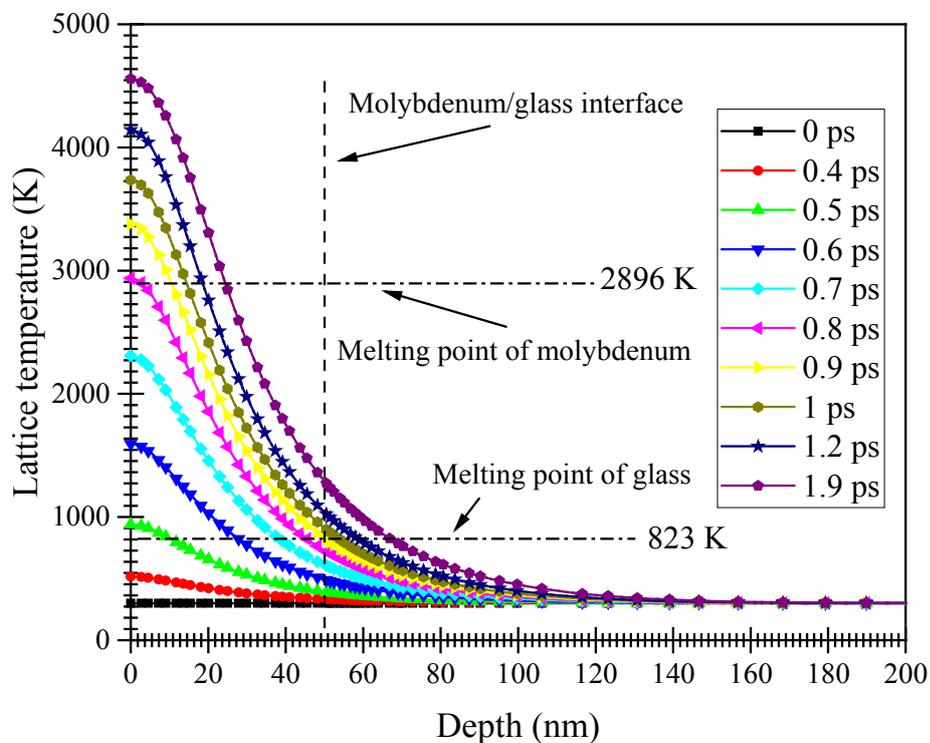


Figure 4.24: The variation in the peak temperature of the lattice for different depths in the molybdenum thin film and near surface region of the glass substrate at different times after the peak pulse (peak absorbed fluence 0.1 Jcm^{-2}) was applied to the materials

During the femtosecond laser processing, when the time needed to initiate a collective motion of atoms on the lattice within the absorbing volume is greater than the duration at which the energy is supplied to the material determined by the duration of the laser pulse, laser modification of the molybdenum target occurs within a volume condition that is approximately constant. This confinement of energy leads to high stresses shown in the Figure 4.25.

The coordinate system used for the mechanical simulations was shown in the Figure 3.24 (chapter 3, section 3.7.3). The σ_{XZ} measures the shear stress induced on the XY plane ($Z=\text{constant}$) and

acting in the X- direction. Similarly, the tensile stress σ_{XX} measures the stress component acting in the X direction and on the plane YZ.

In this study, the expansion of the film vertically with respect to the horizontal the interface at the solid substrate which is a likely relaxation route for a laterally confined compressive stress. As the thermal expansion of the molybdenum thin film is confined in the horizontal direction (XY plane), a high stress (σ_{XX}) is developed in the film. It was observed that this stress is compressive in the region of absorption and exerts an expansion force which acts both laterally and vertically in directions parallel and perpendicularly across the film substrate interface. The build-up of the lateral compressive stress at the film surface, produced by 1030 nm femtosecond laser at 0.1 Jcm^{-2} fluence, is shown in the Figure 4.25. The graphs were calculated on the surface at $Z = 0$, at different times before the heating of the molybdenum film by the laser source causes the melting of molybdenum. The release of stress at the melting temperature was ignored for the low fluences used in this study. The simulation suggests that the compressive stress reaches a peak value at time 1.93 picoseconds; the corresponding temperature at this time was found to be 4560 K. The high compressive stress is established even before the melting of molybdenum that take place at 0.8 picoseconds. The peak value of the compressive stress at the surface of the film at a fixed time is observed at the centre of the focussed laser spot. In this model, it is observed that the compressive stress reaches to its maximum value, after the melting of molybdenum lattice. The graphs are calculated at the point corresponding to the maximum stress (σ_{XX}), at the centre of the focused laser spot ($X = 0, Y = 0$), and on the surface at $Z = 0$ (is $X = 0, Y = 0, Z = 0$).

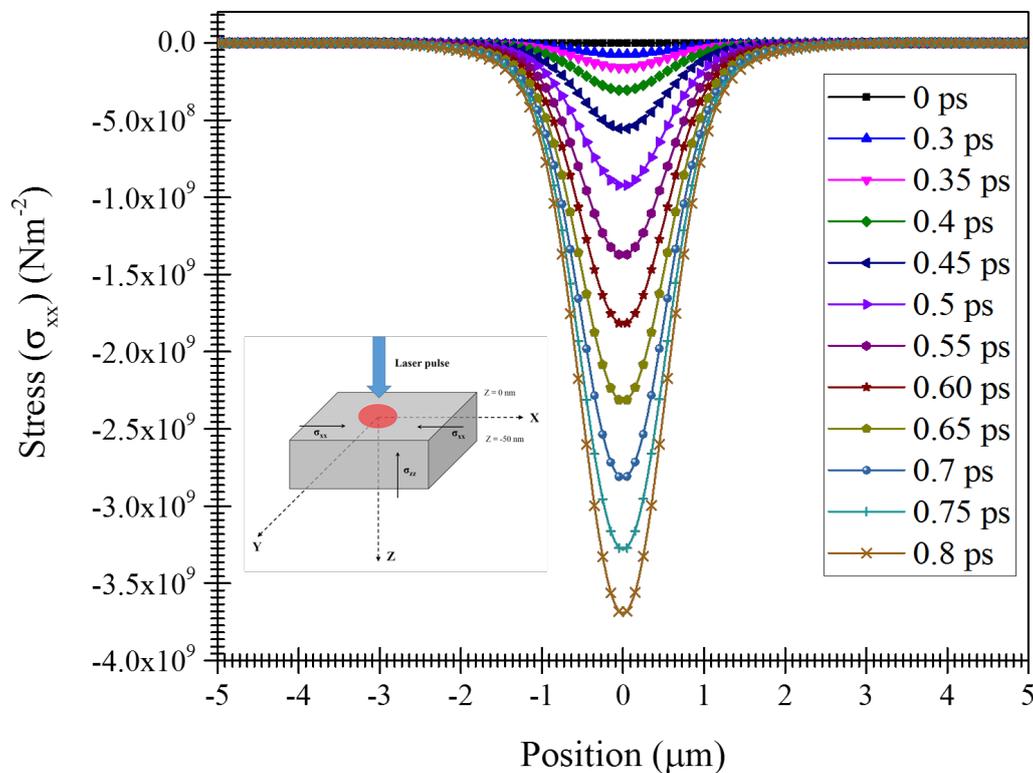


Figure 4.25: Transient expansion of compressive stress (σ_{xx}) at the film surface

Figure 4.26 shows the transient compressive stress in the plane (XY plane) and at different depths (different Z) of the molybdenum film at the centre of the laser spot i.e. $X = 0, Y = 0$.

It was found that the compressive stress is triggered by the lattice temperature after electron-phonon coupling. At $t = 0$, no stress in the film is observed. The peak value of the compressive stress was observed after the melting, when the temperature of the lattice reaches to its maximum temperature. The peak value of the compressive stress is found to decrease with increasing distance from the surface of the film ($Z = 0$). It is also observed that the stress peaks reach at different time at different depths from the surface. Stresses at other points away from the centre of the laser spot also occur at times which are after that when the molten phase has started to form.

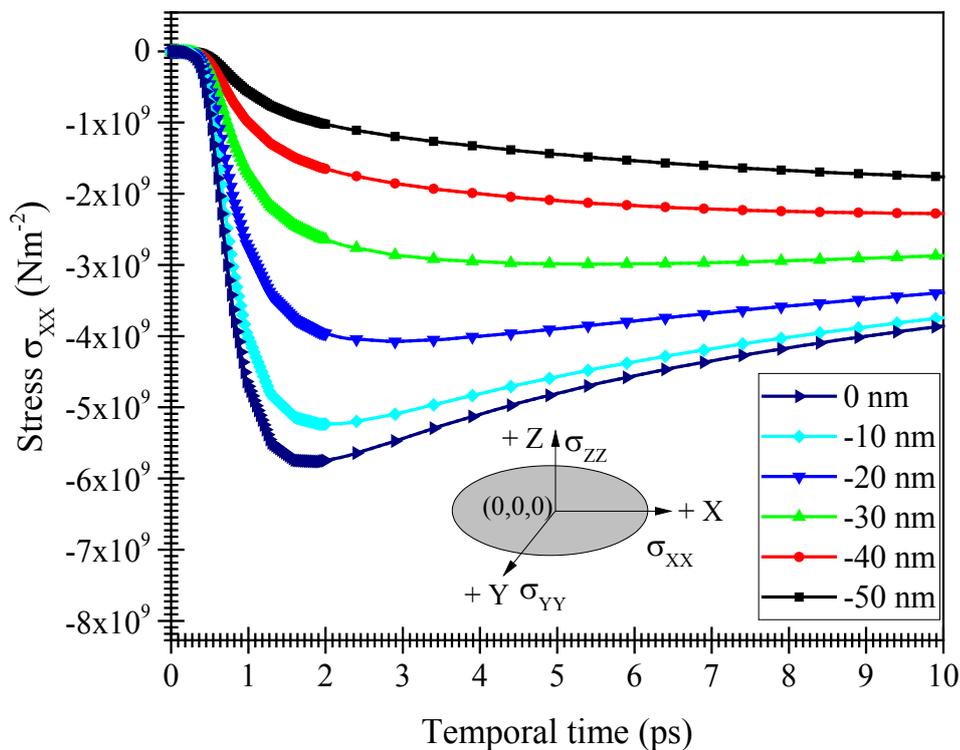


Figure 4.26: Compressive stress (σ_{xx}) at different depth from molybdenum film surface to the molybdenum-substrate interface. The insert shows the Cartesian coordinate system and the direction of the different stress components

The peak value of the compressive stress at the film surface and the molybdenum/glass interface occurs at 1.5 and 21 picoseconds at the onset of the laser pulse, respectively. The decrease of the peak value of compressive impulse is due to the reduction in temperature. These results suggest that we can only consider stresses up to 0.8 picoseconds in duration.

Lattice heating of the molybdenum film would lead to thermal expansion of the material if it were free to expand. This in turn would generate strain in the film. The only direction in which the laser irradiated part of the film can expand is in the vertical direction, perpendicular to the plane of the thin film at the air interface. Numerical simulations indicate that approximately 2.5% and 5% peak strain is observed in the vertical direction for fluence values of 0.05 Jcm^{-2} and 0.1 Jcm^{-2} respectively. This displacement of material leads to a tensile stress at the thin film substrate

interface in the upward direction. An important observation from the model is that this tensile stress evolves more quickly than the compressive stress generated in the plane of the thin film. The peak tensile stress (σ_{ZZ}) at the thin film-glass interface, in the perpendicular direction occurs 1.3 picoseconds before the peak compressive (σ_{XX}) stress observed in the lateral direction.

Figure 4.27 presents the transient behaviour of tensile stress at the film-substrate interface compared with the compressive stress in the plane of the material.

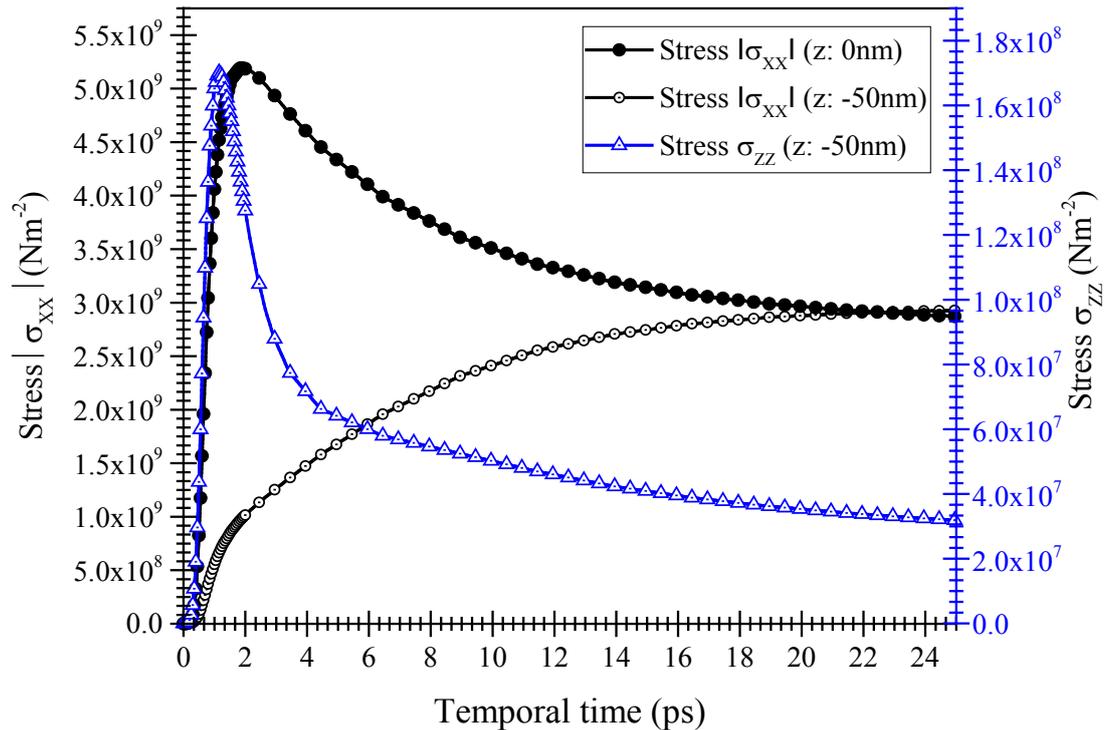


Figure 4.27: Transient nature of the peak orthogonal stress (σ_{ZZ}) the magnitude of the lateral compressive stress (σ_{XX}) at the thin film-glass interface

The predicted peak value of the tensile stress σ_{ZZ} , ($1.68 \times 10^8 \text{ Nm}^{-2}$) was found to be comparatively smaller than the compressive stress σ_{XX} , ($5.21 \times 10^9 \text{ Nm}^{-2}$) generated due to the confined thermal stress in the lateral direction.

It is understood from the numerical simulation and the experimental evidence that due to the high compressive stress in the laser irradiated molybdenum film, the fracture limit for delamination often takes place. Hence the removal of molybdenum takes place prior to the time molybdenum reaches its melting temperature. This observation is supported by the presence of fracture fragments Figure 4.10(a) which on close observation does not show any melting (Figure 4.10(b)).

The combination of the tensile and compressive stress results in the fragmentation of molybdenum (shown in the AFM image, Figure 4.13). The model indicates that this happens as follows. The thin film is perturbed and displaced in the vertical direction according to the Gaussian profile of the laser pulse. Following this perturbation, a small component of the high compressive stress, σ_{XX} is then aligned in the vertical direction (σ_{ZZ}). This leads to partial relaxation of the confined stress

which in turn leads to delamination and subsequent fragmentation of the loosely bound molybdenum film from the glass substrate [106].

The simulation also predicts that the peak temperature of the substrate reaches above its melting temperature at the time of 0.9 picoseconds. Although, experimental observation indicates that the melting of the molybdenum and the substrate does not take place. Therefore, the discrepancy between the simulated and experimental results can be interpreted as follows:

1. Removal of molybdenum thin film may take place prior to molybdenum undergoing melting (0.8 picoseconds).
2. The loss of electron by means of the thermionic emission and the photoelectric effect was ignored. These effects reduce the number of electrons available to transfer energy to the cold lattice; as a result, the effective lattice temperature may be less than that predicted by the model. The emission of the electrons by the thermionic effect will be discussed in the chapter discussed in the chapter 5.

Therefore, it is concluded that the removal of the molybdenum take place before the temperature of the lattice reaches its melting temperature (at 0.8 picoseconds). Thus, the melting of the molybdenum and glass was ignored, and the numerical simulation was considered from 0 picosecond to 0.8 picoseconds, at which time the molybdenum undergoes to melting.

A second attempt was made to investigate the evolution of electron (T_e) and lattice temperature (T_l) in molybdenum thin film, using fixed value for the electron-phonon coupling coefficient ($13 \times 10^{16} \text{ Wm}^{-1}\text{K}^{-1}$). Figure 4.28 presents the evolution of transient temperature of the electron and lattice after the interaction of molybdenum thin film with femtosecond laser of wavelength of 1030 nm at an absorbed fluence of 0.1 Jcm^{-2} .

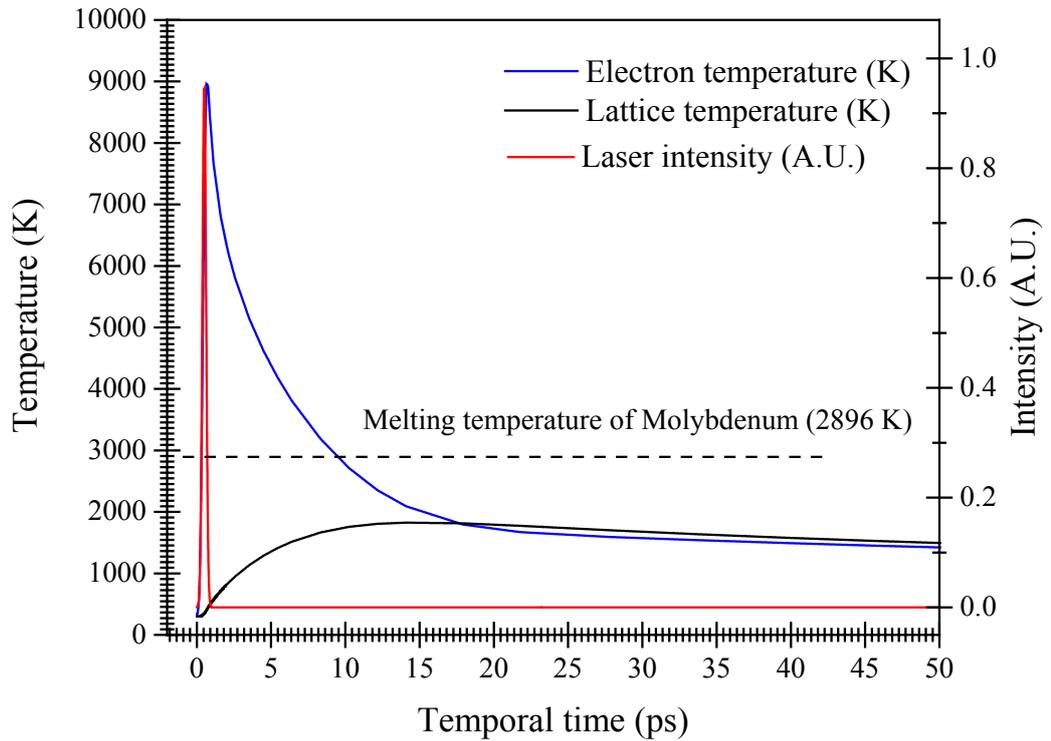


Figure 4.28: The increase of the temperature of electronic (blue line) and lattice (black line) subsystem with a normalised arbitrary laser intensity (red line). The peak value of the laser pulse intensity was taken at 0.5 picoseconds from an arbitrary reference. A temperature independent value of the electron-phonon coupling constant was used for the simulation

The laser pulse has a peak value at 0.5 picoseconds, measured from an arbitrary time (t_0). A rapid increase of the peak temperature of the electronic subsystem (T_e) was observed. The maximum temperature of the electronic subsystem was observed at an additional 0.65 picoseconds from t_0 and was found to be 8956 K. The peak temperature of electron (T_e) and lattice (T_l) reaches to an equilibrium after 17.5 picoseconds from the arbitrary time (t_0). The peak temperature of the lattice at the surface of the film was determined to be 1825 K. The temperature of the thin film-substrate interface reached to its peak value at 17.9 picoseconds and determined to be 1559 K.

Thus, this second model with fixed value of electron-phonon coupling coefficient indicates that the peak temperature of the molybdenum lattice does not exceed the melting temperature (2896 K). This simulation satisfies the experimental evidence which indicates the non-existence of molten molybdenum. Although, the simulation also predicts that the peak temperature of the glass exceeds to its melting temperature (823 K) and contradicts the experimental observation, it is concluded that the removal of molybdenum thin film may take place prior to the time allowed for the peak temperature of glass to its melting temperature.

4.2.3.2. Interaction of thin molybdenum film with short pulse laser using combined heat diffusion and thermal stress modelling

To better understand stress and strain confinement during nanosecond laser processing, a thermal stress model was integrated with the heat diffusion model (section 3.7.1).

Figure 4.29 shows the estimate of two peak temperature profiles on the molybdenum surface, at the centre of the Gaussian laser beam, during nanosecond laser (9 ns at FWHM, wavelength 1064 nm) irradiation using absorbed peak fluences of 0.1 Jcm^{-2} and 0.05 Jcm^{-2} . The red line indicates the normalised incident laser pulse intensity. The peak value of the incident laser pulse was set at 20 ns from an arbitrary reference time.

The simulations predict that the molybdenum surface reaches its peak temperature 4 ns after the laser pulse reaches its maximum intensity. Once the peak temperature has been attained, the temperature in the film decreases as conduction drives the heat to the colder substrate.

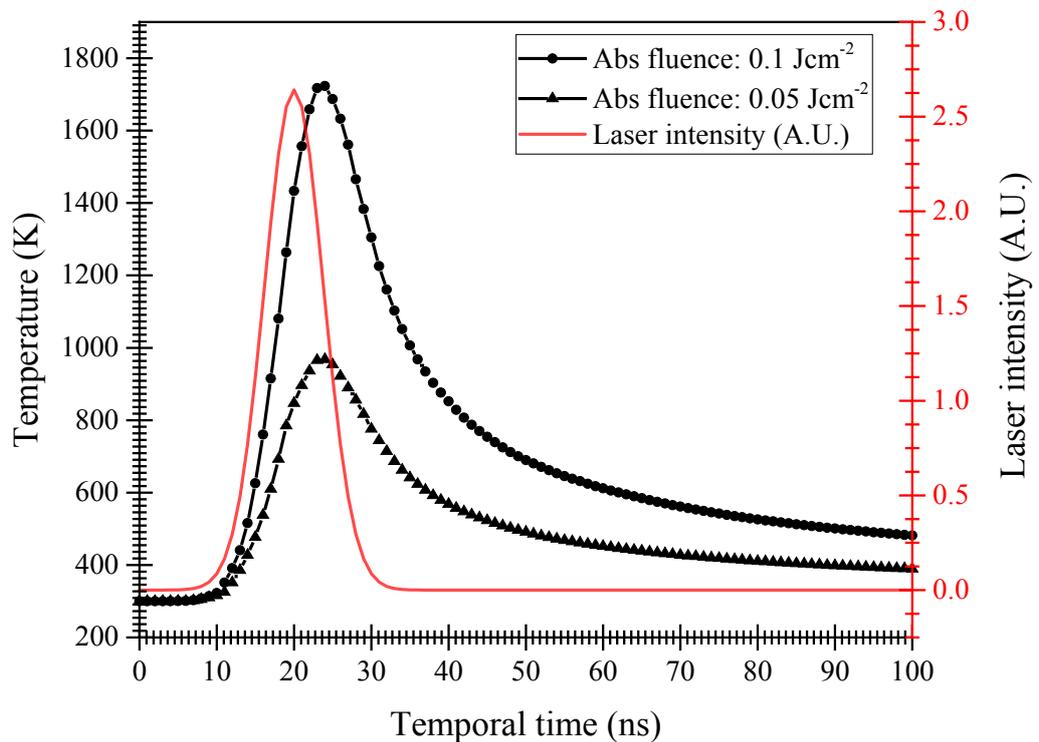


Figure 4.29: Thermal response of lattice temperature at the surface of the molybdenum thin film ($Z=0$) after incident of nanosecond laser of absorbed fluence 0.1 and 0.05 Jcm^{-2} . The peak temperature of the lattice occurs in the film 4 ns after the laser pulse. The peak temperature of the lattice does not exceed the melting temperature of molybdenum.

The simulation suggests that as the film absorbs the laser pulse, the lattice heats up until the temperature of the film reaches the maximum value (1723 K and 968 K at fluences 0.1 and 0.05 Jcm^{-2} , respectively). It is observed that the peak temperature on the surface of the molybdenum film does not exceed the value of its melting temperature (melting point of Molybdenum 2895 K). As the film is much thinner (50 nm) than the large thermal heat diffusion length associated with the nanosecond laser, estimated to be $l_T = \sqrt{D\tau} \sim 700 \text{ nm}$ for $\tau = 9 \text{ ns}$, an almost uniform temperature distribution ($\Delta T < 20 \text{ K}$) is established across the depth of molybdenum film

extending from the surface to the interface with the substrate. The temperature distribution in the depth of the film is shown in the Figure 4.30.

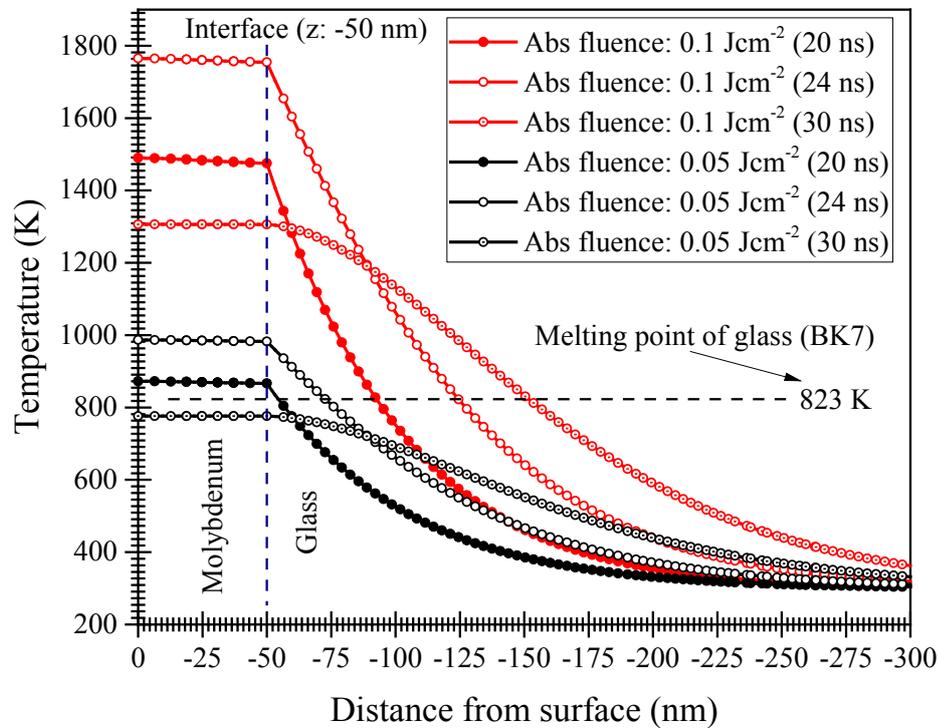


Figure 4.30: The variation in the peak temperature of the lattice for different depths in the molybdenum thin film and near surface region of the glass substrate at different time after the peak pulse was applied to the materials at a reference time of 20 ns duration

Initial observations suggest that the temperature profile in the molybdenum film along the depth is almost constant and a rapid decrease in the temperature is observed at the substrate. Initially, the Gaussian distribution of the laser beam determines the temperature profile at the surface; as the time progressed a minor temperature gradient throughout the depth is observed. The temperature gradient is $\Delta T/\Delta x = 2.85 \times 10^{-10}$ and 0.84×10^{-10} Kelvin/m for the absorbed fluences of 0.1 and 0.05 Jcm^{-2} at 4 ns after the intensity of laser pulse reaches to its maximum value. A small reduction in the temperature at the thin film substrate interface compared with surface is observed as time evolves and this is attributed to the temperature gradient and heat conduction in the radial direction. As time progresses, the temperature of the lattice decreases and reaches towards the initial temperature (300 K). Therefore, as a result, a decrease of the slope of the temperature of the substrate is observed with the distance from the surface (as seen among the line shapes of the temperature). Despite this, the temperature at molybdenum-glass interface exceeds the melting temperature of the glass substrate (annealing point of BK7: 823K) [203]. Therefore, in nanosecond case, it is expected that the glass can reach high temperatures, 1754 K and 982 K at fluences of 0.1 and 0.05 Jcm^{-2} , way in excess of its molten temperatures with similar to that observed in the film. The high temperature achieved in the glass suggests that the phase change (melting) of the glass at the film-substrate interface disrupts the attachment of the thin film

to the substrate. This hypothesis is supported by evidence obtained using the AFM on nanosecond produced craters. Figure 4.31 shows that the surface of the glass materials is clearly observed to have been reconstructed in the centre of the crater of molybdenum thin film above the threshold fluence.

Heating of molybdenum film results in the expansion of molybdenum both in planar direction and out of plane direction. As in the case of femtosecond laser pulses, a large tensile compressive stress σ_{XX} develops in the film as the material is not allowed to expand along the spatial direction of the laser pulse due to the confinement of the surrounding cold lattice. Fast relaxation of this high compressive stress makes the film fragile.

Figure 4.31 shows the time-dependent compressive stress (magnitude) at the film surface ($X = 0, Y = 0, Z = 0$) and at the thin film-substrate interface ($X = 0, Y = 0, Z = -50$ nm) at fluence levels 0.1 Jcm^{-2} and 0.05 Jcm^{-2} . The peak values of the compressive stress σ_{XX} is shown in the Figure 4.31.

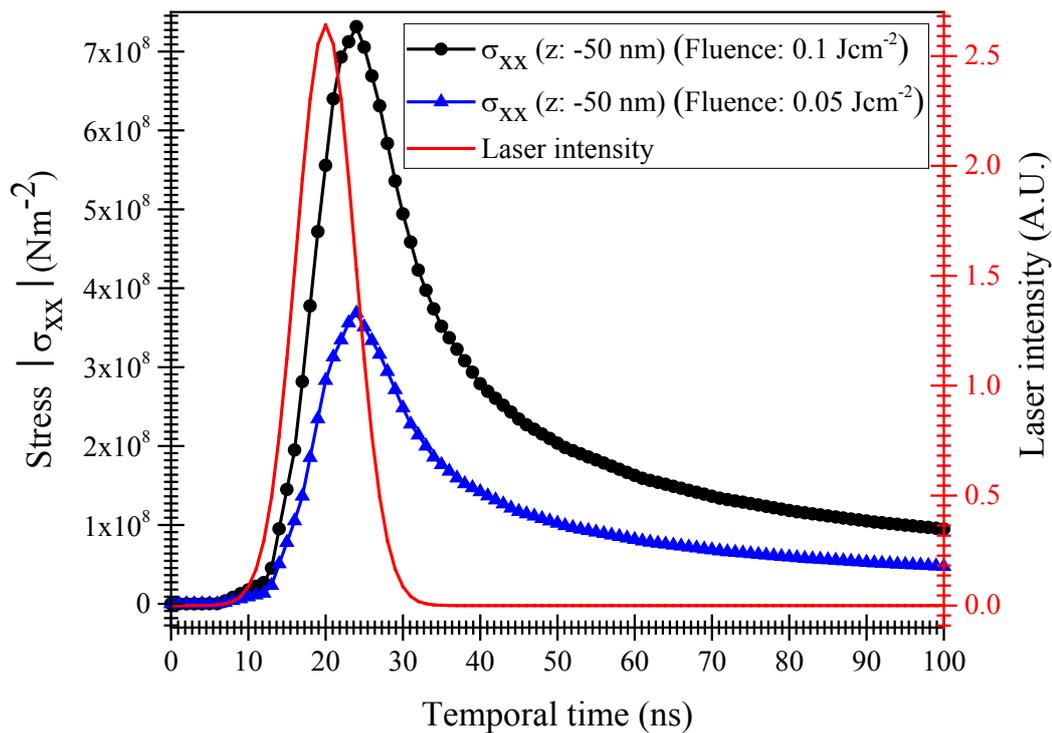


Figure 4.31: Magnitude of the compressive stress (σ_{XX}) at the film surface and interface during nanosecond laser ablation

The overall increase of the magnitude of the compressive stress σ_{XX} follows the temporal behaviour of peak temperature of the molybdenum film and glass substrate. Maximum values of $|\sigma_{XX}|$ are observed at 24 ns at the interface for both fluences and measured to be $0.73 \times 10^9 \text{ Nm}^{-2}$ (0.1 Jcm^{-2}) and $0.39 \times 10^9 \text{ Nm}^{-2}$ (0.05 Jcm^{-2}), respectively; this is the time when the lattice

temperature reaches to its maximum value (1723 K and 968 K at fluences 0.1 and 0.05 Jcm⁻², respectively).

Expansion of the molybdenum film and the glass in vertical direction leads to an outer plane deformation in the molybdenum and glass substrate. The higher coefficient of thermal expansion of glass ($8.6 \times 10^{-6} \text{ K}^{-1}$ at 300 K) compared to molybdenum ($4.8 \times 10^{-6} \text{ K}^{-1}$ at 300 K) results in a deformed interface [191, 197, 204]. The thermal expansion of the glass in the vertical direction is immediate and leads to strain (ϵ_{ZZ}) in the glass and an upward expansion takes place, prior to the molten phase being established. The expansion of glass exerts an upward pressure against the molybdenum film. The upward pressure is the reason for a vertical stress σ_{ZZ} .

Figure 4.32 presents the stress, σ_{ZZ} and strain ϵ_{ZZ} , in the perpendicular direction at the interface of the film surface and the substrate,

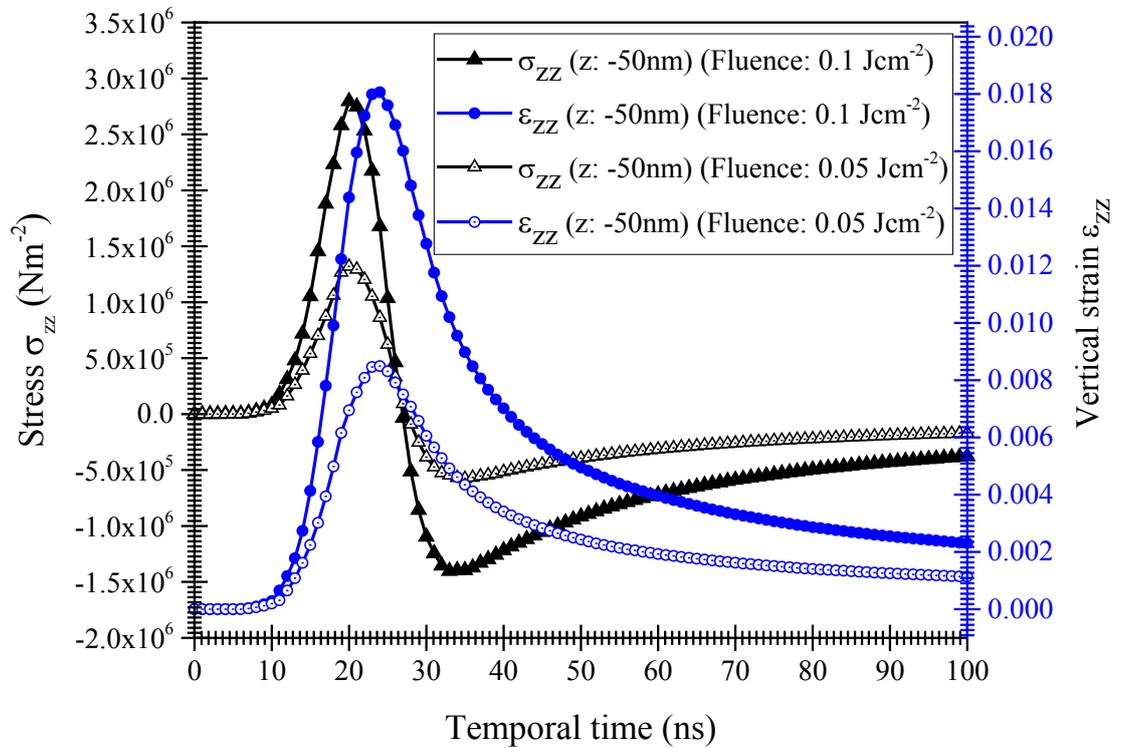


Figure 4.32: Transient behaviour of expansion stress σ_{ZZ} and strain ϵ_{ZZ} at molybdenum film and the interface during nanosecond laser ablation. The peak tensile stress was observed 4 ns prior to the peak vertical strain

The adhesion of the molybdenum layer to the substrate is greatly reduced as soon as the temperature of glass increases towards its melting point and becomes fluid. The peak value of σ_{ZZ} (at the surface of the glass $X = 0, Y = 0, Z = -50 \text{ nm}$) was found at 20 ns ($2.8 \times 10^6 \text{ Nm}^{-2}$ at peak fluence: 0.1 Jcm⁻² and $1.3 \times 10^6 \text{ Nm}^{-2}$ at peak fluence: 0.05 Jcm⁻²). It was estimated that the tensile stress along vertical direction (σ_{ZZ}) is smaller than the compressive stress (σ_{XX}), as the thickness of the film (50 nm) is very thin compared with the lateral dimension of the film (0.7 mm). Also, it was noticed that the compressive stress (σ_{XX}) at the film near the interface ($X = 0, Y = 0, Z = -50 \text{ nm}$) is larger than that at the top of film surface ($X = 0, Y = 0, Z = 0$) used in this

study. Similarly, the expansion strain, ϵ_{ZZ} has peak values at the interface between molybdenum and glass substrate. The associated peak interfacial strain (ϵ_{ZZ}) with the molybdenum film was found to be 0.018 and 0.008 at absorbed fluence of 0.1 Jcm^{-2} and 0.05 Jcm^{-2} at the centre of the laser spot ($X = 0, Y = 0, Z = -50 \text{ nm}$). It was also found that the stress and strain distribute radially with the Gaussian laser intensity distribution.

Moreover, the higher coefficient of thermal expansion of glass compared to molybdenum results in thermal expansion of glass at the interface. The thermal expansion of the glass leads to strain (ϵ_{ZZ}) at the glass and an upward expansion takes place. The expansion of glass exerts an upward pressure against the molybdenum film. The upward pressure is the reason for a vertical stress σ_{ZZ} . The upward stress on the glass-molybdenum interface exerts pressure on the film and delamination of the film is observed during short pulse laser ablation [37, 100].

The inner diameter observed on the glass substrate was measured by an optical microscope operating in a transmission microscope in a phase contrast mode. The inner diameter at the fluences of 0.082, 0.095, 0.108, 0.123, 0.138 and 0.166 Jcm^{-2} . This inner diameter on the glass substrate was then compared with the numerically determined modified area (the area where the glass exceeds its melting temperature) of the glass.

The diameter of the modified area are estimated and tabulated in the Table 4.7. These diameters are comparable with the experimentally determined inner diameter on the glass substrate. This confirms the modified area on the substrate results from melting of glass by nanosecond laser irradiation.

Table 4.7: Comparison of the inner diameter on the glass substrate measured by an optical microscope with the numerically estimated diameter where the temperature of glass reaches its melting temperature

| Peak absorbed fluence (Jcm^{-2}) | Inner diameter (μm) estimated using | |
|---|--|-----------------------------|
| | Optical microscope | Numerical simulation |
| 0.082 | 13.60 ± 0.10 | 13.21 |
| 0.095 | 17.90 ± 0.07 | 17.66 |
| 0.108 | 23.78 ± 0.08 | 24.35 |
| 0.123 | 30.21 ± 0.06 | 29.65 |
| 0.138 | 34.21 ± 0.06 | 33.77 |
| 0.166 | 41.14 ± 0.03 | 41.56 |

4.3. Chapter conclusions

This chapter consists of the study of the laser-material interaction of molybdenum bulk (thickness $250 \mu\text{m}$) and thin film (thickness 50 nm) using lasers of femtosecond (fundamental: 500 fs , wavelength 1030 nm) and nanosecond (fundamental: 9 ns , wavelength 1064 nm) pulse durations, across a range of wavelengths using optical beam delivery system. The absorbed intensity of the incident laser pulse in the molybdenum bulk and thin film was estimated using an integrating sphere.

(a) Interaction of bulk molybdenum with femtosecond laser

- It is estimated that the laser intensity absorbed by the molybdenum is dependent on the wavelength of the incident laser pulse. Almost 65, 55 and 54 percent of the incident laser pulse was found to reflect from the molybdenum bulk sample at wavelength of 1030, 515 and 343 nm, respectively. A negligible transmission of incident laser intensity is observed from the molybdenum bulk samples.
- The interaction of an ultrashort laser pulse with a molybdenum bulk sample was investigated at different peak absorbed fluences (0.1 to 3 Jcm⁻²). The ablation threshold fluence of the molybdenum bulk sample was calculated using three different wavelengths of 1030, 515 and 343 nm and estimated to be 0.16 ± 0.01 , 0.17 ± 0.001 and 0.12 ± 0.01 Jcm⁻², respectively.
- Femtosecond laser interaction with molybdenum bulk at different peak absorbed fluences (0.1, 0.15, 0.25, 0.3, 0.4 and 0.5 Jcm⁻²) was studied numerically using finite element method (FEM). The peak absorbed fluence required to ablate a molybdenum by femtosecond laser source was estimated using numerical simulation. The experimental observations and the expected results from the numerical simulation were compared. It is predicted that the rapid thermalisation of hot electrons into the lattice by electron-phonon coupling during interaction of ultrashort laser pulse with molybdenum results in a highly compressive stress. Relaxation of the compressive stress results in the spallation and fracture of the molybdenum at absorbed fluences and occurs at energy densities less than the values predicted by traditional melting (0.16 Jcm⁻²) and evaporative phase changes alone.

(b) Interaction of thin film with femtosecond laser

- Almost 60.3, 51.6 and 51.5% of incident laser intensity was found to reflect from the thin molybdenum film at laser wavelength of 1030, 515 and 343 nm, respectively. It was observed that the fraction of transmitted laser intensity increases with increasing incident laser wavelength. It was observed that 7.9, 4.1 and 2.7% of laser intensity transmit through molybdenum thin film and the substrate at incident laser wavelength of 1030, 515 and 343 nm, respectively. The reflected and transmitted fraction of incident laser intensity were used to determine the pulse energy absorbed by molybdenum thin film.
- It was estimated that the fluence required to remove molybdenum film from the glass substrate is sufficiently smaller than those for bulk molybdenum sample. The ablation threshold of the molybdenum thin film was measured at the femtosecond laser wavelengths of 1030, 515 and 343 nm and determined to be 0.018 ± 0.001 , 0.021 ± 0.001 and 0.016 ± 0.001 Jcm⁻², respectively.
- When a laser of certain wavelength is incident on a sample surface, electrons in a particular energy band absorb the laser energy and is being excited to an upper energy state. Electrons respond differently to different incident laser wavelengths. We expect that electrons absorb the UV energy interband absorption; IR energy is absorbed by intra-band absorption. The UV absorption is expected to be more efficient, resulting in a rapid increase of lattice energy which ultimately results in mechanical fracture of the thin film. The coupling of a higher amount of UV laser energy to the molybdenum lattice results in lowering of damage threshold of molybdenum.

- Micro-structuring of 50 nm thick molybdenum thin film was carried out using a femtosecond laser pulse at wavelengths of 1030, 515, and 343 nm. An increase of the square of the crater diameter was observed with increasing laser fluence. ‘Peeling off’ of molybdenum thin film was observed at fluences above the ablation threshold. Several loosely adhered particles were found around the laser ablated crater. Number of fragmented particles were found to increase with increasing laser fluence.
- Delamination of the molybdenum thin film was observed at various absorbed fluences. AFM and SEM analysis of the ablated craters indicates complete removal of molybdenum thin film with minimal substrate damage. At low fluence, brittle fracture of thin molybdenum film was observed using AFM microscopy technique.
- At a fluence (0.1 Jcm^{-2}) above the ablation threshold, the laser-molybdenum interaction was understood numerically using a computational model based on two temperature model integrated with the thermal stress. Two different approaches were conducted using two separate values of electron-phonon coupling coefficient.
- A varying electron-phonon coupling constant [150] depends upon the temperature of electronic subsystem was used in the first approach. The free electrons present in the molybdenum film absorb the photon energy of the laser and a high electronic temperature establishes. The electron temperature couples to molybdenum lattice by means of electron-phonon coupling. The temperature of the molybdenum lattice reaches an equilibrium with electron temperature after the electron-phonon coupling time. Also, the model predicts that the peak temperature of the molybdenum lattice reaches to the melting temperature of molybdenum (2896 K). The heat developed in the molybdenum lattice conducts laterally and vertically towards the substrate. A high compressive stress (σ_{xx}) develops on the molybdenum because of the temperature confinement of the molybdenum crater (Figure 4.24). The stress exerts an expansion force acts both laterally and vertically in directions parallel and perpendicular across the thin film-substrate interface (Figure 4.25). The lattice heating of molybdenum thin film also results in the displacement of film along vertical direction. This expansion of the material leads to a tensile stress (σ_{zz}) at the thin film substrate interface in the upward direction (Figure 4.26). The combination of the tensile stress and the relaxation of this highly compressive stress in molybdenum film results in the deformation (Figure 4.11) and the removal of the molybdenum thin film from the glass substrate.
- A temperature independent electron-phonon coupling term ($13.6 \times 10^{16} \text{ Wm}^{-1}\text{K}^{-1}$) was used in the second attempt to understand the laser molybdenum interaction. The second simulation confirms that the temperature of the molybdenum does not exceed its melting temperature (Figure 4.27) although the temperature of glass reaches to its melting temperature at the peak fluence of 0.1 Jcm^{-2} . It is predicted that the removal of molybdenum thin film take place prior to the glass substrate exceeds the melting temperature.
- The constant electron-phonon coupling coefficient shows a better fit of the experimental data. Simulation of lattice temperature using the variable electron phonon coupling factor results in the peak temperature of molybdenum rising above its melting temperature. This is contrary to the experimental evidence. The strong variable electron-phonon coupling

coefficient constant results in a rapid increase of the lattice temperature, which in turn leads to an increase in the peak temperature of the lattice. The variable electric phonon coupling factor was taken from the theoretical work carried by Leonid V. Zhigilei et al. The approach proposed by Zhigilei seeks to offer a more accurate response than that obtained using a constant value. The variable electron phonon coupling factor for molybdenum depends upon several factors including electron density of states, electron heat capacity, Debye temperature, number density of electron, and electron-phonon coupling time. These parameters may vary from those associated with the different experimental samples. In this present work of study, we did not have the capacity to change such parameters used by Zhigilei's model. Thus, it is likely that the variable electron-phonon coupling constant factor used is itself an approximation.

Hence, our findings are that the constant electron-phonon coupling factor is a better approximation for describing the femtosecond laser thin film molybdenum interaction when compared with considering a variable constant electron-phonon coupling factor.

(c) Interaction of molybdenum thin film nanosecond laser

- The amount of laser intensity absorbed by the molybdenum thin film was determined using the integrating sphere. It was estimated that the (23 ± 1) , (39 ± 1) and (44 ± 1) % of incident laser intensity is absorbed by the molybdenum thin film at wavelength of 1064, 532 and 355 nm, respectively.
- Molybdenum thin film interaction with a nanosecond laser was studied using wavelengths of 1064, 532 and 355 nm wavelengths at different peak absorbed fluences. Similar to femtosecond case, peak absorbed ablation threshold was determined to be 0.043, 0.012 and 0.026 Jcm⁻², for the laser wavelength of 1064, 532 and 355 nm, respectively. Fragmentation of the molybdenum thin film (Figure 4.19) was observed during nanosecond laser (at all wavelengths) interaction with molybdenum film. Interaction of nanosecond laser pulse with molybdenum thin film results in a complete removal of the film with significant damage on the surface of the glass (Figure 4.21).
- Nanosecond laser-molybdenum thin film interaction with nanosecond laser source was understood, numerically, using a heat diffusion model integrated with thermally assisted stress model. A computational simulation was taken place using peak absorbed fluence 0.1 and 0.05 Jcm⁻² at 1064 nm laser wavelength.
- The simulation predicts that almost a uniform temperature distribution establishes from the top surface of molybdenum to the molybdenum/glass interface of the molybdenum thin film (Figure 4.29). The molybdenum thin film reaches to its peak temperature 4 ns after the nanosecond laser pulse reaches to its maximum intensity. At both the fluence, the peak temperature of the molybdenum stays under the melting point of molybdenum. While, the peak temperature of the substrate exceeds the melting temperature of glass (823 K).
- The simulation also predicts that a high compressive stress (σ_{XX}) is established at the laser irradiated area of the thin film (Figure 4.30). This high compressive stress results in fragmentation in the molybdenum thin film (Figure 4.30). Higher thermal expansion of glass than molybdenum leads to a vertical strain (ϵ_{ZZ}) in the glass (Figure 4.31). This vertical strain result is a tensile stress (σ_{ZZ}) formed in the thin film-glass interface. The

tensile deformation on the molybdenum thin film from the molybdenum/glass interface results in the removal of molybdenum film from the glass substrate (Figure 4.19).

Chapter 5: Real-time imaging of laser-molybdenum interaction

The previous chapter provides an understanding of ablation mechanisms in molybdenum bulk and thin films at atmospheric pressure by short and ultra-short laser pulse interactions using three different wavelengths. The findings from the previous chapter are given as follows:

1. The ablation of a molybdenum bulk sample by femtosecond laser pulses mainly governed by thermo-mechanical stress (chapter 4, section 4.1.3.1).
2. The ablation of 50 nm thick molybdenum thin film from a glass substrate upon treatment by an ultra-short femtosecond pulse laser is mainly governed by thermally generated mechanical stress (chapter 4, section 4.2.3.1). It was found that at low fluence ultra-short laser pulses resulted in a minimal damage to the substrate (section 4.2.2.1).
3. The ablation of 50 nm thick molybdenum thin film by a nanosecond laser pulse is most likely due to thermally assisted stress removal triggered by the expansion of the substrate (chapter 4, section 4.2.3.2). An incident nanosecond laser pulse at fluence higher than the ablation threshold provides significant damage to the substrate (section 4.2.2.2).
4. It was observed that the interaction of the ultra-short and short laser pulses with molybdenum have different ablation thresholds which depends on the incident laser wavelength.

An attempt is made in this chapter to apply real-time monitoring techniques to understand the ablation mechanism for bulk and thin film molybdenum samples. The instrumental setup for the time-resolved experiments by ultra-short and short pulse laser were previously discussed in the materials and method section (section 3.6). The main motivation of these experiments follows:

- a. To visualise the material removal effects for bulk molybdenum by an ultrashort pulse laser at 1030, 515 and 343 nm wavelengths.
- b. To interpret the behaviour of ejected materials by ultra-short and short pulse ablation at different fluences.
- c. To understand thin film removal/delamination from the glass substrate by single short and ultra-short pulse laser.
- d. To differentiate the ablation mechanism of molybdenum thin film by ultrashort and short laser pulses.
- e. To understand the interaction mechanism of molybdenum thin film with ultrashort and short pulsed laser sources at IR, green and UV wavelengths; that leads to different values of ablation threshold.

In order to accomplish these objectives, an online diagnostic measurement of the laser-generated plasma plume was performed at different fluence values. First, second, and third harmonics of single pulse femtosecond (FWHM: 500 femtoseconds, fundamental 1030 nm) and nanosecond (FWHM: 9 nanoseconds, fundamental 1064 nm) lasers were used separately as the laser source. To understand the spectral nature of laser generated plasma plume, laser induced breakdown spectroscopy (LIBS) was first performed. The final section consists of spatial imaging of ejected

components during femtosecond and nanosecond laser ablation at various wavelengths using different fluence values.

Optical emission from the plasma plume

As described in the theory chapter (section 2.5.6), the absorption of light energy in the metal takes place by the free electrons via inverse Bremsstrahlung process [60]. As a result, the kinetic energy of the heated electrons increases, and they collide via electron-electron scattering. A fraction of these highly energised electrons can emit from the near-surface metal by thermionic electron emission. The remaining electrons collide with the lattice and electron-lattice coupling takes place. The lattice heating by the laser source result in ablation. The removed material consists of electrons, ions, clusters and neutral fragments or particles. The removed constituents contribute to a plasma plume. In addition to the initial excitation provided by the laser ablation process, the species are further excited by collisions in the plasma plume. De-excitation of the electrons leads to optical emission from the plasma plume. Such optical emission from such atomic transitions is detected in this work.

The ground state of the molybdenum is [Kr] 4d⁵ 5s and is termed as ⁷S₃. It is observed that the spectral line emission in non-ionised molybdenum (Mo I) is most significant in the green region. Three significant lines observed in the line emission of Mo I are 550.6493, 553.3031 and 557.0444 nm [205, 206]. The electronic configuration of these three lines are given below [205-207]:

Table 5.1: Term designation and energy of the upper and lower electronic levels with transition probability of neutral molybdenum (Mo I) atom [6]

| Observed wavelength (nm) | Lower electronic level (^{2S+1}L_J) | Upper electronic level (^{2S+1}L_J) | Energy of the lower state (eV) | Energy of the upper state (eV) | Transition probability (s⁻¹) |
|---------------------------------|--|--|---------------------------------------|---------------------------------------|--|
| 550.6493 | ⁵ S ₂ | ⁵ P ₃ | 1.33510 | 3.58608 | 3.61×10 ⁷ |
| 553.3031 | ⁵ S ₂ | ⁵ P ₂ | 1.33510 | 3.57528 | 3.72×10 ⁷ |
| 557.0444 | ⁵ S ₂ | ⁵ P ₁ | 1.33510 | 3.56024 | 3.20×10 ⁷ |

Here, ^{2S+1}L_J is the term designation of a particular energy level [6]. **L** and **S** are total orbital angular momentum and spin quantum number, respectively, determined from the configuration of electrons of the unfilled electronic level. The total angular momentum, **J** is determined from the vector addition of **L** and **S** (**J=L+S**). For the total angular momentum 0, 1, 2 and 3, the total orbital angular momentum **L** is written as S, P, D and F, respectively.

Similarly, the spectral emission from the singly ionised molybdenum (Mo II) is observed mostly at the UV region of the electromagnetic spectrum. The electronic configuration of the ground state of the singly ionised molybdenum atom is [Kr] 4d⁵ and termed as ⁶S_{5/2} [208]. The three major spectroscopic transitions observed for the transition of Mo II and given below [207, 209]:

Table 5.2: Term designation and energy of the upper and lower electronic levels with transition probability of singly ionised molybdenum atom (Mo II)

| Observed wavelength (nm) | Lower electronic level ($^{2S+1}L_J$) | Upper electronic level ($^{2S+1}L_J$) | Energy of the lower state (eV) | Energy of the upper state (eV) | Transition probability (s^{-1}) |
|---------------------------------|---|---|---------------------------------------|---------------------------------------|---|
| 201.511 | $^6S_{5/2}$ | $^6P_{5/2}$ | 0 | 6.15070 | 0.88×10^8 |
| 202.031 | $^6S_{5/2}$ | $^6P_{7/2}$ | 0 | 6.13487 | 2.15×10^8 |
| 203.845 | $^6S_{5/2}$ | $^6P_{3/2}$ | 0 | 6.08029 | 1.84×10^8 |

Online diagnostics:

The origin of the various optical emission from the laser-produced plasma were described previously in the theory chapter (Section 1.5). In short, during laser ablation, if the incident laser energy exceeds a material's breakdown threshold, the sample becomes dissociated, atomised and partially ionised to form a high-temperature and high-electron-density plasma [210]. The optical emission from the high electron density micro plasma consists of atomic emission (characteristic of neutral and ionised elements) and the black-body radiation (depends upon the overall temperature of the plasma plume). This micro plasma was analysed by optical emission spectrometry (Laser induced breakdown spectroscopy-LIBS). Spectrally and temporally resolved detection of the specific atomic emission reveals information about the elemental composition of the sample.

5.1. Spectral imaging:

The purpose of the spectral imaging of the laser produced plasma plume was to understand the origin of the light in the plume. This initial work was performed using lasers at infrared wavelengths. The exposure time was fixed at 1 μs and centred at 0.7 μs . At this time regime, the plasma plume is assumed to be in local thermal equilibrium (LTE) condition.

For the plasma to be in a complete thermodynamic equilibrium, all the processes are balanced and characterised by a single temperature [211]. Therefore, ideally, the process of excitation of atoms by collisions with electrons is equal to the reverse deactivation process, collisional ionisation is equal to three-body collisional recombination, and radiation emitted is equal to the radiation absorbed [211].

When collision dominates and the same laws describing full thermodynamic equilibrium apply, but radiation disequilibrium exists, the system is treated as complete thermodynamic equilibrium. Considering that radiative transitions between low-lying energy levels (resonance transitions) are characterised by high values of the Einstein coefficient of spontaneous emission, these levels are depopulated much faster than correspondingly higher levels and are therefore more prone to radiative disequilibrium. If these levels are excluded, i.e., only levels above a certain main quantum number are considered in defining the requirements for attaining equilibrium. In such

cases we speak of partial local thermodynamic equilibrium (LTE). This is the common situation with most plasma sources [212].

A Maxwell-Boltzmann electron energy distribution establishes at the LTE [115, 122, 212]. At this condition, the number density of electrons is less than a critical value, imposed by the constraints that the mean difference between thermal electrons should be less than the de Broglie wavelength.

The spectroscopic measurements were performed at the LTE condition. In the spectroscopic study, the broadening of the spectral lines is important as it contains information of the emitter and the surrounding plume. The total broadening in a spectroscopic measurement arises from several broadening mechanisms, such as,

(a) Natural broadening:

Natural broadening arises due to the spontaneous emission when the unperturbed energy level has a finite lifetime. Natural broadening is largest when one of the two levels is dipole-coupled to the ground state. Even in this case, it is usually negligible (of the order of 10^{-4} nm). Thus, in the case of spectral imaging of laser produced molybdenum plasma plume, the natural broadening was not considered.

(b) Doppler broadening:

Doppler broadening is caused by random thermal motion of the emitter. The thermal motion of the absorbing atoms leads to a variation of absorbed frequency due to the Doppler effect. The Doppler broadening at the of a spectral line is Gaussian in nature and the FWHM is estimated using the following relationship,

$$\Delta\lambda_{1/2} = 2\lambda \sqrt{\frac{2kT_e \ln 2}{mc^2}} \quad (27)$$

where, λ is the wavelength (nm) of the spectral line, k is the Boltzmann constant, T_e is the electronic temperature (K), m is the atomic mass (kg) and c is the velocity of light (ms^{-1}).

For neutral molybdenum (Mo-I) the spectral line at 530.65, 553.31 and 557.04 nm, the maximum electronic temperature was estimated to be 20000 K and the corresponding Doppler width is estimated to be 0.0054, 0.0056 and 0.0057 nm. This shows that the contribution of Doppler broadening is very small and thus it can be neglected.

(c) Stark broadening:

Stark broadening plays a key role in LIBS measurement [213]. Predominantly, it is used to evaluate the number density of electrons [115, 214, 215]. The emitting species in the plasma (atoms and ions) are placed under the influence of an electric field by fast-moving electrons and relatively slow-moving ions. Because of the charge separation between electrons and ions splitting of the energy levels take place by the quasi-static perturbed electric field. The lines those arises from the transitions between the split levels are then broadened and the overlap because of the electron collisions.

(d) Instrumental broadening:

Usually, the instrumental broadening is experimentally found by scanning the emission profile of a line emitted by a low-pressure discharge (hollow cathode lamp) or a laser (usually He-Ne). The instrumental broadening is described by a Lorentzian profile [216].

Instrumental broadening is almost negligible at early delay time (at LTE) when the Stark broadening dominates [211]. The instrumental broadening becomes more significant later in the time during plasma evolution as the number density of electrons decays. The instrumental broadening can be measured by the deconvolution method [216, 217].

The broadening due to instrument was considered negligible in the present work. It is assumed that all the broadening takes place due to the Stark broadening effect.

Spectral imaging of bulk and thin film molybdenum samples was performed using a combination of a spectrometer (SHAMROCK 303) and Andor iStar ICCD camera (iStar 334T). Prior to all the experiments, wavelength [218] and intensity calibration [219] of the spectrometer was performed using a mercury spectral lamp and a standard broadband white light source, respectively. Free space optics were used to focus the plasma plume on the spectrometer entrance mirror. The groove density of the two separate grating (1200 lines/mm and 300 lines/mm, blaze wavelength: 500 nm) used for the spectroscopic measurements. The grating 1200 and 300 provides the spectral resolution of 0.08 and 0.33 nm. The full vertical binning of the detected spectral image provides the optical spectrum of emission. Full vertical binning (1:1) was performed using the camera software (Andor SOLIS) for the exposed area of the camera chip.

The wavelength calibration of the spectrometer was performed to correct the systematic deviation of wavelength from the actual value. This was done by comparing the experimentally detected emission lines from a mercury lamp with the corresponding wavelengths obtained from the literature [218, 220].

The response of the spectral system depends upon several factors. These include the detector response, grating efficiency and spectral response of coatings of the mirrors and lenses. A standard white light source (Thorlabs, MWWHL3) was used to correct the intensity in the interval 340 nm to 820 nm [221]. The Figure 5.1(a) presents the standard response and measured light source intensity using the grating 300 lines/mm while, Figure 5.1(b) provides the wavelength dependent intensity response curve.

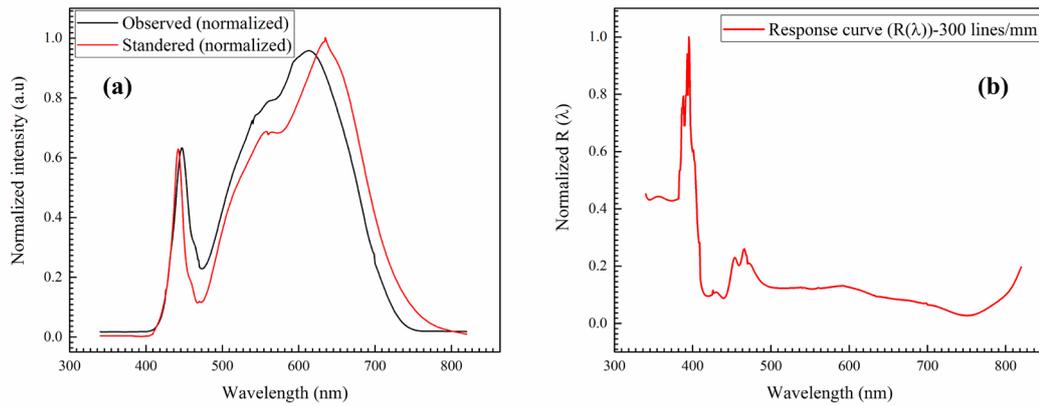


Figure 5.1: Wavelength-dependent intensity response calibration of Andor iStar ICCD and spectrometer, (a) standard and observed intensity of standard light source was used to determine response curve (b) of the spectrometer and Andor iStar ICCD.

The temperature of the detector was set to be at -30° C to reduce noise (dark noise) [222]. The background noise was subtracted by taking the background and reference spectra [223]. The gate width (GW) and the gain of the multi-channel plate (MCP) image intensifier were adjusted from the Andor software interface, to achieve an optimal signal to noise ratio. The camera was gated for single pulse laser exposure.

The spectral response of the laser produced plasma plume was studied at different fluences using a laser at the infrared wavelength. Single laser pulses of femtosecond and nanosecond duration were used as the laser source. The exposure time used on the camera was 1000 ns; while this did not permit the dynamics of ejected plasma plume to be fully investigated, it allowed the principal spectral lines to be assessed. The various peaks of the spectroscopic data were identified from the NIST (National Institute of Standards and Technology) atomic spectra database [224]. The slit width at the entrance to the spectrometer was kept at $150\ \mu\text{m}$ to avoid any unnecessary broadening of peaks at the detector plane.

It is found from the literature that the nature of the plasma at early times (several nanoseconds) are very unstable [225, 226]. This phase of the plasma is characterised by high temperatures (over 10,000 K) and high pressures [227]. The high temperature of the plasma gives rise to black body emission from the plasma [228]. Also, the initial high pressure of the plasma results in spectrally broadened features.

The spectral emission from transitions from electronic states occur after a certain time delay. The recombination of electrons and ions and neutrals are followed by the plasma cooling [225]. Thus, it is important to choose an appropriate delay time to collect the emission due to atomic transitions. In order to avoid such temporal broadening, the spectral measurement was performed after 200 ns (delay time) from when the peak of the laser pulse incident on the sample surface.

The spectral behaviour of the femtosecond and nanosecond laser-induced plasma plume was studied at this time scale to understand the dependence of the atomic emission with the incident laser fluence. The spectral response of the plasma plume was performed for three cases:

- a. Ultra-short pulse laser ablation of molybdenum bulk sample

- b. Ultra-short pulse laser ablation of molybdenum thin film, and
- c. Short pulse laser ablation of molybdenum thin film.

5.1.1. Spectral imaging of ultra-short pulse laser ablation of molybdenum bulk

Spectral imaging of the ablated plume was performed using 1030 nm femtosecond laser. The spot diameter ($2\omega_0$) of the laser beam on the bulk molybdenum surface was calculated using Liu's method discussed earlier (chapter 3, section 3.4.3) and determined to 15.3 μm . The MCP gain used for the spectral imaging of plasma plume was set at 1200 from the Andor software interface. The absorbed fluence used in the spectroscopic experiments were higher than the previously identified melting threshold fluence ($0.16 \pm 0.01 \text{ Jcm}^{-2}$) of the molybdenum (Table 3.4). The different peak values of the absorbed laser fluence are indicated in Figure 5.2.

Figure 5.2 presents the wavelength dependence of the spectral emission from the plasma plume for a range between 546.6 nm and 577.3 nm and centred at 562 nm at different absorbed fluences. In this case, measurements were performed using the grating with 500 lines/mm (groove density) and at blaze wavelength of 500 nm. Peaks were identified using the NIST database [224, 226]. The spectral features arise from emission by discrete molybdenum neutral atoms. The three most intense peaks 550.65 nm, 553.31 nm and 557.04 nm correspond the atomic transition from the electronic configuration $^5\text{P}_3$ to $^5\text{S}_2$, $^5\text{P}_2$ to $^5\text{S}_2$ and $^5\text{P}_1$ to $^5\text{S}_2$, respectively 3.61×10^7 , 3.72×10^7 and $3.30 \times 10^7 \text{ s}^{-1}$ correspond transitions in non-ionised molybdenum (Mo I) [205, 224, 226].

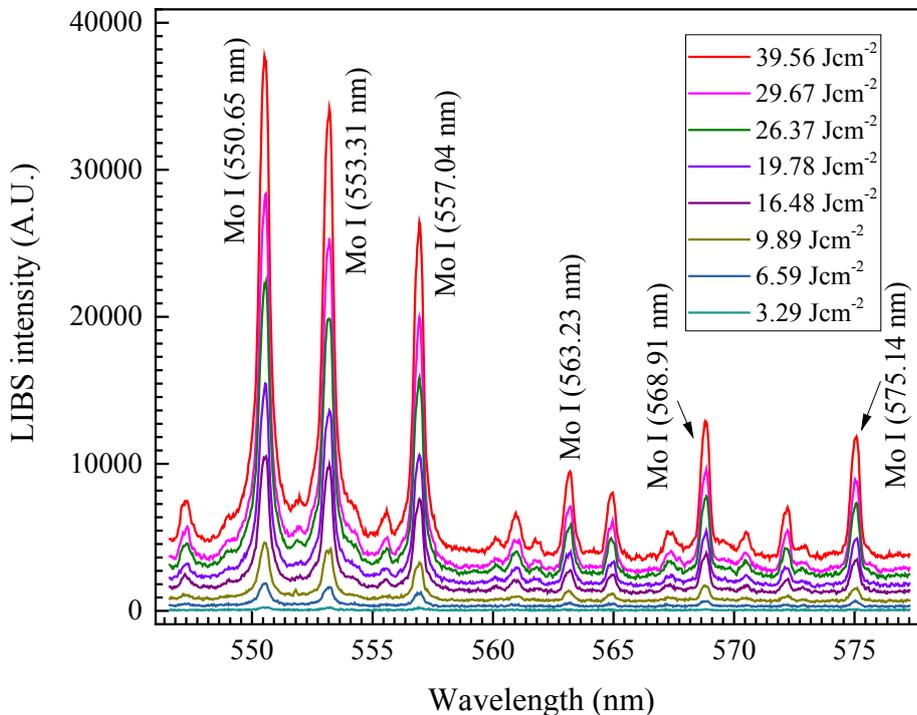


Figure 5.2: Laser-induced breakdown spectroscopy (LIBS) intensities of 1030 nm femtosecond laser ablated molybdenum bulk sample at different absorbed fluences

The other three peaks at 563.25, 568.91 and 575.14 nm corresponds atomic transition from the atomic level 5P_1 to 5D_0 , 5P_1 to 5D_1 and 5P_2 to 5D_2 , respectively. Initial observation suggests that the peak intensity of the laser induced spectral emission increases with increasing laser fluence.

The broadening of the intensity LIBS peaks mainly caused by the Stark broadening (section 5.1(c)) and the spectral curve follows the Lorentzian distribution. Thus, the fitting the intensity (I) of the Lorentzian curve was performed using Levenberg Marquardt iteration algorithm ($I = I_0 + \frac{2A}{\pi} \frac{\Gamma}{4(\lambda - \lambda_c)^2 + \Gamma^2}$) for each of the six most intense spectral features (550.65 nm, 553.31, 557.04, 563.25, 568.91 and 575.14 nm) at different fluences [229, 230]. Here, I_0 defines the base line (background), A is the area under the Lorentzian curve, Γ and λ_c are the FWHM and centre of the curve. Height of the curve was determined using the formula, when $\lambda = \lambda_c$

$$H = \frac{(2 \cdot A)}{(\pi \cdot \Gamma)} \quad (28)$$

The variation of background intensity (I_0), FWHM (Γ), area (A) and the height (H) of the fitted curve at the spectral line centred at 550.65 nm is tabulated in the Table 5.3.

Table 5.3: Variation of the background intensity, FWHM, area and the height of the Lorentzian curve centred at a wavelength of 550.65 nm (interaction of molybdenum bulk with ultra-short pulsed laser)

| Peak fluence (Jcm^{-2}) | Background (I_0) (A.U.) | FWHM (Γ) (nm) | Area under the curve (A) (A.U.) | Height (H) (A.U.) |
|---|---|--|--|--------------------------|
| 0 | NA | NA | NA | NA |
| 3.29 | 55.52 ± 4.612 | 0.56 ± 0.050 | 162.80 ± 14.296 | 184.21 ± 8.343 |
| 6.59 | 344.54 ± 11.328 | 0.50 ± 0.012 | 1232.36 ± 29.428 | 1568.42 ± 18.038 |
| 9.89 | 851.46 ± 22.258 | 0.48 ± 0.009 | 2966.92 ± 57.906 | 3902.61 ± 37.686 |
| 13.19 | 1118.32 ± 34.254 | 0.49 ± 0.011 | 4250.55 ± 91.220 | 5477.56 ± 58.162 |
| 16.48 | 1598.20 ± 58.879 | 0.49 ± 0.011 | 7126.74 ± 157.429 | 9344.69 ± 104.867 |
| 19.78 | 2326.11 ± 83.850 | 0.50 ± 0.011 | 10433.85 ± 224.442 | 13314.80 ± 141.032 |
| 23.08 | 2986.33 ± 68.809 | 0.50 ± 0.008 | 12792.10 ± 195.580 | 16202.73 ± 131.015 |

| | | | | |
|-------|-----------------------|------------------|------------------------|------------------------|
| 26.37 | 3156.85 ± 120.169 | 0.51 ± 0.010 | 15850.24 ± 325.247 | 19816.15 ± 198.967 |
| 29.67 | 3780.80 ± 148.980 | 0.49 ± 0.010 | 19323.23 ± 401.490 | 25269.49 ± 268.272 |
| 32.97 | 4259.59 ± 187.833 | 0.50 ± 0.010 | 24786.15 ± 501.930 | 31766.16 ± 319.321 |
| 39.56 | 5062.07 ± 174.887 | 0.49 ± 0.009 | 26501.83 ± 478.436 | 34087.48 ± 315.596 |

Other tables for the peaks centred at 553.31, 557.04, 563.25, 568.91 and 575.14 nm are mentioned in the Appendix.

It was observed that the background intensity, area under the curve and height increases with increasing peak absorbed fluence. The FWHM of the fitted Lorentzian curve for spectral features at this time scale was constant with laser fluence.

The variation of the peak intensity height (H) of these three curves at different peak fluences are presented in Figure 5.3.

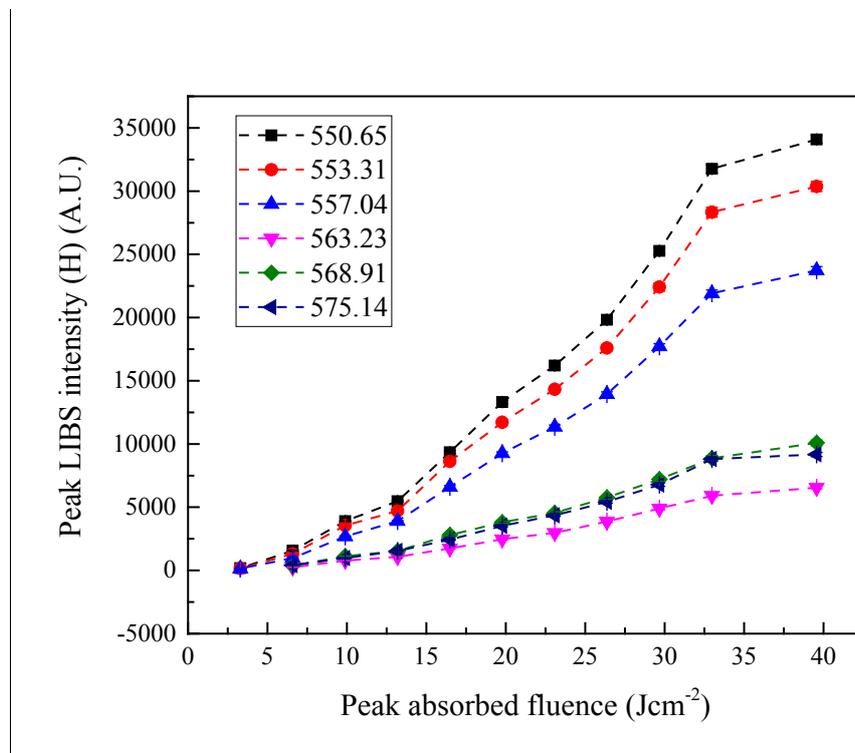


Figure 5.3: Peak LIBS intensity for the six major molybdenum peaks (550.65, 553.31, 557.04, 563.23, 568.91 and 575.14 nm) as a function of absorbed fluence by 1030 nm femtosecond laser. The peak intensity is found the increase with increase peak absorbed fluence

Various laser ablation processes depends upon the intensity of the incident laser pulse [231]. The intensity of the three different peaks increases rapidly with the peak value of the absorbed fluences. At the higher fluence (peak fluence 32.97 Jcm^{-2}) a saturation of the optical emission intensity is observed, although this is based on a single spectrum acquisition.

5.1.2. Spectral imaging of ultra-short laser pulse ablation of molybdenum thin film

Spectral imaging of molybdenum thin film (50 nm) at various fluences were also performed using infrared femtosecond and nanosecond laser pulse durations. The beam diameter of nanosecond laser pulse (wavelength 1030 nm) at the film surface was calculated to $16.54 \mu\text{m}$ using Liu's method by varying applied laser energy. The absorbed laser fluence used for spectral measurements were significantly higher than the ablation threshold of the film (0.023 Jcm^{-2}). Higher MCP gain (2000) was used for molybdenum thin film spectral imaging compared with the molybdenum bulk.

Figure 5.4 illustrates the spectral intensity distribution of 50 nm molybdenum thin film at various fluences between the spectral range of 546.6 nm and 577.3 nm. An increase of noise is noticed for thin film ablation when compared with bulk ablation. Atomic transition of the non-ionised molybdenum was detected by the spectroscopy measurements.

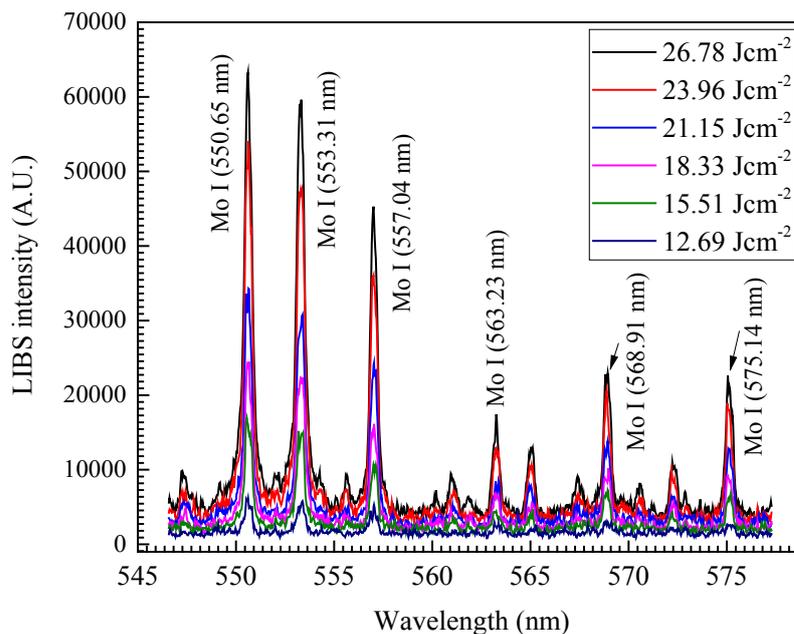


Figure 5.4: Laser-induced breakdown spectroscopy (LIBS) intensities of 1030 nm femtosecond laser ablated 50 nm molybdenum thin film at various absorbed fluences

The variation of the background, FWHM, area and height of the fitted picks are tabulated in Table 5.4.

Table 5.4: Variation of the background intensity, height, FWHM and area under the fitted Lorentzian curve centred at 550.65 nm at different peak fluences (interaction of molybdenum thin film with ultra-short pulsed laser)

| Peak fluence (Jcm^{-2}) | Background (I_0) (A.U.) | FWHM (Γ) (nm) | Area under the curve (A) (A.U.) | Height (H) (A.U.) |
|---|---|--|--|---------------------------|
| 0 | NA | NA | NA | NA |
| 12.69 | 1136.42 ± 72.526 | 0.45 ± 0.058 | 1132.64 ± 157.686 | 1603.17 ± 99.517 |
| 14.09 | 985.15 ± 162.897 | 0.44 ± 0.040 | 3475.63 ± 343.589 | 4988.85 ± 208.649 |
| 15.51 | 1604.745 ± 109.643 | 0.42 ± 0.017 | 6533.09 ± 254.894 | 9860.41 ± 195.779 |
| 16.92 | 1339.60 ± 287.284 | 0.44 ± 0.025 | 10775.27 ± 638.667 | 15718.49 ± 428.977 |
| 18.33 | 1718.14 ± 171.055 | 0.44 ± 0.014 | 12568.43 ± 401.284 | 18365.63 ± 289.661 |
| 19.74 | 2162.25 ± 158.620 | 0.42 ± 0.011 | 14989.43 ± 378.927 | 18365.63 ± 311.520 |
| 21.15 | 2400.51 ± 432.236 | 0.47 ± 0.023 | 20695.47 ± 1032.289 | 22987.95 ± 637.069 |
| 22.53 | 2472.42 ± 357.173 | 0.42 ± 0.016 | 21859.45 ± 825.723 | 27941.80 ± 624.264 |
| 23.96 | 2585.04 ± 422.942 | 0.42 ± 0.015 | 26921.67 ± 958.763 | 32871.98 ± 722.276 |
| 25.38 | 2913.96 ± 443.914 | 0.43 ± 0.013 | 35630.35 ± 1052.266 | 40852.84 ± 784.440 |
| 26.78 | 4223.64 ± 309.371 | 0.44 ± 0.009 | 41694.24 ± 478.218 | 59998.50 ± 612.050 |

Similar to molybdenum bulk, the variation of other tables for the peaks centred at 553.31, 557.04, 563.25, 568.91 and 575.14 nm are mentioned in the Appendix.

It is found that the peak intensity (H) of the six spectral lines again increases with applied laser fluence. The FWHM were similar to all the fluences. Similar to bulk molybdenum, the variation of peak intensity was measured by the Lorentzian curve fitting and illustrated in the Figure A.1.

5.2.3. Spectral imaging of short laser ablation of molybdenum thin film

The LIBS experiments of 50 nm thick molybdenum thin film were performed using an infrared nanosecond laser using different laser energy. The nanosecond laser of wavelength of 1064 nm and beam diameter of 16.53 μm was focussed on the surface of molybdenum thin film. The spectral measurements of the LIBS signal from the molybdenum thin film ablation was performed at a delay time of 200 ns after the nanosecond laser pulse incident on molybdenum surface. The gate width (exposure time) was kept at 1 μs during the spectral acquisition. Similar to the molybdenum thin film ablation by femtosecond laser, the MCP gain for the spectral imaging of nanosecond laser ablation was kept at 2000.

Figure 5.5 indicates the spectral features obtained within a range of 546.6 to 577.3 nm, centred at 562 nm at different fluences greater than ablation threshold (0.043 Jcm^{-2}) of the molybdenum thin film.

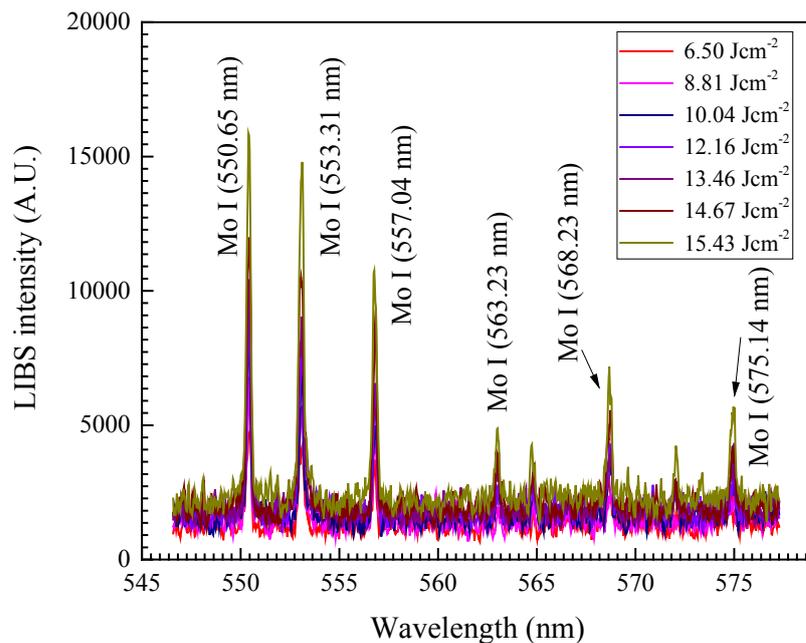


Figure 5.5: Laser-induced breakdown spectroscopy (LIBS) intensities of 1064 nm nanosecond laser abated 50 nm molybdenum thin film at various absorbed fluences

The background, peak height, FWHM and area under the curve were calculated for six major molybdenum peaks using Lorentzian fitting. These calculated parameters for the most intense peak (550.65 nm) is tabulated in Table 5.5.

Table 5.5: Variation of the background intensity, height, FWHM and area under the fitted Lorentzian curve centred at 550.65 nm at different peak fluences (interaction of molybdenum thin film with short pulsed laser)

| Peak fluence (Jcm^{-2}) | Background (I_0) (A.U.) | FWHM (Γ) (nm) | Area under the curve (A) (A.U.) | Height (H) (A.U.) |
|---|---|--|--|----------------------------------|
| 0 | NA | NA | NA | NA |
| 5.29 | 869.54 ± 105.54 | 0.26 ± 0.025 | 1317.47 ± 145.51 | 3224.74 ± 250.62 |
| 6.50 | 906.24 ± 126.238 | 0.27 ± 0.029 | 1708.22 ± 182.396 | 3997.39 ± 208.665 |
| 8.81 | 1175.80 ± 108.537 | 0.29 ± 0.020 | 1952.92 ± 148.590 | 5400.68 ± 140.694 |
| 10.04 | 727.05 ± 313.667 | 0.24 ± 0.023 | 2786.51 ± 323.497 | 6894.74 ± 337.498 |
| 12.16 | 1079.34 ± 401.458 | 0.24 ± 0.030 | 3082.54 ± 438.701 | 8006.98 ± 455.230 |
| 13.46 | 648.85 ± 333.462 | 0.25 ± 0.021 | 3929.32 ± 378.339 | 9857.15 ± 381.579 |
| 14.67 | 617.95 ± 366.048 | 0.27 ± 0.022 | 4892.75 ± 448.682 | 11643.93 ± 434.020 |
| 15.43 | 1450.12 ± 212.858 | 0.23 ± 0.012 | 5479.53 ± 272.362 | 15074.41 ± 382.592 |

The five other spectral lines centred at 553.31, 557.04, 563.23, 568.81 and 575.14 nm are tabulated in the appendix section.

The background intensity, peak intensity and area under the curve again increases with increasing laser fluence. The FWHM is approximately constant at all the fluences. Primary observation suggests that at the similar fluences, the intensity of the nanosecond laser produced plasma plume is more intense than that obtained by femtosecond laser pulse. In the case of interaction of short laser pulse with the molybdenum thin film, the nanosecond laser pulse further interacts with the ablated molybdenum plume due to the plasma shielding effect. As a result, the ablated species are further excited by the laser pulse.

An average FWHM value of 0.25 ± 0.006 nm is estimated for the nanosecond laser produced plasma plume. At the similar fluence, the FWHM of the spectral lines during the nanosecond laser ablation of molybdenum thin film is lesser than that obtained by femtosecond laser interaction. It is well known from the literature that the electron density of the plasma plume is directly proportional to the Lorentzian curve fitted spectral line [232, 233]. This suggests that the electron density of the femtosecond laser produced plasma is higher than the nanosecond laser produced plasma. This evidence suggests that more thermionic emission take place during femtosecond laser pulse interaction with the molybdenum thin film compared with the nanosecond laser pulse interaction.

The variation of molybdenum peaks with a variation of laser fluence is shown in the Figure A.2.

Thus, from the spectral acquisition, the following points are made justified:

1. An increase of laser fluence increases line spectrum signal, which suggests the total number of particles ejected increases with increasing laser fluence.
2. An enhancement of laser fluence resulted in an increase of background intensity, which may be due to a temperature increases with increasing laser fluence.
3. It was observed that at low fluence, the plasma plume observed from the interaction of femtosecond laser pulse with molybdenum bulk is more intense than the femtosecond laser-molybdenum thin film interaction. At higher fluence values, the interaction of laser with molybdenum thin film results in more intense plasma plume than that obtained with molybdenum bulk samples.
4. In case of nanosecond laser ablation of molybdenum thin film, the peak intensity from the spectral line emission of the plasma plume is found to be more intense compared with the femtosecond case.
5. The FWHM of spectral lines of the femtosecond laser plasma plume is wider than that by nanosecond case. This may arise due to more thermionic emission during femtosecond laser interaction with molybdenum samples at ultra-short time frame.

These observations are not conclusive as they are highly dependent on the experimental configuration. Hence, difference between the spectral acquisition obtained for nanosecond and femtosecond laser ablation was not clearly distinguished. Thus, spatial imaging of the plume is required during nanosecond and femtosecond laser ablation. The primary purpose of the spatial imaging was to identify the origin of light observed in the spectral imaging of femtosecond and nanosecond laser ablation which is now described.

5.2. Plasma Imaging

The previous section shows the spectral response of the plasma plume of molybdenum bulk and thin film between the wavelength range of 546.6 nm and 577.3 nm. The spectral lines originate from the atomic transitions in the plasma plume. The spectral acquisition of the plasma was collected for 1000 μ s and delay was kept at 200 ns from the time when the laser pulse incident on the sample surface. Thus, the spectral response detected by the spectrometer are not due to early emission from the molybdenum sample. Also, the region from which the spectral emission was collected was also fixed by the collecting lens. Hence the spectral data does not accurately reflect how the plasma plume evolve with time.

The motivation of a spectral imaging is to understand the ablation mechanism and to identify the time when the thin film detaches from the surface of the substrate. The spatial imaging of the plasma plume was conducted at early times (delay: 0 ns to 200 ns) of the laser ablation. Also, the emitted optical emission during the plasma imaging was collected for the time duration of 5 ns.

The plasma imaging of molybdenum bulk and thin film is of somewhat limited value as it was performed at fluence much higher than the threshold fluence; this is because the detected intensity of the ejected particles was not observable at low fluences. Thus, another major limitation of this study is all the experiments were performed at high fluences.

Real time spatial imaging of the plasma plume was obtained during laser ablation of molybdenum bulk and thin film. The experiment was performed at different fluences for IR, green and UV wavelengths. The objective of the real-time imaging was to understand the evolution of the ejected plasma plume. A time delay between the laser pulses with the plasma plume was noticed, which include the internal (instrumental) delay of the ICCD detector and the time to generate plasma plume after the laser pulse incident on the sample surface. A background image was taken prior to recording images of the laser plume to avoid the noise caused by the background light. The background-corrected image was recorded at a different time delays from the time when the laser plume is detectable. This is recorded to be $t = 0$ s. Normally, the exposure time of each frame was taken to be 5 ns to study real-time dynamics of ejected plasma plume. The gain applied to the micro-channel plate (MCP) (section 3.5.2.1) was set depending on the intensity of the plasma plume and detection efficiency by ICCD. The higher MCP gain leads to an increase of noise in the image. Initially, it was found that the plasma plume intensity was very intense and then decayed gradually with increasing delays. The MCP gain was varied from 150 to 220 for different peak fluences and was kept fixed at a particular fluence to achieve the optimal plasma images for a given laser wavelength and pulse duration. Using the camera software, the auto-scale adjust on image intensity was kept 'ON' to scrutinise ejected particles at various time delay.

5.2.1. Spatial imaging of plasma plume during ablation of molybdenum bulk by ultra-short pulse laser

The evolution of the plasma plume at different fluences using the 1030 nm wavelength of the femtosecond laser is presented in Figure 5.6. The plasma plume was detected (7 ± 1) ns after the peak intensity of the laser pulse. The spot radius (ω_0) of the laser beam focussed on the surface of the samples was nearly 25 μm . Each image recorded, corresponded to a gate width (exposure time) of 5 ns and was taken at an interval of every 10 ns. The intensity of the ejected components (particles and other emission ions etc.) are found to decrease with reducing the peak laser fluence. Figure 5.8 presents the plasma plume dynamics at an absorbed fluence of 1, 1.5 and 2 Jcm^{-2} . The MCP gain was set at 170 to capture the plasma plume at these peak fluences. Initially, the spatial intensity was taken in 32-bit grey scale, and to make the distribution of intensity more evident, the images were converted to RGB scale from grey scale.

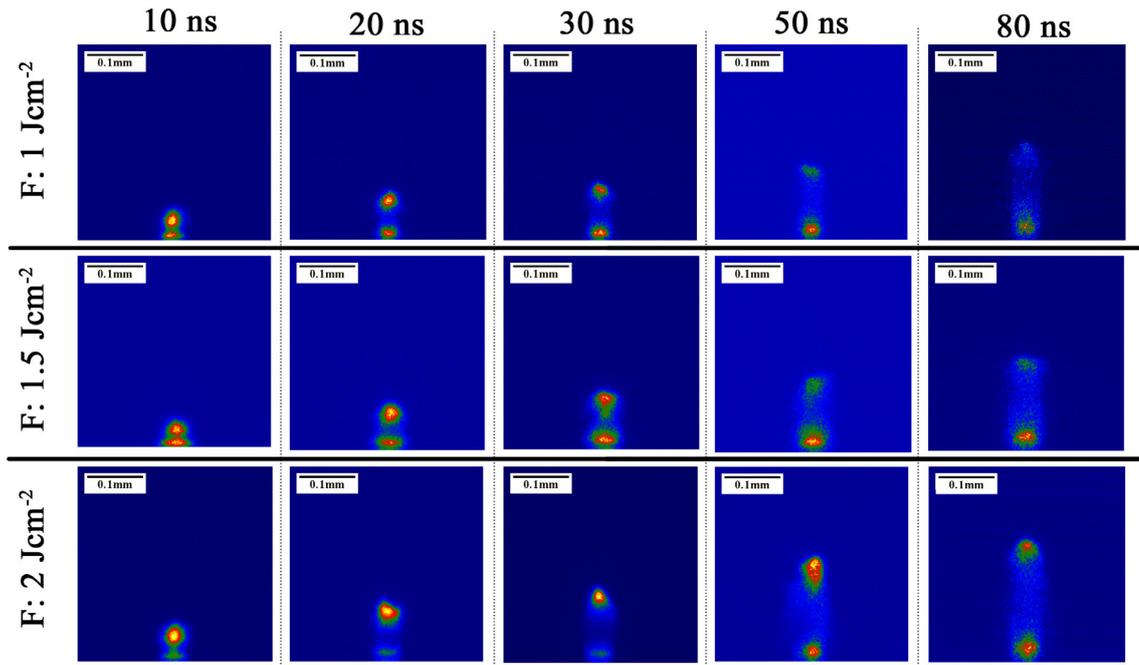


Figure 5.6: Time-resolved plasma plume generated from the molybdenum bulk samples after the interaction of 1030 nm femtosecond laser pulse at fluences (absorbed) 1, 1.5 and 2 Jcm⁻². The MCP gain used for this study was 170.

Figure 5.7 and Figure 5.8 present images of 515 nm and 343 nm produced plasma, respectively, at the same absorbed fluences and at the same delays. The spot radius (ω_0) of the craters produced on the surface of the molybdenum bulk were determined to be 15.51 and 18.57 μm at the laser wavelengths 515 nm and 343 nm, respectively. It was observed that the plasma plumes generated by the laser of wavelength of 515 nm are more intense than 1030 nm and 343 nm produced plasma. Thus, the MCP gain, was reduced to 100 during the capture of the 515 nm femtosecond laser pulse plasma plume images to avoid any intensity saturation by the ICCD detector. The gain used to get plasma images at 343 nm laser wavelength was 220. Also, at early times it was observed that, during the interaction of the femtosecond laser pulse (515 nm) with molybdenum sample, at the intensity of the plasma are so intense that the intensity of plasma saturates at the start of formation of plasma plume.

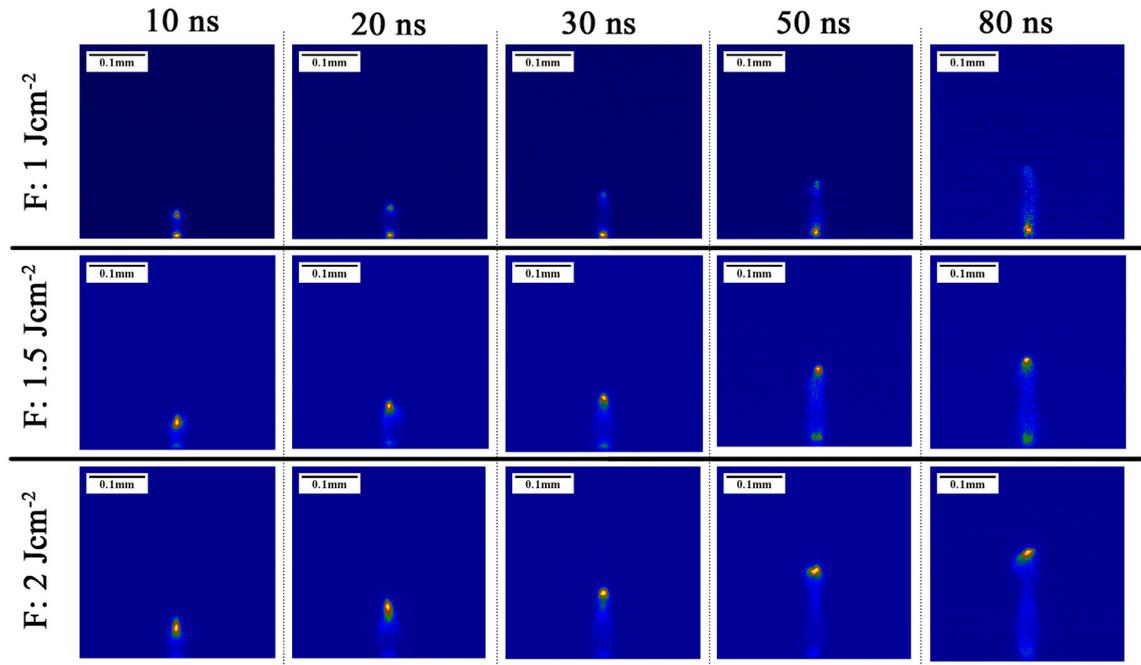


Figure 5.7: Time-resolved plasma plume generated from the molybdenum bulk samples after the interaction of 515 nm femtosecond laser pulse at fluences (absorbed) 1, 1.5 and 2 Jcm^{-2} ; the MCP gain value used for this study was 100.

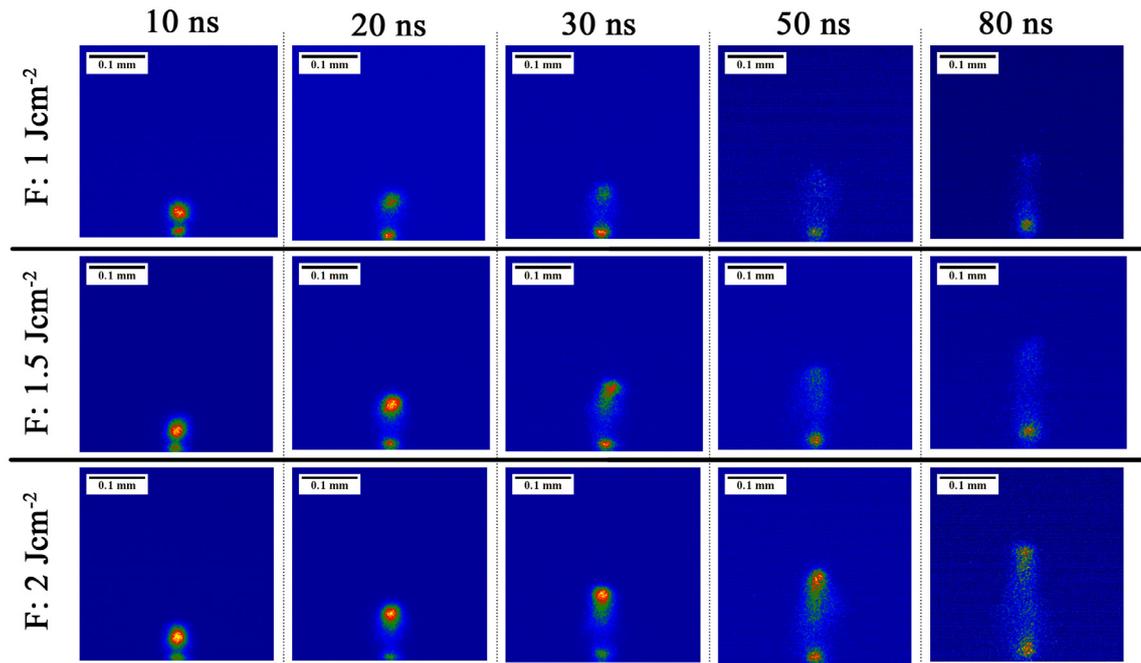


Figure 5.8: Time-resolved plasma plume generated from the molybdenum bulk samples after the interaction of 343 nm femtosecond laser pulse at fluences (absorbed) 1, 1.5 and 2 Jcm^{-2} ; the MCP gain value used for this study was 220.

Initially, at early times (0 to 10 ns), the emission originates from one spatial region in the gated images. The plasma plume then separates at $t > 10$ nanoseconds, a comparatively more intense and faster-moving part separates from the slower part. Eventually, the faster-moving part is first to decrease in intensity at longer times while the component near the surface stay bright longer. In the case of 1030 and 343 nm laser ablation (1.0, 1.5 and 2.0 Jcm^{-2}), the intensity of the faster-moving part of the plasma is less intense at longer delay (≥ 80 ns) compared with slower part.

After the laser interaction of 515 nm femtosecond laser pulse with molybdenum bulk at the peak fluences of 1.0 cm^{-2} , it was observed that the faster moving part of plasma is less intense than the slower part. At higher 515 nm femtosecond laser fluences (1.5 and 2.0 cm^{-2}), it was observed that (from delay 0 ns to 100 ns) the faster-moving part of plasma plume is more intense than the slower moving part.

A cross section of the vertical intensity profile through the centre of the plume was extracted from the images to identify more clearly the expansion dynamics of the plasma plume at various fluences. Figure 5.9 illustrates an example of the temporal evolution of these profiles at different time delays from the incident laser peak for an absorbed fluence of 1 Jcm^{-2} , using femtosecond laser wavelengths of 1030, 515 and 343 nm. The vertical intensity distribution of the plasma plumes was plotted at different delays from 0 ns to 80 ns. The distance on the X-axis presents the distance from the surface of the bulk molybdenum. Two peaks in the profile are typically observed. At the lower fluence, the forward part of plasma plume is initially more intense compared with the lower than the slower part. As the time progresses, the slower moving component becomes more intense than the faster-moving part.

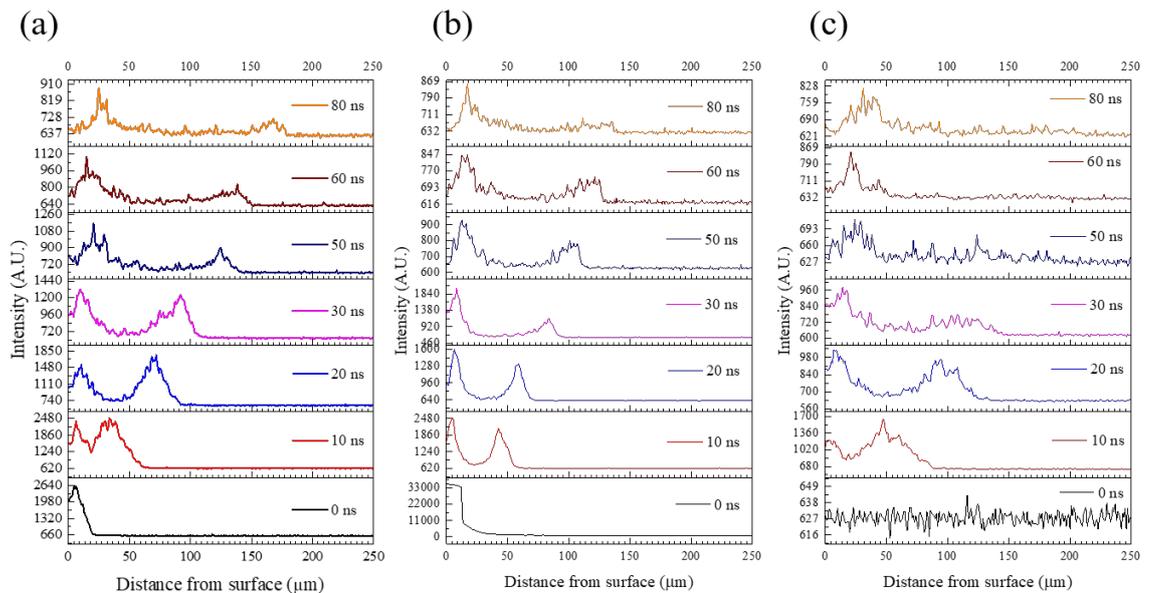


Figure 5.9: Vertical intensity distribution of the emission from the plasma plume, through the centre of the plasma ($X=0$, $Y=0$), after the interaction of molybdenum bulk with the femtosecond laser pulse of wavelength of (a) 1030 nm (b) 515 nm and (c) 343 nm using an absorbed fluence of 1 Jcm^{-2} .

The distribution of intensity through the centre of the plasma plume at laser wavelengths of 1030, 515 and 343 nm are shown in the Figure 5.9. The initial plasma peak (0 ns) separates into two peaks by a delay of 10 ns and the distance between two peaks increases with increasing time delay. The distance of the faster moving part of the 343 nm femtosecond laser pulse produced plasma plume is longer than that of 1030 and 515 nm laser pulse. The faster part of the 343 and 515 nm laser produced plasma plume disappears quicker than the 1030 nm laser produced plasma plume. The slower part of the plume travel relatively less distance at the similar delays.

The origin of the plasma was taken at the surface of the film, where the initiation of plasma plume happens. The reduction of the signal compared to the noise occurs at longer delays when the optical

emission decreases. Initially, the distance of the plasma plume from the surface was calculated in the unit of number of pixel, thereafter it was converted to the unit of length (μm).

The distance of the faster moving part (Figure 5.9) of the plasma plume was calculated using the maximum intensity identified by fitting the intensity profile to a Gaussian shape. The distance to the leading edge of the plume was measured to be when the intensity decays 90% of the peak intensity of the feature at the furthered distance to plume front. The distance travelled by the plasma plume front (R) is calculated. The Plume front position–delay time (R - t) plots were obtained from Figure 5.10 and used to obtain better insights of plasma expansion dynamics at various fluences. Figure 5.10 shows the vertical distance of travelled by 1030 nm produced plasma plume from the sample surface at fluences of 1, 1.5 and 2 Jcm^{-2} (absorbed).

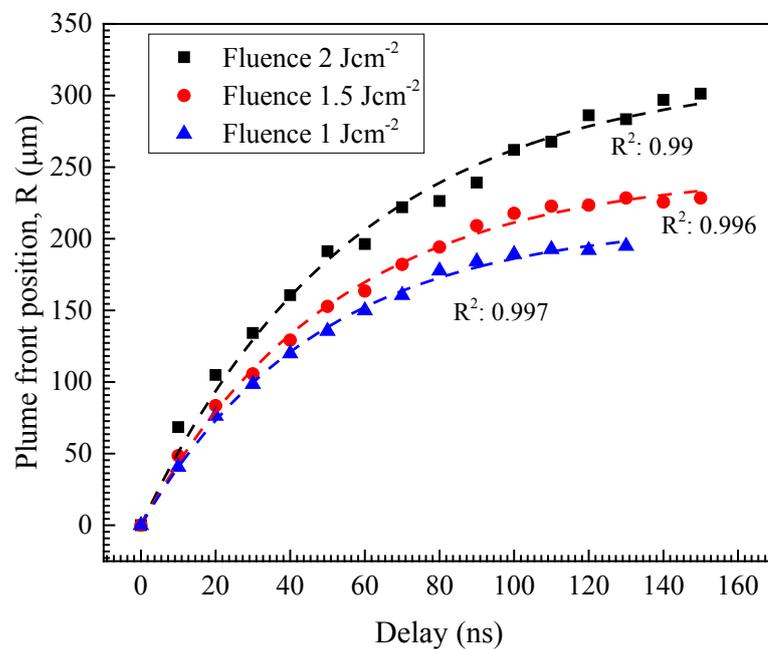


Figure 5.10: Vertical distance travelled plasma front at 1, 1.5 and 2.0 Jcm^{-2} produced by 1030 nm femtosecond laser.

It was found that at early times an almost linear expansion takes place and the expansion decreases exponentially according to the Drag model [234]. An exponential fitting ($R = R_0 \cdot (1 - \exp(-\beta \cdot t))$) was performed on the distance travelled by the front edge of the plasma plume at various fluences [122]. The proportionality coefficients of the exponential fitting R_0 (in μm) and β (in ns^{-1}) presents the stopping distance of the plasma plume and the acceleration/deceleration coefficient, respectively. A Taylor expansion of the exponential fitting at $t = 0$ s provides the average velocity and the de-acceleration of the plasma plume and is given by $v_0 = R_0 \cdot \beta$ and $f = R_0 \cdot \beta^2$.

In a similar way, the peak height of the plasma was obtained to measure the distances of the plasma plume at specific time delays during the interaction of bulk molybdenum samples with femtosecond laser pulse at the wavelengths of 515 nm and 343 nm. In Figure A.3, the vertical distance travelled by 515 nm plasma plume from the surface at time delay of interval 10 ns at fluence values of 1, 1.5 and 2 Jcm^{-2} . Similarly, Figure A.4 presents the 343 nm laser produced

plasma peak height at fluence of 1, 1.5 and 2 Jcm⁻². The exponential fitting of peak position of plasma plume intensity at different fluences were employed and illustrated in the Figure A.3 and Figure A.4.

Using the Drag model, the stopping distance (R_0), average velocity (v_0), deceleration coefficient (β) and the deceleration (f) was calculated for the fluence value of 1, 1.5 and 2 Jcm⁻² (absorbed) and tabulated in Table 5.6.

Table 5.6: Estimated 'stopping distance', 'average velocity' and 'deceleration coefficient' of the faster-moving plasma plume front of bulk molybdenum after exposure of 1030, 515 and 343 nm femtosecond laser at the fluence of 2, 1.5 and 1 Jcm⁻²

| Wavelength (nm) | Fluence (absorbed) Jcm⁻² | Stopping distance (R_0) (μm) | Average velocity ($R_0\beta$) (ms^{-1}) | Deceleration coefficient ($R_0\beta^2$) (ns^{-1}) |
|------------------------|--|--|---|---|
| 1030 | 1 | 211 ± 3 | 4471 | (2.12 ± 0.07) x 10 ² |
| | 1.5 | 246 ± 3 | 4765 | (1.94 ± 0.07) x 10 ² |
| | 2 | 317 ± 8 | 5541 | (1.75 ± 0.11) x 10 ² |
| 515 | 1 | 144 ± 3 | 4594 | (3.19 ± 0.26) x 10 ² |
| | 1.5 | 215 ± 7 | 4837 | (2.25 ± 0.18) x 10 ² |
| | 2 | 252 ± 10 | 5972 | (2.37 ± 0.25) x 10 ² |
| 343 | 1 | 107 ± 6 | 3517 | (3.29 ± 0.33) x 10 ² |
| | 1.5 | 200 ± 6 | 6470 | (3.23 ± 0.28) x 10 ² |
| | 2 | 251 ± 4 | 6669 | (2.66 ± 0.12) x 10 ² |

The following observations are identified from the Table 5.6:

- The stopping distance increases with increasing laser fluence,
- The average velocity of the plasma plume increases with decreasing applied wavelength at a particular absorbed laser fluence, and
- At the same peak fluence value, wavelength dependence of these parameters was observed. The velocity of the plasma plume is maximum for UV wavelength than IR and Green, at a particular peak value of the absorbed fluence. Also, an anomalous plasma velocity is observed in the case of UV femtosecond laser pulse ablation. The reason for that was not understood clearly. Although, we believe that at very high fluence aggressive ablation takes place and a result, the velocity of the plasma plume increases rapidly.

The intensity of the light emitted from ejected components decreases with longer delay, and to accommodate this, the gate width (GW, exposure time) was increased to visualise further emission from the ejected components. The plasma emission from the faster moving part of plume was not detected after 400 ns irrespective of what gate width was used. Figure 5.11 presents the slower

moving components of plasma plume at gate width of 100 ns duration at 200 ns, 250 ns, 350 ns and 450 ns and delay.

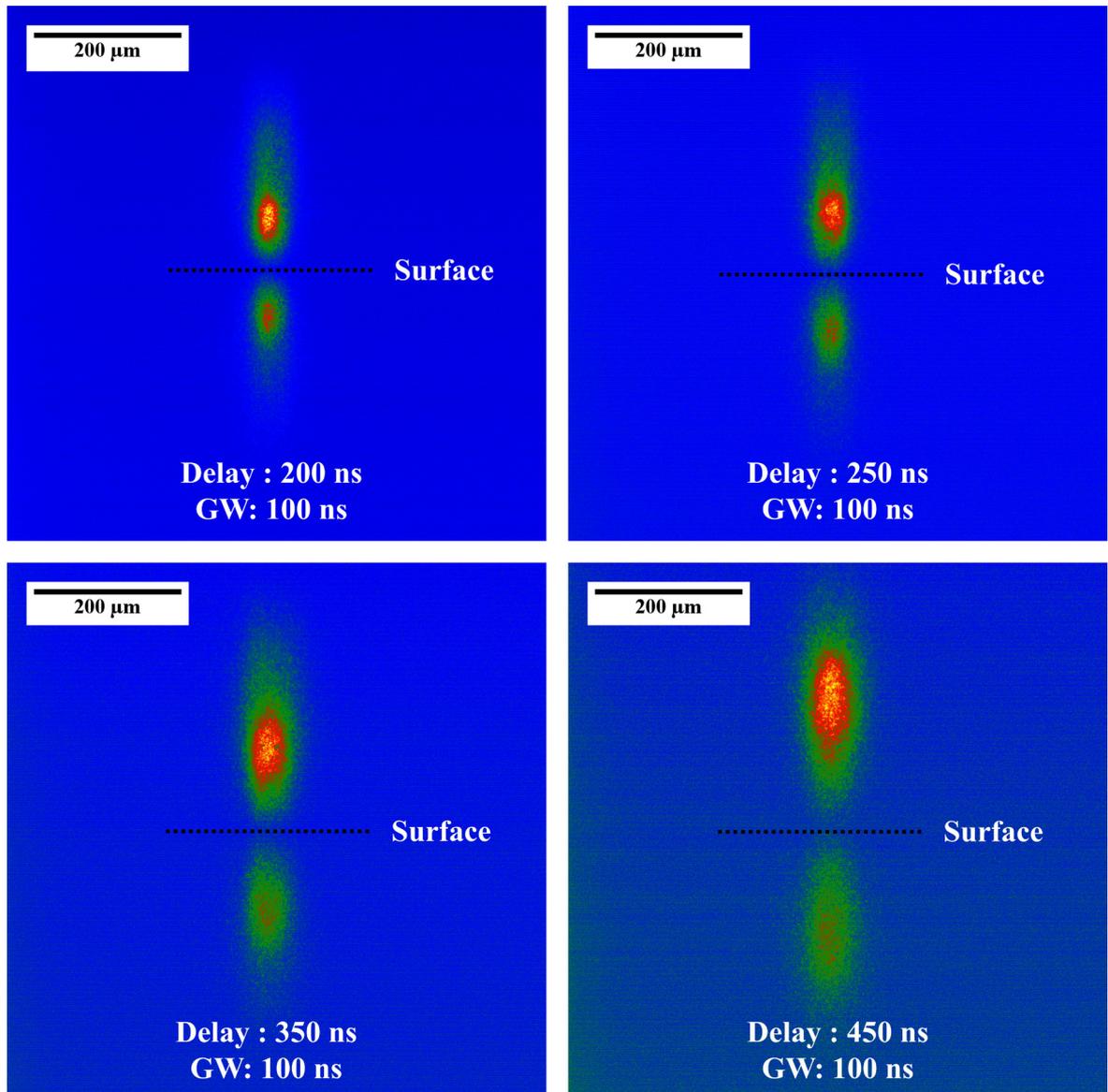


Figure 5.11: Spatial distribution of ejected elements at long delay for a peak absorbed fluence of 1 Jcm^{-2} using wavelength of 1030 nm. The surface of the sample is represented by the black dotted line. Reflection of the plume from the surface of the target resulted in the presence of a light signal was detected at the images below the surface of the target.

At a delay of 200 ns, the intensity of the centred part of the slower moving component of plasma plume is significantly intense compared with the edge parts. Also, the intensity of the centre and edge the plasma plume decreases with increasing the delay. At long delay, although the optical emission from the faster moving part of the plasma plume vanishes, emission from the slower moving components of the plasma plume takes place.

Real time spatial imaging of the plasma plume of molybdenum thin film at different absorbed fluences at 1030 and 515 nm femtosecond laser wavelengths will be discussed in the next section.

5.2.2. Spatial imaging of plasma plume during ablation of molybdenum thin film by ultra-short pulse laser

Temporal dynamics of plasma plume at fluences of 1, 1.5 and 2 Jcm⁻² using 1030 nm femtosecond laser was studied at different delays and is illustrated in Figure 5.12. The time indicated with each image corresponds the ‘delay time’ of detecting the laser produced plasma plume (section 5.2) at an interval of 10 ns. Similar to the molybdenum bulk case, the delay (t) is recorded to zero nanosecond (0 ns), when the detector (ICCD) starts collecting the optical emission from plasma plume. The shape of the plasma plume was found to be completely different than the plasma plume during the interaction of femtosecond laser with bulk molybdenum. In order to visualise detailed spatial evolution of the plasma plume, the gate width (exposure time) of each acquisition was kept at 5 ns. The MCP gain (section 3.2.1) was kept at 220 during all the acquisitions.

From the initial measurement, it was observed that the lifetime of the optical emission depends upon the peak value of the absorbed fluence. The intensity of different parts of plasma plume decreases with reducing the absorbed fluence of the laser. Thus, at low fluence, the intensity of the plasma plume is not detectable by the ICCD. It was presumed that near damage threshold of the molybdenum thin film, the plasma plume may be present but not detectable by the ICCD detector. Thus, the plasma plume detection was again performed at higher value of absorbed fluence.

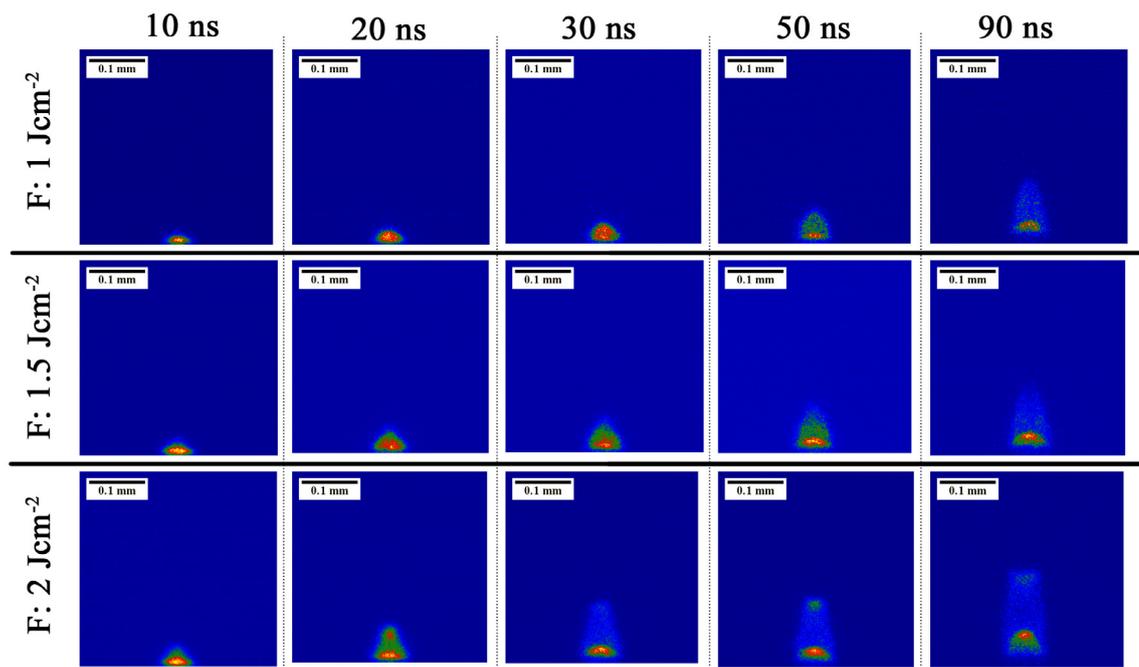


Figure 5.12: Time-resolved plasma plume generated from the 50 nm thin molybdenum thin film after the interaction of 1030 nm femtosecond laser pulse at peak fluences (absorbed) of 1.0, 1.5 and 2.0 Jcm⁻². The MCP gain used for this study is 220.

The detected plasma plume generated by the interaction of 1030 nm femtosecond laser pulse with molybdenum thin film consists of two components. The faster part of the plasma plume ejects with high velocity and disappears quickly. The second part of the plasma plume is more intense and evolves at a slower velocity than the faster component. As the laser pulse is spatially Gaussian, the peak fluence is expected to be at the centre of the spot on the surface of the molybdenum thin film. Thus, it was observed that the height of the plasma plume from the sample surface is

maximum at the centre. As a result, the velocity of the film is expected to increase towards the centre of the plume.

Spatial measurement of the evolution of the plasma plume was conducted for the interaction of the femtosecond laser with molybdenum thin film using green (515 nm) wavelength. The gate width (GW) for each measurement was kept at 5 ns and the detection of 515 nm plasma plume performed at an interim of 10 ns. The MCP gain (section 3.2.1) for the plasma plume detection was fixed at 220. Figure 5.13 presents the spatial dynamics of plasma plume produced by interaction with laser of wavelength of 515 nm at specific time delays for the peak value of fluence of 0.5, 1 and 1.5 Jcm^{-2} . For the detection of the plasma plume, at a peak fluence of 2 Jcm^{-2} , produced by the interaction of molybdenum thin film with femtosecond laser of wavelength of 515 nm, the MCP gain was reduced to 200.

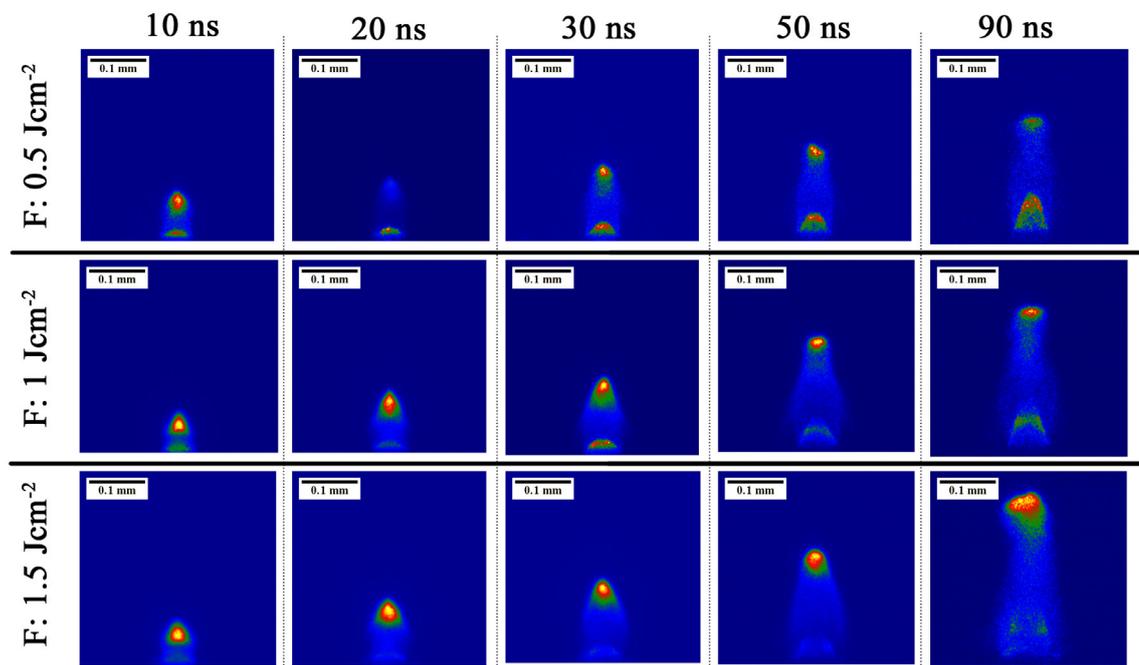


Figure 5.13: Time-resolved plasma plume generated from the 50 nm thin molybdenum thin film after the interaction of 1030 nm femtosecond laser pulse at peak fluences (absorbed) of 0.5, 1.0 and 1.5 Jcm^{-2} . The MCP gain used for this study is 200.

Similar to 1030 nm femtosecond laser, it was observed that the plasma produced during the interaction of molybdenum thin film with 515 nm femtosecond laser, consists of two parts. The forwarded part of the plasma plume is found to have relatively more intensity than the plasma produced by the interaction of femtosecond laser using wavelength 1030 nm. Also, it was observed that unlike the case of interaction with wavelength of 1030 nm, the forwarded part is more relatively intense than the slower part.

The vertical propagation of the plasma plume, produced by the interaction of molybdenum thin film with femtosecond laser, at different time delays is illustrated in the Figure 5.14. This figure presents the intensity profile of plasma plume using femtosecond laser of wavelength of (a) 1030 nm and (b) 515 nm; at a peak absorbed fluence of 1 Jcm^{-2} . The X-axis corresponds to the vertical distance travelled by the plasma plume from the surface of the molybdenum thin film. The Y-axis indicates the number of counts (intensity) detected by the ICCD detector.

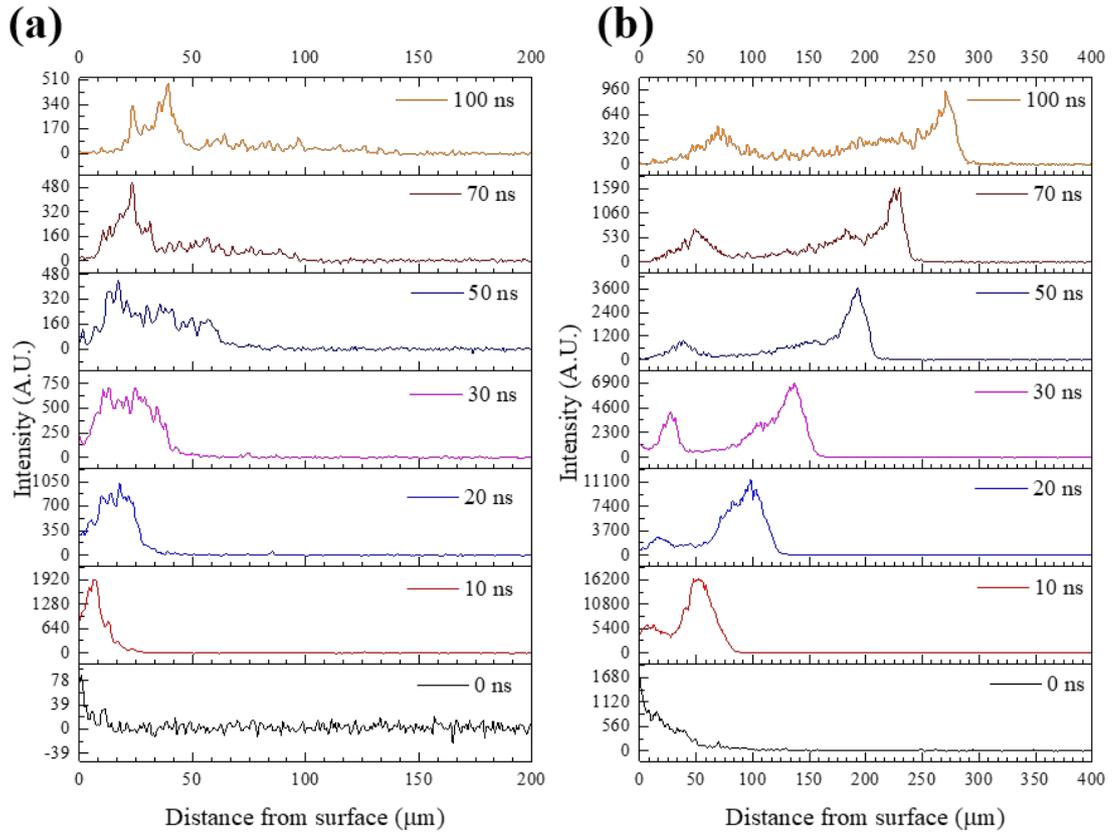


Figure 5.14: Vertical intensity distribution of the emission from the plasma plume, through the centre of the plasma ($X=0$, $Y=0$), after the interaction of molybdenum thin film with the femtosecond laser pulse of wavelength of (a) 1030 nm and (b) 515 nm using an absorbed fluence of 1 Jcm^{-2}

Two distinct peaks of the plasma plume were observed at delays greater than 10 ns. In the case of 1030 nm and at fluence of 1 Jcm^{-2} , the peak height of the forwarded part of the plasma is relatively less intense than the slower component (Figure 5.14(a)). Green femtosecond laser pulse ablation results in relatively more peak intense than the IR plasma (Figure 5.14(b)). Also, at the fluence 1 Jcm^{-2} , the forwarded part of the plasma plume is comparatively more intense than the slower part at delays less than 100 ns.

The vertical intensity distribution of the plasma plume during femtosecond laser ablation at a fluence 2.0 Jcm^{-2} presented in the Figure 5.15. The intensity of plasma peaks at 2 Jcm^{-2} are found significantly higher than that of 1.0 Jcm^{-2} .

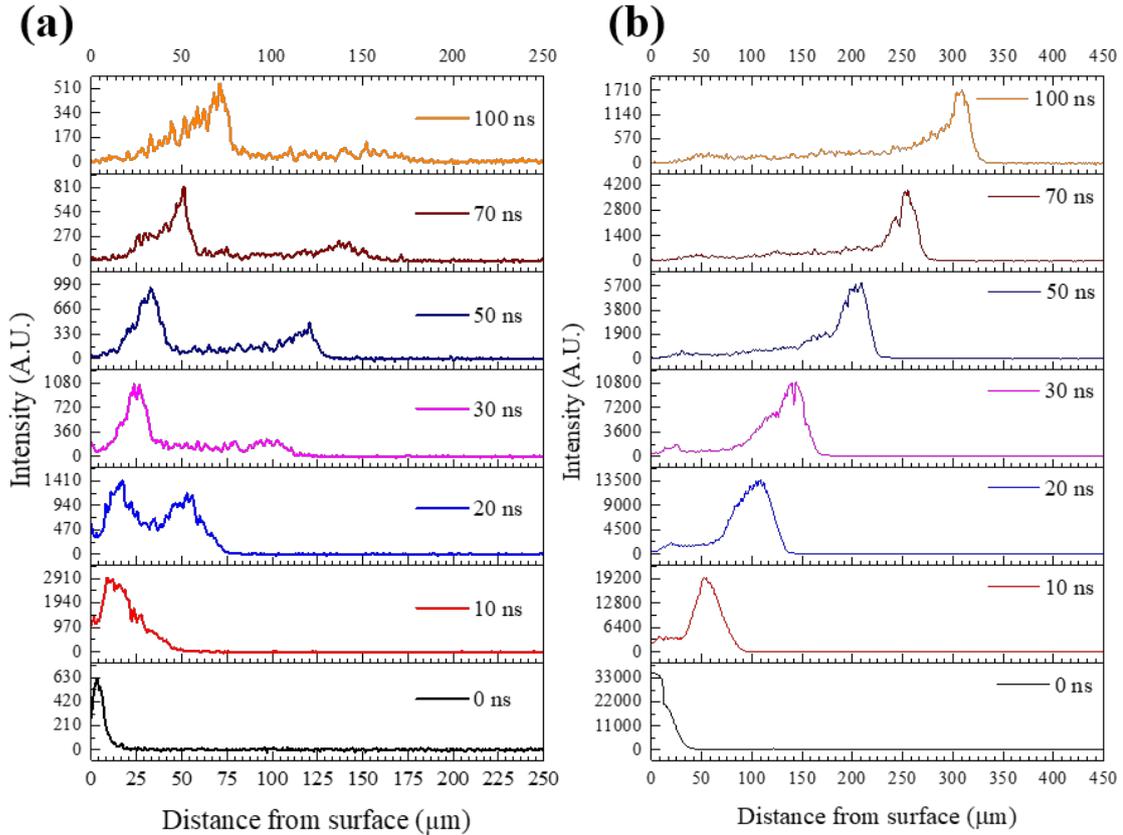


Figure 5.15: Vertical intensity distribution of the emission from the plasma plume, through the centre of the plasma ($X=0$, $Y=0$), after the interaction of molybdenum thin film with the femtosecond laser pulse of wavelength of (a) 1030 nm and (b) 515 nm using an absorbed fluence of 2 Jcm^{-2}

The less intense forwarded part of the plasma plume eventually disappears and only one peak was observed. It was found that high-speed part (forwarded) is ejected rapidly from the surface and expands both vertically and horizontally. The distance of the faster and slower moving components of the plasma plume from the sample surface was estimated from Figure 5.15. As the vertical intensity profile of the faster and slower components are not completely Gaussian, the distance was measured at the position when the intensity reduces to 90% of the peak intensity. The dynamics of the forwarded and delayed part of the plasma plume was investigated for different peak value of absorbed fluences. The forwarded part of the plasma was fitted using the Drag model [122, 234]. It was found that the plasma plume ejects very rapidly from the surface of the plume and then the velocity decreases slowly. The intensity of the high-speed part of the plasma was found to decrease with increasing the time delay.

Similar to the case of bulk molybdenum, the propagation of plasma plume from the surface was measured at a particular delay and when the intensity drops to 90% of the peak value. The distance travelled by the plasma plume were measured at a range of time delays at different fluences. The forwarded and delayed parts of the plasma plume are expressed as the plasma and film front. Figure 5.16 shows the travelled distance by the edge of the front part of 1030 plasma plume at fluence values of 1, 1.5 and 2 Jcm^{-2} . The vertical expansion of front part of the plasma plume at different peak fluences are fitted by the Drag model using the exponential model (described earlier). Measured R -squared values were found to be close to 0.99 indicating a good fitting.

It was found that the slow part of the plasma plume does not decelerate quickly, and it was noticed that the propagation of the component is almost linear. Thus, in the Figure 5.17, a linear fitting ($d = \alpha \cdot t$) was carried out for the expansion of the slow part of the plume and the slope (α) of the linear fitting provides the velocity of the centre part of the slow component. The slower moving part is considered as the particle front of the plasma plume.

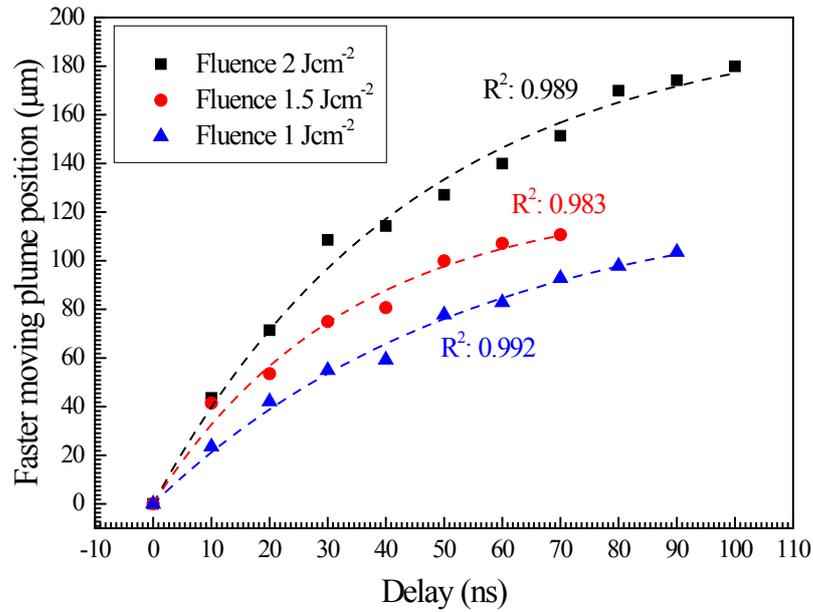


Figure 5.16 Propagation of plasma front at various absorbed fluencies values using 1030 laser wavelength

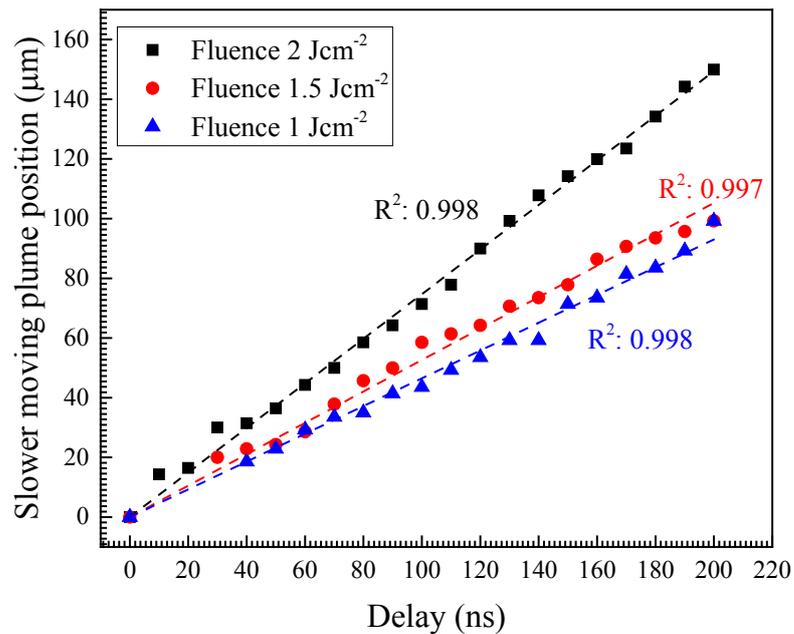


Figure 5.17: Propagation of delaminated film edge at various absorbed fluencies values using 1030 laser wavelength

When the peak value of the absorbed laser fluence was reduced further, spatial acquisition was also carried out to detect the faster and slower moving part of the plasma plume generated due to the interaction of femtosecond laser with molybdenum thin film using wavelength of 1030 nm for the absorbed fluences of 0.25 and 0.5 Jcm⁻². A comparatively less clear and low intense plasma plume was detected. The measurement at these two fluences does not allow to study the propagation of plasma plume.

Similar to the plasma produced by femtosecond laser using wavelength of 1030 nm, the propagation of the forwarded and slower component of 515 nm femtosecond laser generated plasma plume was illustrated in the figures below. Figure A.5 and Figure A.6 present the spatial propagation of the plasma front and particle front at fluence 0.25, 0.5 and 1 Jcm⁻². The separation of the faster and slower moving component of the plasma plume was not clearly visualised during the interaction of femtosecond laser with molybdenum film at absorbed fluence of 2 and 1.5 Jcm⁻² using wavelength of 515 nm. Thus, the propagation of slower moving part was not investigated at these two fluences.

The stopping distance, average velocity and the deceleration coefficient of the faster moving component of the plasma plume at different absorbed fluences at different fluences are tabulated in the Table 5.7.

Table 5.7: The stopping distance, average velocity and the deceleration coefficients of fast components of the plasma plume produced by the interaction of molybdenum thin film with femtosecond laser of wavelength of 1030, 515 nm at different peak absorbed fluences

| Wavelength (nm) | Fluence (absorbed) Jcm⁻² | Stopping distance (R₀) (μm) | Average velocity (R₀β) (ms⁻¹) | Deceleration coefficient (R₀β²) (ns⁻¹) |
|----------------------------|--|--|---|---|
| 1030 | 0.25 | NA | NA | NA |
| | 0.5 | NA | NA | NA |
| | 1 | 127 \pm 7 | 2307 | (1.82 \pm 0.193) x10 ² |
| | 1.5 | 139 \pm 9 | 3363 | (2.42 \pm 0.471) x10 ² |
| | 2 | 198 \pm 8 | 4415 | (2.23 \pm 0.212) x10 ² |
| 515 | 0.25 | 178 \pm 7 | 4565 | (2.56 \pm 0.228) x10 ² |
| | 0.5 | 252 \pm 11 | 5140 | (2.04 \pm 0.17) x10 ² |
| | 1 | 274 \pm 10 | 7124 | (2.60 \pm 0.21) x10 ² |
| | 1.5 | 323 \pm 10 | 8614 | (2.65 \pm 0.36) x10 ² |
| | 2 | 389 \pm 4 | 9152 | (2.83 \pm 0.45) x10 ² |

The average velocity and stopping distance of the plasma plume decreases with applied laser fluence. The component of the plasma plume near the surface of the thin film expands at a comparatively lower velocity. The intensity of the slower moving part decreases comparatively more slowly than the faster moving forwarded segment. The average velocity of the comparatively slower part of the plasma plume was determined and presented in the Table 5.8.

Table 5.8: The stopping distance, average velocity and the deceleration coefficients of slow components femtosecond laser produced plasma using wavelength of the 1030, 515 nm at different peak value of absorbed fluences

| <i>Wavelength (nm)</i> | <i>Fluence (Jcm⁻²)</i> | <i>Average velocity (ms⁻¹)</i> |
|-----------------------------------|--|--|
| <i>1030</i> | 0.25 | NA |
| | 0.5 | NA |
| | 1 | 465 ± 5 |
| | 1.5 | 526 ± 6 |
| | 2 | 747 ± 6 |
| <i>515</i> | 0.25 | 658 ± 15 |
| | 0.5 | 794 ± 15 |
| | 1 | 961 ± 14 |
| | 1.5 | NA |
| | 2 | NA |

It is expected that the deceleration of slower moving part of the plasma plume take place at longer time delay.

The emission lifetime of the slower part of the plasma was found to be larger than the fast component of plume. The Figure 5.18(a) presents the plasma plume at 300 ns delay at fluences of 0.5, 1, 1.5 and 2 Jcm⁻². Also, the intensity profile of the plasma plume at these fluences are presented in the Figure 5.18(b). The X-axis in the Figure 5.18(b) determines the distance from the surface of the thin film and the X axis corresponds the normalised intensity profile of the plasma plume at a delay of 300 ns and gate width (exposure time) of 100 ns. Within the fixed delay and gate width was kept constant, the slower component of the plasma plume was found to travel a greater distance at higher fluence.

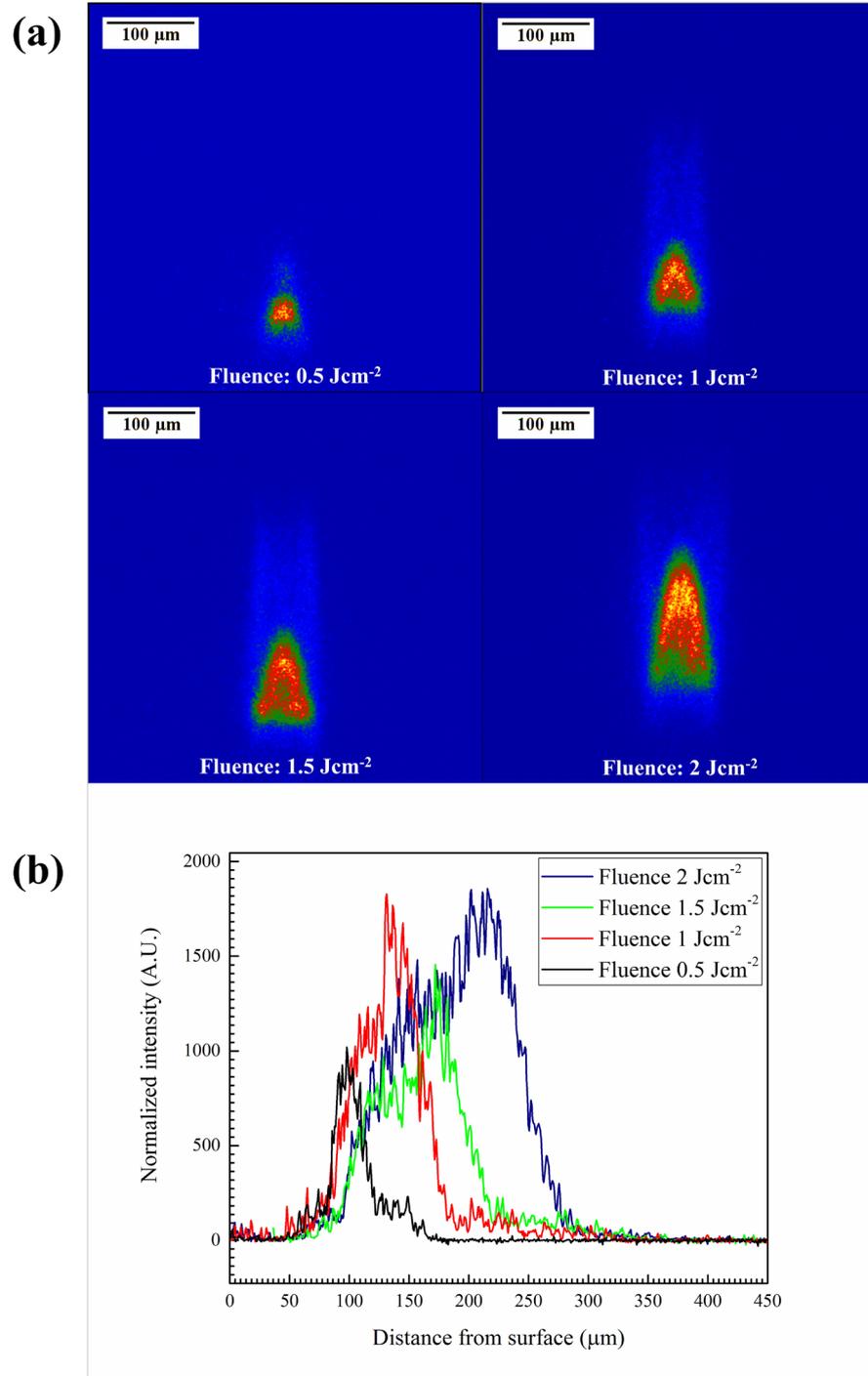


Figure 5.18: Spatial image (a) and intensity profile (b) of the plasma plume at a time delay of 300 ns for 1030 nm femtosecond laser fluence of 0.5, 1, 1.5 and 2 Jcm⁻²

The central part of the slower component of the plasma plume was found to travel more distance than the edge of the plasma plume. This is because the variation of fluence across the surface of the film due to the beam shape.

The plasma plume at a longer delay was achieved using comparatively long gate width (GW). Figure 5.19 indicates the existence of plasma plume at a delay of 300, 500 and 1000 ns using fluence of 1 Jcm⁻². The spot diameter of the laser beam at the surface was measured to ~60 μm. Each image at long delay presents gate width of 100 ns.

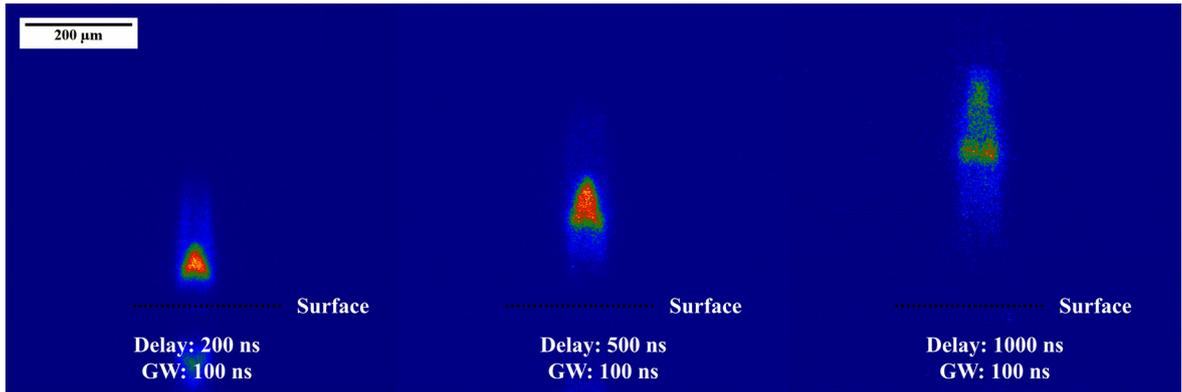


Figure 5.19: Expansion of 1030 nm single pulse femtosecond laser (absorbed fluence 1 Jcm^{-2}) produced Molybdenum thin film plume at delay of 200, 500 and 1000 ns. The gate width was kept at 100 ns. The black dotted line represents the top surface of the thin film.

It was identified clearly that the distance travelled by the comparatively slower component of the plasma plume increases with time, also the intensity of the slower part of plasma plume decreases with longer delay.

The imaging of the plasma plume produced by the interaction of femtosecond laser pulse with molybdenum samples provides the following pieces of information:

- (a) Spatial profile of the plasma plume is different for bulk and thin film ablation by femtosecond laser pulses. Two distinct parts of plasma plume are observed for the interaction of laser pulse with molybdenum bulk and thin film samples.
- (b) Interaction of femtosecond laser with molybdenum at green wavelength provides different plasma emission than IR. The plasma plume is comparatively more intense than that at other wavelengths.
- (c) At a fixed wavelength, the parameters, stopping distance, average velocity increases with increasing fluence.

Real-time plasma imaging of molybdenum film at different fluences at 1064, 532 and 355 nm nanosecond laser wavelengths will be discussed in the next section.

5.2.3. Spatial imaging of plasma plume during ablation of molybdenum thin film by short pulse laser

Figure 5.20 shows nanosecond laser-produced plasma at different time delay using a wavelength of 1064 nm. Each image was taken at a gate width (exposure time) of 5 ns at an interval of 10 ns. Mushroom shaped plasma plume was observed which is entirely different than the ‘jet-like’ femtosecond laser produced plasma. The evolution of mushroom shaped plasma plume at fluence value of 1, 1.5 and 2 Jcm^{-2} is shown in the Figure 5.20.

Primary observation indicates that the forwarded part of the plasma plume is less intense than the delayed part at early time ($\sim 20 \text{ ns}$). The intensity of the delayed part of plasma plume decays very quickly and the relative intensity of the forwarded part increases. It was also found that the plasma stays near to the surface of the sample as the maximum height of the plume is less than the femtosecond case.

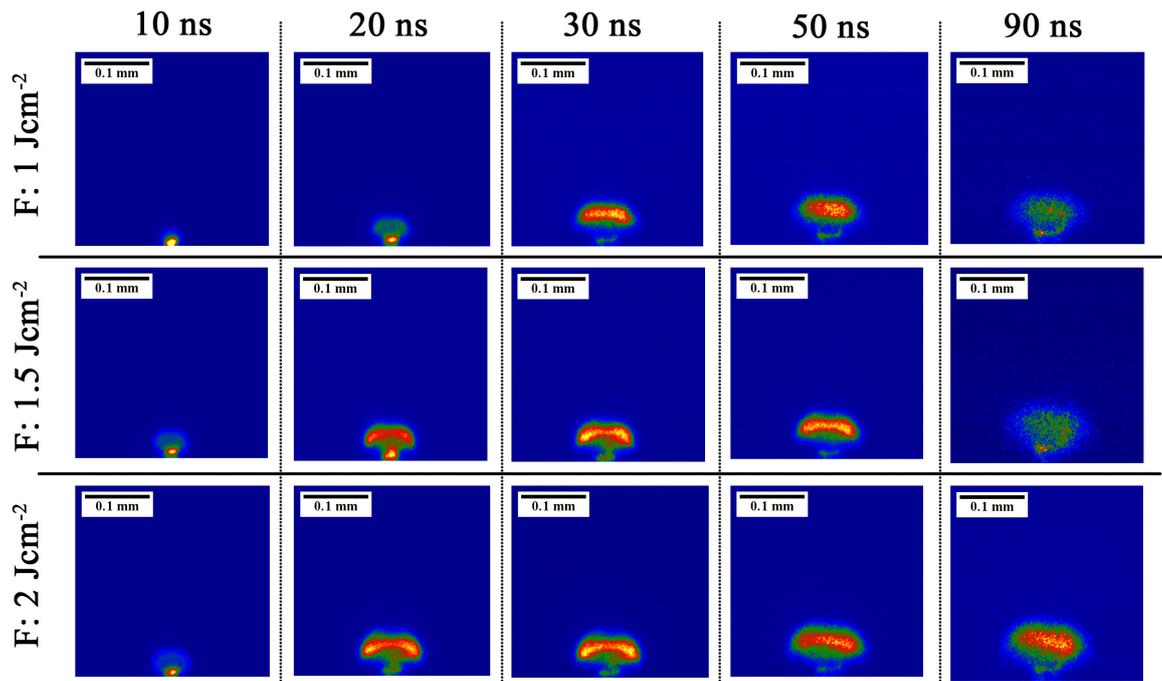


Figure 5.20: Expansion of 1064 nm nanosecond laser produced plasma plume on molybdenum thin film at absorbed fluence of 1.0, 1.5 and 2.0 Jcm⁻²

Detection of plasma plume was also performed during the interaction of femtosecond laser with molybdenum thin film using wavelength of 532 and 355 nm at different peak absorbed fluences. Figure 5.21 and Figure 5.22 present the spatial distribution of plasma profile at 1, 1.5 and 2 Jcm⁻² using nanosecond laser wavelength of 532 nm and 355 nm, respectively. ‘Mushroom’ shaped plasma profiles were also observed for green and UV nanosecond laser wavelength. It was observed that the intensity of the plume decreases with the absorbed laser fluence. As the response of the detector sensor (quantum efficiency) (chapter 3, section 3.6.2.1) is maximum at green wavelength, the MCP gain was reduced to 100 to visualise plasma in case of interaction of molybdenum thin film with nanosecond laser of wavelength of 532 nm. It was observed that the saturation of the intensity of the laser beam takes place at time delay of 20 ns during the interaction of nanosecond laser with molybdenum thin film using wavelength of 532 nm. Screening of incident laser beam by the ejected plasma plume also takes place during the interaction of nanosecond laser with molybdenum thin film. It is also possible that a part of the laser pulse reflects from the surface of the molybdenum thin film to the detector. As a result, as the detector is very sensitive to the green wavelength, saturation of light take place by the ICCD camera.

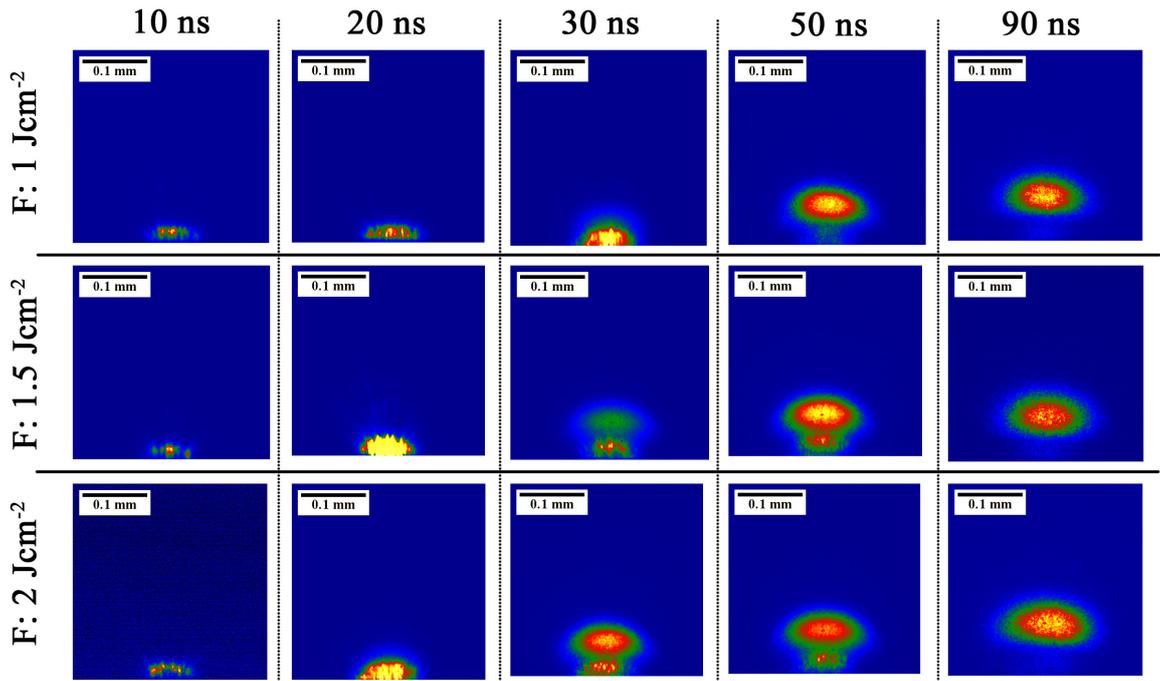


Figure 5.21: Expansion of 532 nm nanosecond laser produced plasma plume on molybdenum thin film at absorbed fluence of 1.0, 1.5 and 2.0 Jcm^{-2}

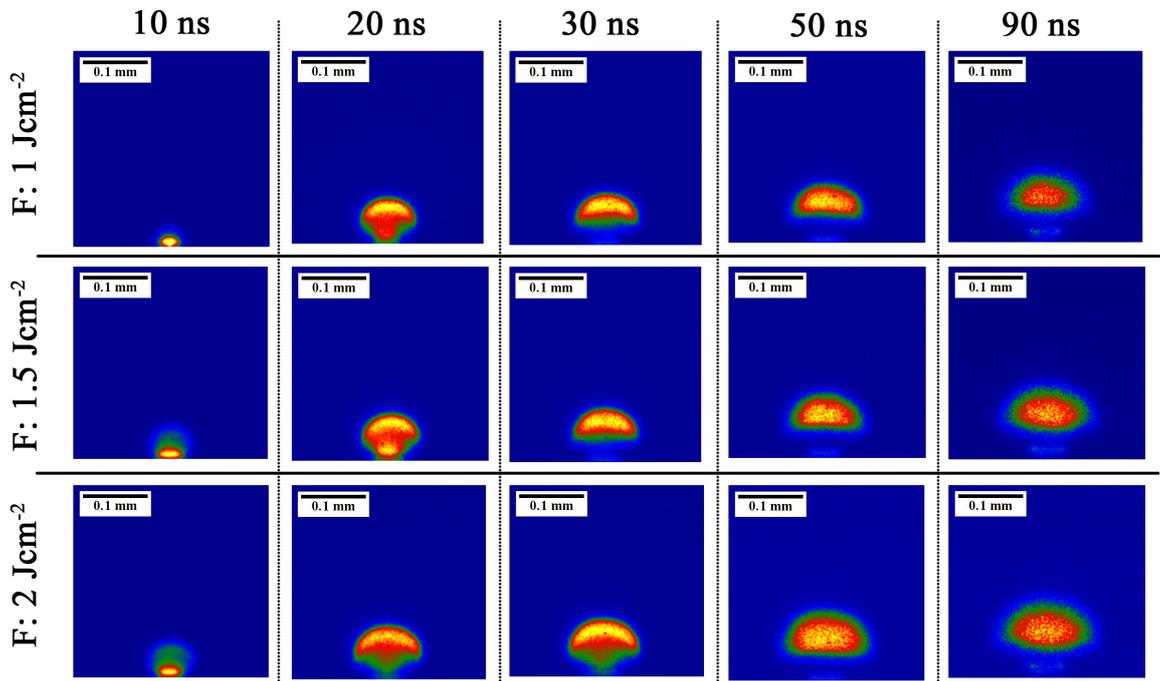


Figure 5.22: Expansion of 355 nm nanosecond laser produced plasma plume on molybdenum thin film at absorbed fluence of 1.0, 1.5 and 2.0 Jcm^{-2}

The intensity of the laser plasma plume increases with increasing the peak value of the absorbed fluence. Similar to the plasma plume generated by the interaction of molybdenum thin film with femtosecond laser, it was observed that the mushroom shaped nanosecond laser produced plasma plume consists of two parts. It was observed that the plasma plume expands in both vertical and horizontal direction.

The vertical expansion of the plasma plume was calculated from the line intensity distribution of plasma at different time delays. Intensity distribution of the laser produced plasma plume provides the vertical expansion of the plasma plume. Vertical propagation of only faster-moving part of plume was measured as the detected slower moving part was less intense and unclear. The propagation of plasma plume was calculated from the vertical intensity profile of the plasma plume and the travelled distance was fitted using the Drag model. Figure 5.23 presents the flight of fast intense part of the plasma plume at fluence value of 0.5, 1, 1.5 and 2 Jcm⁻² using the nanosecond laser of wavelength of 1030 nm. Similarly, Figure A.7 and Figure A.8 shows the vertical distance covered by the faster moving part of the plasma plume produced by nanosecond laser of wavelength of 532 and 355 nm, respectively, at absorbed fluences of 0.5, 1, 1.5 and 2 Jcm⁻². The R² values indicates how well the data fits.

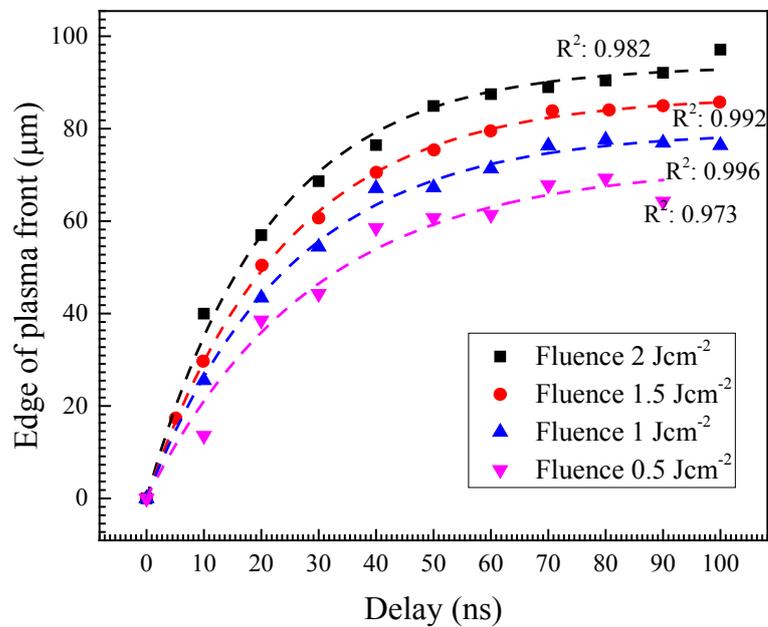


Figure 5.23: Distance travelled by the faster moving part of the plasma plume using the interaction of nanosecond laser (wavelength: 1064 nm) with molybdenum thin film samples at 0.5, 1, 1.5, and 2 Jcm⁻² fluence values

The various parameters, such as stopping distance, average velocity and deceleration coefficient was determined using the exponential fitting of peak position of 1064, 532 and 355 nm plasma and are illustrated in the Table 5.9.

Table 5.9: The stopping distance, average velocity and the deceleration coefficients of fast components of the 1064, 532 and 355 nm plasma plume at different fluences (absorbed).

| Wavelength (nm) | Fluence (absorbed) Jcm^{-2} | Stopping distance (R_0) (μm) | Average velocity ($R_0\beta$) (ms^{-1}) | Deceleration coefficient ($R_0\beta^2$) (ns^{-1}) |
|----------------------------|---|--|--|--|
| 1064 | 0.5 | 72 ± 4 | 2477 | $(3.44 \pm 0.49) \times 10^2$ |
| | 1 | 79 ± 1 | 3186 | $(4.01 \pm 0.19) \times 10^2$ |
| | 1.5 | 87 ± 1 | 3619 | $(4.16 \pm 0.08) \times 10^2$ |
| | 2 | 93 ± 1 | 3953 | $(4.68 \pm 0.27) \times 10^2$ |
| 532 | 0.5 | 97 ± 1 | 2553 | $(2.63 \pm 0.20) \times 10^2$ |
| | 1 | 101 ± 1 | 3364 | $(3.35 \pm 0.08) \times 10^2$ |
| | 1.5 | 111 ± 1 | 3714 | $(3.33 \pm 0.20) \times 10^2$ |
| | 2 | 116 ± 1 | 4352 | $(3.41 \pm 0.12) \times 10^2$ |
| 355 | 0.5 | NA | NA | NA |
| | 1 | 106 ± 1 | 5017 | $(5.43 \pm 0.38) \times 10^2$ |
| | 1.5 | 113 ± 2 | 5266 | $(4.66 \pm 0.48) \times 10^2$ |
| | 2 | 124 ± 1 | 5756 | $(4.05 \pm 0.20) \times 10^2$ |

Figure 5.24 presents the expansion of plasma plume components at a fluence of $0.1 Jcm^{-2}$ (near threshold). At this fluence, a weak plasma signal was observed. The emission from the fast-moving plasma component quickly disappears but the slower component of the plume exists for a longer time. Evidence for ejected matter is observed.

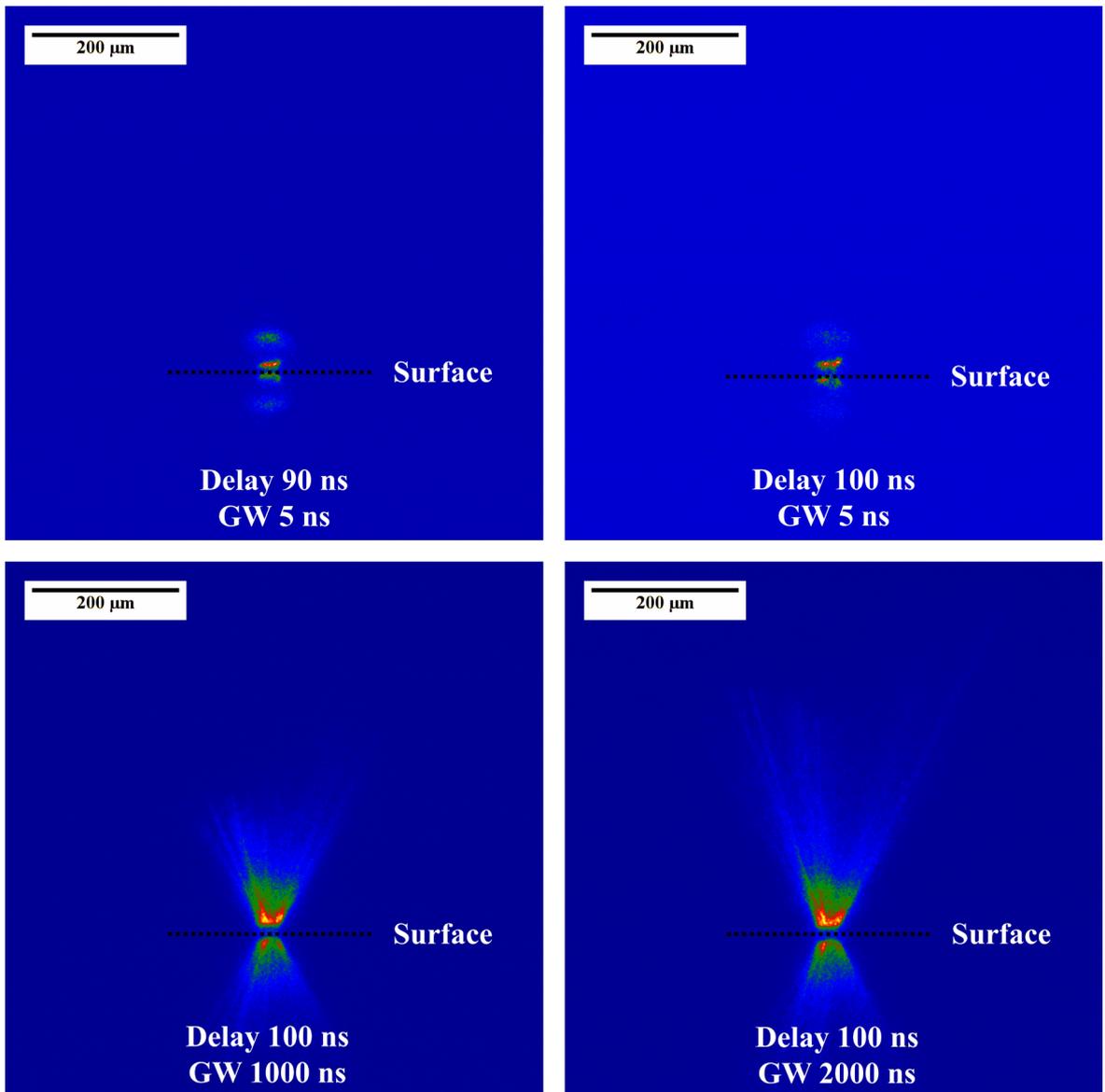


Figure 5.24: Plasma plume imaging of molybdenum film on glass at various gate width (exposure time) at a fluence of 0.1 Jcm^{-2} using 1064 nm nanosecond laser, indicates removal of film.

The plasma plume was observed at long delay at a fluence of 0.5 Jcm^{-2} , well above the threshold fluence of molybdenum film using 1064 nm wavelength. Figure 5.25 presents the ejected plume at a fluence of 0.5 Jcm^{-2} at delay of 200, 500 and 1000 ns when the plasma component does not exist. At these delays, only emission from the slower moving component of the plasma plume was observed.

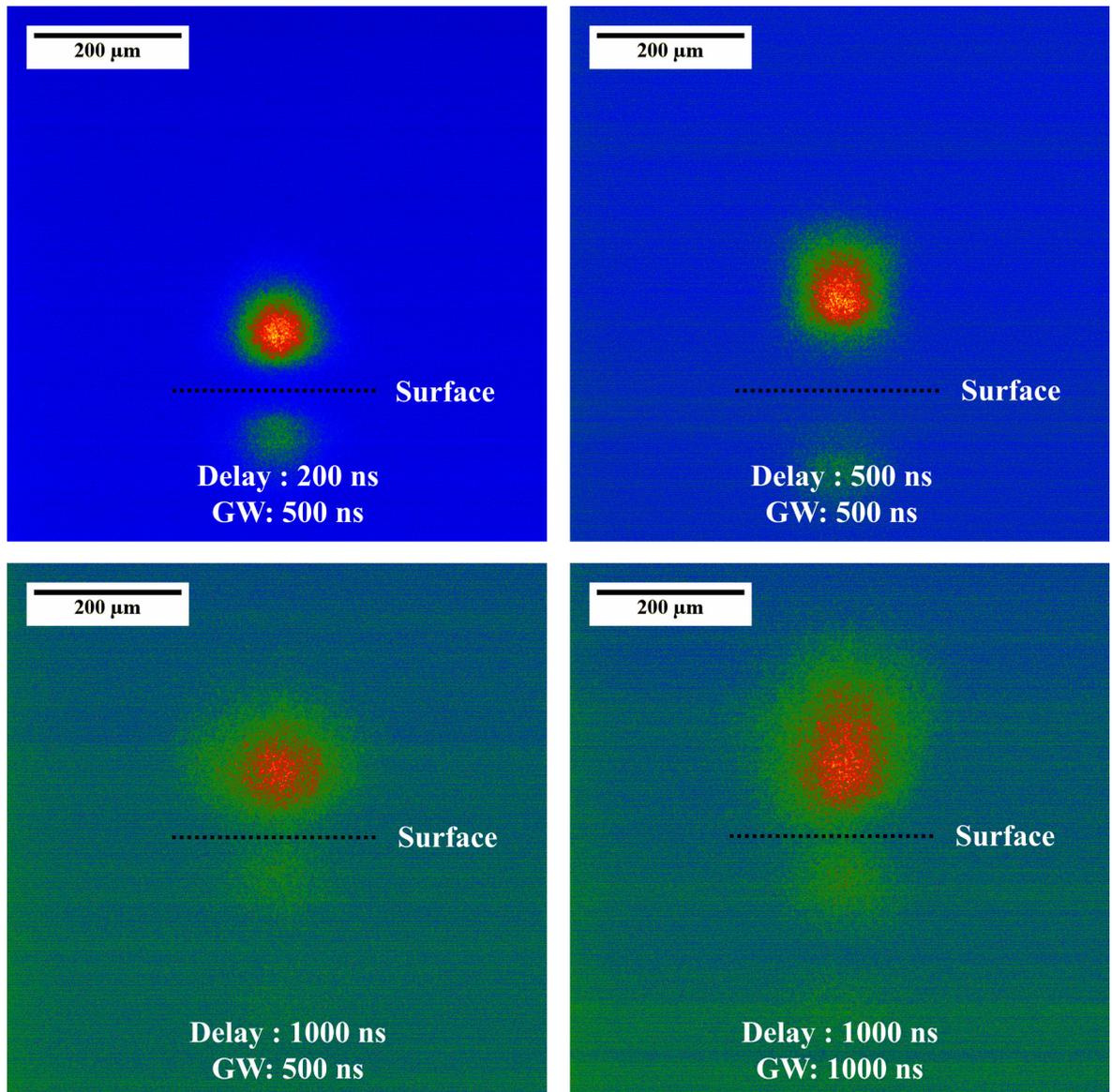


Figure 5.25: Expansion of 1064 nm single pulse nanosecond laser (absorbed fluence 0.5 Jcm^{-2}) produced Molybdenum thin film plume at delay of 200, 500 and 1000 ns.

5.2.4. Discussion

Spectral emissions from the plasma plume evolved by the interaction of femtosecond laser pulse with molybdenum bulk and thin film are presented in Figure 5.2 and Figure 5.4, respectively. The intensity of the LIBS peaks (H) and the background intensity (y_0) increases with increasing peak laser fluence (Table 5.3 and Table 5.4).

When the laser interacts with the molybdenum samples, the free electrons absorb the laser energy and excites to the higher atomic energy level. The energy of the excited electrons couples to the lattice via electron-phonon coupling. When the material removal take place, the electrons and lattice remain energised. The excited electrons bound to the ejected atom relaxes to a lower state via atomic selection rules. Spectral emission from these atomic transitions results in the peaks in the LIBS signal of molybdenum. The de-excitation of electrons to its ground level results in the emission of a photon of energy equivalent to the energy difference between these two electronic energy levels and provides the line emission. An increase of the intensity of the line emission

results from a greater number of excited molybdenum atoms. In the case of molybdenum bulk, the number of molybdenum atoms removed from the sample increases. Also, as the fluence grows up, the amount of molybdenum film removed from the glass surface becomes more. Thus, the amount of atomic transition in the molybdenum increases. As a result, the intensity of peak LIBS intensity increases with increase in applied laser fluence (Figure 5.3 and Figure A.1). Also, with increasing the fluence, the temperature of the removed constituents increases. This may lead to increase of background intensity with increasing laser fluence.

Similar to femtosecond laser ablation, it is observed that from Figure 5.5 that the intensity of the optical emission increases with increasing laser fluence. At the similar fluence level, the intensity of the LIBS signal of the nanosecond laser induced laser plasma plume are found to be higher than that for femtosecond laser ablation. This can be due to further interaction of nanosecond laser pulse with the emitted molybdenum plasma. The evaporated plasma plume is further excited by the laser pulse. As a result, the more emission from the plasma take place and the peak intensity of the peaks of the LIBS spectrum increases. The peak height and the background intensity are also increase with increasing peak laser fluence (Figure A.2).

Also, the FWHM of the peaks in the molybdenum spectrum are expected to increase with increasing laser fluence. As the pulse width of the nanosecond laser pulse (FWHM 9 ns) is longer than the time required for the ejection of ablated species (typically several picosecond) from the thin film, plasma shielding takes place. Plasma shielding leads to higher excitation of ablated species by the laser pulse itself. The excited electrons present in the ablated species results in an electric field. With increasing laser fluence, the amount of excited electron increases and thus the electric field increases. As a result of this electric field, the energies at which the levels are becomes different [235]. As a result, broadening, known as Stark broadening, of emission peaks is expected to observe with the increase of fluence [236, 237]. However, this does not observe here.

Molybdenum bulk plasma plume consists of two components (Figure 5.6, Figure 5.7 and Figure 5.8). The faster-moving part consists of various atomic components like ions, electrons etc. and the slower part is comparatively heavy elements, like neutral particles, clusters etc. [238, 239]. In general, at high fluence, the amount of excited and neutral fragments from the surface are higher compared with low fluence. Similarly, the density of plasma plume (number of emission centres per unit volume) also increases at higher fluence. Thus, at atmospheric pressure, the time required for the excited particles to reach ground state are longer than the time at low fluence. This results in an increase of the stopping distance and average velocity with an increase in the absorbed laser fluence (Table 5.6). The change in velocity of the plasma plume at different fluence caused by the presence of atmospheric pressure by ambient results in deceleration of plasma plume.

The emission from thermalised excited and neutral elements are still observed at longer time delay. The emission from the slower moving component of the plasma plume takes place via atomic transitions of the excited elements of the plume. Also, the broad band spectral emission takes place from the neutral clusters or particle if elements due to their increased temperature is known as black body emission. The black body emission is observed even after several microseconds after the plasma plume disappears. It is proposed that the atomic transitions and the black body emission leads to the emission of radiation from the ejected elements close to the sample surface at longer delay.

Similar to molybdenum bulk plasma plume, the slow and fast-moving component of the plasma plume is observed (Figure 5.12 and Figure 5.13) for thin film ablation by femtosecond laser sources. The intensity of the faster moving component of plasma plume decreases with higher delay. The faster moving component of plasma plume is lighter in weight and consists of several atomic elements like electrons, neutral and ionised particles etc. Because of the light weight of the components of the faster-moving part, they eject quicker (Table 5.7) than the comparatively heavy particles (Table 5.8), clusters or the delaminated film which are the components of the slower part of plasma plume.

Because of the low mass of the components of the faster-moving part, they eject quicker than the comparatively heavy particles, clusters or the delaminated film which are expected to be the slower components of the plasma plume. The origin of the slower part, which is caused from the atomic transition from the excited neutral components and from the thermal (black body) radiation of the hot elements. The quick ionisation rates of the atomic components of the faster part of the plasma plume leads to fast decay of its intensity. Comparatively slower decay rate resulted in longer lifetime of the heavier parts.

The quick ionisation rates of the atomic components of the faster part of the plasma plume leads to fast decay of its intensity. Because of the Gaussian nature of the laser pulse, at longer delay the expansion of the central portion of the slower component of the plasma plume is higher than the edge (Figure 5.18). The intensity of the slower moving part of the plasma decreases with increasing delay. This suggests as the time progresses, the temperature and atomic transition from the slower moving component of the plasma plume decreases (Figure 5.19).

The Mushroom shaped plasma plume produced by interaction of nanosecond laser pulse with molybdenum thin film (Figure 5.20, Figure 5.21 and Figure 5.22). Unlike the femtosecond case, the laser produced plasma plume produced by nanosecond laser pulse stays near the sample surface and thus comparatively smaller stopping distance and average velocity is observed (Table 5.9). As the pulse width of the nanosecond laser source is larger, the laser pulse further interacts with the ejected plasma plume and the intensity of the plasma plume increases.

Numerical simulation suggests at these fluences, the temperature of the substrate (BK7) reaches beyond its vaporisation temperature (section 4.2.3.2). The vertical stress on molybdenum film by the vaporised glass becomes stronger and comparatively higher velocity of plasma plume was observed. As a result, the components of plasma plume consist of excited and neutral molybdenum with vaporised glass.

When laser energy is deposited on the surface of a metal, the following phenomena can happen,

1. Emission of surface electrons take place due to photoelectric and thermionic emission phenomena.
2. Electron-phonon coupling take place and electronic energy transfers to lattice.
3. Further interaction of laser pulse with the ablated plume (for longer laser pulses e.g. nanosecond laser).

The photon energy ($h\nu$) of the laser pulse is absorbed by the free electrons present in the molybdenum and the electrons gain their kinetic energy. When the energy of the electron exceeds the work function ($e\phi$) of the metal, the electrons are emitted from the metal [65, 240, 241] if they travel in the direction of the surface. The emitted electrons are known as photoelectrons. The emitted electrons eject with an effective kinetic energy in the ambient equal to,

$$E_k = (h\nu - e\phi) \quad (29)$$

The excited electrons remaining in the metal surface undergo electron-electron scattering. Because of the electron-electron scattering, a very high electron temperature (T_e) establishes in the sample. The number of escaped electrons (J) per unit surface area per unit time is given by the Richardson equation, given by, [241-243]

$$J = \frac{e}{2\pi^2\hbar^3} (kT_e)^2 \exp\left(-\frac{e\phi}{kT_e}\right) = AT_e^2 \exp\left(-\frac{e\phi}{kT_e}\right) \quad (30)$$

where, k is the Boltzmann constant and $\hbar = \frac{h}{2\pi}$, where h is the Planck's constant. The value A is known as a constant known as Richardson coefficient equal to $1.20 \times 10^6 \text{ Am}^{-2} \text{ K}^{-2}$. The number of thermionic electrons escaped per unit area per unit time was estimated for molybdenum. Figure 5.26 presents the number of thermionic electrons escaped from the surface of molybdenum as a function of electron temperature,

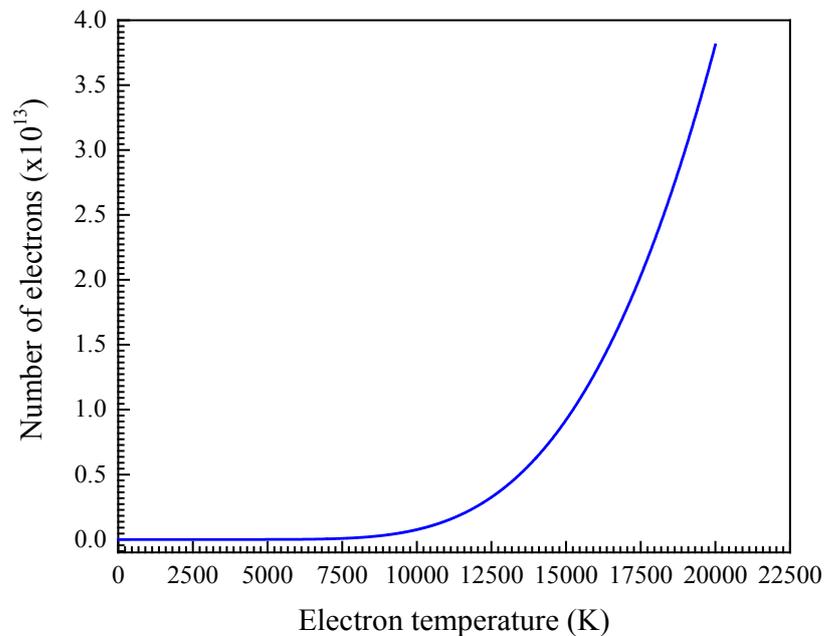


Figure 5.26: Estimated number of electron emitted per unit area per unit time from molybdenum with corresponding electron temperature

Thus, for the higher electronic temperature, the greater electron emission takes place from molybdenum. The peak electron temperature was estimated at different absorbed fluences for IR (1030 nm) and green (515 nm) wavelength.

Figure 5.27 presents the peak electron temperature as a function of the laser fluence absorbed by molybdenum simulated from the TTM simulation (Section 3.7.2). The temperature of electronic subsystem increases with increasing laser fluence. Also, it was found that at a particular fluence, the peak temperature of electron increases with decreasing wavelength (from 1030 nm to 515 nm). Thus, at a constant same absorbed fluence, the number of emitted thermionic electrons is to be more at Green (515 nm) than IR (1030 nm) wavelength.

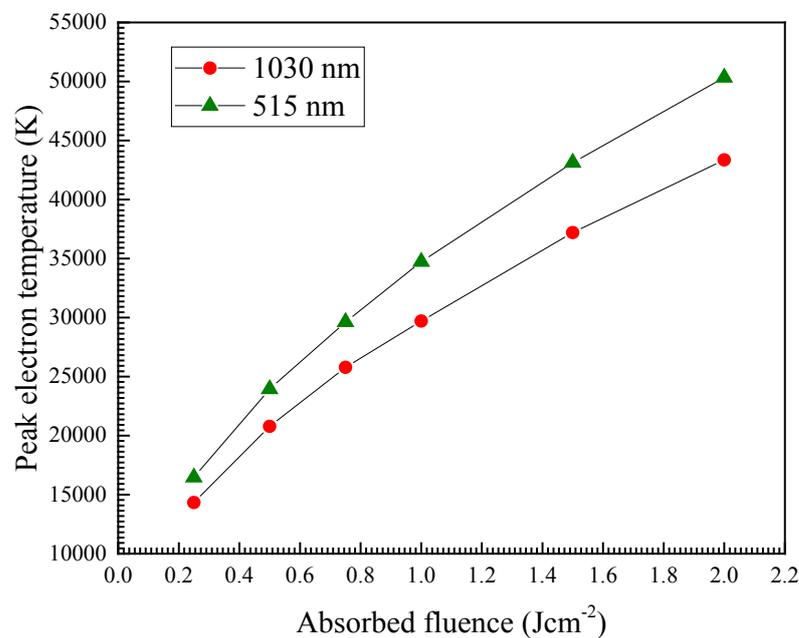


Figure 5.27: Numerical simulation predicts increase of absorbed fluence leads to increase of peak temperature of electron. At a particular fluence, 515 nm laser produced electron becomes hotter than electrons generated by 1030 nm laser pulse

The band structure of molybdenum was understood by several groups using augmented plane wave - non self-consistent (APW-NSC) [244], Korringa-Kohn-Rostoker - self-consistent (KKR-SC) [245], non local pseudopotential - self-consistent (NPL-SC) [246], APW-SC [247], linear combination of Gaussian orbitals - self-consistence (LCGO-SC) method [248]. Figure 5.28 presents the self-consistent band structure of energy bands of body centre cubic (BCC) molybdenum, obtained by a linear combination of Gaussian atomic orbitals using local density approximation (LDA) method [248].

The energy dispersion curve (E vs k) of the molybdenum lattice is obtained by the overlap and hybridization of an electron s-p band with d-band electrons. In the case of molybdenum, the Fermi energy (E_F) exists in a range of energies in which the occupancy of the d-electron density of state is not large.

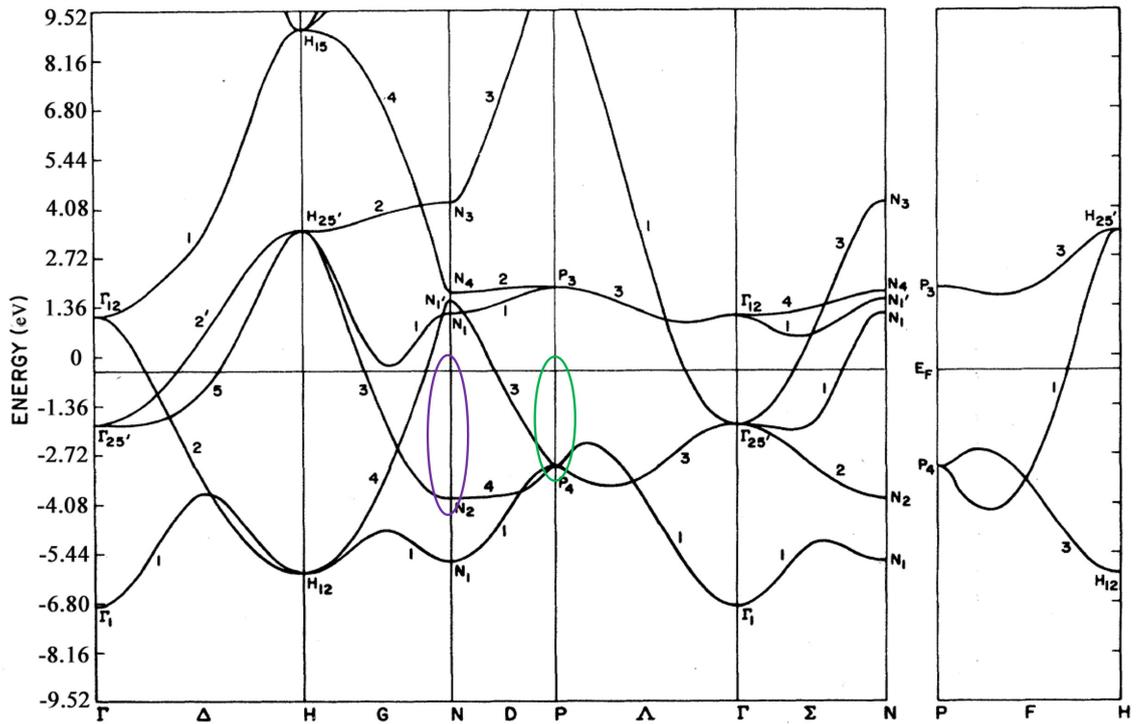


Figure 5.28: Electronic band structure of bcc molybdenum crystal, adapted from [248]. The insert shows the possibility of interband absorption during interaction of Green and UV laser photon with molybdenum sample, adapted from [248].

The number of electron states is maximised when the dispersion curve (E vs k curve) becomes flat. In this figure, the separation between $H'_{25} - \Gamma_1$ is known as the s-d band width and found to be 10.35 eV. Similarly, the energy difference between H'_{25} and H_{12} (9.42 eV) measures the width of the d-band. The solid line indicates the Fermi energy (E_F) of the molybdenum lattice. In general, the electrons are occupied below the Fermi energy (E_F) and above this, electron occupancy is zero. It is found from the literature that the density of states above the Fermi energy (E_F) come from the outermost electron ($5s^1$) [248]. The peak of the density of states from the $5s^1$ is found to be 2.24 eV [248].

At room temperature, the free electrons occupy the higher electronic energy levels. The energy differences between the occupied portion of the s-d band ($E_F - \varepsilon(\Gamma_1)$) and d band ($E_F - \varepsilon(H_{12})$) are found to be 6.47 and 5.55 eV, respectively. Below E_F , there are three main curves observed (Figure 5.28) and found to be at -3.92, -3.02 and -1.64 eV, relative to E_F . Apart from these points, the electronic band structure indicates energy differences of -2.61 and -3.51 eV between the Fermi energy and the points P4 and N2 on the energy band [248], respectively. These two energy differences suggest that absorption of energy by the free electrons from the P4 and N2 to the Fermi energy by green and UV photons is possible. The flat dispersion curve at these points also suggests a high probability of electron transition by absorbing green and UV photon to the Fermi energy. The interband optical conductivity of molybdenum [249, 250] at green and UV wavelength is therefore higher than the IR wavelength [248, 249]. The IR transition is expected to take place from Fermi level (E_F) to upper empty states by the intraband transition. Thus, the molybdenum plasma is at green wavelength (Figure 5.13) becomes more intense and energetic than IR wavelength (Figure 5.14).

The remaining energy in the free electron after the photoelectric effect and the thermionic effect, couples to the lattice into the molybdenum lattice by electron-phonon scattering. The electron and lattice set in an equilibrium by electron-phonon coupling. The increase of the temperature of the lattice resulted in the structural and mechanical changes in the sample. The energy lost by the thermionic and photoelectric emission are higher for green wavelength than the IR wavelength. Thus, in case of IR laser wavelength, a higher fraction of energy couples to molybdenum lattice than green laser. This causes lower damage threshold of molybdenum by IR femtosecond laser pulse than green wavelength.

When a laser of certain wavelength incident on a sample surface, free electrons of a particular energy band absorbs the laser energy and they excites to an upper energy state. Electrons at different energy state respond to the incident laser wavelength differently. We expect that upon the irradiation of UV wavelength, the electrons absorb the UV energy and the coupling of energy to the lattice take place very quickly. This results in a rapid increase of lattice energy which ultimately results in mechanical fracture in the thin film. The coupling of a higher amount of UV laser energy to the molybdenum lattice results in lowering of damage threshold of molybdenum.

5.3. Conclusions of the chapter

This chapter provides online characterisation of laser-produced plasma by analysing spectral and spatial images.

(a) Spectral imaging:

1. Existence of molybdenum was detected from the spectral imaging of molybdenum bulk and thin film by femtosecond laser at wavelength 1030 nm. The spectral response of the plasma plume originates from the atomic transitions in the excited molybdenum constituents.
2. The increase of the intensity of molybdenum peaks suggests increase of molybdenum removal with increasing laser fluence. Also, the background intensity at those peak increases which indicates increases of temperature of the ejected components of the plasma plume.
3. The increase of laser fluence resulted in an increase in the electric field at the electron cloud of the ablated components. Stark broadening was observed with increasing laser fluence. Thus, with increasing applied laser fluence, broadening at the molybdenum peaks take place.

(b) Spatial (plasma) imaging:

1. Plasma imaging of at various delay was performed for molybdenum bulk and thin film by femtosecond laser. Initially, only one component of plasma plume was observed, and the splitting of the plume take place at ~ 10 ns.
2. The intensity of the plasma plume increases with increasing laser fluence.
3. Initially, the relative intensity of the faster component of the plasma plume is found to more intense than the slower component. At longer time, the relative intensity of slower component becomes more intense.

4. Different component of the plasma plume expands at the ambient and it was found that for femtosecond laser ablation of molybdenum bulk, the vertical expansion of plasma is more than the horizontal expansion.
5. The stopping distance and the velocity increases with increasing laser fluence. Generally, the fast-moving component consists ions, electrons and lighter neutral particles. With increasing laser fluence, lighter and heavier particles eject from the sample which lead to an increase of plasma intensity. Also, it was found that the forwarding component of the plasma plume expands exponentially away from the surface of the molybdenum sample.
6. In case of molybdenum thin film, two components of the plasma plume were observed during interaction of femtosecond laser beam. Although, the spectral calibration of the ICCD was not performed for plasma imaging, it was observed that the average velocity and the stopping distance of the 515 nm plasma plume is higher than 1030 nm plasma plume.
7. The faster component of the plasma plume of molybdenum thin film expands exponentially at a direction vertically away from the surface. And the intensity of the component decreases with increasing delay. It was also observed that the intensity of this faster moving component decreases rapidly, and it disappears after almost 100-200 ns, although the decay depends upon the applied laser fluence.
8. The expansion of the slower component was found almost linear and the intensity of this component does not decrease as rapidly like the faster component consisting ionised particles.
9. In case of interaction of nanosecond laser with molybdenum film, a comparatively smaller and mushroom shaped plasma was observed. The splitting of the plasma take place at a longer delay.
10. It was found that the plasma stays close to the surface and the plasma expansion take place both vertically and horizontally. Compared with femtosecond case it was found that a less vertical expansion take place during nanosecond laser ablation.

(c) Plasma shielding:

In the case of multi-pulse laser processing, for example in the case of making channels, scanning speed is an important factor. For the cases of femtosecond and nanosecond laser ablation, the plasma plume was observed for at least 2 μ s from the time when the laser pulse incident on the sample surface. It is expected that the laser induced plasma plume exists for 10 μ s. Thus, in the case of laser ablative processing, plasma shielding is not expected for laser repetition rate below 100 kHz.

Chapter 6: Interaction of laser pulses with molybdenum based heterostructure

In this chapter, the structuring of the molybdenum-based multi-layered heterostructure by the interaction with laser pulses will be presented. The multi-layered heterostructure is referred to MAM and consists of an aluminium layer sandwiched between two thin molybdenum layers (Chapter 3, section 3.2.2). This multilayered thin film is deposited on indium tin oxide (ITO)/soda lime glass (SLG). This chapter mainly focusses on

1. Micro- and nano-structuring and surface modification of MAM samples by a femtosecond laser of wavelength of 1030 (IR), 515 (green) and 343 (UV) nm using a range of absorbed laser fluences.
2. Micro-structuring of MAM samples a nanosecond laser of wavelength of 1064 (IR), 532 (green) and 355 (UV) nm by different peak fluences.
3. Morphological characterisation of femtosecond and nanosecond ablated craters by the scanning electron microscopy (SEM) and atomic force microscopy (AFM) techniques.
4. The elemental analysis of the ablated craters by the energy dispersive X-ray (EDX) technique.
5. Numerical simulations of ultrashort and short pulse laser ablation on the multi-layered MAM sample at low fluence to understand the material response.

Laser processing of MAM was carried out by femtosecond and nanosecond lasers at 1030, 515 and 343 nm wavelengths. When a laser pulse is incident on the MAM sample, a significant fraction of the laser energy reflects from the surface of the molybdenum layer. A small portion of the incident laser beam is transmitted from the molybdenum layer and absorbed by the aluminium layer underneath. Thus, to measure the amount of optical energy absorbed by the material, reflectivity and transmissivity measurement were undertaken place using an integrating sphere.

6.1. Reflectivity measurement by integrating sphere

The reflectivity and transmissivity of multi-layered MAM were performed using an integrating sphere (3.2.2). The laser fluence used in the reflectivity measurements was less than the value of 0.02 Jcm^{-2} . Table 6.1 presents the fraction of the laser beam reflected by the MAM surface in the presence of femtosecond and nanosecond laser at IR, green and UV wavelength.

Table 6.1: Reflectivity (R) of multi-layered MAM under femtosecond and nanosecond laser pulse using an integrating sphere

| <i>Wavelength</i> | <i>Reflectivity (R)</i> | |
|-------------------|---------------------------|---------------------------|
| | <i>Femtosecond laser</i> | <i>Nanosecond laser</i> |
| <i>IR</i> | 0.68 ± 0.01 (1030 nm) | 0.47 ± 0.01 (1064 nm) |
| <i>Green</i> | 0.51 ± 0.01 (515 nm) | 0.54 ± 0.0 (532 nm) |
| <i>UV</i> | 0.50 ± 0.03 (343 nm) | 0.38 ± 0.02 (355 nm) |

The fraction of the incident light that is transmitted through the MAM sample was also measured using the integration sphere. A negligible amount (less than 0.01 %) of the incident laser intensity was detected after the beam transmits through the MAM sample. Thus, the transmitted amount was neglected in the further calculations. The factor (1-R) multiplied by the incident energy of the laser pulse provides the laser energy absorbed by the MAM sample. For simplicity, it was assumed that the reflectivity (R) does not depend on the intensity of the laser pulse.

In the following section, the structuring of MAM by femtosecond and nanosecond laser pulses will be discussed. Prior to the processing of the MAM samples by different laser sources, the sample surface was cleaned by passing air through an air blower; this removed any specks of dust from the surface of MAM samples.

6.2. Processing of MAM by femtosecond (FS) laser source

Femtosecond laser beam of wavelengths of 1030, 515 and 343 nm was focussed by a beam delivery system using a galvanometer (chapter 3, section 3.3.1). The energy of the laser pulse was varied externally using a combination of a half-wave plate and a beam splitting cube. Figure 6.1 presents the optical microscope images of the different craters produced on the MAM surface at different absorbed femtosecond laser fluence. All the fluences indicated in the Figure 6.1 are the peak value of absorbed fluence.

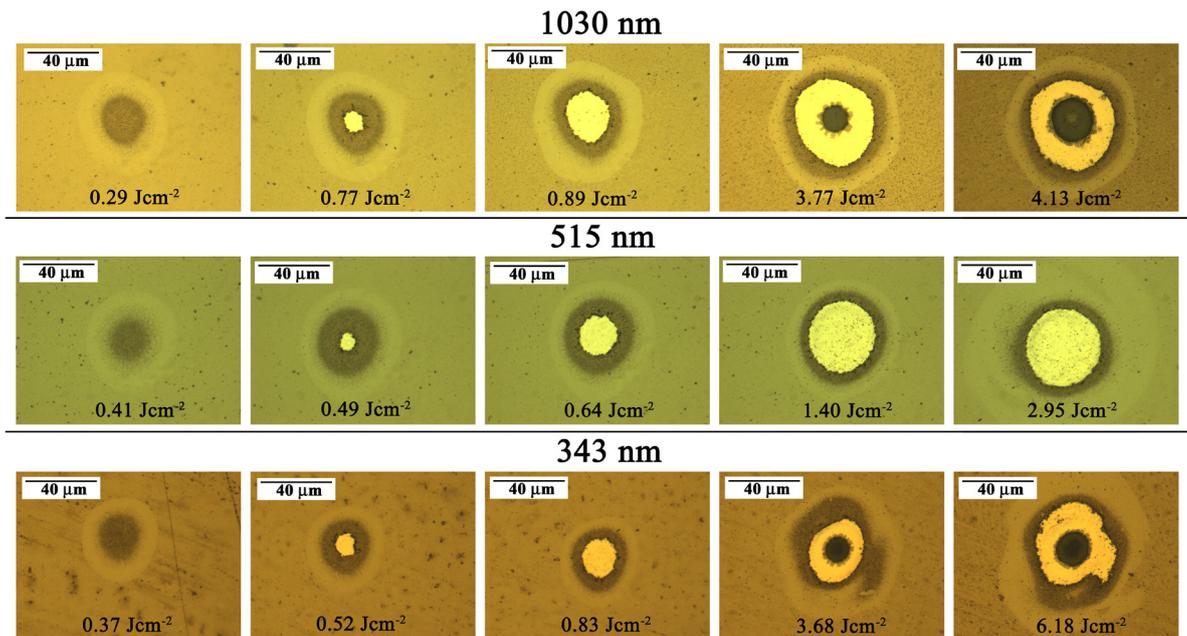


Figure 6.1: Optical microscope images of different craters on MAM surface at different absorbed fluences using 1030, 515 and 343 nm single pulse femtosecond laser.

Different features on MAM surface are observed from the Figure 6.1. At low fluence, two diameters are observed from fluences of 0.29 (1030 nm), 0.41 (515 nm) and 0.37 (343 nm) Jcm^{-2} . An increase of the fluence of the laser pulse results in the formation of a third crater inside the two outer craters (1030 nm: 0.77, 0.89 Jcm^{-2} ; 515 nm: 0.49, 0.64, 1.40 and 2.95 Jcm^{-2} ; 343 nm: 0.52, 0.53 Jcm^{-2}). It is observed that the outer diameter of the craters produced by 343 nm femtosecond laser is not perfectly circular. This is due to the imperfect spatial shape of the laser beam (343 nm: 3.68 and 6.18 Jcm^{-2}) at the time of the study. The diameter of the outermost feature is described

as D1; the inner diameters are followed by D2, D3 and D4. Figure 6.2 shows how the different diameters D1, D2, D3 and D4 are associated with features on the surface of MAM. At low fluence, a feature with two concentric features of diameters D1 and D2 are observed (Figure 6.2a). While features with four diameters are observed on the surface of the MAM at high fluence (Figure 6.2b)

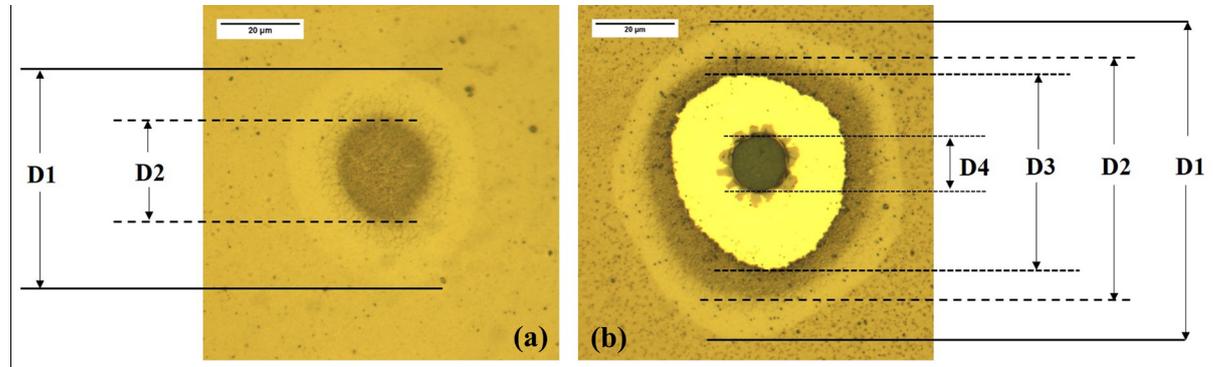


Figure 6.2: Nomenclature of different diameters created on multi-layered MAM surface at (a) low (0.29 Jcm^{-2}) and (b) high (3.77 Jcm^{-2}) fluence, wavelength 1030 nm , as observed by the optical microscope.

Furthermore, after the interaction of 515 nm femtosecond laser pulse with the MAM sample using the galvanometer beam delivery setup, the features with diameter D4 was not obtained from the optical microscope images. The reason for this could be of the high damage threshold fluence of the feature associated with diameter D4 for 515 nm femtosecond laser pulse. A fixed lens beam delivery system, numerical aperture (NA) 0.13 , (experimental setup described in section 3.2) was used to achieve higher laser intensity and thus the laser fluence to make D4 on MAM surface using this wavelength. Figure 6.3 presents an optical microscope image of a crater on MAM surface using 515 nm femtosecond laser at a fluence of 6.6 Jcm^{-2} . The spot radius of the 515 nm femtosecond laser beam using fixed lens setup was determined by Liu's method and calculated to be $8.2 \pm 0.03 \mu\text{m}$.

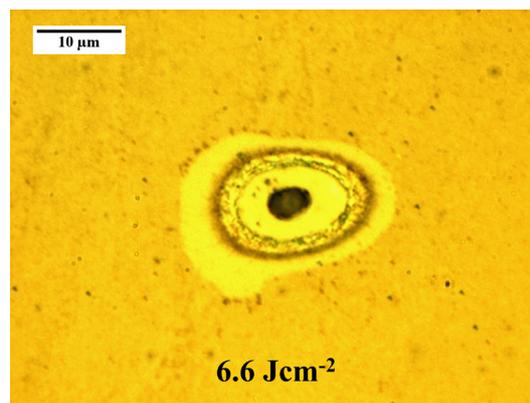


Figure 6.3: Optical microscope image of crater on MAM surface after irradiation of 515 nm femtosecond laser of fluence 6.6 Jcm^{-2} , numerical aperture (NA) of the focusing lens: 0.13 .

6.2.1. Measurement of threshold fluence

The relationship between the threshold fluence with different diameters on the MAM surface is presented in Figure 6.4. The Gaussian-shaped laser pulse is responsible for a Gaussian fluence distribution on the surface of MAM. The threshold fluence required to obtain the diameters D1, D2, D3 and D4 are denoted as F^{D1} , F^{D2} , F^{D3} and F^{D4} . Thus, a Gaussian-shaped laser beam of a

particular fluence (F) results in different fluence regimes on the surface of the MAM sample. For example, if a laser beam of peak fluence of F , where $F > F^{D4}$, incident on the surface of the multi-layered MAM sample, five types of fluence regime were observed on the sample surface. By the increasing order, the fluence regimes are defined as on the multi-layered film surface, given by $F < F^{D1}$, $F^{D1} < F < F^{D2}$, $F^{D2} < F < F^{D3}$, $F^{D3} < F < F^{D4}$ and $F > F^{D4}$. When the peak fluence is higher than F^{D1} , but less than F^{D2} , ($F^{D1} < F < F^{D2}$) the observed diameter on the MAM surface is $D1$. Thus, two fluence regimes are observed given by $F < F^{D1}$ and $F^{D1} < F < F^{D2}$. Features with two diameters were noticed when the peak fluence is higher than F^{D2} , but less than F^{D3} ($F^{D2} < F < F^{D3}$). Similarly, additional diameters $D3$ and $D4$ were observed for the fluences $F^{D3} < F < F^{D4}$ and $F > F^{D4}$.

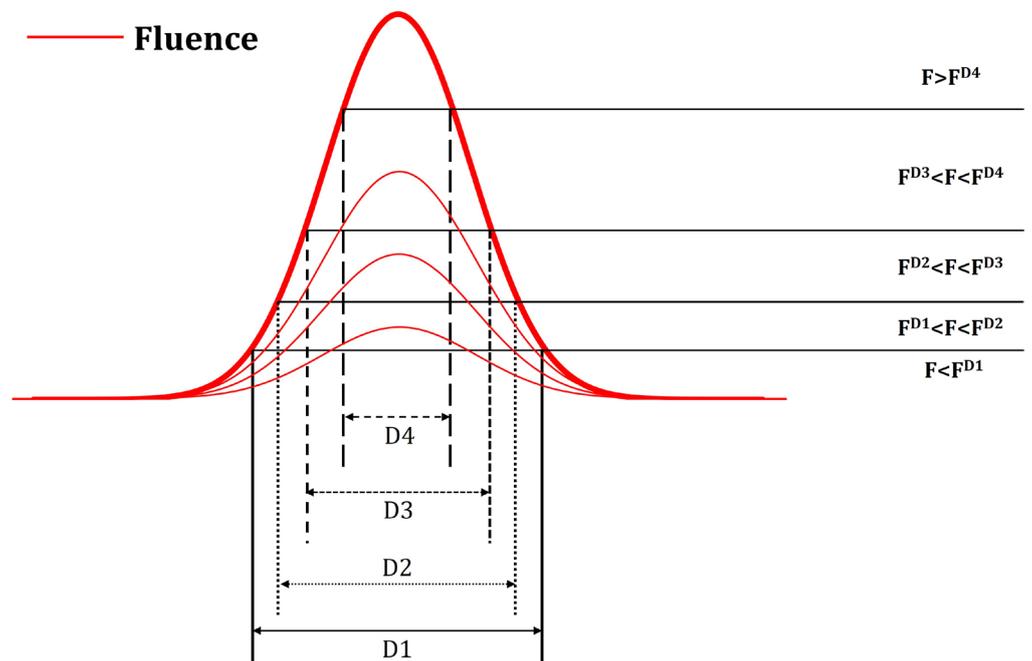


Figure 6.4: Understanding of different fluence regimes associated with the various diameters on MAM surface by a spatially Gaussian femtosecond laser source.

Figure 6.5 presents the relationship between the squared diameter and the natural logarithm of absorbed fluence for diameters $D1$, $D2$ and $D3$ using wavelengths of 1030, 515 and 343 nm. The squared diameter of the craters increases with increasing the absorbed fluence. The dependence of the diameter of the focused laser beam and threshold fluence were calculated by linear fitting of the squared diameter, D^2 (Y-axis), to the natural logarithm of the peak value of the absorbed fluence (X-axis). Different values of threshold fluences corresponding to each feature are tabulated in Figure 6.5.

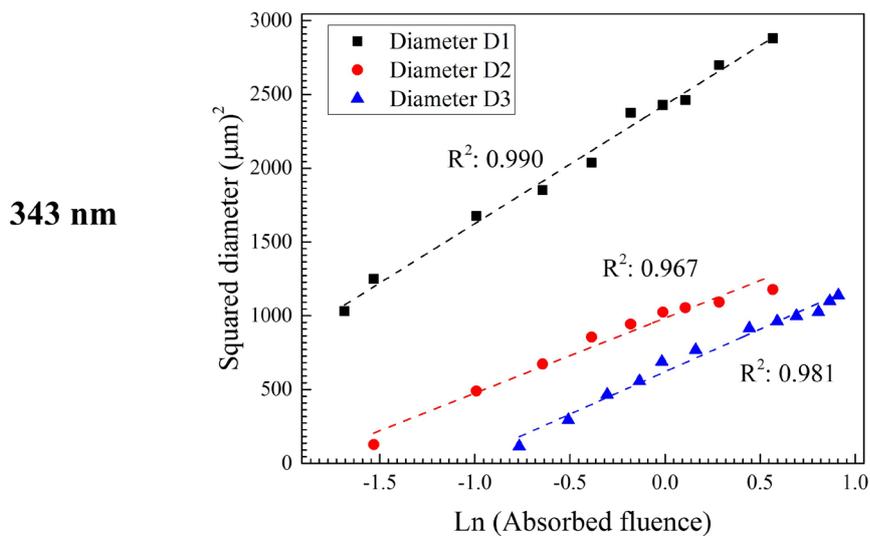
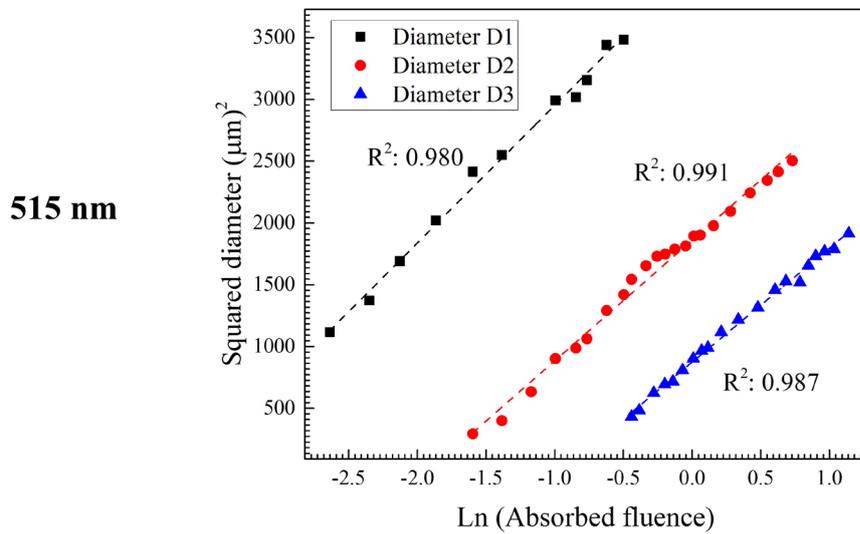
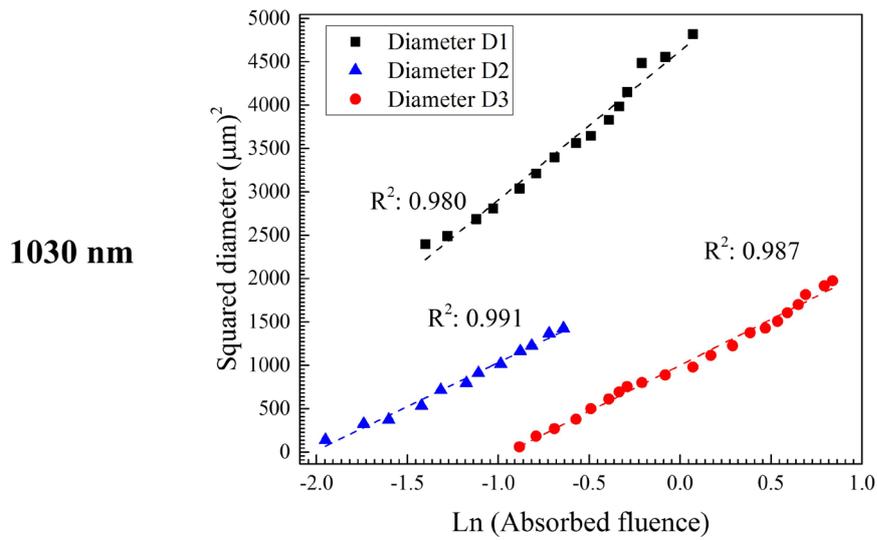


Figure 6.5: The relationship between the squared diameter and logarithmic fluence to determine different threshold fluence associated with the square diameters D1, D2 and D3, for a femtosecond laser of a wavelength at 1030, 515 and 343 nm.

The amount of absorbed fluence to achieve D1, D2 and D3 on a MAM surface and termed as F^{D1} , F^{D2} and F^{D3} by three different laser wavelengths are presented in Table 6.3.

Table 6.2: The estimated threshold fluence required to produce the diameters D1, D2 and D3 by femtosecond laser ablation using 1030, 515 and 343 nm wavelength.

| Threshold fluence corresponding diameter | Threshold Fluence (Jcm^{-2}) | | |
|---|--|-------------------|-------------------|
| | 1030 nm | 515 nm | 343 nm |
| F^{D1} | 0.068 ± 0.005 | 0.026 ± 0.001 | 0.019 ± 0.006 |
| F^{D2} | 0.133 ± 0.001 | 0.162 ± 0.004 | 0.117 ± 0.009 |
| F^{D3} | 0.348 ± 0.003 | 0.422 ± 0.001 | 0.384 ± 0.008 |

The upper molybdenum layer experiences no observable physical damage, detected by optical microscopy, below F^{D1} . Also, for fluence regimes defined by $F^{D1} < F < F^{D2}$, only visual changes in molybdenum take place without any significant damage, and the structural changes remain the same as the laser unaffected regime ($F < F^{D1}$). The threshold fluence (F^{D1}) decreases with decreasing wavelength of the incident laser pulse. The absorption coefficients of the incident laser pulse at wavelengths 1030, 515 and 343 nm are given by 5.17×10^5 , 9.32×10^5 and 1.18×10^6 cm^{-1} , respectively [148]. Exponential decay of the incident laser intensity inside molybdenum suggests that the optical penetration depth of 19.5, 10.8 and 8.4 nm for the wavelengths 1030 (IR), 515 (green) and 343 (UV) nm, respectively. Thus, the intensity of the laser beam is more confined at the surface of molybdenum at a lower wavelength. This results in a decrease of threshold fluence (F^{D1}) with lower values of laser wavelength.

However, comparatively higher threshold fluence values were observed to obtain the circular craters of diameters of D2 (F^{D2}) and D3 (F^{D3}) on the surface of MAM for 515 nm femtosecond laser when compared with 1030 and 343 nm wavelengths. This is probably lower optical penetration depth of the green and UV wavelengths in MAM sample when compared penetration by IR laser wavelength.

A further increase of the laser fluence resulted in an additional feature of diameter D4. An estimation of F^{D4} was performed using the Liu's method and the estimated damage threshold corresponding to F^{D4} for 1030, 515 and 343 nm laser are approximatively estimated to be 3.5 ± 0.3 , 6.3 ± 0.5 and 3.1 ± 0.2 Jcm^{-2} , respectively.

6.2.2. Characterisation by scanning electron microscope (SEM) technique

Investigation of the different craters by femtosecond laser was carried out using a scanning electron microscope (Hitachi). Figure 6.6, Figure 6.7 and Figure 6.8 present the SEM images of the different craters on the surface of MAM, after interaction with the femtosecond laser using 1030, 515 and 343 nm laser wavelength, respectively. The peak fluence values associated with each crater are indicated on the individual images.

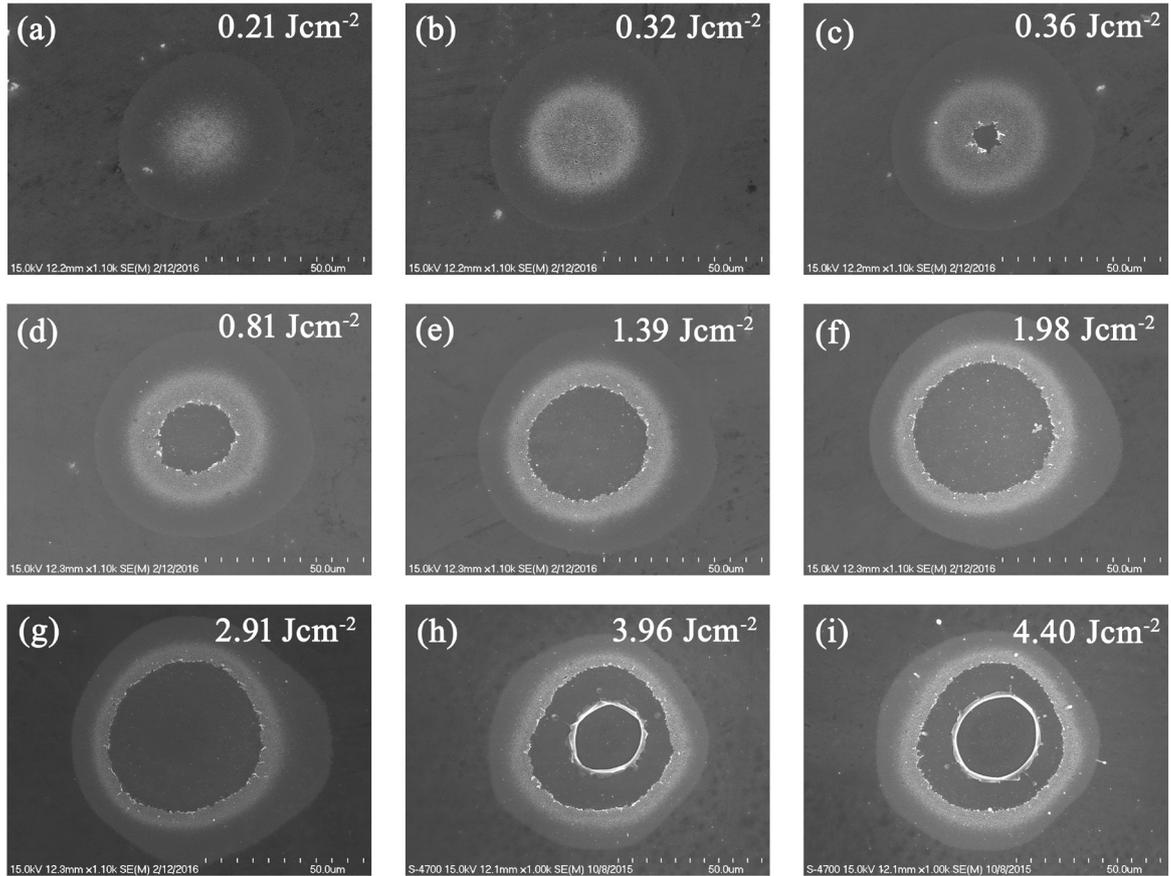


Figure 6.6: Scanning electron microscope images of a 1030 nm laser created craters at different peak absorbed fluences, indicated with each image. The spot radius of the laser beam (peak intensity of laser beam drops to $1/e^2$ times) is 26.55 μm .

Features with diameters, D1 and D2 are observed on the surface of MAM sample at the peak fluences of 0.21 and 0.32 Jcm^{-2} . These two fluences represent the regime $F^{D2} < F < F^{D3}$, where F^{D2} and F^{D3} are the damage threshold ($0.133 \pm 0.001 \text{ Jcm}^{-2}$) and the threshold when the upper molybdenum layer is penetrated ($0.348 \pm 0.003 \text{ Jcm}^{-2}$). When the peak fluence increases above the penetration threshold, D3 starts forming. Fluences of 0.36, 0.81, 1.39, 1.98 and 2.91 Jcm^{-2} present the fluence regime $F^{D3} < F < F^{D4}$. The increase of the laser fluence above F^{D4} ($3.5 \pm 0.3 \text{ Jcm}^{-2}$), results in formation of D4 on the MAM surface. The threshold fluences were also determined from the SEM microscopy measurement of the ablated craters. The values of the threshold fluences to achieve D1, D2 and D3 are determined to be 0.065 ± 0.002 , 0.135 ± 0.005 and $0.34 \pm 0.03 \text{ Jcm}^{-2}$, respectively.

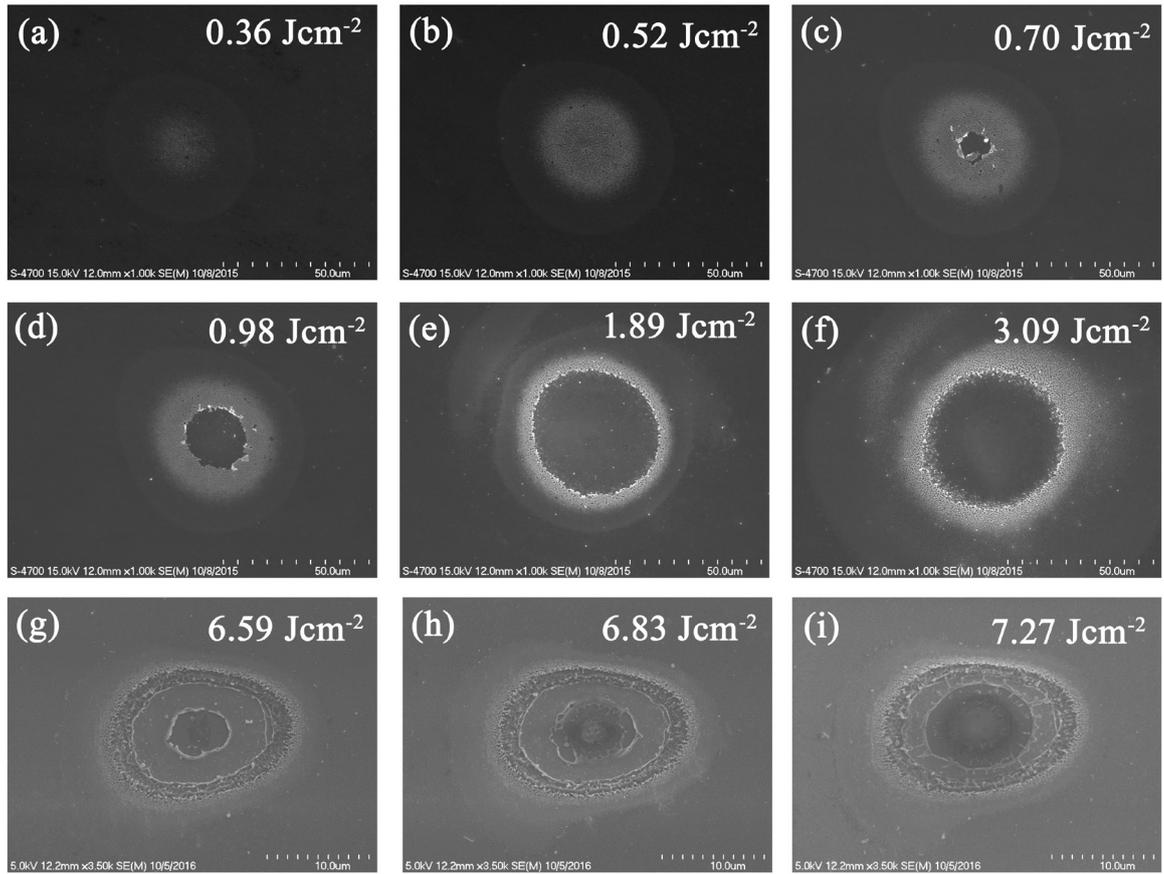


Figure 6.7: Scanning electron microscope images of a 515 nm laser created craters at different peak absorbed fluences, indicated with each image. A fixed lens (NA: 0.13) was used to achieve smaller spot size and thus higher fluence to get D4 on the MAM surface. The spot radius of the galvanometer and fixed lens are 22.08 and 8.2 μm , respectively.

Similarly, the scanning electron microscope measurement were performed for 515 nm laser ablated MAM samples. The diameters D1 and D2 were observed at fluences of 0.36 and 0.52 Jcm^{-2} . The diameter D3 was detected above the penetration threshold fluence $F^{\text{D}3}$ (0.422 Jcm^{-2}). A fixed lens setup with higher numerical aperture (NA: 0.13) was used to reduce the spot radius ($8.2 \pm 0.1 \mu\text{m}$) of the incident laser beam on the surface of the MAM. The reduction of the spot size results in an increases of the laser fluence. Peak fluences of 6.59, 6.83 and 7.27 Jcm^{-2} present the crater higher than the $F^{\text{D}4}$ (6.3 Jcm^{-2}). The threshold fluences were calculated using Liu's method from the SEM measurements of the craters and determined to be 0.027 ± 0.001 ($F^{\text{D}1}$), 0.163 ± 0.002 ($F^{\text{D}2}$) and 0.43 ± 0.01 ($F^{\text{D}3}$) Jcm^{-2} .

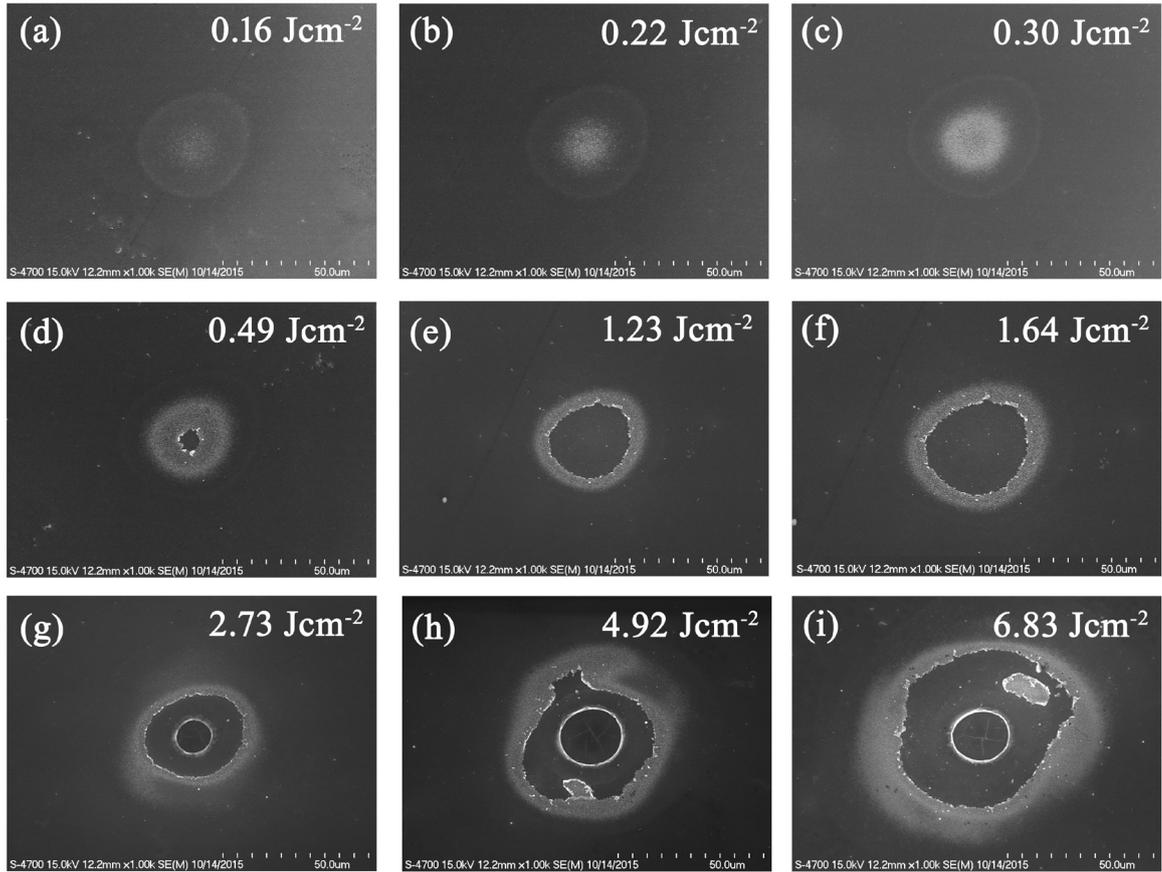


Figure 6.8: Scanning electron microscope images of 343 nm laser created craters at different peak absorbed fluences, indicated with each image. The spot radius of the laser beam (peak intensity of laser beam drops to $1/e^2$ times) is $16.96 \mu\text{m}$.

It is observed that the outer ring of the ablation crater is not regular (Figure 6.8) at high fluence in case of femtosecond laser interaction using 343 nm wavelength. This is because of the beam shape of the 343 nm femtosecond laser beam, which is not perfectly Gaussian. The radius of 343 nm femtosecond laser pulse on the MAM surface was determined to be $16.96 \pm 0.006 \mu\text{m}$. Peak fluences of 0.16 , 0.22 and 0.30 Jcm^{-2} present the fluence regime in between the damage threshold ($0.117 \pm 0.009 \text{ Jcm}^{-2}$) and the penetration threshold ($0.384 \pm 0.008 \text{ Jcm}^{-2}$) of the MAM surface. The increase of the fluence above the penetration threshold results in the formation of the feature of diameter of D_3 . Fluences of 0.49 , 1.23 and 1.64 Jcm^{-2} present the peak fluence regime $F^{D_3} < F < F^{D_4}$. When the peak value of the fluence exceeds F^{D_4} , complete removal of the MAM is observed (2.73 , 4.92 and 6.83 Jcm^{-2}). The threshold fluences calculated from the SEM measurements are given by $0.019 \pm 0.002 (F^{D_1})$, $0.124 \pm 0.001 (F^{D_2})$ and $0.373 \pm 0.005 (F^{D_3}) \text{ Jcm}^{-2}$, respectively.

It was observed from scanning electron microscope images that the diameter of the laser craters increases with increasing laser fluence. Several interesting phenomena were noticed on the craters after laser ablation; these are described below,

(a) Figure 6.9 present craters produced on MAM surface after irradiation of femtosecond laser pulse of wavelength of 1030, 515 and 343 nm laser. The crater produced on the surface of MAM after the interaction of femtosecond laser pulse of peak fluence of 2.49 , 0.93 and 1.23 Jcm^{-2} are presented in the Figure 6.9b, Figure 6.9d and Figure 6.9f, respectively. The expanded region of

the crater is defined by crater D1, D2 and D3 and presented in the Figure 6.9a, Figure 6.9c and Figure 6.9e. It was observed that the surface morphology changes at each feature which is defined by each diameter.

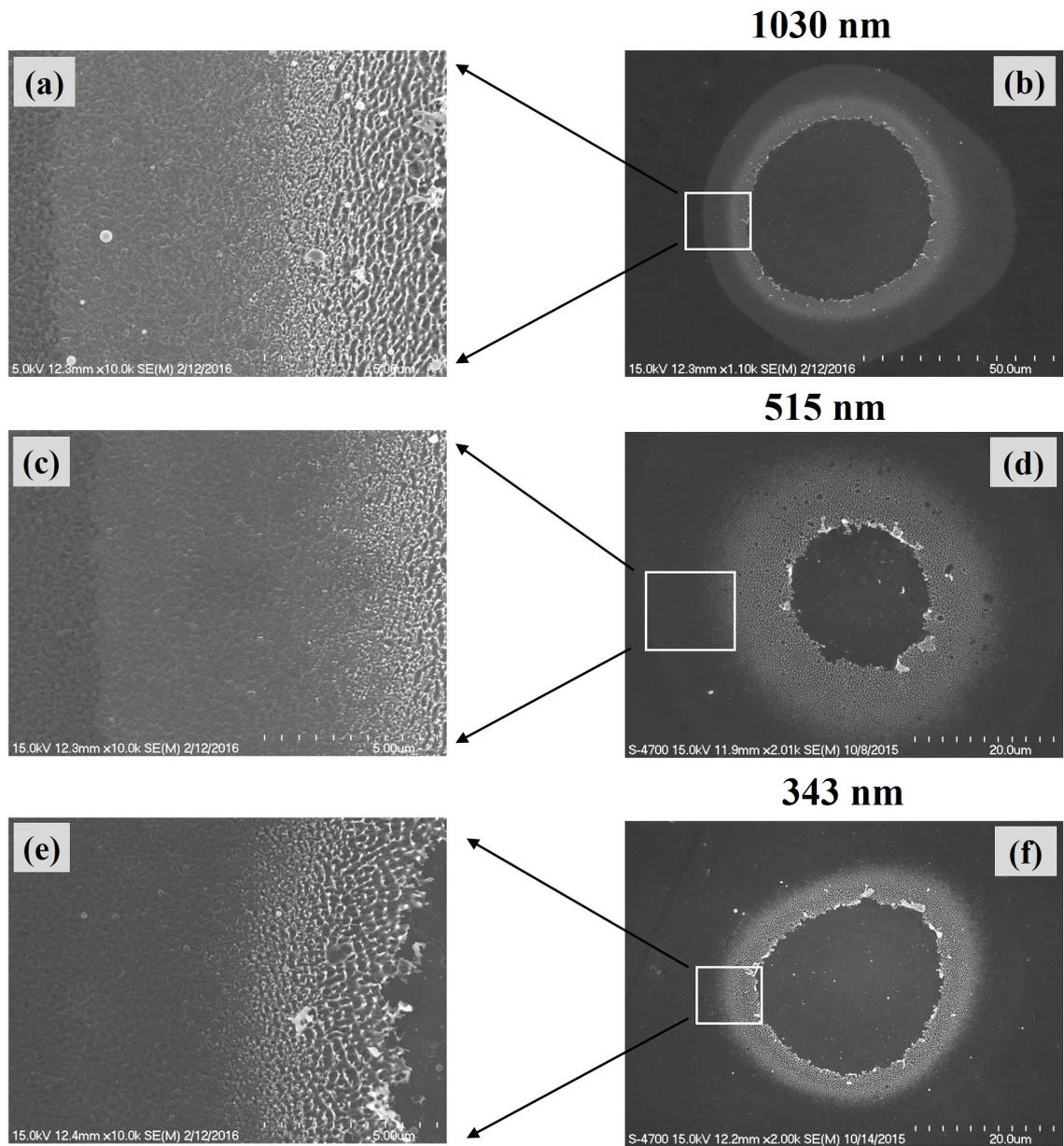


Figure 6.9: Structural difference of fluence regimes among $F < F^{D1}$, $F^{D1} < F < F^{D2}$ and $F^{D1} < F < F^{D2}$ for 1030 (a & b), 515 (c & d) and 343 (e & f) nm laser wavelength, respectively. Corresponding peak fluence for b, d and f are 2.49, 0.93 and 1.23 Jcm^{-2} .

(b) Figure 6.10 presents a crater of fluence $0.42 Jcm^{-2}$, and the magnified region accounts for a transition from the fluence regime $F < F^{D1}$ to $F^{D1} < F < F^{D2}$. The fluence regime $F < F^{D1}$ is relatively dark than the regime $F^{D1} < F < F^{D2}$. A minimal change in grain structure was observed between these two regimes. Thus, it was assumed that the structural modification does not take place in this fluence regime and thus only modification is observed.

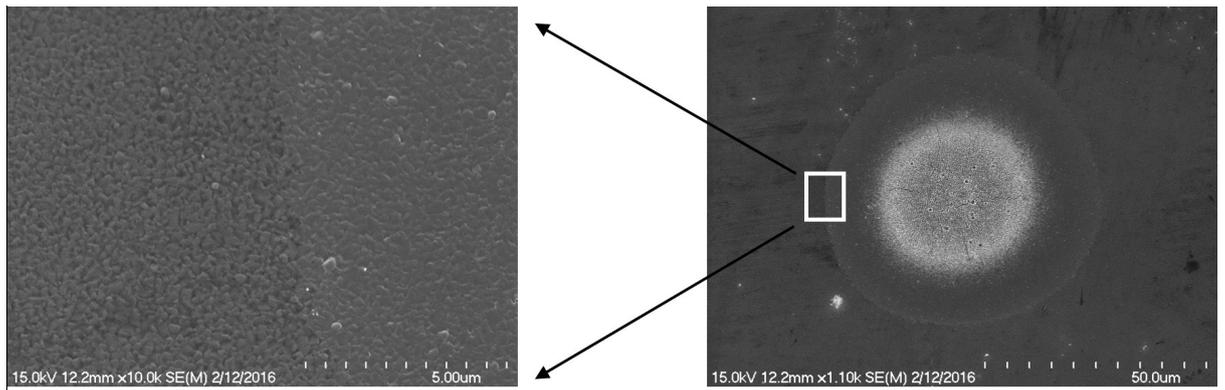


Figure 6.10: Optical changes between the fluence regime $F < F^{D1}$ and $F^{D1} < F < F^{D2}$, where F^{D1} and F^{D2} present laser exposed, and unexposed laser treated the area, respectively.

Several cracks at this region were observed in this region. Figure 6.11 indicate the centre part of the craters at peak fluence $F > F^{D2}$. The values of the peak fluences are indicated with each image. At this regime, several nano structures produced on the surface of molybdenum film.

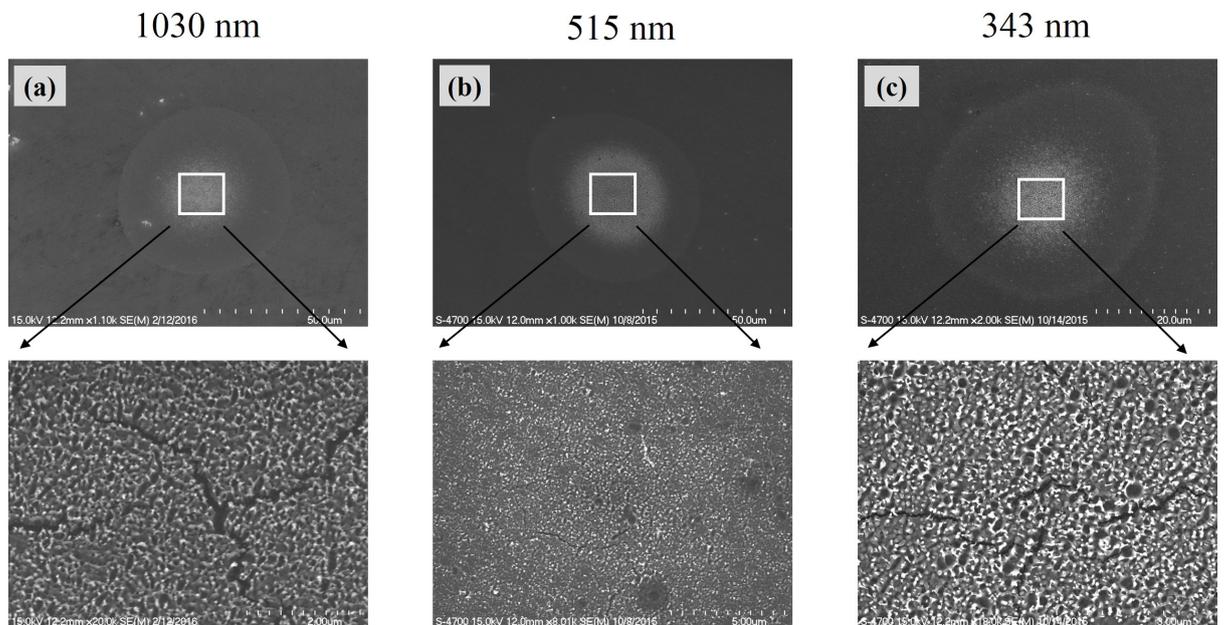


Figure 6.11: Several nano-cracks was observed at the centre of the region defined by the peak fluence $F^{D2} < F < F^{D3}$ for (a) 1030, (b) 515 and (c) 343 nm laser wavelength at fluence value of 0.29, 0.56 and 0.22 Jcm^{-2} , respectively.

(c) A significant structural and optical modification in this region is observed at the fluence regime $F^{D2} < F < F^{D3}$ (Figure 6.12). Visually, a brighter area and grains was found from the SEM microscope images. Figure 6.12 illustrates the magnified image of the craters at the fluence regime $F^{D2} < F < F^{D3}$ and its transition from $F < F^{D2}$ and $F > F^{D3}$, using 1030 (Figure 6.12a), 515 (Figure 6.12b) and 343 (Figure 6.12c) nm laser wavelengths.

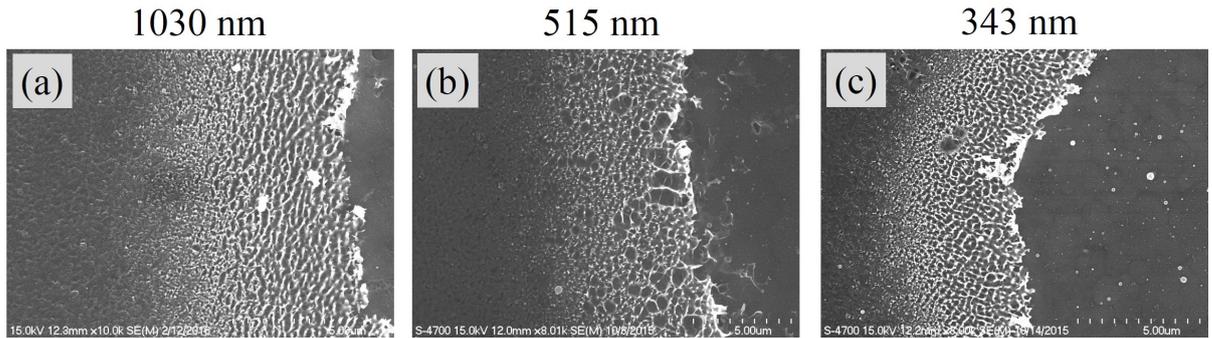


Figure 6.12: Structural modification of MAM layer at a region defined by $F^{D2} < F < F^{D3}$ from $F^{D1} < F < F^{D2}$ by 1030 (a), 515 and 343 nm femtosecond laser ablation at 1.98, 1.59 and 1.23 Jcm⁻², respectively.

When the peak fluence exceeds the value F^{D3} , removal of the upper layer is observed. At the fluence $F > F^{D3}$, delamination of a layer is observed. $F^{D2} < F < F^{D3}$. Figure 6.13 presents crater image at fluences $F > F^{D3}$ indicating delamination.

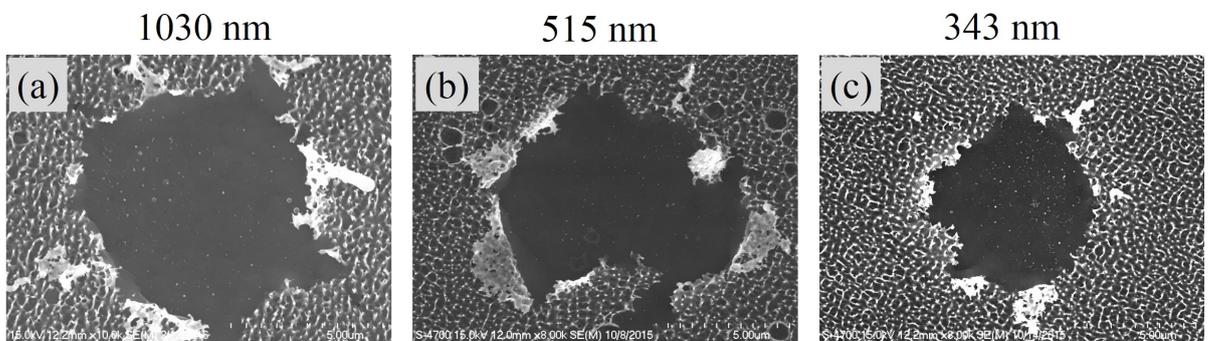


Figure 6.13: Delamination of molybdenum layer at the edge of the fluence regime defined by, $F^{D3} < F$ during femtosecond laser ablation using 1030, 515 and 343 nm wavelength.

A magnified view of crater confirming delamination of a thin film layer ablated using femtosecond laser of wavelength of 1030, 515 and 343 nm by fluence 0.58, 0.71 and 0.49 Jcm⁻², respectively are presented in the Figure 6.1.

(d) In between the peak fluences of F^{D3} and F^{D4} , enlarged grains in the aluminium layer by SEM was observed. The large grain corresponds the aluminium layer (will be discussed later). From the SEM microscopy images, it was also noticed that the grain size increases with increasing peak fluence and the distribution of grains are minimum at the centre. Figure 6.14 shows SEM images of grains at different fluence at fluences 0.64 (a), 0.81 (b), 1.39 (c) and 1.96 (d) Jcm⁻².

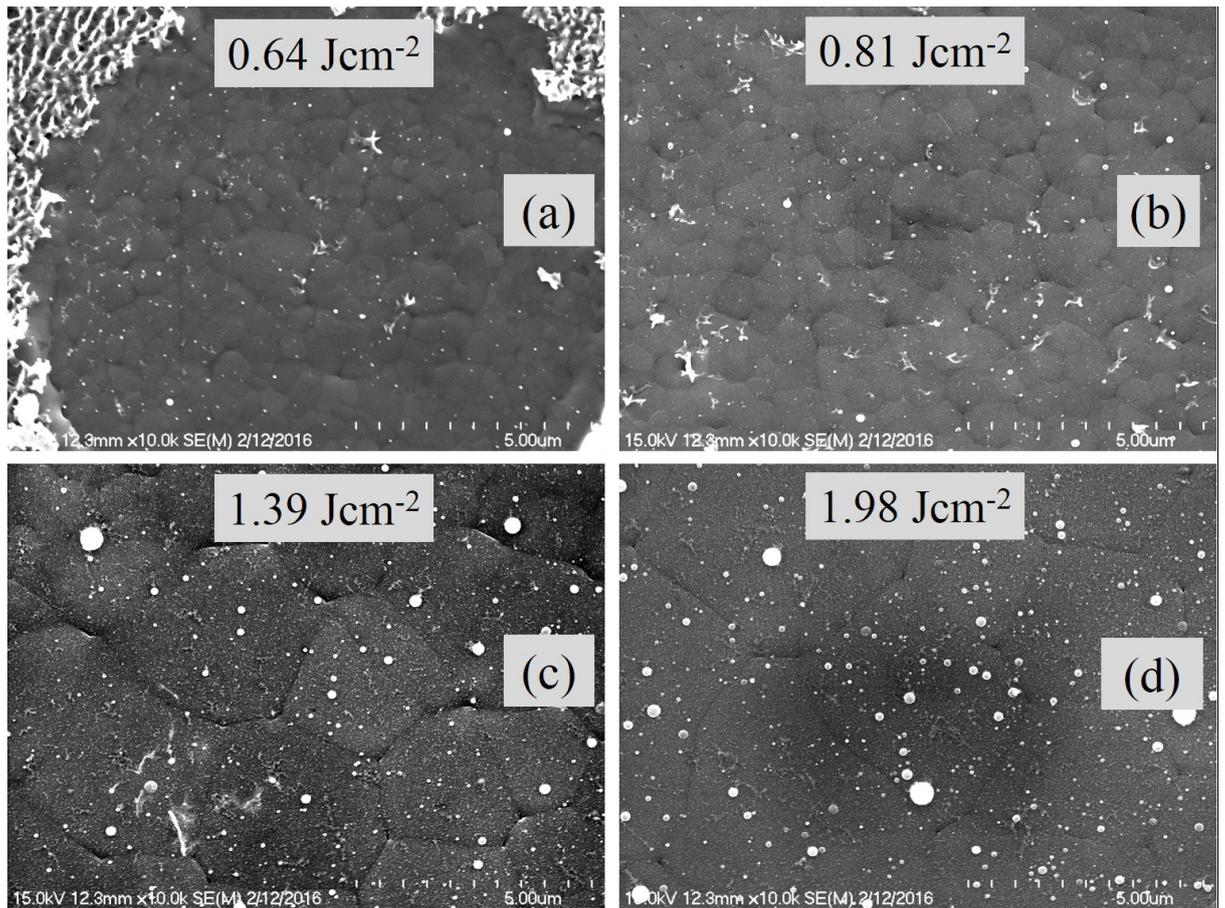


Figure 6.14: Increase in grain size of the layer at the peak fluence $F^{D3} < F < F^{D4}$ with increasing laser (515 nm) fluence. The value of absorbed fluence associated with images a, b, c and d are 0.64, 0.81, 1.39 and 1.98 Jcm^{-2} .

The increase of grain size of this region resulted in fewer grain boundaries. This would lead to a decrease of the electron scattering that would take place during conduction of electron on the material.

(e) Figure 6.15 presents the magnified view of the crater produced by a femtosecond laser pulse of the wavelength of 343 nm. The peak fluences applied to the MAM are $F > F^{D4}$ at the wavelength 343 nm. It was found that at fluence regime, some cracks initiates at the surface of MAM. Left and right SEM images correspond a peak fluence value of 2.73 (a) and 4.92 (b) Jcm^{-2} .

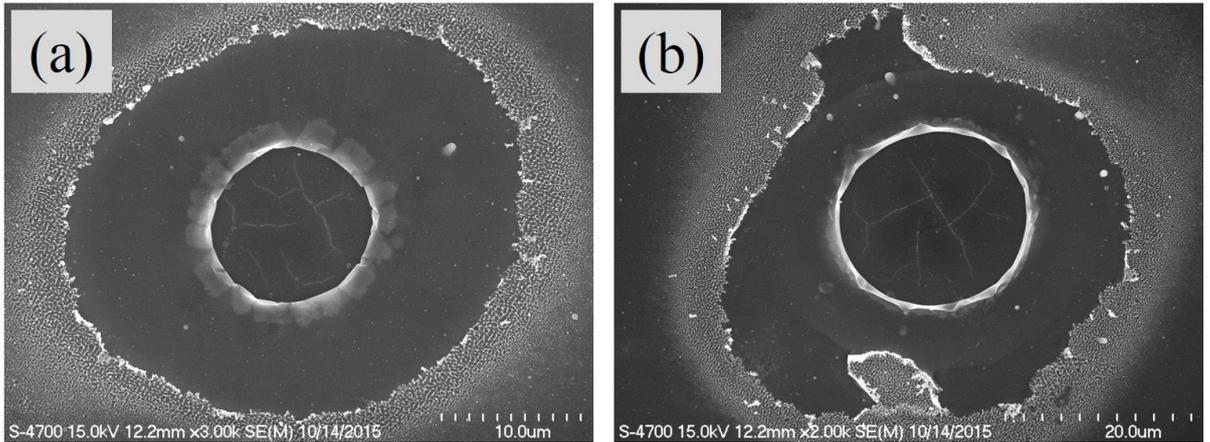


Figure 6.15: Several nano-cracks at the centre of fluence regime $F > F^{D4}$ for 343 nm femtosecond laser, with a delamination of another layer.

Delamination of the third layer (Mo) and fourth layer (ITO) was also observed during laser ablation at high fluence. Delamination of the layer was also noted for the wavelengths 1030 and 515 nm, of the femtosecond laser (Figure 6.6 and Figure 6.7).

The atomic force microscopy (AFM) technique was used to perform depth profile of the craters at different fluence and to analysis the ablated layer. In the next section, the atomic microscope image of ablated craters with the surface profile will be presented.

6.2.3. Characterisation by atomic force microscope (AFM) technique

Crater analysis of the femtosecond laser processed multi-layered structure was performed using atomic force microscope operating in the contact mode. Figure 6.16, Figure 6.17 and Figure 6.18 present atomic force microscope images of ablated craters using 1030, 515 and 343 nm femtosecond laser wavelengths at different fluences, respectively.

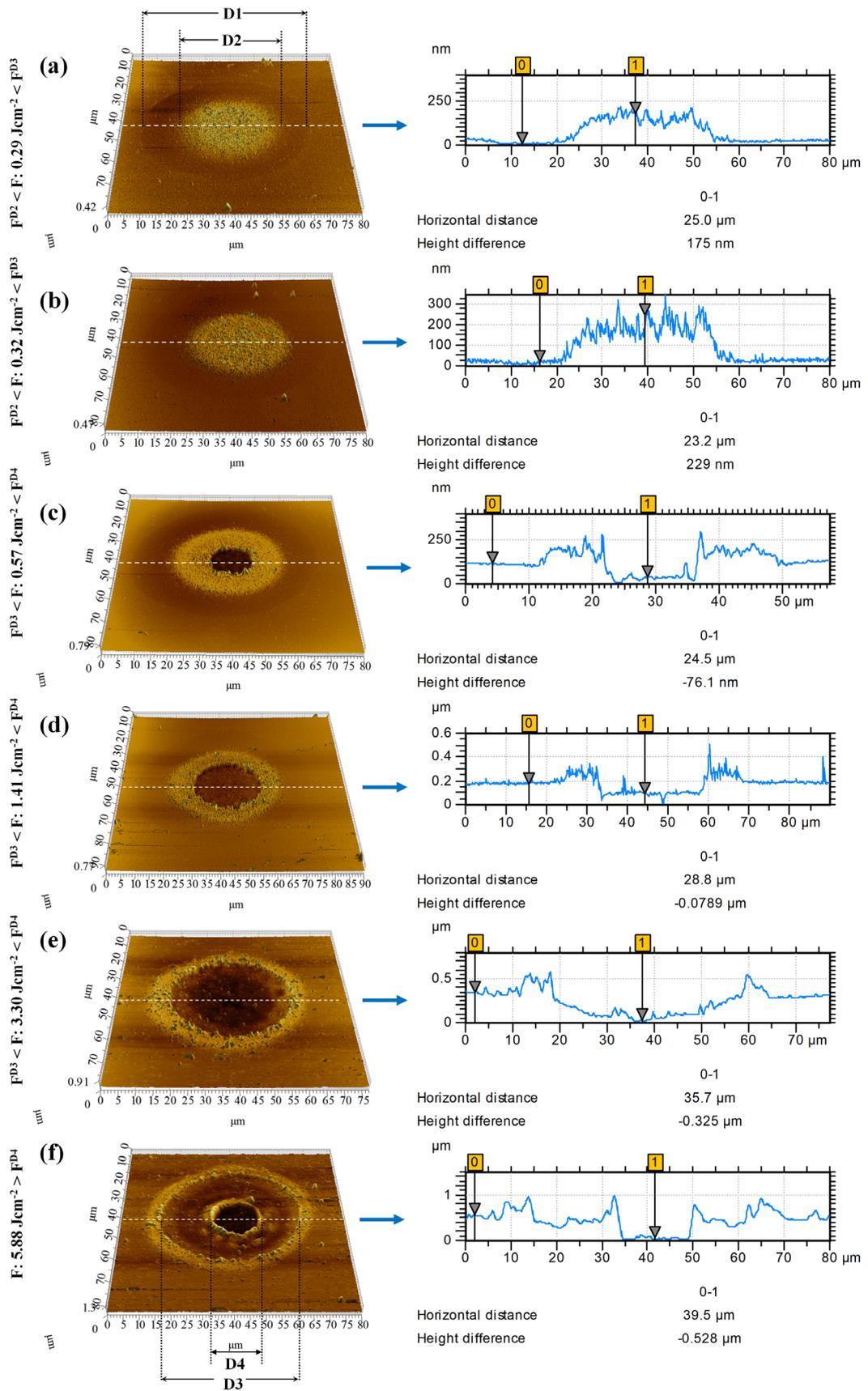


Figure 6.16: Atomic force microscope (AFM) images of 1030 nm femtosecond laser induced craters with a corresponding surface profile at different fluences, showing the maximum depth. Radius of the laser beam was set at $29.06 \pm 0.002 \mu\text{m}$.

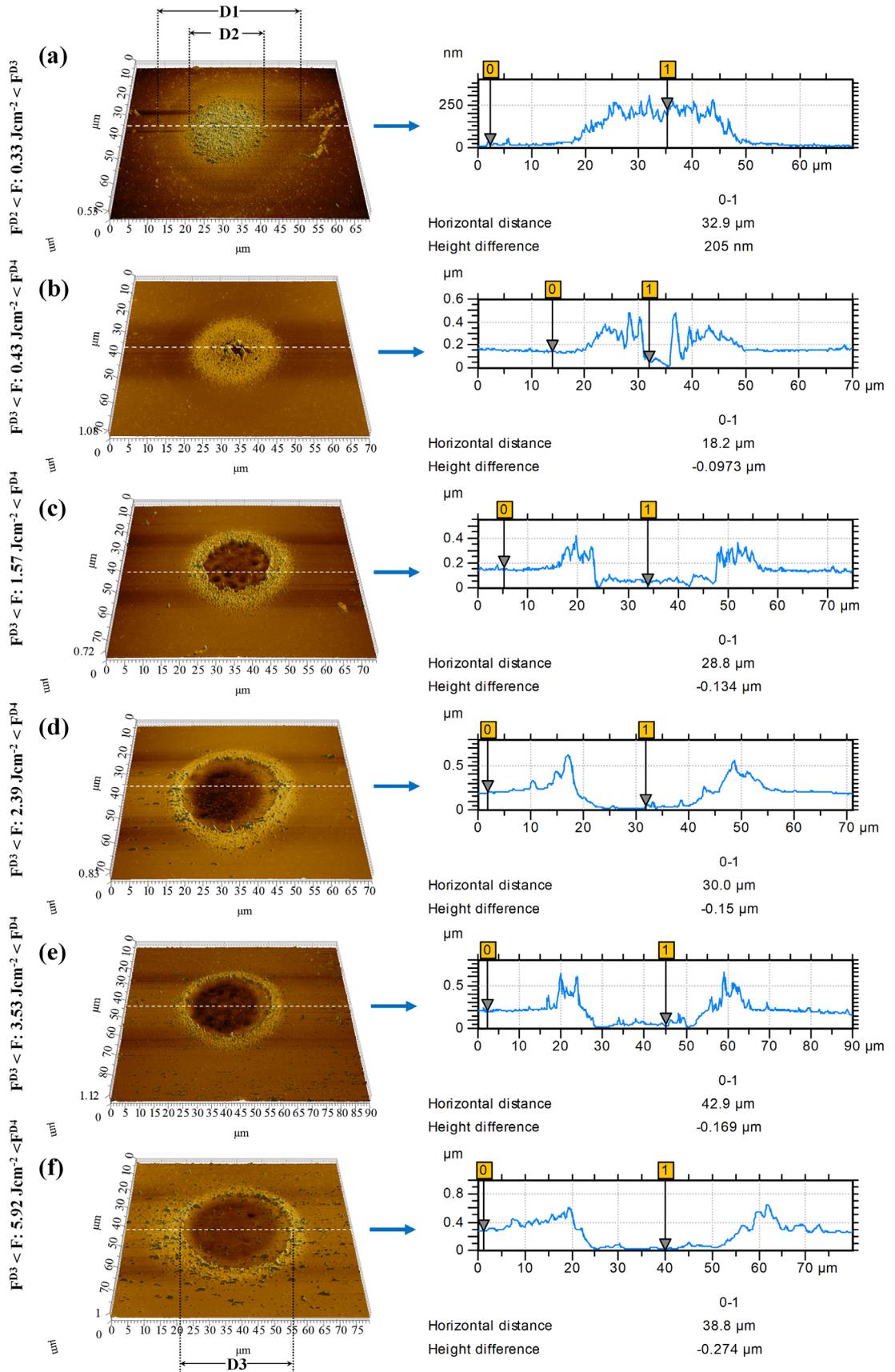


Figure 6.17: Atomic force microscope (AFM) images of 515 nm femtosecond laser induced craters with a corresponding surface profile at different fluences, showing the maximum depth. The beam radius of the 515 nm laser spot at the surface of MAM is $22.08 \pm 0.001 \mu\text{m}$.

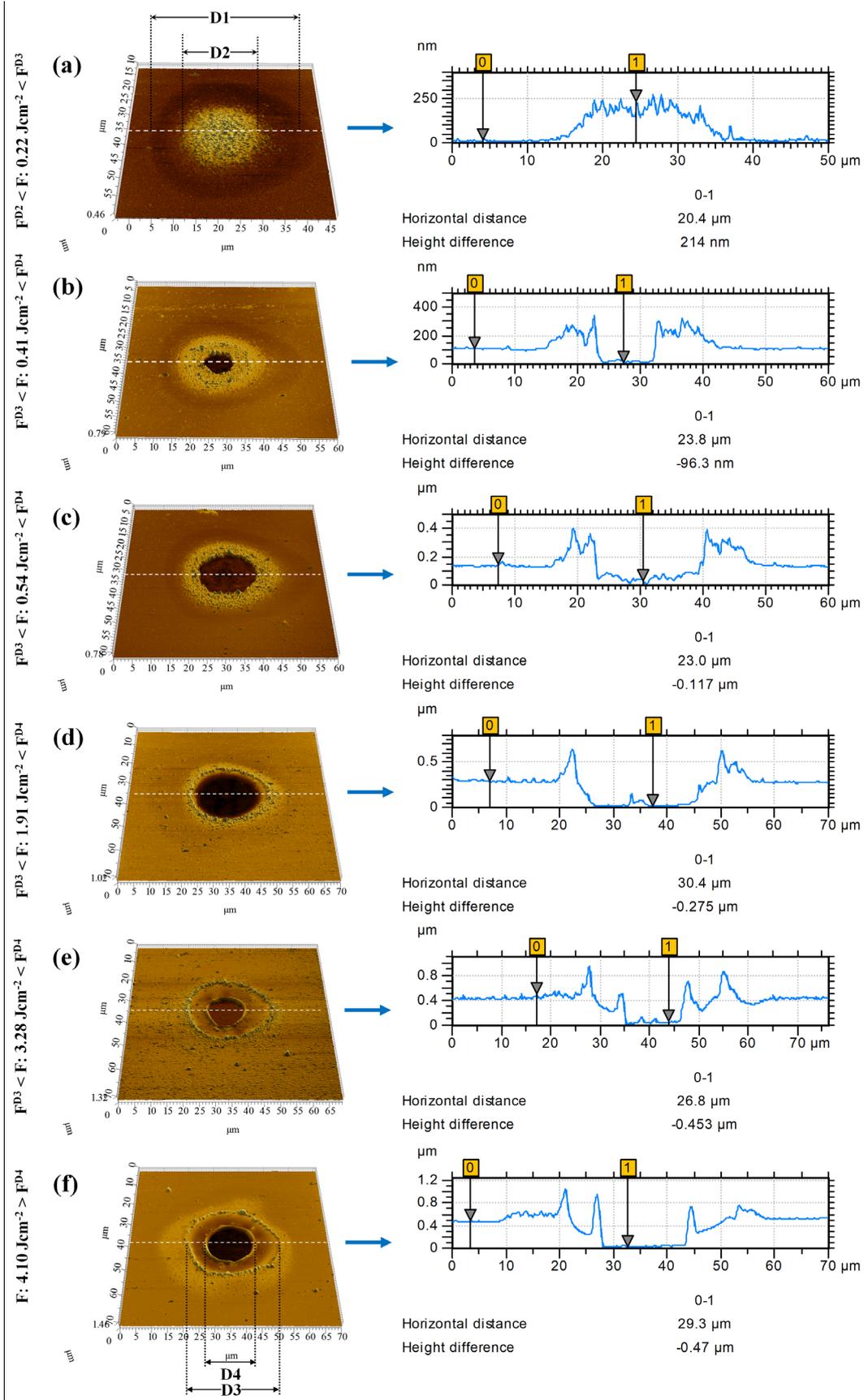


Figure 6.18: Atomic force microscope (AFM) images of 343 nm femtosecond laser induced craters with a corresponding surface profile at different fluences, showing the maximum depth. The beam radius of the 343 nm laser spot at the surface of MAM is $16.96 \pm 0.005 \mu\text{m}$.

The surface profile of the craters was extracted from AFM images, and these measurements provide information on the depth of the ablated layer. In the above profiles of each crater, the difference in height from the surface to centre of the crater was measured and provides maximum ablation depth. It was found that the ablation depth changes with increasing laser fluence.

There is no significant difference of surface profile (height) was noticed on the craters between the fluence regime $F < F^{D1}$ and $F^{D1} < F < F^{D2}$ from the Figure 6.16, Figure 6.17 and Figure 6.18. The surface was found to raise when the fluence exceeds F^{D2} . At the fluence of $F^{D2} < F < F^{D3}$, a 'nano-bump' is created on the top surface. The 'nano-bump' on the MAM craters are noticed for IR (Figure 6.16, F: 0.29 and 0.32 Jcm⁻²), Green (Figure 6.17, F: 0.33 Jcm⁻²) and UV wavelengths (Figure 6.18, F: 0.22 Jcm⁻²). Profile measurement by AFM provides the height of the 'nano-bump' (varies from 150 nm to 350 nm). The peak height of the 'nano-bump' was found to be 175 and 225 nm for the peak fluence 0.29 and 0.32 Jcm⁻², respectively using laser pulse of wavelength 1030 nm. It was found that the peak height of the 'nano-bump' increases with increasing incident laser fluence. Similarly, the peak height of the 'nano-bumps' were measured for the crater produced by 515 and 343 nm laser pulse interaction with MAM samples and shown in the Figure 6.17 (0.33 Jcm⁻²) and Figure 6.18 (0.22 Jcm⁻²).

At a fluence higher than F^{D3} , a well develop at the centre of the crater. The well at the crater is defined by the feature of diameter D3. The extracted profile of the craters in Figure 6.16 determines the diameter and the depth of the feature of diameter D3. The diameter, D3, and the depth of the craters were measured at different fluences for the femtosecond laser pulses at IR, green and UV wavelengths. The diameter and the maximum depth of the feature of diameter D3 increase with increasing laser fluence, as observed from the Figure 6.16, Figure 6.17 and Figure 6.18. Peak depth of the ablated craters indicates that the removal of material took place of the upper molybdenum (complete removal) and aluminium (partial removal) layer. The increase of the laser fluence resulted in an increase of peak depth from the top surface of the multi-layered film and indicates that the removal of an ablated material increases with increasing applied laser fluence.

Laser fluence higher than F^{D4} resulted in another feature gives rise at the centre of D3. Figure 6.16f shows the AFM microscope image of the crater at a peak absorbed fluence of 5.88 Jcm⁻² using a laser pulse of wavelength 1030 nm. Using AFM technique, the feature of diameter D4 was not detected on the crater produced by femtosecond laser of wavelength 515 nm. The feature of diameter D4 was measured on the craters on the surface, produced by the interaction of 343 nm femtosecond laser pulse (Figure 6.12, F: 3.28 and 4.10 Jcm⁻²), on the MAM samples. The average depth of D4 was found to be 528 nm for the peak fluence 5.88 Jcm⁻² (1030 nm, Figure 6.16f) and 450 and 470 nm for the peak fluence 3.28 and 4.10 Jcm⁻² (343 nm, Figure 6.18e,f). The peak height of the D4 was found almost equal to the total depth of multi-layered structure (535 ± 75 nm) on the glass substrate. Thus, the ablation of the MAM samples at the peak fluence higher than F^{D4} confirms complete removal of thin film assembly from the glass substrate.

A further experiment was performed using EDX technique for detection of the remaining ablated layer after ablation at different peak fluences. During EDX analysis, the energy of the incident electron beam kept at 5 Kev to obtain minimum penetration depth. It was found that the spatial resolution (vertical direction) of the electron of energy 5 Kev is almost 100 nm [251]. Thus, in the

case of multi-layered film, if the thickness of the top layer is less than 100 nm, characteristic X-ray detection from the second layer is possible to be observed.

6.2.4. Energy dispersive X-ray analysis

The elemental measurement was taken at different fluence regimes of the ablated craters. Figure 6.19 present the electron microscope image of ablated craters at three different peak fluences by femtosecond laser pulse of wavelength 343 nm. Laser ablated crater at peak fluences $0.22 (F^{D2} < F < F^{D3})$, $0.51 (F^{D3} < F < F^{D4})$ and $2.73 (F < F^{D4})$ Jcm^{-2} are presented in Figure 6.199 (a), Figure 6.19 (b) and Figure 6.12 (c), respectively.

The representation of different points of interest on the surface of MAM craters are presented in the Figure 6.19 (d). For each peak fluence, a fluence regime outside the feature of diameter was described as R0, and the region inside at the fluence regime $F^{D1} < F < F^{D2}$, $F^{D2} < F < F^{D3}$, $F^{D3} < F < F^{D4}$ and $F > F^{D4}$ are termed as R1, R2, R3 and R4, respectively.

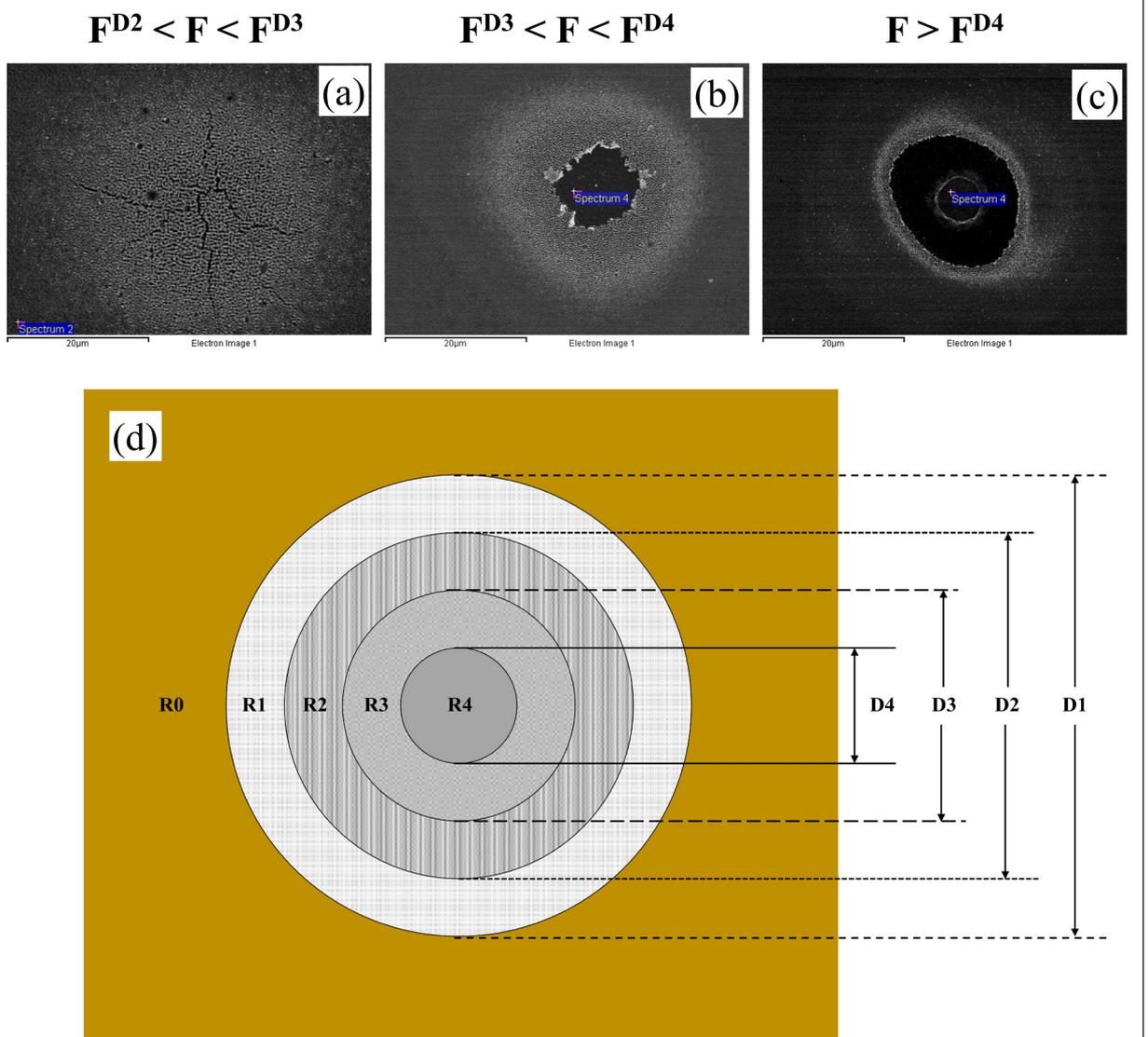


Figure 6.19: Electron microscope image presents ablated craters at three peak fluences, and the elemental analysis was carried out at different fluence regimes

(a) Fluence 1: (Peak fluence $F^{D2} < F < F^{D3}$)

Fluence 1 presents the crater created on the MAM surface at a peak fluence of 0.22 Jcm^{-2} (Figure 6.19a). At this peak fluence, the laser pulse results in two concentric features of diameters $D1$ and $D2$. EDX measurement was performed in three different regions, $R0$, $R1$ and $R2$. $R0$ represents a region outside $D1$, where the laser beam did not significantly interact with the top layer of the MAM sample. The elemental composition of the different regions on the MAM craters are presented in the Table 6.3. EDX measurement in the area $R0$ indicates the coexistence of molybdenum and aluminium (Table 6.3, region $R0$). This is due to the fact that the depth of the upper molybdenum ($40 \pm 10 \text{ nm}$) and parts of the aluminium layer exceeds 100 nm because of the large spatial resolution of the highly energised incident electrons used for the EDX measurement. $R1$ presents an area where fluence values are between those required to create the feature of diameter $D1$, but less than the threshold F^{D2} . Some change in atomic compositional difference between $R1$ and $R2$ was observed which confirms non-removal of molybdenum and aluminium (Table 6.3, region $R1$). The region $R2$ is the centre of the ‘*nano-bump*’ of diameter $D2$ and presents an area where the fluence value exceeds F^{D2} , but less than F^{D3} . The atomic concentration of aluminium was found to increase in the region $R2$ compared with $R0$ and $R1$ (Table 6.3, region $R2$).

(b) Fluence 2: (Peak fluence $F^{D3} < F < F^{D4}$)

The increase of the peak laser fluence beyond F^{D3} results in the formation of the feature of diameter $D3$. EDX measurement was taken place inside and outside of different features of the laser ablated MAM surface at an incident laser fluence of 0.51 Jcm^{-2} (Figure 6.19b). In Figure 6.19b, the different regions R_i ($i = 1$ to 3) indicates a region inside a feature of diameter D_i ($i = 1$ to 3) and at outside the laser exposed area ($R0$). Different atomic concentration at different regions are tabulated in Table 6.3. The atomic concentrations of elements do not change significantly at region $R0$ and $R1$ (Table 6.3, region $R1$ and $R2$); confirms that the region $R1$ is not much affected by laser pulse. Whereas, the increase of aluminium concentration at region $R2$ reveals structurally affected area by the laser pulse. The existence of molybdenum was not detected at the region $R3$ (Table 6.3, region $R3$) inside a feature of diameter $D3$; here the peak absorbed fluence higher than F^{D3} but lower than F^{D4} . This indicates complete removal of molybdenum at the area defined by $F^{D3} < F < F^{D4}$ and confirms the partial removal of aluminium.

(c) Fluence 3: (Peak fluence $F > F^{D4}$)

Laser fluence above fluence F^{D4} establishes one more feature inside the crater defined by the diameter $D4$. The Figure 6.19c presents scanning electron microscopy image of a crater on MAM at a fluence of 2.73 cm^{-2} . Similar to the previous measurements, EDX measurement were performed at regions $R0$, $R1$, $R2$, $R3$ and $R4$ and tabulated in Table 6.3. The simultaneous existence of molybdenum and aluminium was observed at regions $R0$, $R1$ and with possible increasing atomic concentration of aluminium at $R2$. Only one element (aluminium) was seen at $R3$. This confirms complete removal of molybdenum from MAM surface with partial removal of aluminium. Elemental analysis measurement at $R4$ results in the presence of silicon and oxygen and indicate the existence of glass (SiO_2).

Table 6.3: Atomic percentage of detected elements at different femtosecond fluence regimes using EDX technique.

| Peak Fluence | Region of interest | Molybdenum (% Mo) | Aluminium (% Al) | Indium (% In) | Silicon (% Si) | Oxygen (% O) |
|---|---------------------------|--------------------------|-------------------------|----------------------|-----------------------|---------------------|
| <i>Fluence 1</i> ($F^{D2} < F < F^{D3}$) | R0 | 64.46 | 35.54 | 0 | 0 | 0 |
| | R1 | 70.22 | 29.78 | 0 | 0 | 0 |
| | R2 | 38.83 | 61.17 | 0 | 0 | 0 |
| <i>Fluence 2</i> ($F^{D3} < F < F^{D4}$) | R0 | 64.62 | 35.38 | 0 | 0 | 0 |
| | R1 | 68.71 | 31.29 | 0 | 0 | 0 |
| | R2 | 36.09 | 63.09 | 0 | 0 | 0 |
| | R3 | 0 | 100 | 0 | 0 | 0 |
| <i>Fluence 3</i> ($F > F^{D4}$) | R0 | 65.56 | 34.42 | 0 | 0 | 0 |
| | R1 | 68.43 | 31.57 | 0 | 0 | 0 |
| | R2 | 28.74 | 71.26 | 0 | 0 | 0 |
| | R3 | 0 | 100 | 0 | 0 | 0 |
| | R4 | 0 | 0 | 0 | 73.73 | 26.27 |

6.2.5. Numerical simulation of femtosecond laser ablation at low fluence

A numerical simulation was developed based on two temperature model (TTM) to understand the evolution of temperature at different layers of the MAM sample. The beam diameter was normalised to 2 μm for the computational convenience (Chapter 3, section 3.7). Transient behaviour of electron and lattice temperature were examined at two threshold fluences (incident laser beam wavelength 1030 nm, pulse width 500 fs) given by, $F^{D1} = 0.068 \text{ Jcm}^{-2}$ and $F^{D2} = 0.133 \text{ Jcm}^{-2}$. The geometry of the multi-layered structure used for the two temperature simulation is shown in the Figure 6.20.

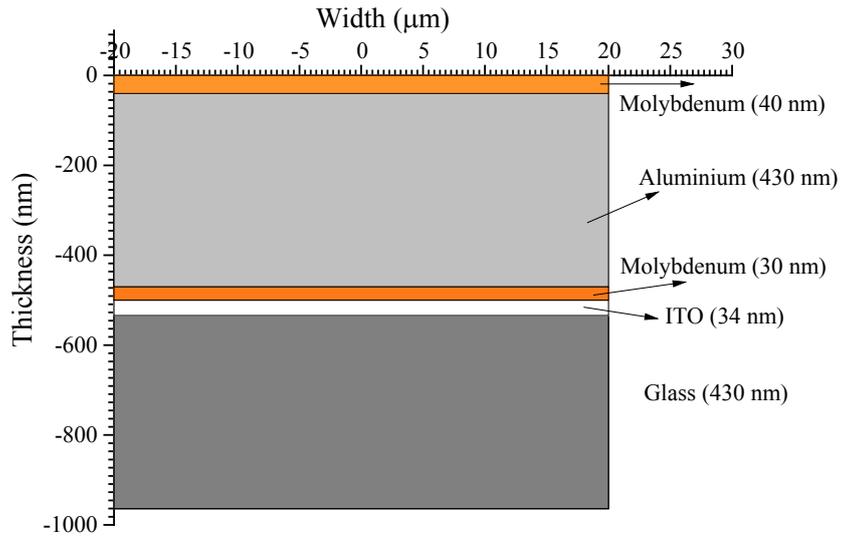


Figure 6.20: Cartesian geometry used for the simulation of temperature evolution in MAM during femtosecond laser ablation. The incident laser beam diameter was set at $2\ \mu\text{m}$.

The peak intensity of the incident laser pulse was set to be 0.5 picoseconds. The increase of electron temperature is almost instantaneous. The peak value of the electronic temperature was found to occur at 0.18 picosecond on the surface of molybdenum ($X = 0, Y = 0, Z = 0$) after the intensity of the laser pulse reaches to the maximum value. The temperature of the electron subsystem couples to the lattice via the electron-phonon coupling [67]. Figure 6.21 presents the transient electron (T_e) and lattice (T_l) temperature at the peak absorbed fluence of F^{D1} ($0.068\ \text{Jcm}^{-2}$) and F^{D2} ($0.133\ \text{Jcm}^{-2}$).

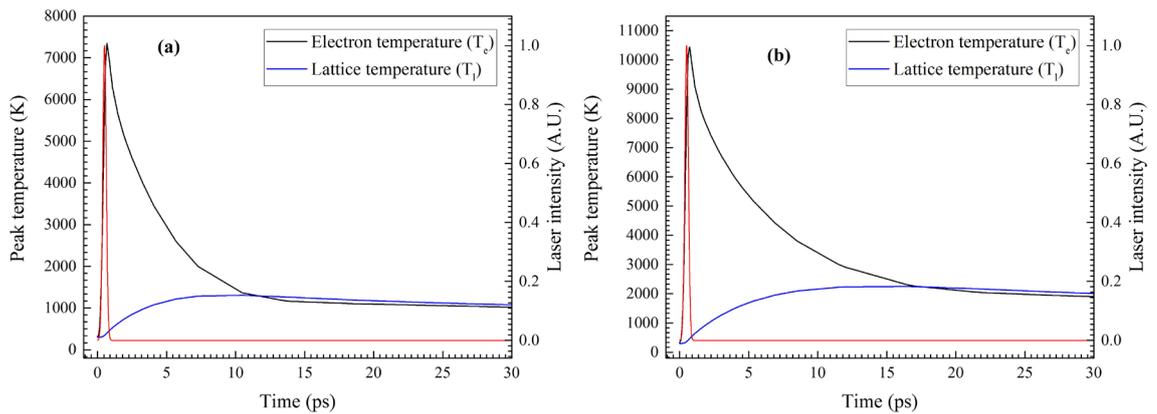


Figure 6.21: Two temperature modelling of femtosecond laser interaction (FWHM 500 fs, wavelength 1030 nm) with MAM sample at the peak absorbed fluence of (a) 0.068 and (b) $0.133\ \text{Jcm}^{-2}$. The black and blue line indicate the time dependent electronic and lattice temperature, respectively. The red line indicates normalised intensity of the laser beam.

At the peak fluence F^{D1} ($0.068\ \text{Jcm}^{-2}$), the maximum temperature of the molybdenum lattice (thickness of layer 40 nm) takes place at the centre of the laser beam on the MAM surface ($X = 0, Y = 0, Z = 0$) at a time of 10.5 picoseconds (i.e. 10 picoseconds after the intensity of the

femtosecond laser pulse reaches to its maximum value). The maximum temperature of the 40 nm thick molybdenum layer is determined to be 1305 K. Similarly, molybdenum reaches to its maximum temperature (2249 K) at 16.5 picosecond at the absorbed fluence of F^{D2} (0.133 Jcm^{-2}). It is evident from the numerical simulation that the peak temperature of the molybdenum does not exceed its melting transformation temperature (2897 K).

Figure 6.22 presents the temporal behaviour of the peak lattice temperature at the surface of top molybdenum layer ($Z = 0 \text{ nm}$), at $Z = -20 \text{ nm}$ and at the interface between molybdenum and aluminium layer at the peak absorbed fluence of 0.068 Jcm^{-2} . The simulation predicts that the peak temperature of aluminium takes place at the interface between molybdenum and aluminium ($X = 0, Y = 0, Z = -40 \text{ nm}$). As the aim of this simple numerical study was to understand the interaction of femtosecond laser pulse with MAM at low fluence and to understand the interplay between molybdenum (thickness 40 nm) and aluminium (thickness 430 nm) layers, the temperature profile of the other layers was not undertaken, as to do so it is required greater stability and development of the numerical model. The maximum temperature in aluminium reaches at 1085 and 1914 K for fluences of $F = F^{D1}$ and $F = F^{D2}$, respectively. Thus, at both the fluences, the peak lattice temperature of aluminium exceeds its melting temperature (933 K).

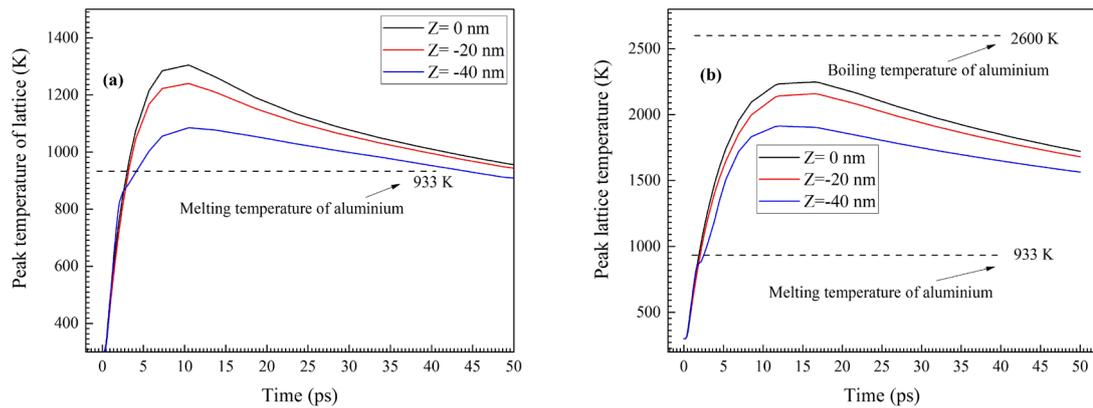


Figure 6.22: Transient behaviour of the lattice temperature at different depths of the MAM sample indicate the temperature of the molybdenum does not exceed the melting temperature, while solid to liquid phase change take place at the aluminium layer after the interaction with femtosecond laser at the peak absorbed fluence of (a) 0.068 and (b) 0.133 Jcm^{-2} .

The temperature of the lattice subsystem cools down via heat conduction and radiation cooling to the ambient. The lattice temperature conducts laterally through the film and vertically down towards the glass substrate. It is estimated that the peak temperature of aluminium stays above the melting temperature for the time duration of 40 and 120 picoseconds. The molten aluminium underneath the solid molybdenum layer (40 nm thick) eventually cools down and re-solidifies. As a result of the heating of aluminium, some structural changes on the MAM surface are observed (SEM and AFM images). Although, it is found from the experimental observations (Figure 6.16, Figure 6.17 and Figure 6.18) that significant material removal does not take place at these fluence regimes.

In summary, femtosecond laser processing with MAM samples indicates the following observations

1. Selective laser ablation of different layers at different peak fluences.
2. The ablation depends upon the incident laser wavelength and the applied fluence.
3. Evidence of recrystallisation of aluminium layer is observed. With increasing applied femtosecond laser fluence, average grain size of the aluminium layer increases.

For the comparison of ablation mechanism by short and ultrashort laser pulses, interaction of nanosecond laser pulse with molybdenum-aluminium-molybdenum (MAM) heterostructure will be discussed in the next section.

6.3. Processing of MAM by nanosecond (NS) laser sources

Nanosecond laser beam of wavelength 1064, 532 and 355 nm were focussed using a galvanometer scanning system (chapter 3, section 3.3.2). The repetition rate (frequency) of the laser system was set at 40 kHz. Similar to femtosecond case, the pulse energy of laser beams was varied using a combination of half-wave plate and a beam splitting cube. The Figure 6.23 presents the optical microscope images of the different craters produced on MAM surface at different pulse energy at these three different fluences.

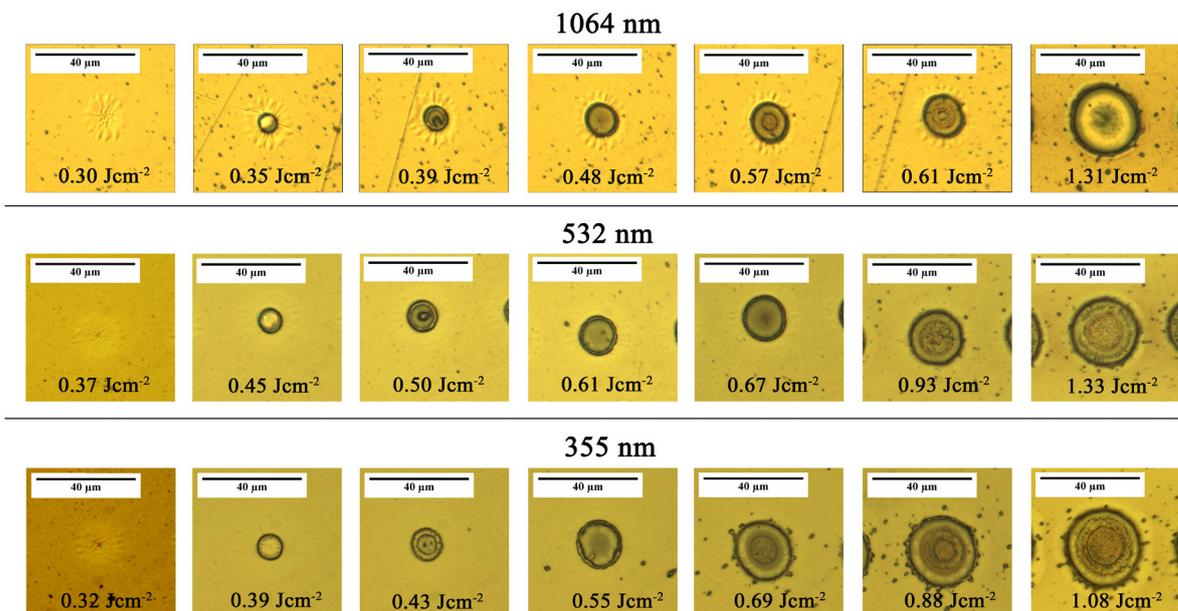


Figure 6.23: Optical microscope images of different craters on MAM surface at different absorbed fluences using 1064, 532 and 355 nm single pulse nanosecond laser.

The laser beam radius (ω_0) on the surface of MAM was measured to be 19.61 ± 0.002 (1064 nm), 16.49 ± 0.004 (532 nm) and 21.09 ± 0.001 (355 nm) μm from the relationship between the average pulse energy and the crater diameter. The focused beam diameter was used to determine absorbed fluence associated with crater created using a nanosecond laser pulse.

Similar to the femtosecond case, different craters were observed on crater at MAM surface at different fluences. It was noted that the diameters of each feature increase with increasing absorbed laser fluence. As before, the diameters of these features are denoted as D1, D2, D3 and D4. Figure 6.24 presents the optical microscope image of the ablated MAM crater at low (left) and high (right) fluence by nanosecond laser.

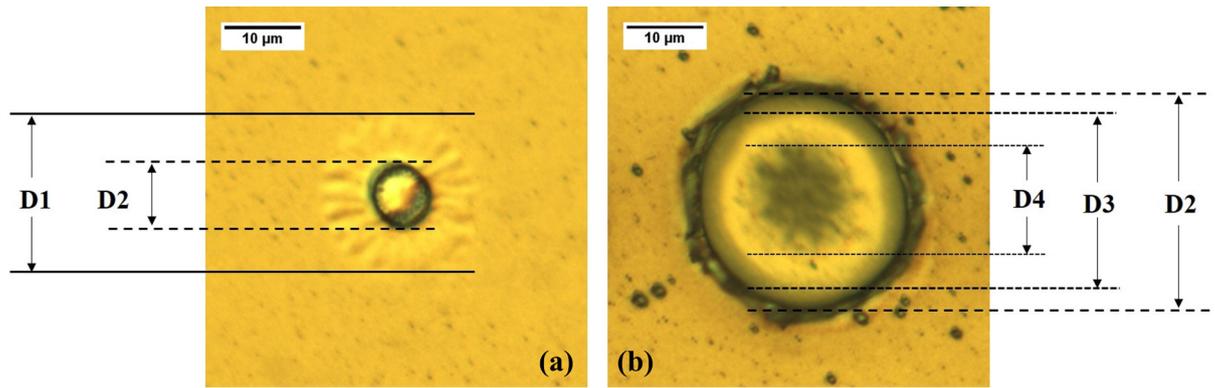


Figure 6.24: Nomenclatures of different diameters created on multi-layered MAM surface at (a) low (0.35 Jcm^{-2}) and (b) high (1.46 Jcm^{-2}) fluence, wavelength 1064 nm

6.3.1. Measurement of threshold fluence

The nanosecond threshold fluence of MAM for different diameters (D1 and D2) were calculated using Liu's method. The Figure 6.25 presents the relationship between squared diameters of craters with logarithmic of absorbed laser fluence. Linear fitting of the data was performed to identify threshold fluence (F^{D1} and F^{D2}) of the multi-layered film using 1064, 532 and 355 nm laser wavelength.

The interaction of nanosecond laser with the MAM sample surface resulted in diameters D3 and D4 at high fluence (Figure 6.24). However, measurements were not performed to calculate the threshold fluences required to get the craters defined by the diameters D3 and D4 on MAM surface because the edge was too poorly defined at these fluence regimes.

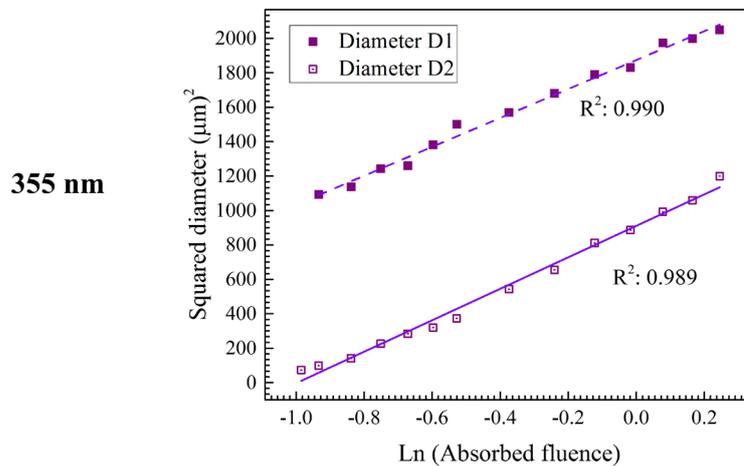
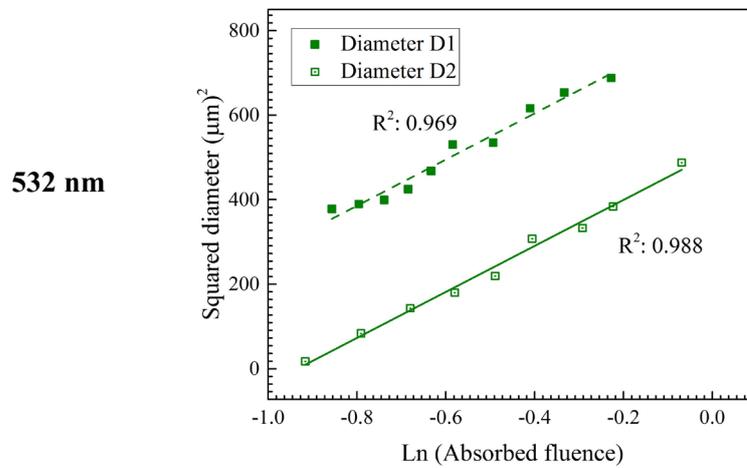
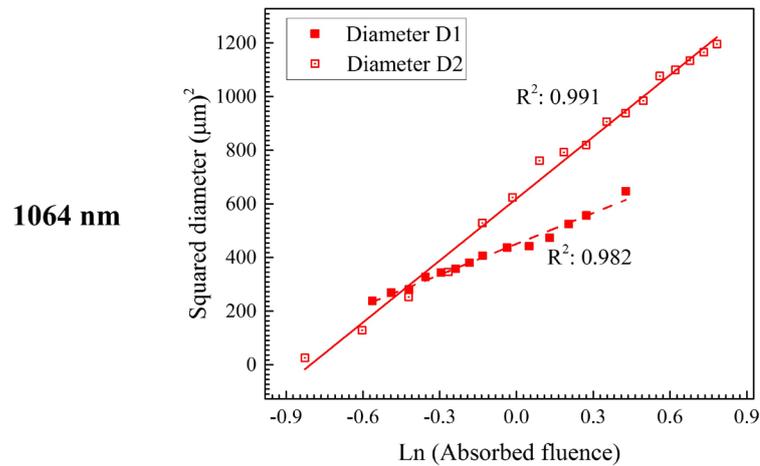


Figure 6.25: Relationship between squared diameter and logarithmic fluence to determine different threshold fluence associated with the square diameters D1, D2 and D3, for a nanosecond laser of a wavelength at 1064, 532 and 355 nm.

In the case of nanosecond laser material interaction, the absorption of light energy by the material depends on the optical penetration depth and the heat diffusion length. The penetration depth (laser intensity drops to 1/e times of its maximum value) of 1064, 532 and 355 nm laser pulse in molybdenum was estimated using Beer-Lambert's law [252] and found to be 19.14 ± 0.005 , 11.67 ± 0.005 and 8.81 ± 0.005 nm, respectively. A simple mathematical calculation indicates that the peak laser intensity drops to 12.37, 3.12 and 1.07 % after it travels 40 nm through molybdenum

layer and is incident on the aluminium layer. Thus, higher optical penetration depth at 1064 nm wavelength leads to a higher temperature of the second layer (aluminium) due to direct optical absorption by aluminium. As a result, thermal expansion of the aluminium is more for 1064 nm laser than 532 nm laser. The heat diffusion is proportional to the pulse width of the laser beam. In our nanosecond laser system, the pulse width of 355 nm laser (~20 ns) is almost double than the IR and green (~9 ns) wavelength (chapter 3, section 3.3.2) used in this study. Thus, the interplay between the optical penetration and heat diffusion play a vital role during the ablation process. The variation of the pulse duration may have an impact on the ablation process.

As before, the different values of threshold fluences corresponding to each diameter are termed as F^{D1} , F^{D2} , F^{D3} and F^{D4} . The calculated values of the threshold fluences F^{D1} and F^{D2} are tabulated in the table below in the units of Jcm^{-2} .

Table 6.4: Estimated threshold fluence require to get the diameters D1 and D2 by nanosecond laser ablation using 1064, 532 and 355 nm wavelength

| Threshold fluence corresponding diameter | Threshold Fluence (Jcm^{-2}) | | |
|---|--|-------------------|-------------------|
| | 1064 nm | 532 nm | 355 nm |
| F^{D1} | 0.155 ± 0.009 | 0.221 ± 0.001 | 0.101 ± 0.001 |
| F^{D2} | 0.309 ± 0.009 | 0.392 ± 0.005 | 0.366 ± 0.004 |

An electron microscopy study was undertaken to understand the different ablation regime during the interaction of MAM with nanosecond laser pulse.

6.3.2. Characterisation by scanning electron microscope (SEM) technique

It was found that at low fluence, the laser pulse resulted in the flower/petal-like structure on the surface of MAM. The increase of laser fluence resulted in a change in crater morphology, and the Figure 6.26, Figure 6.27 and Figure 6.28 exhibits femtosecond processed MAM image under scanning electron microscope system at different fluences using 1064, 532 and 355 laser wavelengths, respectively.

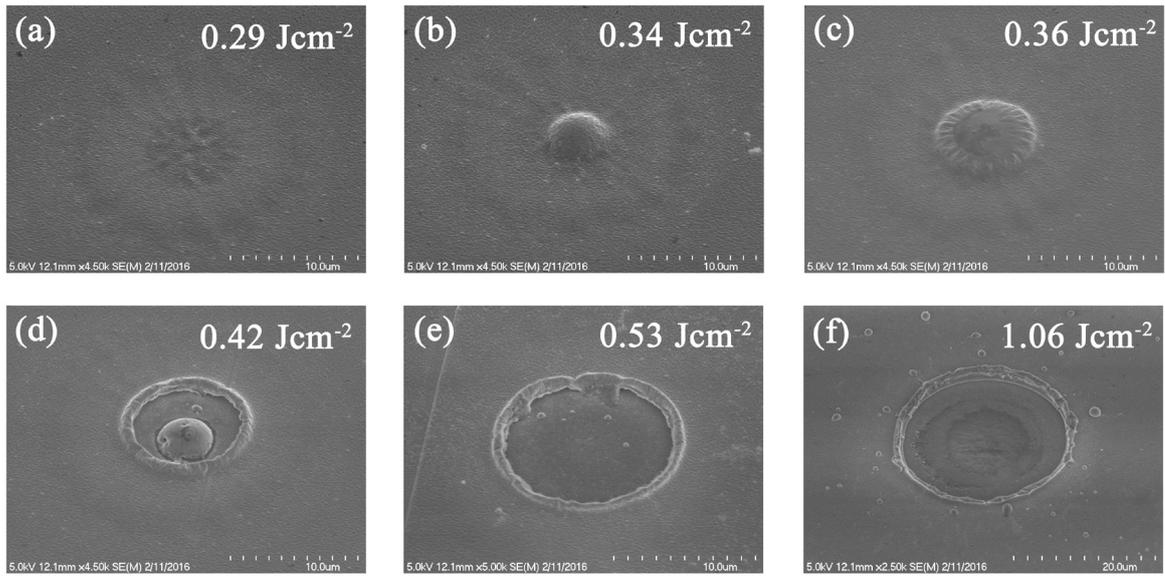


Figure 6.26: Scanning electron microscope images of a 1064 nm nanosecond laser created craters at different absorbed peak fluences, indicated with each image. The spot radius of the laser beam is $19.96 \pm 0.002 \mu\text{m}$.

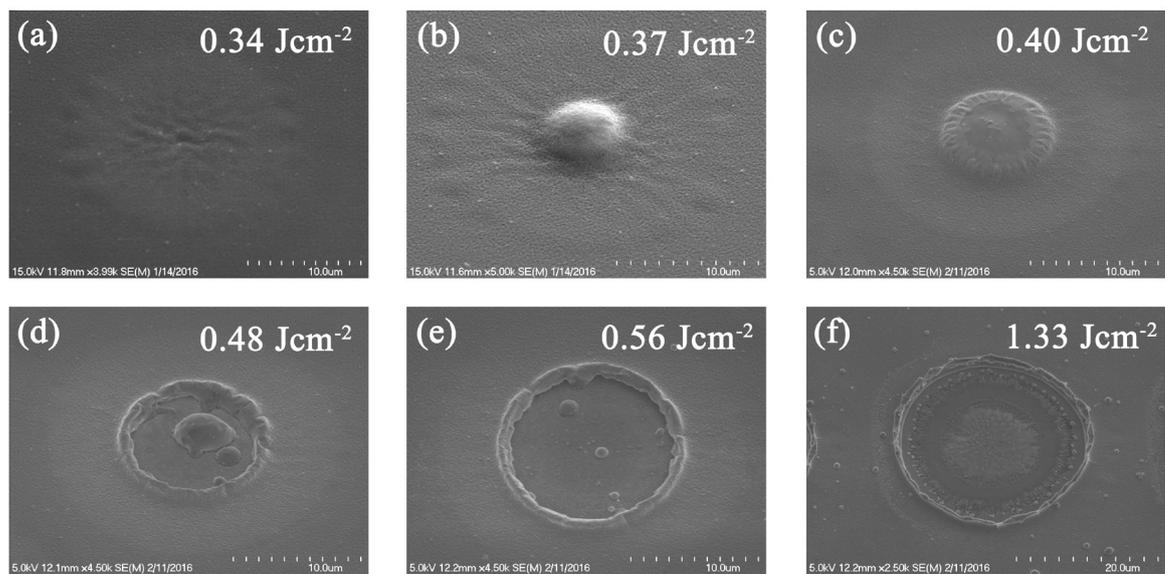


Figure 6.27: Scanning electron microscope images of a 532 nm nanosecond laser created craters at different absorbed peak fluences, indicated with each image. The spot radius of the laser beam is $16.49 \pm 0.004 \mu\text{m}$.

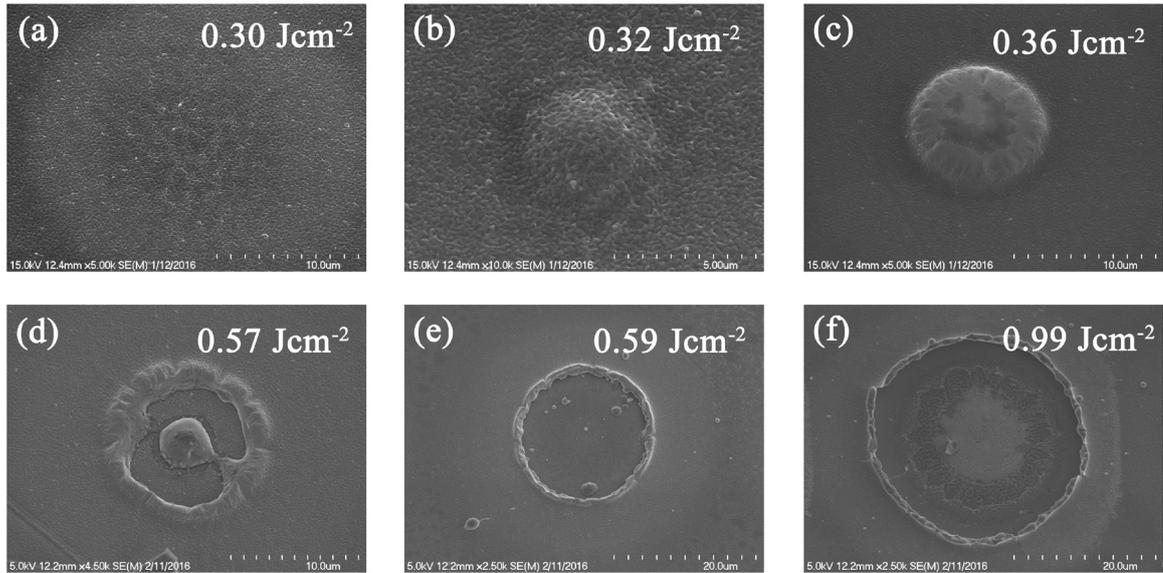


Figure 6.28: Scanning electron microscope images of a 355 nm nanosecond laser created craters at different absorbed peak fluences, indicated with each image. The spot radius of the laser beam is $21.01 \pm 0.001 \mu\text{m}$.

For a better view of the craters on MAM surface, scanning electron micrograph took place at an angle 20° . The scanning electron microscope image of the ablated craters by nanosecond laser of wavelength of 1064, 532 and 355 nm are presented in the Figure 6.26, Figure 6.27 and Figure 6.28, respectively. Different peak fluence used for the scanning electron microscopy study are mentioned with each crater. The Diameters of different features increases with increases peak laser fluence. At low fluence (1064 nm: peak fluence 0.29 Jcm^{-2} , 532 nm: 0.34 Jcm^{-2} and 355 nm: 0.30 Jcm^{-2}), only one feature of diameter D1 is observed. Increase of the peak laser fluence resulted in formation of the feature of diameter D2 (1064 nm: peak fluence 0.34, 0.36 Jcm^{-2} , 532 nm: 0.37, 0.40 Jcm^{-2} and 355 nm: 0.32, 0.36 Jcm^{-2}), surrounded by the diameter D1. The diameter D2 is found to increase with increasing peak laser fluence. Strained surface at the periphery of the feature of diameter D2 was also observed (0.36 Jcm^{-2} : 1064 nm, 0.40 Jcm^{-2} : 532 nm and 0.36 Jcm^{-2} : 355 nm). Increase of peak laser fluence results in results in fracture of the feature of diameter D2. These are observed from Figure 6.26, Figure 6.27 and Figure 6.28 using the peak fluences of 0.42 Jcm^{-2} (1064 nm), 0.45 Jcm^{-2} (532 nm) and 0.57 Jcm^{-2} (355 nm), respectively.

Further increase of peak laser fluence results in the formation of diameter D3 and D4 on the surface of MAM. Further investigation on the ablated surface was carried out using atomic microscope technique.

6.3.3. Characterisation by atomic force microscope (AFM) technique

Crater analysis of the femtosecond laser processed multi-layered structure was performed using atomic force microscope operating in the contact mode. Figure 6.29, Figure 6.30 and Figure 6.31 present atomic force microscope images of ablated craters using 1064, 532 and 355 nm nanosecond laser wavelengths at different peak fluences, respectively.

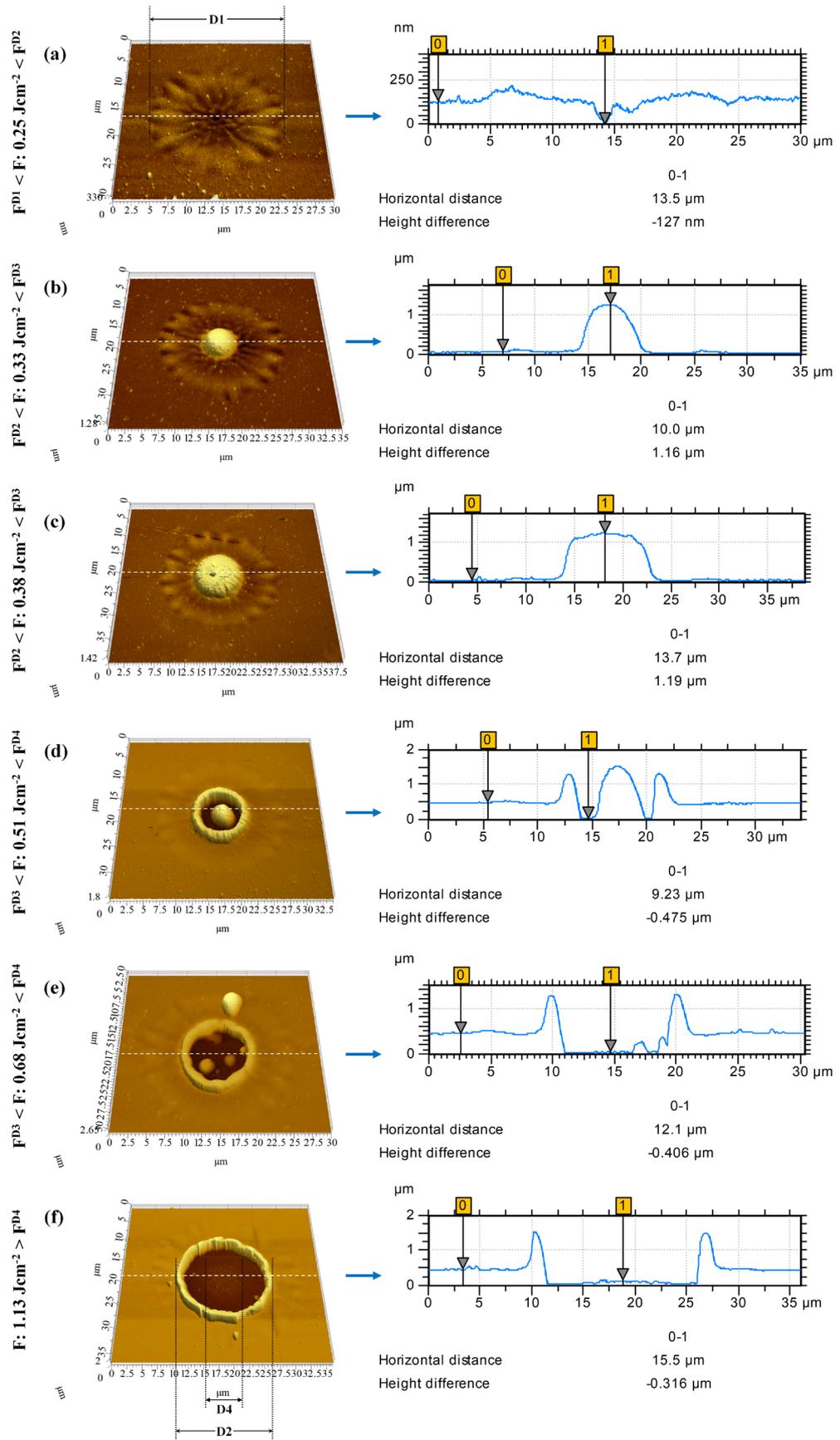


Figure 6.29: Atomic force microscope (AFM) images of 1064 nm nanosecond laser induced craters with a corresponding surface profile at different peak fluences, showing the maximum depth. The spot radius of the 1064 laser beam at the sample surface was set at 19.27 μm .

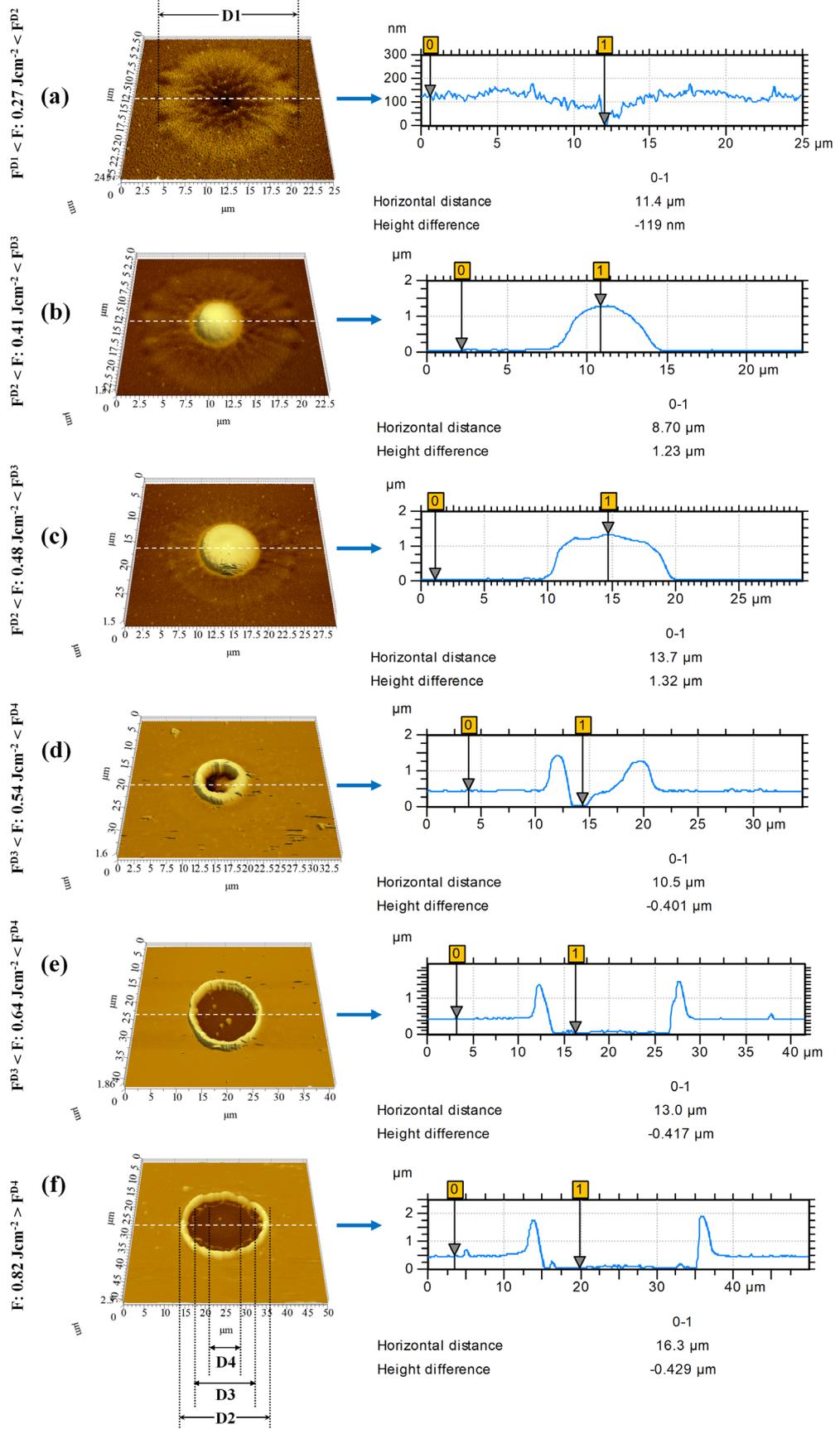


Figure 6.30: Atomic force microscope (AFM) images of 532 nm nanosecond laser induced craters with a corresponding surface profile at different peak fluences, showing the maximum depth. The spot radius of the 532 laser beam at the sample surface was set at 20.22 μm

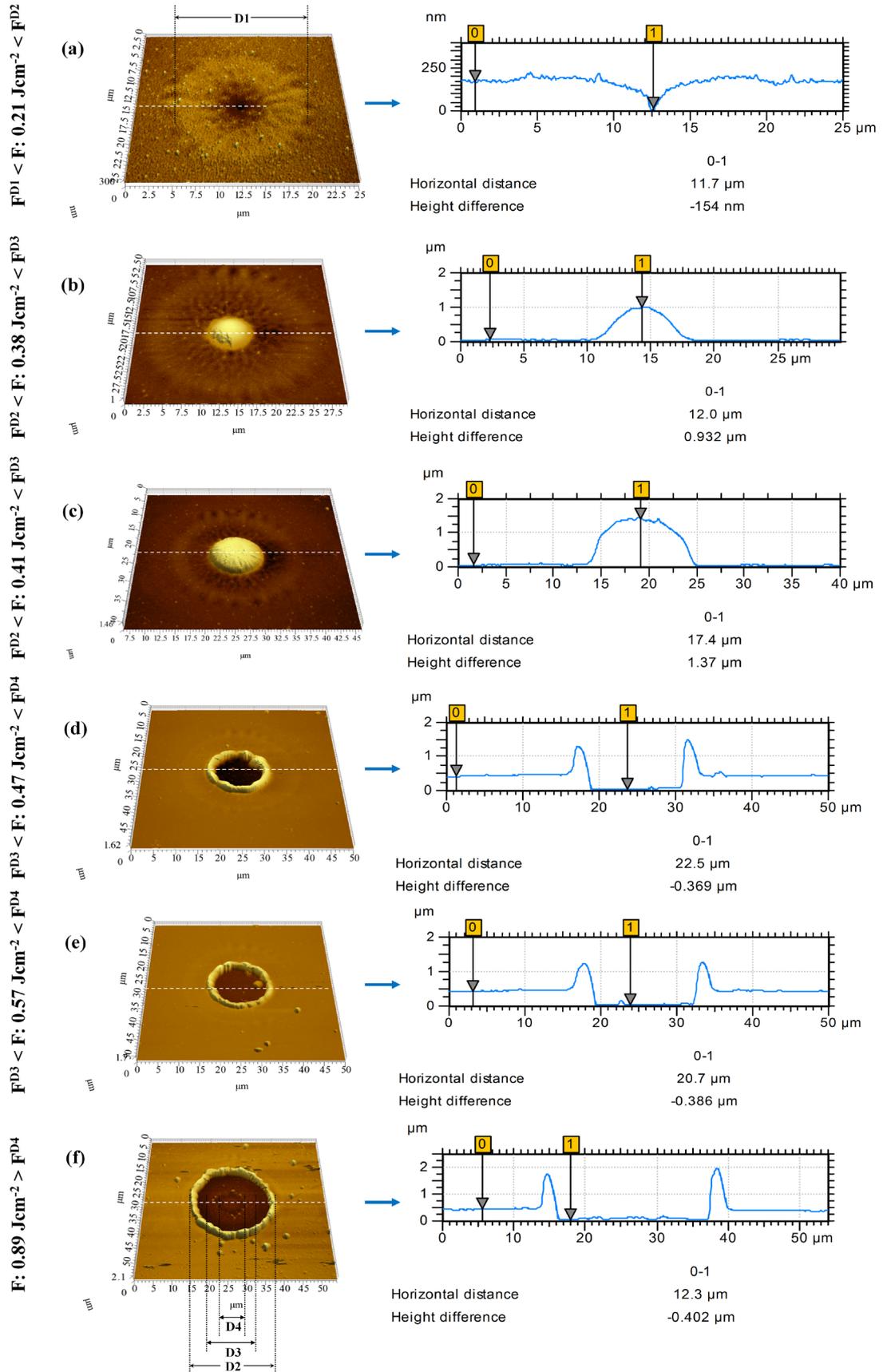


Figure 6.31: Atomic force microscope (AFM) images of 355 nm nanosecond laser induced craters with a corresponding surface profile at different peak fluences, showing the maximum depth. The spot radius of the 355 laser beam at the sample surface was set at 21.10 μm.

The AFM scanning was taken place at the fluence regimes $F^{D1} < F < F^{D2}$, $F^{D2} < F < F^{D3}$, $F^{D3} < F < F^{D4}$ and $F^{D4} < F$, respectively. The surface profile, indicated with each AFM images of ablated crater, is used to determine crater depth produced on multi-layered MAM. The first fluence regime ($F^{D1} < F < F^{D2}$) reveal the formation of a ‘sub-micro-hole’ at the centre of the laser spot and spot gets distorted and forms a ‘flower-like’ surface. Second fluence regime ($F^{D1} < F < F^{D2}$) suggests the formation of the ‘micro-bump’ on the MAM surface. The increase of the applied laser fluence results in a development of a well in MAM at ablated craters. When the value of the peak fluence increases to higher than the F^{D4} , almost total removal of MAM was observed with a significant damage on MAM craters.

Similar to femtosecond ablation of MAM, some interesting phenomena was observed by SEM technique, and several facts were found by SEM and AFM techniques.

Figure 6.32 presents SEM and AFM image of the surface of MAM without any interaction with nanosecond laser beam. The average grain size was calculated using AFM technique [37]. The mean grain size of an unprocessed MAM surface is $0.130 \mu\text{m}^2$.

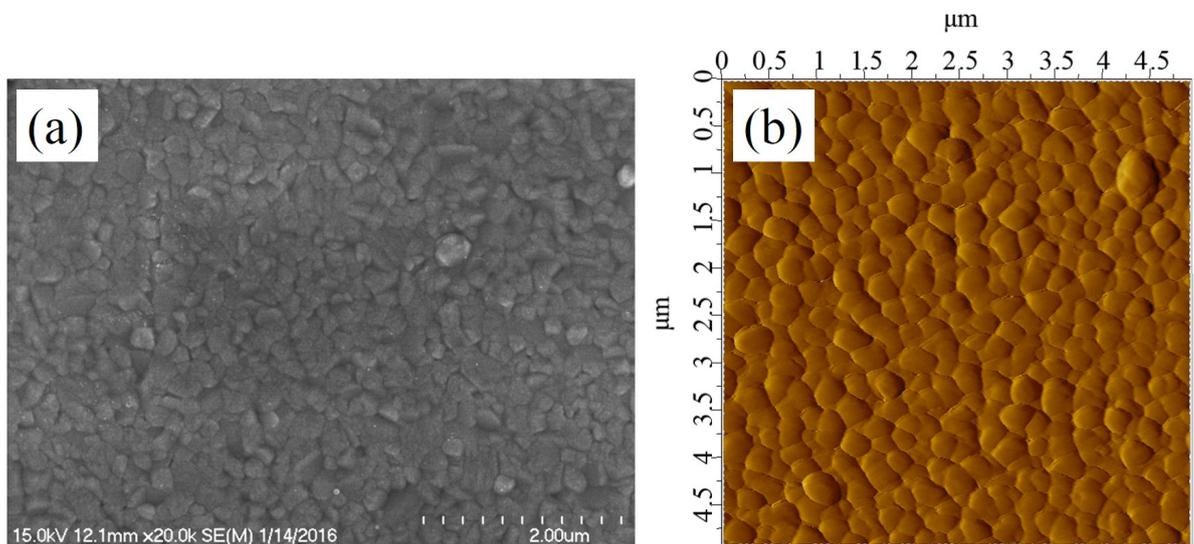


Figure 6.32: Surface of MAM without any interaction with the laser beam, showing grain structure on MAM surface using (a) SEM and (b) AFM techniques

(a) It was found that the surface morphology changes with increasing laser fluence. **Figure 6.33** present the SEM images of ablated craters at fluences (a) 0.317, (b) 0.337 and (c) 0.357 Jcm^{-2} . Initially, at low fluence using 355 nm nanosecond laser. The grain structure almost unaltered at the region F^{D2} . The increase of laser fluence resulted in a change in surface morphology between two fluence regimes. Also, at the periphery of the feature of diameter $D2$, a strained surface was observed.

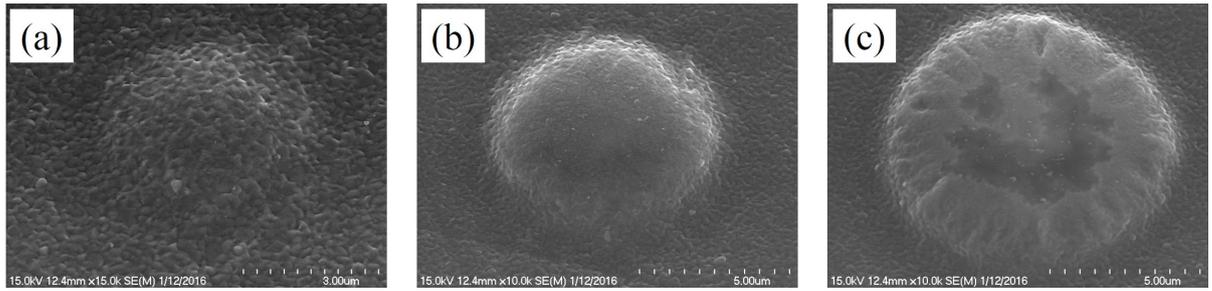


Figure 6.33: Change in surface morphology at the ‘micro-bump’ with increasing laser fluence. Figure (a), (b) and (c) represent crater with peak absorbed fluences of (a) 0.317, (b) 0.337 and (c) 0.357 Jcm⁻², respectively.

(b) Figure 6.34 presents the scanning electron image of a crater using fluence 0.451 Jcm⁻² after interaction of MAM surface with 532 nm nanosecond laser. A change in surface morphology is observed between two fluence regimes. Also, there is no difference in grain structure was found between the laser unexposed area and the fluence regime defined by the peak fluence $F^{D1} < F < F^{D2}$.

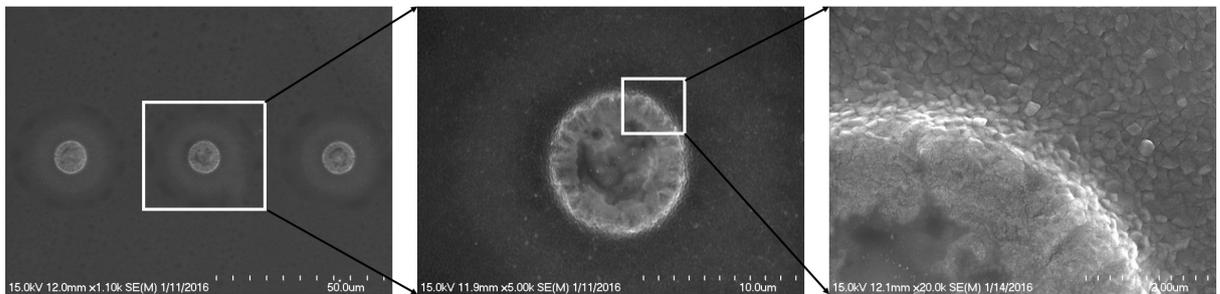


Figure 6.34: Formation of micro bumps on the surface of MAM surface and the difference in surface morphology between two fluence regimes, $F^{D1} < F < F^{D2}$ and $F^{D2} < F < F^{D3}$, wavelength 355 nm.

(c) At a peak fluence just above F^{D2} , the fracture of the micro-bumps starts from the centre. Melting of layers was also identified at this fluence regime (Figure 6.35b). Further increase of the laser fluence resulted in sub-micro well inside the craters.

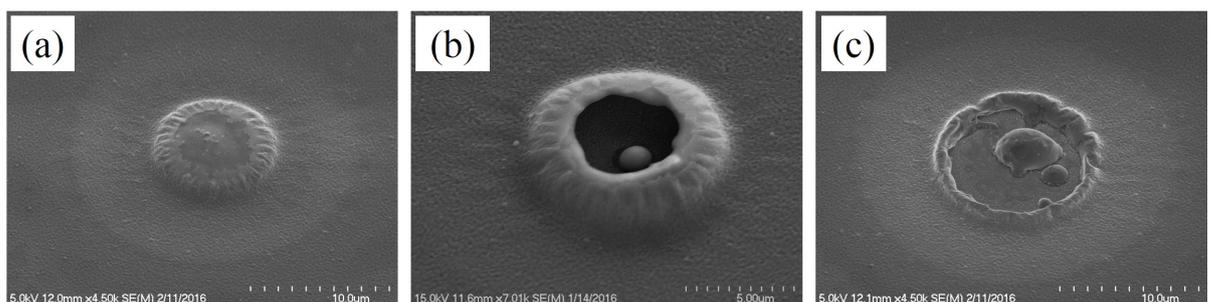


Figure 6.35: Permanent deformation of the surface of MAM with the initiation of fracture from the centre of the crater. The craters correspond to the peak absorbed fluences of 0.482, 0.505 and 0.536 Jcm⁻².

A flower-like structure is observed in the fluence regime defined by $F^{D1} < F < F^{D2}$. It was noted that at certain fluence, ‘micro-bump’ is established on the multi-layered film surface and the increase of fluence resulted in an increase of the peak height of these bumps. Further increase of the fluence led to a sub-micron hole (Figure 6.35b) at the centre of the ablated craters.

(d) Figure 6.36a, Figure 6.36b and Figure 6.36c present AFM images of the craters produced by the nanosecond laser ablation at fluence 0.53, 0.59 and 0.63 Jcm⁻². At low fluence, the surface

profile indicates a sharp jet at the centre of the ablated craters (Figure 6.36a). An increase of the laser fluence results in the emergence of a flatter micro bumps, as observed in Figure 6.36b. Further increases of applied laser fluence resulted in the sub-micro cavity, and the thickness of these micro wells are nearly comparable to the total thickness of molybdenum and aluminium (470 ± 70 nm).

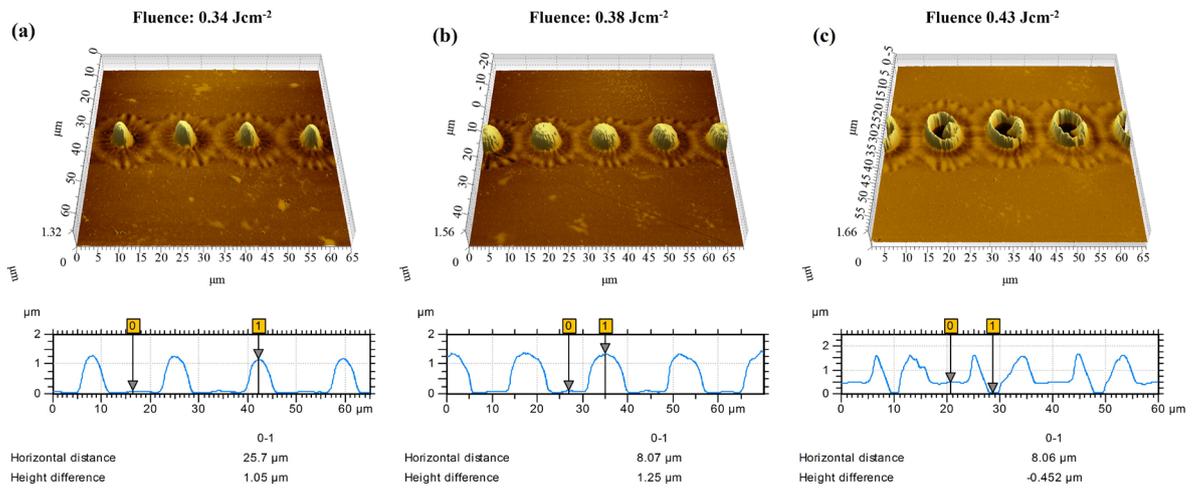


Figure 6.36: Different surface structures on MAM surface after irradiation of a nanosecond laser pulse indicating different ablation phenomena and the surface profile across these craters present a change in height between sample surfaces.

(e) At high fluence, significant damage is observed at the centre of MAM. Figure 6.37a presents the scanning electron micrographs of ablated crater at a fluence 0.63 Jcm^{-2} . Figure 6.37b presents the magnified image of the central region of the crater. The surface profile at the centre of the damage region presents height variations of up to 273 nm and this is indicative of indicates high damage at the centred peak of the laser spot.

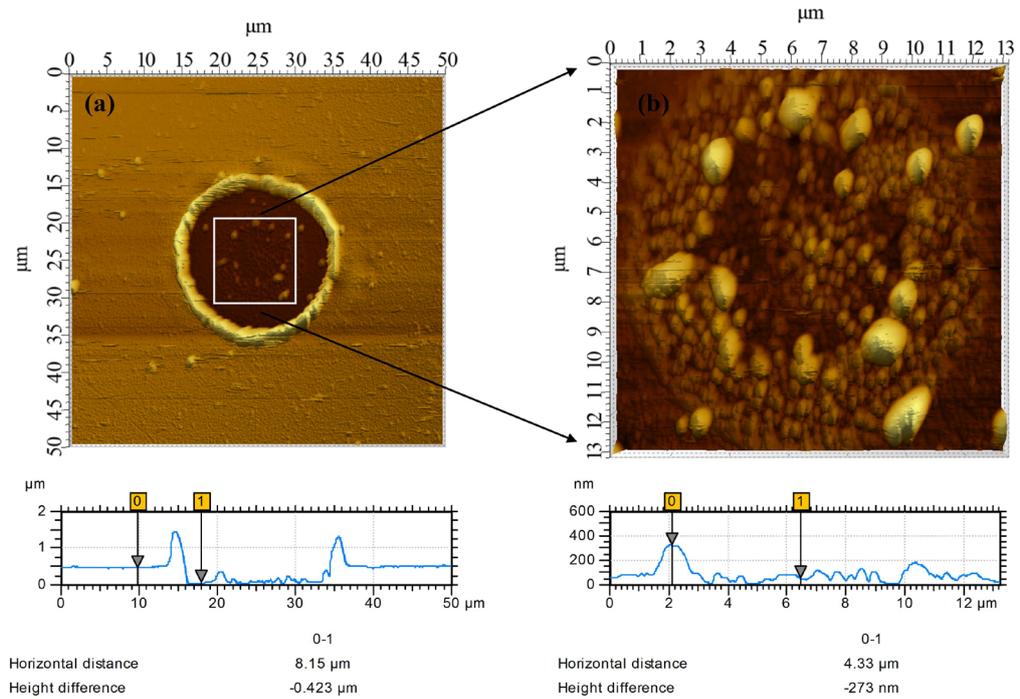


Figure 6.37: Atomic force micrograph of ablated crater at peak fluence of 0.63 Jcm^{-2} (a), the close-up inspection (b) shows significant substrate damage at the core of the crater, wavelength 532 nm

6.3.4. Energy dispersive X-ray analysis

Figure 6.38 presents energy dispersive X-ray analysis of single pulse nanosecond laser at four different peak fluences defined by (a) $F^{D1} < F < F^{D2}$, (b) $F^{D2} < F < F^{D3}$, (c) $F^{D3} < F < F^{D4}$ and (d) $F > F^{D4}$. Similar to femtosecond case, the different regions on the craters were selected for the elemental analysis.

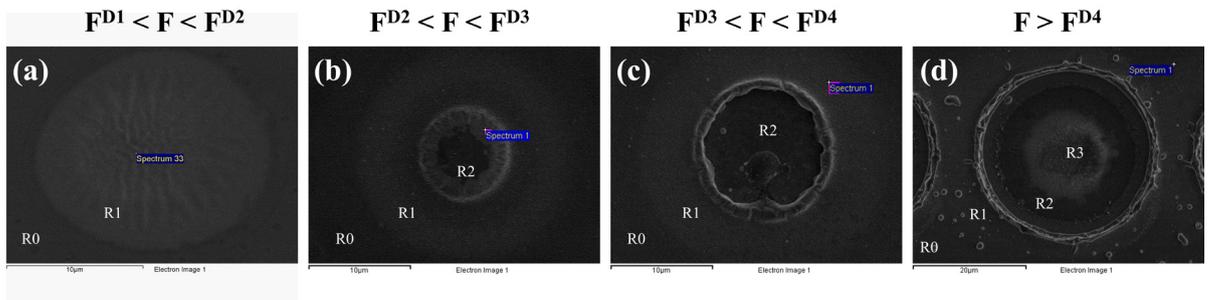


Figure 6.38: Electron microscope image presents ablated craters at four peak fluences, and the elemental analysis were carried out at different fluence regimes, wavelength 532 nm

(a) Fluence 1: (Peak fluence: $F^{D1} < F < F^{D2}$)

Figure 6.38a accounts for a crater on MAM surface after irradiation a nanosecond laser pulse of the fluence of 0.28 Jcm^{-2} . At this fluence, only one crater (diameter $D1$) is observed at the MAM surface, and the peak fluence of the laser pulse is higher than F^{D1} but lower than F^{D2} . At this fluence (below F^{D2}) the laser pulse resulted in a flowerlike structure on MAM surface. Elemental analysis was performed at the regions outside and inside the feature of a diameter of $D1$ on MAM and are termed as $R0$ and $R1$. Despite some structural changes in the MAM surface a small difference between the elemental composition between molybdenum and aluminium is observed.

(b) Fluence 2: (Peak fluence $F^{D2} < F < F^{D3}$)

At a fluence higher than slightly greater than F^{D2} , ‘*micro-bump*’ is started forming, and the Figure 6.38b presents SEM image of a crater after the incidence of nanosecond laser with fluence 0.41 Jcm^{-2} . Thus, the EDX measurement was taken place at three different fluence regimes at the crater, $F < F^{D1}$, $F^{D1} < F < F^{D2}$ and at $F^{D2} < F < F^{D3}$. The existence of molybdenum and aluminium were found at these three different regions, R0, R1 and R2 and the elemental compositions are tabulated in Table 6.5.

(c) Fluence 3: (Peak fluence $F^{D3} < F < F^{D4}$)

It was found that when the increases further, the ‘*micro-bump*’ does not exist at the centre of the feature with diameter D2, instead, a ‘sub-micro-well, develops (Figure 6.38c). The absorbed fluence at the crater was 0.45 Jcm^{-2} . The elemental compositions of are given in Table 6.5 and the existence of aluminium, molybdenum, indium, silicon and oxygen was observed in the region R3.

(d) Fluence 4: (Peak fluence: $F > F^{D4}$)

At higher peak fluence ($F > F^{D4}$), four diameters are observed on the MAM surface. The Figure 6.38d presents a crater on MAM surface by a nanosecond laser with 532 nm wavelength at a fluence of 1.13 Jcm^{-2} . EDX measurement was performed at four different areas at four different fluence regimes. Table 6.5 indicates different elemental compositions at four different fluence regimes.

Table 6.5: Atomic percentage of detected elements at different nanosecond fluence regimes using EDX technique

| Peak Fluence | Region of interest | Molybdenum (% Mo) | Aluminium (% Al) | Indium (% In) | Silicon (% Si) | Oxygen (% O) |
|---|---------------------------|--------------------------|-------------------------|----------------------|-----------------------|---------------------|
| <i>Fluence 1</i> ($F^{D1} < F < F^{D2}$) | R0 | 64.74 | 35.26 | 0 | 0 | 0 |
| | R1 | 51.54 | 48.46 | 0 | 0 | 0 |
| <i>Fluence 2</i> ($F^{D2} < F < F^{D3}$) | R0 | 64.74 | 35.26 | 0 | 0 | 0 |
| | R1 | 52.46 | 47.54 | 0 | 0 | 0 |
| | R2 | 39.60 | 60.40 | 0 | 0 | 0 |
| <i>Fluence 3</i> ($F^{D3} < F < F^{D4}$) | R0 | 64.47 | 35.53 | 0 | 0 | 0 |
| | R1 | 53.69 | 46.71 | 0 | 0 | 0 |
| | R2 | 0 | 10.52 | 23.13 | 14.68 | 51.67 |
| <i>Fluence 4</i> ($F > F^{D4}$) | R0 | 64.66 | 35.64 | 0 | 0 | 0 |
| | R1 | 50.96 | 49.04 | 0 | 0 | 0 |
| | R2 | 0 | 100 | 0 | 0 | 0 |

| | | | | | | |
|--|----|---|------|-------|-------|-------|
| | R3 | 0 | 0 | 16.59 | 17.30 | 66.10 |
| | R4 | 0 | 4.90 | 0 | 26.41 | 68.69 |

6.3.5. Numerical simulation of nanosecond laser ablation at low fluence

Numerical simulation of the interaction of a nanosecond laser pulse (wavelength 1064 nm) with MAM sample was carried out using single temperature heat diffusion model (chapter 3, section 3.7.1) at two absorbed threshold fluence, given by, F^{D1} (0.155 Jcm^{-2}) and F^{D2} (0.309 Jcm^{-2}). The evolution of the temperature at different layers of MAM sample was determined for these two fluences. Plasma shield effect was not considered in the simulation which is appropriate for this timescale and these fluences.

The laser pulse of duration (τ) 9 ns has a maximum intensity at $t = 20$ ns. The temperature MAM sample increases once it interacts with the laser pulse.

Figure 6.39 presents the peak temperature at $Z = 0$, at the surface and $Z = -40$ nm, at the interface after the interaction of nanosecond laser pulse with the MAM sample.

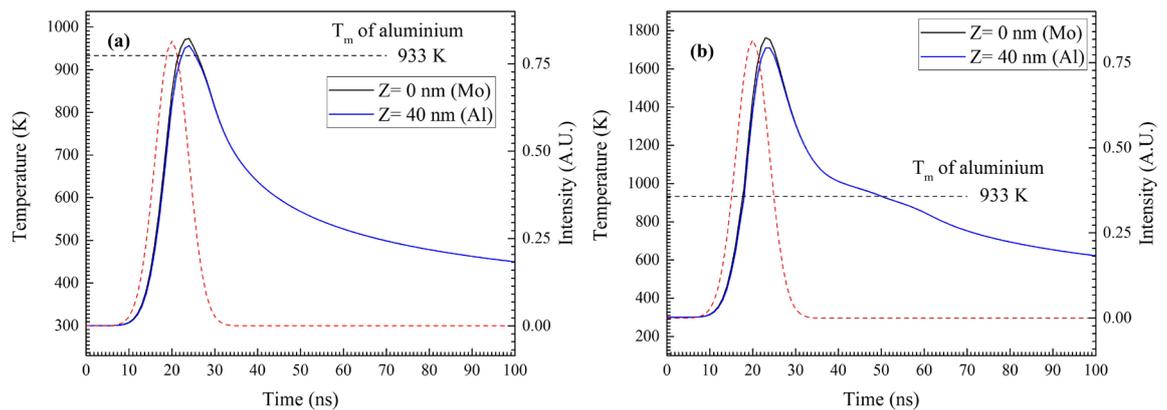


Figure 6.39: The transient peak lattice temperature on the surface $Z = 0$ and $Z = -40$ nm, resulted from the interaction of nanosecond laser (wavelength 1064 nm, pulse width 9 ns) of the fluences of (a) 0.155 and (b) 0.309 Jcm^{-2} . At the fluence 0.155 Jcm^{-2} , the peak temperature of aluminium layer just exceeds the melting temperature

The maximum peak temperatures of molybdenum layer take place at 24 ns (i.e. 4 ns after the peak laser intensity) and are found to be 973 and 1763 K for the peak value of absorbed fluence 0.155 and 0.309 Jcm^{-2} . It is obtained from the simulation that the peak temperature of the molybdenum stays below the melting temperature. The temperature of the molybdenum diffuses to lower surface via conduction. Figure 6.40 shows the time dependent peak temperature distribution across different depths inside the MAM sample at the absorbed fluences of 0.155 (Figure 6.40a) and 0.309 Jcm^{-2} (Figure 6.40b).

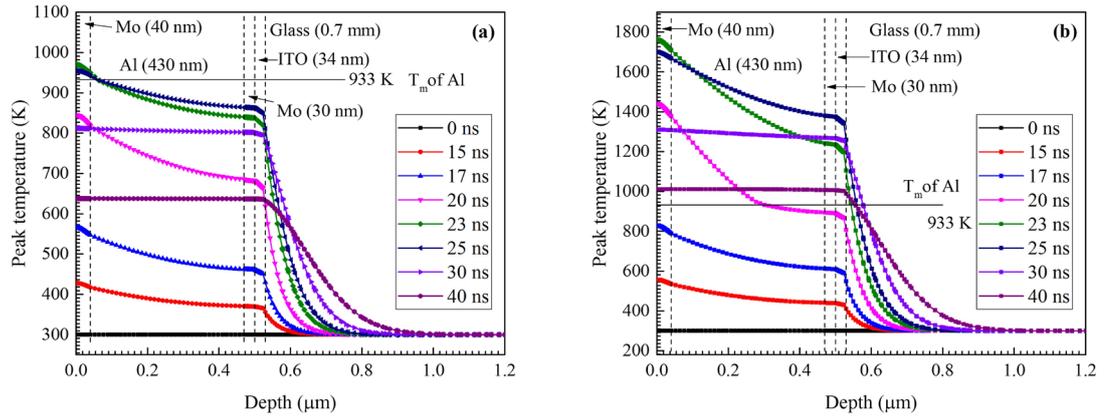


Figure 6.40: Peak temperature at different time delays as a function of the depth of the multi-layered MAM film at the peak fluences of (a) 0.155 and (b) 0.309 Jcm^{-2} . Nanosecond laser pulse of wavelength of 1064 nm and pulse width of 9 ns was used as a source.

Initially (0 to 25 ns), a sharp temperature gradient is found across the depth of the MAM sample. The decay rate of the lattice temperature increases in glass substrate because of its low thermal conductivity. At higher depth ($>1 \mu\text{m}$), where the depth increases the heat diffusion length, the peak temperature of the glass does not increase significantly and remains at the room temperature (300 K). Higher heat diffusion lengths of molybdenum ($\sqrt{D\tau} \sim 693 \text{ nm}$) and aluminium ($\sqrt{D\tau} \sim 669 \text{ nm}$) lead to almost a uniform temperature distribution across the depth of the molybdenum and aluminium. It is observed that at the fluence $F^{D1} = 0.155 \text{ Jcm}^{-2}$, the temperature of the aluminium just exceeds the melting temperature. The increase of the temperature leads to thermal expansion of different layers. The thermal expansion induces strain at different layers. Figure 6.41 presents a 2D representative image the vertically directed tensile strain at (ϵ_{ZZ}) throughout an un-deformed layer of the MAM sample. The scale bars are displayed along with each image.

The maximum peak strain was observed at the interface between molybdenum and aluminium (layer 1 and layer 2). Almost 3% and 6% peak strain (ϵ_{ZZ}) were observed at the interface ($Z = -40 \text{ nm}$), caused by the higher thermal expansion coefficient of aluminium ($23 \times 10^6 \text{ K}^{-1}$) [199] than molybdenum ($4.8 \times 10^6 \text{ K}^{-1}$) [45].

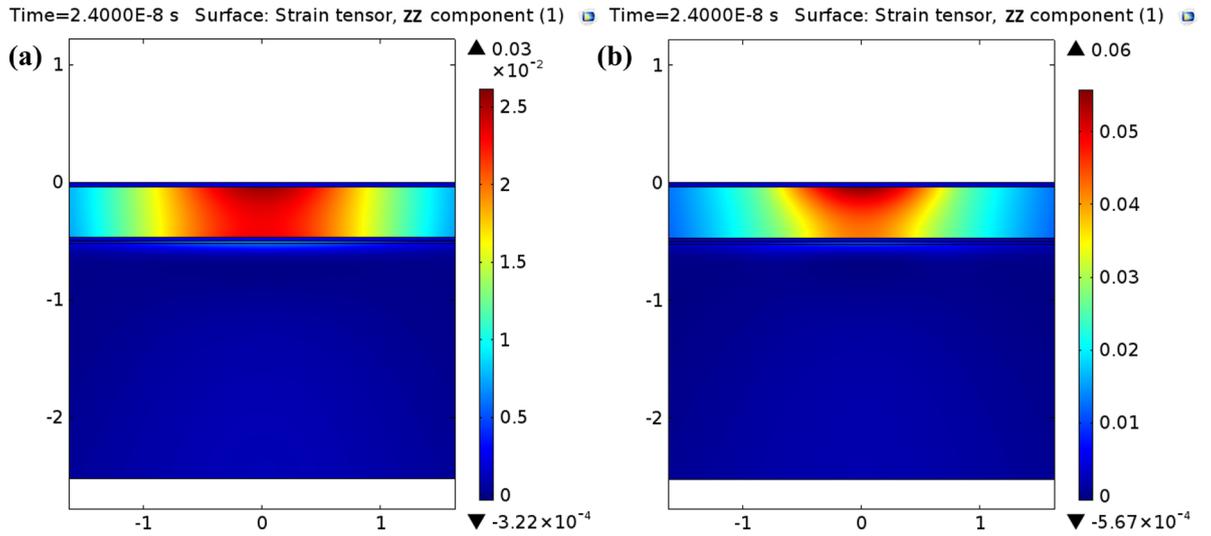


Figure 6.41: Thermally induced strain (ϵ_{ZZ}) at different layers of the MAM sample at the peak fluence of (a) 0.155 and (b) 0.309 Jcm^{-2} . First (40 nm), second (430 nm), third (30 nm) and fourth (34 nm) layers correspond molybdenum, aluminium, molybdenum and ITO film, respectively and presented in the Figure 6.20.

The increase of the vertical strain leads to an increase of the pressure, directed normal to the molybdenum at the molybdenum/aluminium interface. Figure 6.42 presents the origin of the vertically directed pressure exerted on the molybdenum layer.

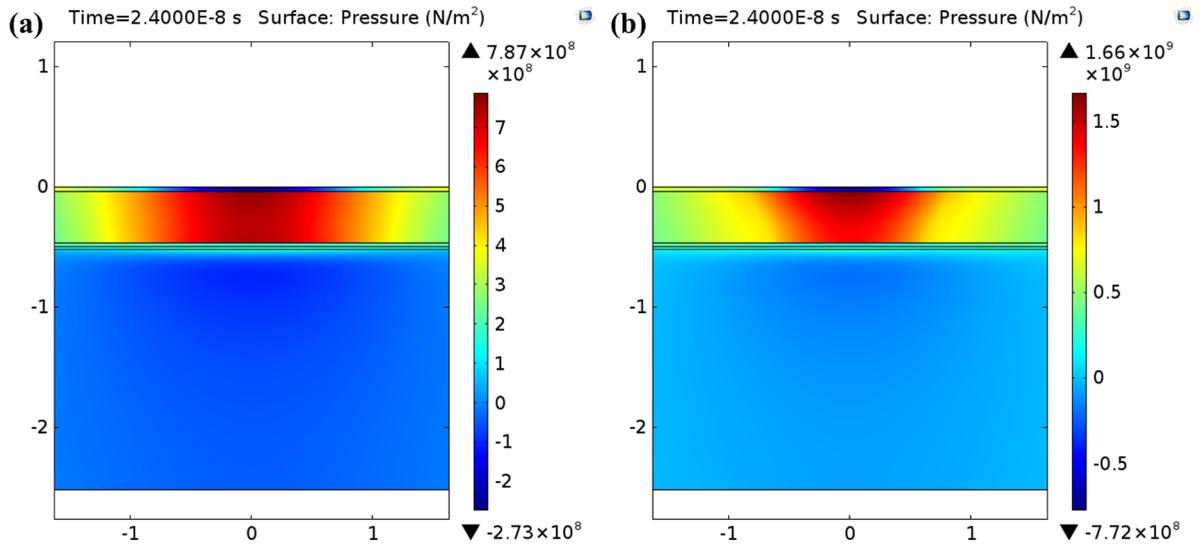


Figure 6.42: Cross-section of the MAM sample indicate the source of the induced pressure due to the thermal expansion of different layers at the peak fluence of (a) 0.155 and (b) 0.309 Jcm^{-2} .

The peak pressure acts on the molybdenum layer ($X = 0, Y = 0, Z = -40 \text{ nm}$) is found to be 7.87×10^8 ($F = F^{D1} = 0.155 \text{ Jcm}^{-2}$) Nm^{-2} and 1.66×10^9 ($F = F^{D1} = 0.309 \text{ Jcm}^{-2}$) at the time $t = 24 \text{ ns}$ at the surface $Z = -40 \text{ nm}$.

6.4. Discussion

Both laser systems (femtosecond and nanosecond) generate Gaussian (spatial and temporal) pulses. The incident laser pulse induces a Gaussian fluence distribution on the surface of MAM sample when focussed on the sample surface. The fluence absorbed by the MAM sample was varied by adjusting the energy of the incident laser pulse. Several interesting features were

identified on the surface of MAM craters from the optical microscopy images for femtosecond (Figure 6.1) and nanosecond (Figure 6.23) laser experiments.

6.4.1. Femtosecond laser ablation

The femtosecond laser ablation at three wavelengths with the MAM samples for a range of fluence regimes are identified in the Figure 6.16, 6.17 and 6.18. Three fluence regimes will be discussed in this section defined by $F^{D2} < F < F^{D3}$, $F^{D3} < F < F^{D4}$ and $F > F^{D4}$.

1. Peak fluence ($F^{D2} < F < F^{D3}$): The peak fluence in between F^{D2} and F^{D3} are presented in the Figure 6.16a, b (1030 nm), 6.17a (515 nm) and 6.18a (343 nm). Formation of a ‘*nano-bump*’ is observed at this fluence range. As the fluence exceeds F^{D2} , a significant difference in the surface morphology is observed by the scanning electron microscopy (Figure 6.9).

We attribute the ‘*nano-bump*’ formation to the following process. Absorption of the laser pulse resulted in a ‘sudden’ ($< 10^{12}$ s) increase of electronic temperature molybdenum film. This electronic energy couples to the molybdenum lattice. Similar to the ultrashort laser ablation of molybdenum thin film on glass (Chapter 3), the localised heating in the solid molybdenum film and its low thermal conductivity results in a spatial confinement of the stress for a time interval of $\sim 10^{-11}$ s [175]. During the build-up of the compressive stress, the stress relaxes via vertical expansion of the molybdenum film, as it is free to expand in that direction [167, 173]. On a nanometre scale, a pressure wave reflects back from the molybdenum/aluminium interface and causes nanostructures to form on the upper surface of the molybdenum film; this is expected to occur in less than nanoseconds. On a micro scale, due to the mismatch of the thermal expansion between molybdenum and aluminium [191, 199], the aluminium layer expands more rapidly than the molybdenum layer and thereby exerting an upward stress at molybdenum/aluminium interface. We expect this bump formation occurs at longer time frame than nanoscale process. The combination of the relaxation of the compressive stress, reflected pressure wave and the pressure of the highly expanding aluminium layer causes the separation of loosely adhered molybdenum layer from aluminium and thereby creates the condition required for ‘*nano-bump*’ formation. When the vertical expansion of molybdenum reaches beyond the plastic limit of the material (~ 500 MPa), a permanent nanobump is established at the MAM surface. The compressive stress on molybdenum and the upward pressure by aluminium initiates several cracks on the molybdenum layer (Figure 6.11a,b,c). The numerical simulation suggests that as the peak fluence of the laser pulse exceeds F^{D2} , the temperature of the aluminium layer exceeds its melting temperature, and it is possible for the molten aluminium to come out through these cracks driven by the hydrostatic pressure thermally induced by the thermal energy in the aluminium layer. As the molten aluminium cools down and solidifies, the aluminium would most likely be retained in these cracks. As there is no evidence to confirm this process, we conclude that model overestimates the temperature of aluminium or the aluminium-molybdenum surfaces do not allow such fluid flow.

2. Peak fluence ($F^{D3} < F < F^{D4}$): The peak fluence in between F^{D3} and F^{D4} are presented in the Figure 6.16c,d,e (1030 nm), 6.17b,c,d,e,f (515 nm) and 6.18b,c,d (343 nm). The increase of the peak fluence above the penetration threshold (F^{D3}); the penetration threshold is the fluence required to penetrate a hole in the molybdenum film. It results in a clear delamination of the upper molybdenum layer for all three wavelengths (Figure 6.13).

We expect mechanical fracture in the molybdenum layer takes place at the fluence above this penetration threshold (F^{D3}), again due to the stress confinement [175]. The relaxation of the highly compressive stress takes place by the expansion of the molybdenum film away from the surface. A pressure is also generated in the molybdenum because of rapid heating of this layer by the incident laser pulse. At fluences higher than F^{D3} , the sudden stress on the molybdenum film is likely reach to its ultimate fracture strength. Again, the compressive stress, pressure wave and the thermal expansion result in delamination of the molybdenum layer with a bump-like feature on its surface.

It is interesting that a well of a depth greater than the thickness of molybdenum film is formed inside the craters. This effect is observed for all wavelengths. The typical depths are listed in the Figure 6.16 (1030 nm), Figure 6.17 (515 nm) and Figure 6.18 (343 nm). It suggests that removal of some melted aluminium also takes place along with the delamination of the top molybdenum layer (Figure 6.16c,d,e, 6.17b,c,d,e,f and 6.18b,c,d). Numerical simulation suggests that at this fluence (higher than F^{D3} , but lower than F^{D4}), the laser fluence is not sufficient to increase the temperature of the entire aluminium layer (430 ± 50 nm) beyond its melting temperature. The depths of the craters are found to be less than the entire thickness of the aluminium layer. The formation of crater shape in aluminium below the molybdenum surface is intriguing. We propose two mechanisms for the ablation of MAM samples at difference peak fluences. It is interesting that the lower surface profile of these craters is flat for lower fluences and does not indicate a molten phase has formed. While at higher fluences the profile is bowed indicating redistribution of molten fluid flow.

(a) *Lower fluence*: Figure 6.16c,d (1030 nm), Figure 6.17b,c (515 nm) and Figure 6.18b,c (343 nm) shows the crater having a flat aluminium crater floor and suggests a non-thermal ablation mechanism. The numerical simulation suggests at this fluence (F^{D3}), the temperature of aluminium reaches its melting temperature (Figure 6.22). The evidence from the experiments and the numerical simulations are considered further:

It was considered in the numerical simulation that molybdenum and aluminium both stay in contact. The temperature of aluminium increases via heat conduction from molybdenum to aluminium layer and aluminium reaches its melting temperature at ~ 2 picoseconds after the peak laser pulse intensity. Perhaps this contact is the reason for over estimation of the temperature of aluminium compared with experimental findings. Three cases need to be considered.

- We first consider the case where the removal of the molybdenum may take place on shorter time scale compared to the time over which the temperature of aluminium approaches its melt temperature. In such scenario, the removal of molybdenum occurs from the solid aluminium surface. Because of the early removal of the molybdenum layer, less heat flux is conducted from molybdenum to aluminium. Thereby, the temperature of aluminium does not reach its melting temperature. In this case, the removal of molybdenum would take place at a time less than 2 picoseconds from the peak intensity of the incident laser pulse. However, it is estimated that the removal time is less than the time required to reflect a pressure wave from the molybdenum/aluminium interface to create nanostructures on the nanobump. This time scale is estimated to be ~ 6.4 picoseconds. Hence, in this case, the removal of aluminium in this crater is not understood clearly for this timescale. Perhaps

the temperature increase induced in the aluminium may somehow cause mechanical fracture within the upper surface of solid aluminium layer. The schematic interpretation is presented in Figure 6.43.

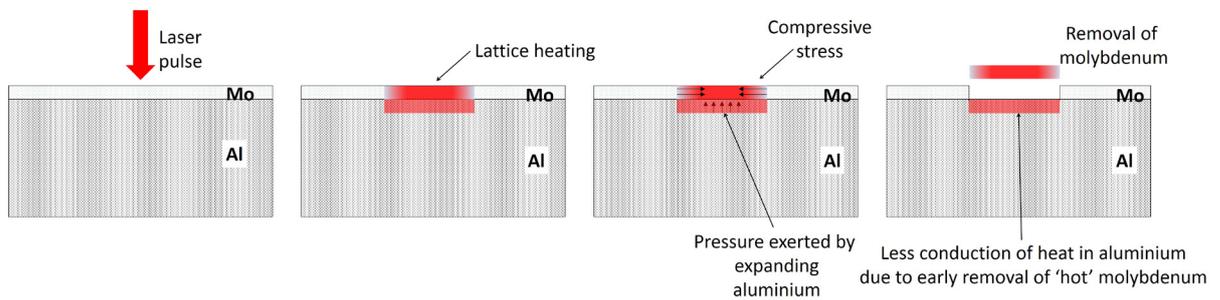


Figure 6.43: Predicted early removal mechanism of molybdenum thin film from aluminium layer

- In the second case, we consider the case where molybdenum is removed over longer time scale. In this case it is expected that the delamination of molybdenum thin film causes a separation between it and aluminium layer. At the delaminated area of the molybdenum thin film, the vertical conduction of heat from the bottom surface of molybdenum to the aluminium does not take place. Most of the thermal energy of the molybdenum layer conducts along the radial directions and some energy can be radiated from the surfaces. The thermal energy induced in the molybdenum layer can conduct to the aluminium layer only at the non-delaminated periphery. The temperature of the aluminium layer can be increased further via the radiation of thermal energy from the molybdenum surface. The radiation of thermal energy from the separated molybdenum results in a reduced temperature of layer resulting in a slower heating rate in the centre of the crater of the aluminium surface. Also as the molybdenum and aluminium are no longer in contact inside the feature of diameter D2 (Figure 6.2b), a slower cooling rate of remaining aluminium takes place. We anticipate these slow heating and cooling rates can cause a redistribution of solid aluminium grains via diffusion. This consolidating densifies of the material structure and reducing its profile. The evidence for crystal growth is presented in Figure 6.14(a) and (b). There is no aluminium droplet was found on the surface of aluminium crater. The schematic interpretation is shown in Figure 6.44.

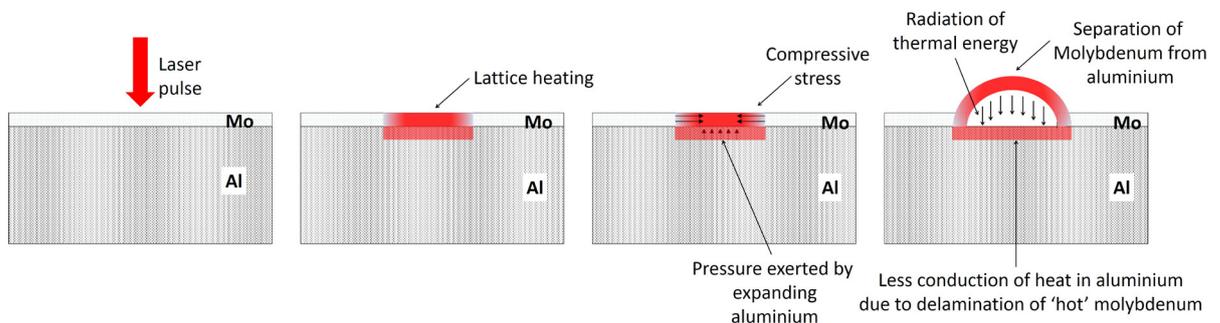


Figure 6.44: Delamination mechanism of molybdenum from the aluminium layer. The separation between molybdenum and aluminium results in less conduction of thermal energy from molybdenum to aluminium

- In the third case, we consider a separate mechanism. The absorption of laser pulse by the molybdenum thin film causes the increase of electron temperature (T_e) of molybdenum.

Peak electronic temperature at the molybdenum was estimated using the numerical simulation and estimated to be ~ 18000 K. Highly energised electrons (energy $kT_e \sim 1.55$ eV) diffuse and scatter via electron-electron scattering processes to establish this electron temperature. At this temperature, it is considered that some electrons can be emitted from the molybdenum surface via the thermionic effect. The emitted electrons from the lower surface can further energise aluminium lattice forming a dense electron cloud in the aluminium. The additional electrons occupy higher energy states which may reduce the strength of the material. Due to this, the fragmentation of aluminium layer may take place more or less uniformly across a region defined by the beam shape.

(b) *Higher fluence*: The craters obtained at higher fluence are presented in the Figure 6.16e (1030 nm) Figure 6.17d,e,f and 6.18d (343 nm). At high fluences, the relatively smooth profile of aluminium suggests significant melting and redistribution of aluminium melt flow across the crater.

An increase of laser fluence induces a greater temperature increase in material. With increasing peak fluence, more removal of aluminium takes place and the maximum depth obtained for craters increases. As the laser fluence is highest at the centre of the beam, the maximum depth of the aluminium crater is observed at the centre of the crater.

Of particular importance, the interaction of MAM sample with femtosecond laser pulse shows a remarkable effect in Figure 6.14. The significant increase of the grain structure of aluminium with increasing applied laser fluence is shown in the Figure 6.14.

Laser annealing is a popular method for improving the crystallinity of materials [253, 254]. At minimum, short pulse laser source is long enough to sustain atomic diffusion that provides the solid-state crystallisation [255-257]. At higher fluences a molten phase is established and crystal may form when cooling proceeds at a reasonably slow rate. We propose that the metal molybdenum layer serves to

- a. Increase the duration of time the aluminium stays at a high temperature
- b. Increases the cooling rate of aluminium
- c. Allows high pressure re-crystallisation
- d. Facilitates surface diffusion

It is predicted that as the time required to cool the molten aluminium below the melting temperature increases with increasing fluence, the probability of surface diffusion of aluminium on the molybdenum layer increases at the aluminium/molybdenum interface. The surface diffusion (D) (in m^2s^{-1}) of aluminium was estimated from Arrhenius behaviour with respect to the lattice temperature (T) given by, $D = D_0 e^{-E_{av}/kT}$ [258-260]. Where, D_0 is the temperature independent pre-exponential factor (m^2s^{-1}), E_{av} is the activation energy (Joule) for the diffusion and k is the Boltzmann's constant. Thus, it is expected from this equation that diffusion increases with increasing the lattice temperature. The mean surface diffusion length, \bar{l} , (in meter) is then estimated from $\bar{l} = 2\sqrt{Dt_0}$ [261], where t_0 (in sec) is the time required to cool the lattice temperature to a particular value. It was estimated from the numerical simulation that the cooling time of the aluminium lattice from the peak value to a value (2/3 of the melting temperature) are

200 picoseconds and 5 ns for the fluences of F^{D1} and F^{D2} , respectively. The surface diffusion length of the aluminium lattice to molybdenum in the aluminium and molybdenum materials lattice are calculated to be 13.8 Å and 256 Å, for the peak absorbed fluence of 0.068 and 0.133 Jcm⁻², respectively. Thus, as the time to cool down the aluminium increases with increasing laser fluence, the probability of reconstruction of aluminium grain (lattice constant of aluminium: 4.05 Å [262]) increases.

Detail analysis of the relationship between the fluence and grain size was stimulated by this work and has been undertaken for polysilicon and this is subject to a separate study.

3. Peak fluence ($F > F^{D4}$):

The crater on the MAM samples at peak fluence above F^{D4} are presented in the Figure 6.16f (1030 nm) and 6.18e,f (343 nm). The increase of the peak fluence above the F^{D4} results in a complete delamination of MAM sample from the glass. This is also supported by the EDX measurements of the craters (Table 6.3). This is not observed at green wavelength (515 nm). The reason for this is not understood clearly.

Although the numerical simulation was not conducted at this fluence region, it is proposed that at this high fluence the laser pulse induces a very high temperature in MAM samples. It is predicted that above F^{D4} , the peak temperature of molybdenum, aluminium and ITO layers exceed their vaporisation temperature.

6.4.2. Nanosecond laser ablation

The nanosecond laser ablation at three wavelengths (1064, 532 and 355 nm) with the MAM samples at a range of fluences are presented in Figure 6.29, 6.30 and 6.31. Four fluence regimes will be discussed in this section defined by, $F^{D1} < F < F^{D2}$, $F^{D2} < F < F^{D3}$, $F^{D3} < F < F^{D4}$ and $F > F^{D4}$.

1. Peak fluence ($F^{D1} < F < F^{D2}$): First we consider the situation when the peak fluence exceeds F^{D1} but stays less than F^{D2} , a flower-like structure with a sharp dip at the centre is produced on the surface of MAM sample (Figure 6.29a, Figure 6.30a and Figure 6.31a). AFM profiles suggest the centre of these features consists of nano hole that extends to the depth of aluminium layer. This conclusion is supported by the presence of particles on the surface of craters at each wavelength. The presence of such deep holes is not observed on the SEM images presented in Figure 6.26(a), Figure 6.27(a) and Figure 6.28(a). It is not absolutely clear whether this is real or an artefact of the AFM.

The case for thinking these deep holes is as follows. The interaction of a nanosecond pulse with MAM sample results in an increase of lattice temperature of the molybdenum and aluminium layers. Like the interaction of short pulse laser interaction with molybdenum thin film, it is observed that the nanosecond laser pulse induces a significant thermal effect on the layer underneath molybdenum as seen from Figure 6.26 (1064 nm), Figure 6.27 (532 nm) and Figure 6.28 (355 nm). Numerical simulation suggests that the high thermal diffusion length of the thin film layers during the interaction of MAM with nanosecond laser pulse (molybdenum ~ 693 nm, aluminium ~ 669 nm, 9 ns laser pulse) causes almost a uniform temperature distribution throughout the molybdenum layer (Figure 6.40(b)). The increase of temperature in the MAM

sample causes thermal expansion of molybdenum and aluminium layer. In the case of the molybdenum layer, the maximum expansion takes place at its top surface at the centre of the incident laser pulse i.e. at $X=0, Y=0, Z=0$. Also, the numerical simulation (Figure 6.40 (a)) suggests that at the fluence higher than F^{D1} , the molybdenum stays below its melt temperature (2897 K) while the peak temperature of aluminium just reaches its melting point (933 K). We believe that at this fluence, due to the thermal expansion, the molybdenum layer extends beyond its plastic limit (~ 500 MPa). This results in a permanent deformation of molybdenum layer. Also, the molten aluminium is forced to travel radially away from the centre. As a result, it is expected that the molybdenum film separates from the melted aluminium at the Mo/Al interface. The deformation in the molybdenum film is constrained and forces the expanding aluminium to push through the regions underneath the molybdenum layer. In this scenario, the maximum stress appears at the centre, created by the radial expansion of the petal-like features. The dip in the profile at the centre of the crater is likely to lead to a ductile deformation of the molybdenum layer. In such case, this may lead to the formation of a nano-hole through which aluminium can vent and be resolidified as particles. Within the vertical range of the AFM images (Figure 6.26a, Figure 6.26b and Figure 6.26c), the solidified particles are observed on the surface.

2. Peak fluence ($F^{D2} < F < F^{D3}$): At the peak fluence higher than F^{D2} , a laser pulse induced ‘*micro-bump*’ is observed centred at the point $X = 0, Y = 0$ (Figure 6.29b, c, Figure 6.30b, c and Figure 6.31b, c). The height of the ‘*micro-bump*’ increases with increasing peak value of laser fluence (Figure 6.36).

The numerical simulation predicts, at the fluence F^{D2} , the peak temperature of the entire aluminium layer (throughout the depth) in the enclosed system exceeds the melting temperature (Figure 6.40(b)) due to the high thermal diffusion length. While, the peak temperature of molybdenum stays below its melting temperature. The aluminium expands more than the molybdenum because of the higher thermal expansion coefficient. The high-volume expansion of aluminium, confined by the edge of the crater, at the interface causes the molybdenum layer to push upward normal to the surface. The stress induced by the aluminium leads to a ductile deformation of solid molybdenum layer (Figure 6.33a). This figure shows an intact of molybdenum layer raised in the form of a ‘*micro-bump*’. When this stress in the molybdenum layer is just less than a fracture limit, the strained molybdenum layer is further deformed (Figure 6.33b). A further increase of fluence leads to a disruption of the molybdenum layer (Figure 6.33c). In each case, when the temperature cools down, the molybdenum surface remains strained and does not return to its initial position. Unlike the generation of ‘*nano-bump*’ during femtosecond laser interaction, the temperature of the entire aluminium layer exceeds its melting temperature when the fluence exceeds F^{D2} . The peak height of the ‘*micro-bump*’ are found to be ~ 1 μm for all wavelengths.

It is expected that the increase of applied laser fluence leads to an increase of the temperature of the aluminium. At higher fluence, the aluminium exerts a stronger upward pressure on the Mo/Al interface (Figure 6.33b). As a result, the peak height of the ‘*micro-bump*’ increases with laser fluence (Figure 6.36). Also, with increasing applied laser fluence, the ratio between the peak height and the peak width of the ‘*micro-bump*’ are found to decrease from 0.15 ± 0.01 to 0.09 ± 0.01 , 0.17 ± 0.01 to 0.12 ± 0.01 and 0.11 ± 0.01 to 0.09 ± 0.01 using the incident laser wavelengths of 1064, 532 and 355 nm, respectively. This indicates that the radial expansion of the ‘*micro-bump*’

also takes place. This radial expansion of the ‘*micro-bump*’ is also supported from the SEM microscopy measurements shown in Figure 6.33. We expect that, first, a ‘*micro-bump*’ of molybdenum of ‘sharp tip’ is produced on the MAM surface (Figure 6.33a). The sharp tip of the microbump is observed from the AFM microscopy image of the crater (Figure 6.36a). An increase of fluence results in radial expansion of the microbump (Figure 6.33b). This radial expansion results in a ‘*micro-bump*’ of comparatively flatter tip. We anticipate that this radial expansion arises from the molten aluminium inside the ‘micro-bump’. The radial expansion of aluminium pushes the wall of the molybdenum film from inside at the direction away from the centre. This results in micro-bump with relatively flatter top of molybdenum. A further increase in fluence results in fracture of molybdenum exposing the likely presence of aluminium inside a molybdenum shell (Figure 6.33c).

3. Peak fluence ($F^{D3} < F < F^{D4}$): The upward stress increases with increasing peak laser fluence (Figure 6.42). When the upward stress exceeds the limit of fracture of a thin molybdenum film, the deformed molybdenum breaks and the sub-surface molten aluminium emerges as a jet-like feature in the centre of the crater. When this molten aluminium jet cools down, it can form a droplet on the remaining surface (Figure 6.29d, e and Figure 6.30d). This jet-like structure is surrounded with a ring-like feature. This ring-line feature observed in the nanosecond interaction is different to the fracture features obtained in the femtosecond case. Although the simulations are ever more inaccurate as fluence increases, it is expected that at this high fluence, the laser pulse induces high-temperature distribution across the MAM sample and the peak temperature of molybdenum, aluminium and ITO approaches their melting temperature. The molten layers cause the formation of a ridge-like boundary at the edge of the crater. Most of these materials ejected from the crater and rest of the melted ITO and aluminium redistribute on the craters. Detected of aluminium and indium is due to the redistribution of dissolved aluminium and ITO (Table 6.5).

It is expected that increase of fluence above F^{D3} , results in complete removal of aluminium and 2nd molybdenum layer (thickness 30 nm) of MAM samples. The ITO layer undergoes melting and redistributes on the centre of the crater.

4. Peak fluence ($F > F^{D4}$): When the laser fluence above F^{D4} , the laser ablation leads to the formation of a feature on the crater of diameter $D4$. Above this fluence, significant damage occurs on the glass surface (Figure 6.37). In-depth analysis of craters at these fluence regimes will be done in the future.

6.4.3. Optimisation of molybdenum-aluminium-molybdenum sample processing by femtosecond and nanosecond laser sources

In summary, the optimization of MAM processing by femtosecond and nanosecond laser sources is indicated in the Table 6.6,

Table 6.6: Preferred parameters to process molybdenum-aluminium-molybdenum sample by femtosecond and nanosecond laser sources

| <i>Name</i> | <i>Preferred laser parameter</i> |
|---|-------------------------------------|
| <i>Selective ablation of different layers</i> | Femtosecond laser (1030 and 343 nm) |
| <i>Less melting of different layers</i> | Femtosecond laser |
| <i>Clean ablation</i> | Femtosecond laser |

| | |
|--|----------------------------|
| <i>Solid state crystallisation of aluminium</i> | Femtosecond laser |
| <i>Lower fluence for complete removal</i> | Nanosecond laser (355 nm) |
| <i>Complete removal of first layer (Mo: 40 nm)</i> | Nanosecond laser (1064 nm) |
| <i>Nanostructure formation of molybdenum</i> | Femtosecond laser (343 nm) |
| <i>Molybdenum bump formation</i> | Femtosecond laser |
| <i>Higher processing speed</i> | Nanosecond laser |

The thesis has described technical and scientific merits of the laser material interaction. In this section we attempt to elaborate the potential economical benefit of the interaction. We do this for the most enabling process documented in the thesis, the laser induced crystallinity process. We present a simple cost benefit analysis using this approach compared with an alternative laser induced crystallinity process demonstrated by an excimer laser.

The assumption used in generating this economic assessment are as follows:

1. A generation 10 (G10) sized sheet of a molybdenum heterostructure is processed to generate a laser induced crystalline layer. Each G10 sheet consist of 6 individual 70-inch screens; the object is to crystallise the gate electrode for each pixel in each screen.
2. The aspect ratio of each molybdenum sheet is 16:9. Number of pixels in a single screen along the horizontal and vertical directions are 7680 and 4320, respectively; 33177600 pixels are equivalent to a TV screen of 8K resolution.
3. The size of each pixel (processing area) is estimated to be 0.020178 x 0.020178 cm².
4. The depreciation time of the laser is 5 years.

Table 6.7 presents analysis of cost of a molybdenum G10 sheet processed by a femtosecond and an excimer (nanosecond) laser.

Table 6.7: Comparison of cost of a G10 sheet processed by femtosecond and nanosecond laser pulses

| Femtosecond laser | Excimer laser |
|---|--|
| <ul style="list-style-type: none"> • Total cost of process setup: 1160 k€ • Approximate cost of the laser: 140 k€ • Cost of the scanner: 15 k€ • Cost of optics: 5 k€ • Cost of stages: 1000 k€ • Depreciation rate per hour: 0.026 k€/hour • Maximum repetition rate of laser pulse: 100 kHz • Spot size of a focussed femtosecond laser beam: 30 μm. • Maximum speed of the stage: 10 ms⁻¹. • Total transit time to cover a full G10 sheet: 1.67 hours • Total cost of processing of a G10 sheet: 43.33 € | <ul style="list-style-type: none"> • Total cost of process setup: 3600 k€ • Approximate cost of the laser: 2000 k€ • Cost of the beam homogeniser: 500 k€ • Cost of optics: 100 k€ • Cost of stages: 1000 k€ • Depreciation rate per hour: 0.082 k€/hour • Maximum repetition rate of laser pulse: 600 Hz • Spot size of excimer laser beam along x and y direction: 0.75 m and 30 μm. • No of shots required to achieve the laser induced crystallinity: 20. • Total transit time to cover a full G10 sheet: 3.71 hours |

- Total cost of processing of a G10 sheet:
304.93 €

This simple cost estimation per device shows an advantage of achieving crystallinity by a femtosecond over an excimer laser (nanosecond). These values are an approximation and need further review, but they give a sense of processing cost on the molybdenum sample.

6.5. Chapter conclusion

This chapter investigated the interaction of molybdenum–aluminium–molybdenum multi-layered thin film (MAM) with ultra-short and short pulsed laser sources. The interplay between molybdenum and aluminium was studied using different off-line characterisation techniques.

Femtosecond laser ablation on MAM:

1. Femtosecond laser interaction of MAM at 1030, 515 and 343 nm wavelength leads to the selective structuring of different layers.
2. Multiple features with different diameters indicate different fluence regimes on the craters.
3. It was found that the damage threshold required for the outermost ring decreases with reducing the wavelength of the incident laser. The threshold limit of other diameters is higher for 515 nm than 1030 and 343 nm laser wavelength. Thus, 515 nm femtosecond laser is not suitable for complete elimination of multi-layered film assembly from the glass substrate with respect to 1030 and 343 nm laser.
4. Single pulsed UV femtosecond laser resulted in several nano-cracks on glass (fluence regime $F^{D^4} < F$). We did not observe any cracks by 1030 nm laser wavelength. We are unable to clarify this beyond reasonable doubt. It is known that the cracking of glass is observed when the glass undergoes a tensile stress. It is expected approximately 0.1% of the incident laser energy is directly absorbed by the glass substrate. Higher absorption of UV laser energy is expected to take place when compared with IR and green wavelengths. The absorption of optical energy in glass leads to an increase of temperature. The higher temperature, the greater the initial compressive stress. A tensile stress follows this compression on cooling. The greatest expansion occurs at the hottest part of the glass where the surface tension is lowest. Cracking of the glass is observed on cooling for appreciable fluences (higher than F^{D^4}). The crack density and directionality presented in the Figure 6.15 are insufficient to indicate the origin of the cracks during selective ablation.
5. Delamination of the top layer by femtosecond laser indicates the removal of molybdenum layer mainly takes place by the generation of highly compressive stress by a photomechanical mechanism combined with the pressure originated from the highly expandable aluminium gives rise to mechanical fracture of molybdenum layer. The interaction of laser with MAM indicates a thermoelastic ablation and the thermal effect increases with increasing absorbed fluence.
6. Re-crystallisation of the aluminium layer is achieved by a single femtosecond pulse. This result in an increase of grain size of aluminium layer with increasing incident laser fluence. The increase in grain size may lead to an increase in conductivity of the aluminium layer.
7. Several particles are observed at the surrounding of ablated crater. Thus, cleaning of the sample surface is required after surface structuring using femtosecond laser pulse.

Nanosecond laser ablation of MAM:

1. Several novel sub-micro and microstructure are formed at different fluence on the surface multi-layered thin film assembly.
2. Similar to femtosecond case, the interaction of nanosecond laser pulse indicates different fluence regimes. At low fluence (below F^{D2}), a flower like structure resulted from the thermal expansion of molybdenum and aluminium layer.
3. Hollow '*micro-bumps*' of molybdenum are formed on the multi-layered film induced by nanosecond laser ablation by impinging the molybdenum layer. The formation of the microprotrusion is most likely due to a photo-thermal subsurface expansion of aluminium layer.
4. If upward pressure created by melted aluminium increases beyond the fracture limit of molybdenum, the removal of molten aluminium come out from the molybdenum like a volcano and results in a sub micro-cavity.
5. The thermal effect increases with increasing laser fluence, as observed by the scanning electron and microscope. Thus, at high fluence, the interaction of MAM indicates a thermal ablation.
6. Optical microscope (OM) images suggest that the careful structuring at high fluence is tough to achieve by 1064 nm nanosecond laser. Although, OM images indicate an increase in selective ablation during the interaction of MAM with 532 and 355 nm laser.

Chapter 7: Conclusions and future work

The key findings of the experimental works are presented at the end of each result chapters. The purpose of this section of the thesis is to summarise the key results in the context of the state of the art in the literature and to identify their potential impact.

This work primarily investigates the interaction of ultra-short and short laser pulses with the molybdenum bulk and 50 nm thin film samples. The interaction processes were understood by investigating the ablation mechanism of molybdenum samples using a femtosecond and a nanosecond laser pulse operating in IR, Green and UV wavelengths. To do so, firstly, the amount of laser energy absorbed by the samples were determined from the reflectivity and transmissivity measurement by an integrating sphere. The ablation threshold fluence of the molybdenum samples was determined using Liu's method. The surface morphology of the ablated craters was identified using SEM measurements. In-depth analysis of the surface topography and the profile of the ablated craters were performed using AFM operating in contact mode. Real-time characterisations of laser-molybdenum interaction (laser induced breakdown spectroscopy and plasma imaging) were also studied using time-resolved experiments. The wavelength dependence of the ablation mechanism by short and ultra-short pulsed laser with molybdenum samples was identified. Numerical simulations based on finite element method (FEM) were performed to understand the interaction of short and ultra-short laser pulses with molybdenum specimens. The parameters such as peak temperature, stress, strain were examined using the numerical simulation.

Finally, the interaction of the laser pulses with a molybdenum based heterostructure structure was studied. Ablation of the multilayered structure was taken place by femtosecond and nanosecond laser pulses using a range of fluences. An in-depth examination of the different molybdenum craters was conducted by the AFM and SEM measurements. The elemental composition of the ablated crater on the multilayered thin film surface was taken place using the energy dispersive X-ray analysis (EDX) technique. The interaction mechanisms were understood by numerical simulation using COMSOL Multiphysics software.

- a) The first step of understanding the laser-molybdenum interaction was to investigate the ablation mechanism of molybdenum bulk samples using an ultrashort laser pulse. At low fluence, the rapid thermalisation of the electronic subsystem into the lattice results in a high compressive stress. The relaxation of the high compressive stress leads to fracture and spallation of molybdenum. It is also predicted that at higher fluences the ablation takes place predominately by the melting and vaporisation of molybdenum lattice. The electronic subsystem in molybdenum absorbs less IR laser energy by the via intraband absorption. While the electrons absorb more laser energy of a wavelength of Green and UV via interband absorption. As a result, more thermionic electron emission by Green and UV laser sources than IR. This confirms relatively more optical emission takes place at laser wavelength Green compared with IR.
- b) Comparatively lower ablation fluence is observed for molybdenum thin film than the bulk samples. Interaction of molybdenum thin film with ultra-short laser pulse resulted in an

apparent delamination mechanism without melting of molybdenum. AFM and SEM measurements of the ablated craters indicate complete removal of molybdenum film from BK7 substrate with minimal damage.

The heat developed at the molybdenum thin film during the interaction of femtosecond laser pulse with molybdenum conducts laterally and vertically towards the substrate. Due to the temperature confinement in the lattice, a high compressive stress develops on the molybdenum thin film. The stress exerts an expansion force that acts both laterally and vertically in directions parallel and perpendicular to the thin film-substrate interface. Also, a displacement of the molybdenum thin film takes place along the vertical direction. This expansion of the material leads to a tensile stress at the thin film substrate interface in the upward direction. The combination of the tensile stress and the relaxation of this highly compressive stress in molybdenum film results in the deformation and the removal of the molybdenum thin film from the glass substrate.

- c) During short pulse laser interaction, the removal of molybdenum film takes place via fragmentation process with significant substrate damage. During the interaction of nanosecond laser pulse with molybdenum thin film, almost a uniform temperature distribution establishes from the top surface of molybdenum to the molybdenum/glass interface of the molybdenum thin film. At low fluences (0.05 and 0.1 Jcm^{-2}), the peak temperature of the molybdenum stays under the melting point of molybdenum. While the peak temperature of the substrate exceeds the melting temperature of the glass substrate.

The numerical simulation predicts that a high compressive stress is established at the laser irradiated area of the thin film. This high compressive stress results in fragmentation in the molybdenum thin film. Higher thermal expansion of glass than molybdenum leads to a vertical strain in the glass. This vertical strain result is a tensile stress formed in the thin film-glass interface. The tensile deformation on the molybdenum thin film from the molybdenum/glass interface results in the removal of molybdenum film from the glass substrate.

- d) The interaction of femtosecond laser with MAM samples leads to the selective structuring of different layers. With a variation of laser fluence, four different fluence regimes of features with different diameters produced on the multilayered surface. Threshold fluences corresponding each diameter were measured. The choice of incident laser wavelength for laser interaction was found to have an impact on the film ablation process. The interplay between different layers has several valuable effects on the laser ablation that depends on the applied laser fluence.

At low fluence (Higher than F^{D1} but lower than F^{D2}) minimal structural modification takes place on the 1st layer (molybdenum) surface. At this fluence, the peak temperature of molybdenum layer stays above its melting temperature. The conduction of temperature towards the molybdenum/aluminium interface leads to increase of peak temperature of aluminium and the aluminium layer exceeds the melting temperature. Gradually both the films cool down the room temperature.

At the fluence $F^{D2} < F < F^{D3}$ the high compressive stress due to the confined heating of molybdenum takes place. Delamination of molybdenum is observed at this fluence regime. This delamination is occurred due to the vertical relaxation of the highly compressive stress by a photomechanical mechanism combined with the pressure originated from the highly

expandable aluminium gives rise to mechanical fracture of molybdenum layer. When the expansion exceeds the plastic limit of molybdenum, a permanent deformation of molybdenum layer occurs. As a result, nano-bump of molybdenum layer is produced on the top surface. It is likely that the nanostructures at this fluence regime are developed when a pressure wave reflects from the interface.

At comparatively higher fluence (greater than F^{D3}), the stress exceeds the fracture limit of molybdenum and removal of the top layer molybdenum layer takes place.

At high fluence (F^{D4}), the UV femtosecond laser interaction with MAM samples resulted in several nano-cracks on the glass.

An increase of grain size partially removed aluminium layer is observed with increasing incident laser fluence. The increase in grain size may lead to an increase in conductivity of the aluminium layer.

- e) Like the femtosecond case, different features were identified on the craters at different nanosecond applied fluences. The threshold fluences corresponding these features were determined. Wavelength dependence of the threshold fluences is due to the interplay between the optical penetration depth and heat penetration depth of MAM layers.

At low fluence ($F^{D1} < F < F^{D2}$), a flower-like structure with a dip at the centre of the crater of depth nearly 100 nm is produced on the surface of MAM sample. The interaction of a nanosecond pulse with MAM causes a uniform temperature distribution throughout the molybdenum layer and thus at the Mo/Al interface due to the high thermal diffusion length and the lattice temperature remains almost constant. At the fluence higher than F^{D1} , the sandwiched aluminium becomes molten in phase underneath the solid molybdenum layer. The temperature increase in MAM causes thermal expansion at molybdenum and aluminium layer. In the case of the molybdenum layer, the maximum expansion takes place at the centre of the spot. The molten aluminium forced to travel radially away from the centre. As a result, the molybdenum film separates from the melted aluminium at the Mo/Al. The maximum stress created by the radial expansion of the petal-like structures takes place at the centre of the crater. It is expected that the dip in the centre of the crater is due to the ductile deformation of molybdenum layer.

At the peak fluence between F^{D2} and F^{D3} , a 'micro-bump' is produced on the top molybdenum layer. The thermal expansion of the aluminium layer causes an upwards pressure pushes the molybdenum layer upward normal to the surface. This results in a permanent deformation on the molybdenum layer and a 'micro-bump' creates. As the fluence increases, the upward pressure due to the thermal expansion of aluminium increases and the peak height of the 'micro-bump' increases.

The upwards stress increases with increasing peak laser fluence. When the upward stress exceeds the limit of fracture of a thin molybdenum film, the deformed molybdenum breaks and the underneath molten aluminium forms comes out like a jet. Eventually, the molten aluminium cools down and forms a droplet on the surface on MAM. As the fluence increases, the molten aluminium redistributes on the surface of the MAM.

At the fluence higher than F^{D3} , a sub-micro well creates at the centre of the ablated crater. During laser ablation, high-temperature on the MAM results in melting of aluminium and ITO. Most of these materials ejected from the crater and rest of the melted ITO and aluminium redistribute on the craters.

When the peak fluence exceeds F^{D4} , significant damage is occurred on the glass surface.

The laser material interaction for the forms (bulk, thin film and heterostructure) of three molybdenum investigated in this study is summarised in Figure 7.1.

In the case of molybdenum bulk interactions, femtosecond laser melting of molybdenum is observed. The lowest damage threshold was observed at laser wavelength of 343 nm. It is observed that this mechanism generally takes place at the laser spot radius between 10 to 50 μm and at peak absorbed fluence 0.12-0.45 Jcm^{-2} .

The interaction of a laser pulse with a loosely adhered molybdenum thin film shows a delamination effect. In the case of femtosecond laser – molybdenum thin film interactions, the relaxation of highly compressive stress in the molybdenum results in the removal of the molybdenum film. This phenomenon is observed at all wavelengths but dominates at the laser wavelength of 343 nm. On the other hand, in the case of interactions with nanosecond laser pulses show that the removal of the molybdenum film originates from an expansive stress generated in the substrate combined with the compressive stress in the film. The optimal laser wavelength for this process is found to be 532 nm as the damage threshold is least for this wavelength.

In the case of the molybdenum aluminium heterostructure, enhanced laser induced crystallinity in aluminium is observed in the case of femtosecond laser-molybdenum interactions. This phenomenon is well observed in the aluminium layer at the laser wavelength of 515 nm for peak fluence range of 0.42 to 5.5 Jcm^{-2} . Nanosecond laser interaction with molybdenum heterostructure results in formation of a microbump in the molybdenum upper layer due to upward pressure caused by the thermally expanded aluminium layer.

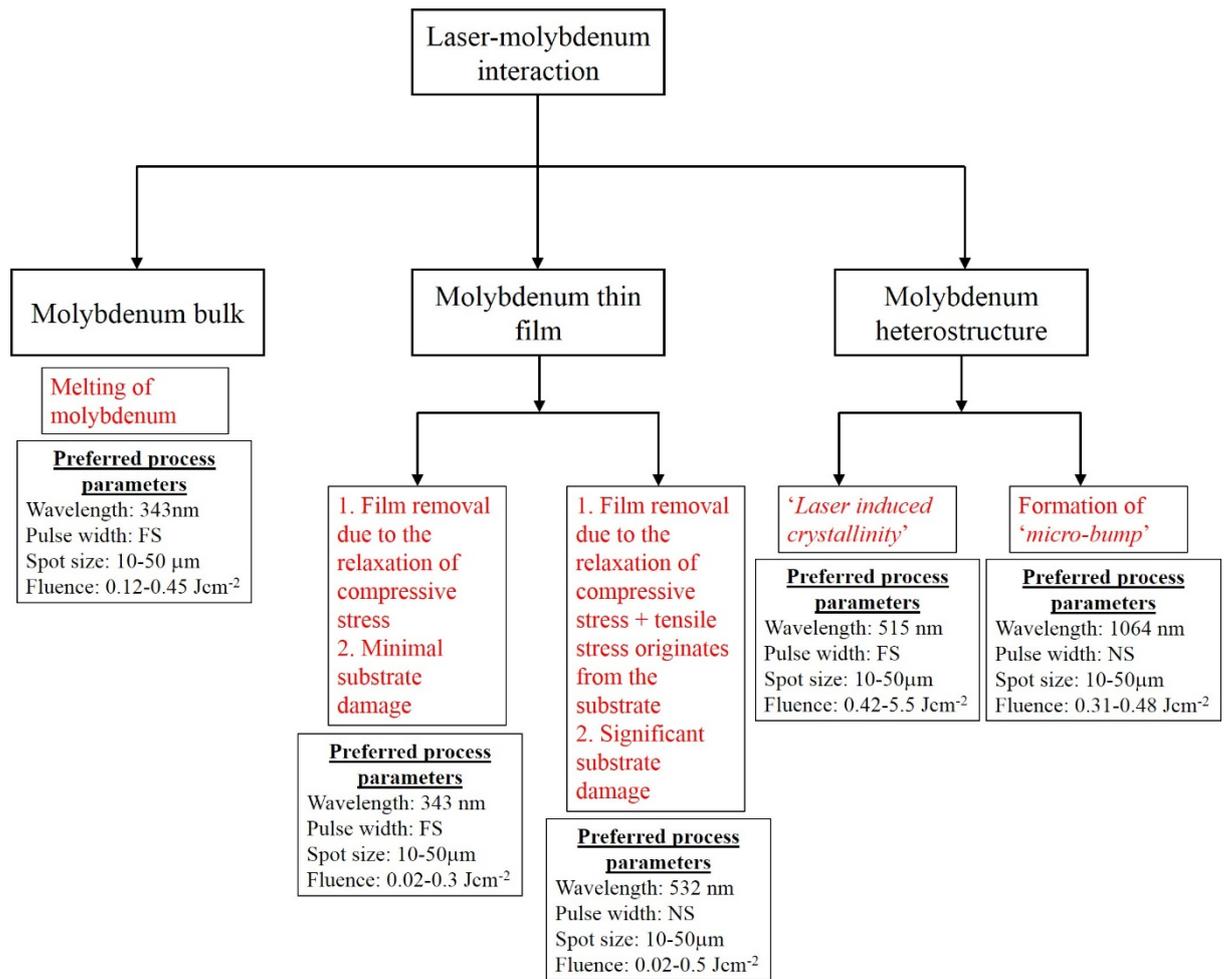


Figure 7.1: A summary of laser molybdenum processing

7.1. Opportunities for future work

In this work, further insight into the thin film removal process depending upon other parameters and other characterisation techniques can be developed for further characterisation of the thin film removal mechanism.

1. Improvement of the real-time imaging setup:

The improvement of the real-time imaging setup is required to for the further understanding of the thin film removal mechanism. This includes the development of LIBS, Schlieren and shadowgraphy measurement. Chapter 5 describes the atomic spectra of the plasma plume at different fluences. The ions and electrons have different emission spectra. By identifying the different constituents of the plasma plume, the mechanism of laser ablation can be understood better. Again, the spatially resolved LIBS provides the spectral response of the plasma plume provides the spectral variation of different constituents. By detecting the emission of electrons and ions as a function of applied fluence, further information on the film removal process may be identified.

Soon, a workstation for the Schlieren and shadowgraphy technique will be developed. This will allow us to the real-time study of material removal mechanism by laser ablation. As it is found that different process involves with ablation of bulk and thin molybdenum, it is expected

that material removal of molybdenum bulk and thin film take place at different time delays. Also, a variation of pulse duration and applied laser wavelength leads to different interaction process. Real-time investigation of material removal by Schlieren and shadowgraphy technique will enable an in-depth investigation of removal mechanism.

2. Development of a Langmuir probe:

A separate development of the set up called Langmuir probe is required to understand different features in plasma plume which includes electron and lattice current, the evolution of electron and ion density, current etc. These factors depend directly on the mechanism of interaction of laser pulse with the material.

3. Variation of the local conductivity of multilayered structure:

It is observed from the Figure 6.14 that the variation of incident laser fluence leads to a change of grain structure on the aluminium layer which is considered to be a material having excellent conductivity. Thus, it would be interesting to understand the variation of local conductivity with laser fluence. And it is important to understand if any other material exhibits this variation of grain structure and thus the electrical conductivity.

4. Analysis of nanostructures produced on molybdenum surface:

Femtosecond laser interaction of molybdenum heterostructure at fluence higher than the damage threshold leads to the formation of several nanostructures. An example of the nanostructure produced on the surface of molybdenum is shown below:

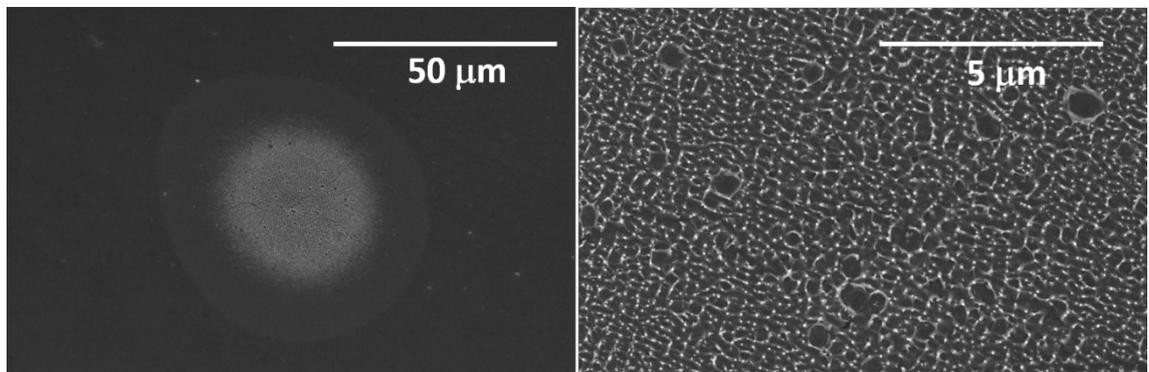


Figure 7.2: Scanning electron microscopy image of a crater on the surface of MAM, produced by a 515 nm femtosecond laser pulse at a fluence of 0.56 Jcm^{-2} . The right image shows the magnified view of the centre of the crater shows several nanostructures on the MAM surface

The above figure shows the crater produced on the surface of the heterostructure after the interaction of femtosecond laser pulse (wavelength 515 nm) of the fluence of 0.56 Jcm^{-2} . The right image of the crater is the magnified image of the centre portion of the crater which shows several nanostructures on the MAM surface. It will be interesting to understand the origin of these nanostructures.

Appendix

Variation of peak LIBS line intensities from the molybdenum thin film plasma plume induced by femtosecond laser pulse of wavelength of 1030 nm:

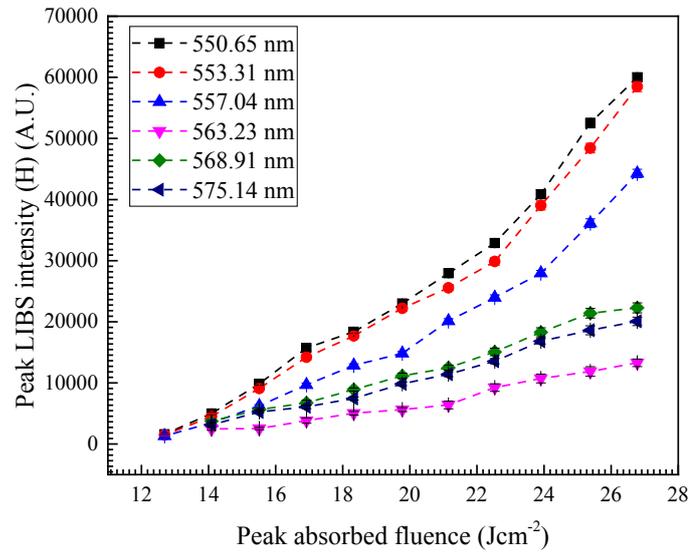


Figure A.1: Dependence of peak femtosecond LIBS intensity of molybdenum thin film centred at 550.65, 553.31, 557.04, 563.23, 568.81 and 575.14 nm by different fluences.

Variation of peak LIBS line intensities from the molybdenum thin film plasma plume induced by femtosecond laser pulse of wavelength of 1030 nm:

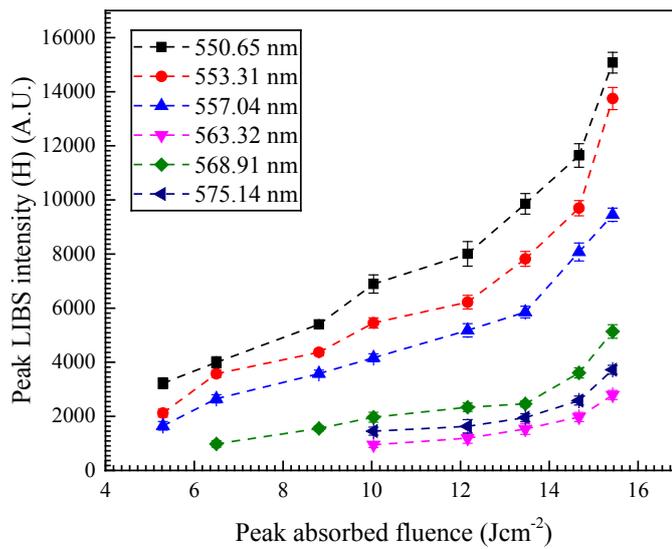


Figure A.2: Dependence of peak nanosecond LIBS intensity of molybdenum thin film centred at 550.65, 553.31, 557.04, 563.32 and 575.14 nm by different fluences

Vertical distance travelled by fast component of molybdenum bulk plasma plume induced by different 515 nm femtosecond laser peak fluences:

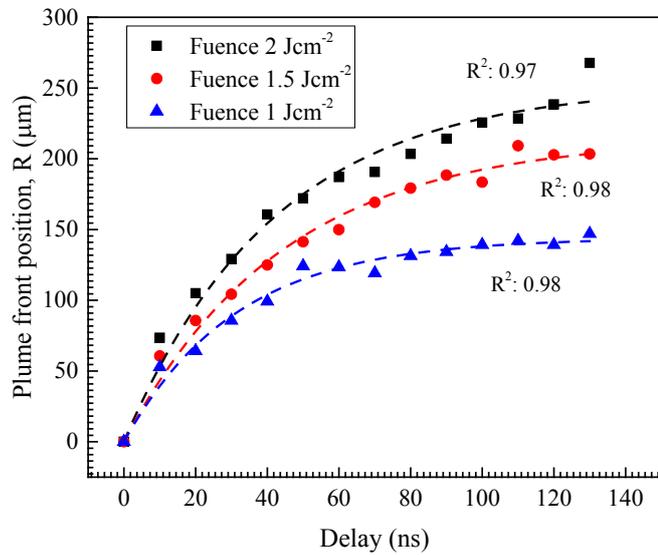


Figure A.3: Vertical distance travelled by 515 nm produced plasma plume front at 1, 1.5 and 2.0 Jcm⁻²

Vertical distance travelled by fast component of molybdenum bulk plasma plume induced by different 343 nm femtosecond laser peak fluences:

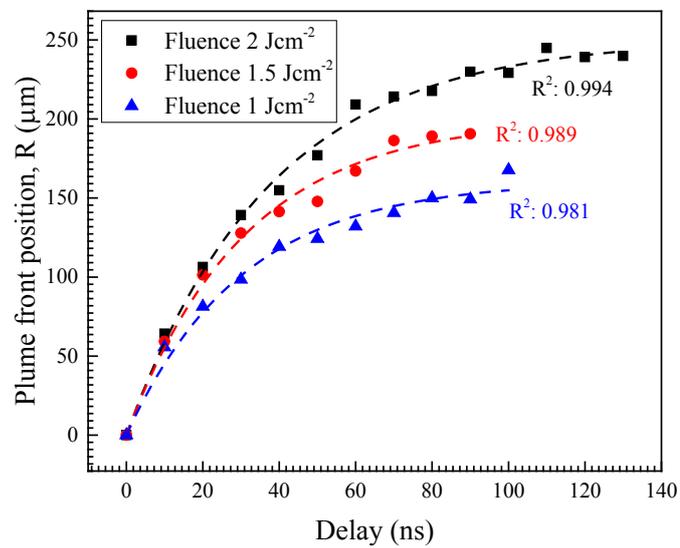


Figure A.4: Vertical distance travelled by 343 nm, femtosecond laser produced plasma plume front at specific fluences

Position of faster moving component of 515 nm femtosecond laser produced plasma plume (Molybdenum thin film – FS laser interaction)

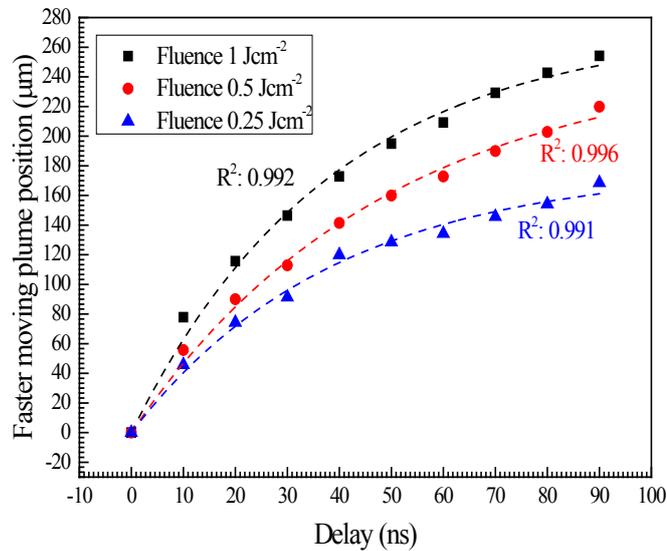


Figure A.5: Propagation of 515 nm femtosecond laser produced plasma front of molybdenum thin film at different fluence values

Position of slower moving component of 515 nm femtosecond laser produced plasma plume (Molybdenum thin film – FS laser interaction)

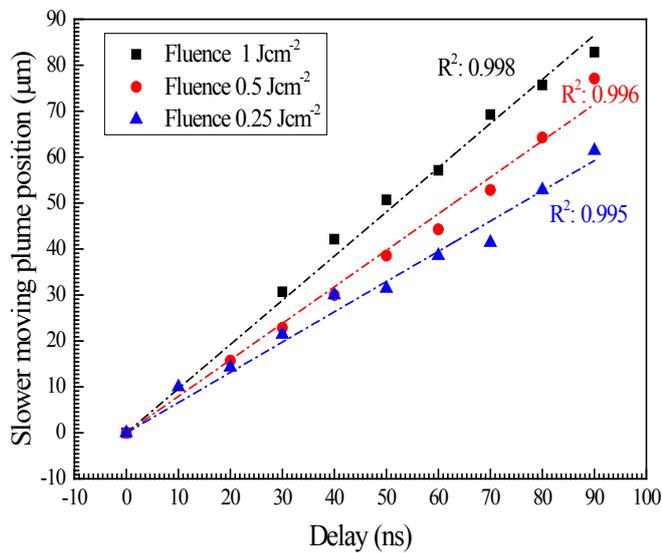


Figure A.6: Propagation of delaminated film edge at different peak absorbed fluence (0.25, 0.5 and 1 Jcm⁻²) values using 515 nm laser wavelength

Vertical distance covered by the faster moving part of the plasma plume produced by nanosecond laser of wavelength of 532 nm:

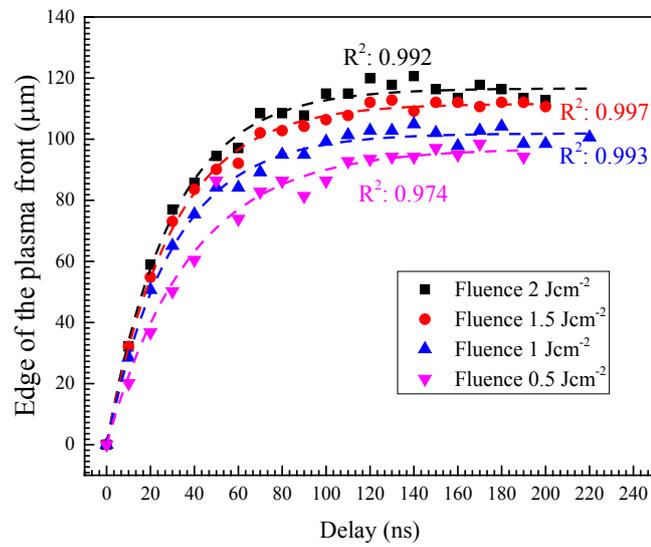


Figure A.7: Distance travelled by the faster moving part of the plasma plume using the interaction of nanosecond laser (wavelength: 532 nm) with molybdenum thin film samples at 0.5, 1, 1.5, and 2 Jcm⁻² fluence values

Vertical distance covered by the faster moving part of the plasma plume produced by nanosecond laser of wavelength of 355 nm

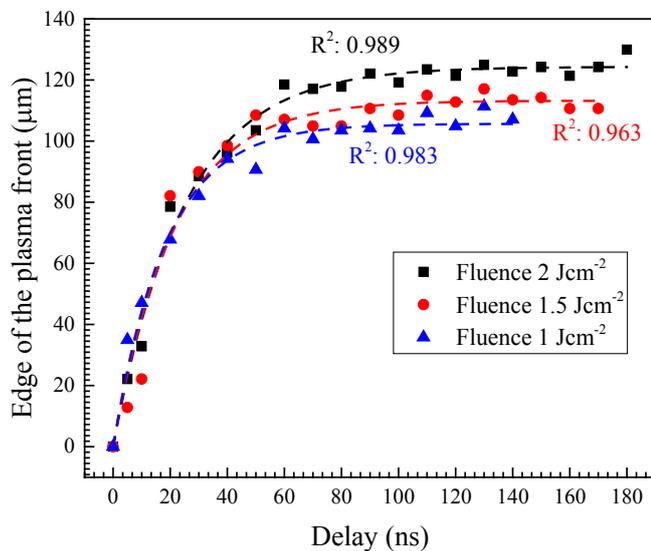


Figure A.8: Distance travelled by the faster moving part of the plasma plume using the interaction of nanosecond laser (wavelength: 355 nm) with molybdenum thin film at 0.5, 1, 1.5, and 2 Jcm⁻² fluence values

Spectral lines: Interaction of femtosecond laser pulse with molybdenum bulk

Table A.1: Variation of the background intensity, FWHM, area and the height of the Lorentzian curve centred at a wavelength of 553.31 nm (interaction of molybdenum bulk with ultra-short pulsed laser)

| Peak fluence (Jcm^{-2}) | Background (I_0) (A.U.) | FWHM (Γ) (nm) | Area under the curve (A) (A.U.) | Height (H) (A.U.) |
|---|---|--|--|----------------------------------|
| 0 | NA | NA | NA | NA |
| 3.29 | 62.77 | 0.41 | 104.52 | 160.45 |
| 6.59 | 349.57 | 0.48 | 986.92 | 1308.37 |
| 9.89 | 794.66 | 0.49 | 2729.90 | 3555.80 |
| 13.19 | 1204.22 | 0.47 | 3449.30 | 4709.11 |
| 16.48 | 1632.77 | 0.46 | 6175.77 | 8625.51 |
| 19.78 | 2451.89 | 0.47 | 8690.53 | 11710.29 |
| 23.08 | 3083.81 | 0.48 | 10824.26 | 14322.37 |
| 26.37 | 3348.63 | 0.48 | 13306.47 | 17602.14 |
| 29.67 | 3814.57 | 0.47 | 16600.99 | 22415.89 |
| 29.67 | 3814.57 | 0.47 | 16600.99 | 22415.89 |
| 32.97 | 4497.24 | 0.47 | 20913.45 | 28335.15 |
| 39.56 | 5088.24 | 0.48 | 22761.64 | 30372.74 |

Table A.2: Variation of the background intensity, FWHM, area and the height of the Lorentzian curve centred at a wavelength of 557.04 nm (interaction of molybdenum bulk with ultra-short pulsed laser)

| Peak fluence (Jcm^{-2}) | Background (I_0) (A.U.) | FWHM (Γ) (nm) | Area under the curve (A) (A.U.) | Height (H) (A.U.) |
|---|---|--|--|----------------------------------|
| 0 | NA | NA | NA | NA |
| 3.29 | 49.42 | 0.48 | 106.95 | 142.26 |
| 6.59 | 273.66 | 0.47 | 727.84 | 976.24 |
| 9.89 | 658.89 | 0.45 | 1909.84 | 2682.90 |
| 13.19 | 881.90 | 0.44 | 2686.27 | 3897.21 |

| | | | | |
|-------|---------|------|----------|----------|
| 16.48 | 1254.96 | 0.44 | 4538.95 | 6606.00 |
| 19.78 | 1723.18 | 0.45 | 6540.09 | 9257.27 |
| 23.08 | 2216.71 | 0.45 | 8095.51 | 11353.16 |
| 26.37 | 2342.11 | 0.45 | 9925.15 | 13938.79 |
| 29.67 | 2762.14 | 0.43 | 12002.74 | 17712.19 |
| 32.97 | 3098.77 | 0.45 | 15362.78 | 21913.46 |
| 39.56 | 3603.65 | 0.45 | 16833.79 | 23725.93 |

Table A.3: Variation of the background intensity, FWHM, area and the height of the Lorentzian curve centred at a wavelength of 563.23 nm (interaction of molybdenum bulk with ultra-short pulsed laser)

| Peak fluence (Jcm⁻²) | Background (I₀) (A.U.) | FWHM (Γ) (nm) | Area under the curve (A) (A.U.) | Height (H) (A.U.) |
|--|--|----------------------|--|--------------------------|
| 0 | NA | NA | NA | NA |
| 3.29 | NA | NA | NA | NA |
| 6.59 | 269.97 | 0.54 | 209.81 | 246.42 |
| 9.89 | 590.19 | 0.45 | 551.75 | 774.81 |
| 13.19 | 811.07 | 0.45 | 762.32 | 1075.49 |
| 16.48 | 1044.60 | 0.50 | 1373.86 | 1750.63 |
| 19.78 | 1525.02 | 0.49 | 1885.73 | 2463.60 |
| 23.08 | 1936.32 | 0.46 | 2160.77 | 2970.93 |
| 26.37 | 2023.64 | 0.46 | 2785.13 | 3860.08 |
| 29.67 | 2407.64 | 0.45 | 3344.98 | 4893.23 |
| 32.97 | 2917.15 | 0.43 | 3986.46 | 5912.70 |
| 39.56 | 3138.26 | 0.44 | 4658.93 | 6546.29 |

Table A.4: Variation of the background intensity, FWHM, area and the height of the Lorentzian curve centred at a wavelength of 568.91 nm (interaction of molybdenum bulk with ultra-short pulsed laser)

| Peak fluence (Jcm^{-2}) | Background (I_0) (A.U.) | FWHM (Γ) (nm) | Area under the curve (A) (A.U.) | Height (H) (A.U.) |
|---|---|--|--|----------------------------------|
| 0 | NA | NA | NA | NA |
| 3.29 | NA | NA | NA | NA |
| 6.59 | 288.45 | 0.46 | 275.70 | 385.05 |
| 9.89 | 680.84 | 0.37 | 652.81 | 1118.30 |
| 13.19 | 814.00 | 0.42 | 1019.41 | 1538.14 |
| 16.48 | 1153.52 | 0.41 | 1826.26 | 2808.76 |
| 19.78 | 1674.27 | 0.40 | 2411.64 | 3802.81 |
| 23.08 | 2117.89 | 0.40 | 2870.82 | 4552.06 |
| 26.37 | 2316.02 | 0.39 | 3558.22 | 5761.21 |
| 29.67 | 2706.97 | 0.39 | 4462.47 | 7203.71 |
| 32.97 | 3220.82 | 0.40 | 5564.96 | 8871.73 |
| 39.56 | 3358.56 | 0.41 | 6466.43 | 10087.33 |

Table A.5: Variation of the background intensity, FWHM, area and the height of the Lorentzian curve centred at a wavelength of 575.14 nm (interaction of molybdenum bulk with ultra-short pulsed laser)

| Peak fluence (Jcm^{-2}) | Background (I_0) (A.U.) | FWHM (Γ) (nm) | Area under the curve (A) (A.U.) | Height (H) (A.U.) |
|---|---|--|--|----------------------------------|
| 0 | NA | NA | NA | NA |
| 3.29 | NA | NA | NA | NA |
| 6.59 | 248.93 | 0.41 | 268.82 | 415.87 |
| 9.89 | 597.26 | 0.43 | 665.50 | 976.79 |
| 13.19 | 791.43 | 0.41 | 983.97 | 1546.25 |
| 16.48 | 1135.56 | 0.42 | 1604.37 | 2434.91 |
| 19.78 | 1585.31 | 0.39 | 2165.42 | 3522.73 |

| | | | | |
|-------|---------|------|---------|---------|
| 23.08 | 1867.65 | 0.43 | 2910.14 | 4358.76 |
| 26.37 | 2109.03 | 0.41 | 3470.78 | 5424.20 |
| 29.67 | 2482.21 | 0.39 | 4179.55 | 6790.20 |
| 32.97 | 2440.08 | 0.43 | 5919.60 | 8802.51 |
| 39.56 | 3251.57 | 0.40 | 5757.11 | 9173.17 |

Spectral lines: Interaction of femtosecond laser pulse with molybdenum thin film

Table A.6: Variation of the background intensity, height, FWHM and area under the fitted Lorentzian curve centred at 553.31 nm at different peak fluences (interaction of molybdenum thin film with ultra-short pulsed laser)

| Peak fluence (Jcm⁻²) | Background (I₀) (A.U.) | FWHM (Γ) (nm) | Area under the curve (A) (A.U.) | Height (H) (A.U.) |
|--|--|--|--|--|
| 0 | NA | NA | NA | NA |
| 12.69 | 1300.04 | 0.25 | 575.30 | 1476.45 |
| 14.09 | 990.71 | 0.52 | 3692.89 | 4501.61 |
| 15.51 | 1670.76 | 0.40 | 5748.74 | 9095.30 |
| 16.92 | 1305.12 | 0.48 | 10731.42 | 14208.38 |
| 18.33 | 1971.04 | 0.43 | 12049.58 | 17680.25 |
| 19.74 | 1619.46 | 0.50 | 17393.88 | 22215.36 |
| 21.15 | 2020.67 | 0.46 | 18603.28 | 25550.09 |
| 22.53 | 2017.48 | 0.48 | 22472.01 | 29869.07 |
| 23.96 | 2191.94 | 0.45 | 27835.73 | 39031.32 |
| 25.38 | 2410.88 | 0.47 | 35382.97 | 48420.00 |
| 26.78 | 3566.86 | 0.46 | 42104.60 | 58475.67 |

Table A.7: Variation of the background intensity, height, FWHM and area under the fitted Lorentzian curve centred at 557.04 nm at different peak fluences (interaction of molybdenum thin film with ultra-short pulsed laser)

| Peak fluence (Jcm^{-2}) | Background (I_0) (A.U.) | FWHM (Γ) (nm) | Area under the curve (A) (A.U.) | Height (H) (A.U.) |
|---|---|--|--|----------------------------------|
| 0 | NA | NA | NA | NA |
| 12.69 | 711.40 | 0.46 | 1788.20 | 1322.84 |
| 14.09 | 1127.43 | 0.46 | 2517.36 | 3475.09 |
| 15.51 | 1531.05 | 0.37 | 3619.82 | 6256.01 |
| 16.92 | 1406.91 | 0.42 | 6456.73 | 9695.71 |
| 18.33 | 1627.62 | 0.40 | 8170.74 | 12875.62 |
| 19.74 | 1487.98 | 0.42 | 9867.22 | 14836.60 |
| 21.15 | 1484.66 | 0.40 | 12771.08 | 20121.90 |
| 22.53 | 1048.20 | 0.44 | 16459.09 | 23972.42 |
| 23.96 | 1983.47 | 0.40 | 17483.31 | 27951.67 |
| 25.38 | 1733.61 | 0.42 | 23986.83 | 36130.60 |
| 26.78 | 2316.18 | 0.41 | 28279.93 | 44273.19 |

Table A.8: Variation of the background intensity, height, FWHM and area under the fitted Lorentzian curve centred at 563.23 nm at different peak fluences (interaction of molybdenum thin film with ultra-short pulsed laser)

| Peak fluence (Jcm^{-2}) | Background (I_0) (A.U.) | FWHM (Γ) (nm) | Area under the curve (A) (A.U.) | Height (H) (A.U.) |
|---|---|--|--|----------------------------------|
| 0 | NA | NA | NA | NA |
| 12.69 | 1001.60 | 0.57 | 1419.64 | 1494.52 |
| 14.09 | 1609.09 | 0.37 | 1313.61 | 2475.73 |
| 15.51 | 1661.75 | 0.36 | 2915.12 | 2529.08 |
| 16.92 | 2030.47 | 0.38 | 1196.27 | 3837.37 |
| 18.33 | 2025.51 | 0.36 | 2691.35 | 5037.36 |
| 19.74 | 2070.25 | 0.42 | 3572.42 | 5630.38 |

| | | | | |
|-------|---------|------|---------|----------|
| 21.15 | 2065.13 | 0.44 | 4173.24 | 6406.08 |
| 22.53 | 2130.36 | 0.42 | 6117.05 | 9240.97 |
| 23.96 | 2679.42 | 0.40 | 6790.71 | 10719.00 |
| 25.38 | 2417.38 | 0.46 | 7776.99 | 11876.36 |
| 26.78 | 3373.02 | 0.38 | 7729.21 | 13298.17 |

Table A.9: Variation of the background intensity, height, FWHM and area under the fitted Lorentzian curve centred at 568.91 nm at different peak fluences (interaction of molybdenum thin film with ultra-short pulsed laser)

| Peak fluence (Jcm^{-2}) | Background (I_0) (A.U.) | FWHM (Γ) (nm) | Area under the curve (A) (A.U.) | Height (H) (A.U.) |
|---|---|--|--|--------------------------|
| 0 | NA | NA | NA | NA |
| 12.69 | 1293.39 | 0.53 | 1258.56 | 1497.45 |
| 14.09 | 1773.88 | 0.34 | 2064.93 | 3735.77 |
| 15.51 | 1705.75 | 0.39 | 2441.19 | 5625.89 |
| 16.92 | 2720.50 | 0.34 | 2491.28 | 6746.27 |
| 18.33 | 1974.85 | 0.45 | 5448.17 | 8921.90 |
| 19.74 | 2409.64 | 0.35 | 5266.27 | 11150.25 |
| 21.15 | 2581.90 | 0.38 | 6887.06 | 12487.27 |
| 22.53 | 2643.30 | 0.37 | 8033.57 | 15076.40 |
| 23.96 | 3089.55 | 0.35 | 9645.63 | 18280.98 |
| 25.38 | 3971.34 | 0.35 | 10331.33 | 21395.25 |
| 26.78 | 3600.11 | 0.40 | 12902.71 | 22284.32 |

Table A.10: Variation of the background intensity, height, FWHM and area under the fitted Lorentzian curve centred at 575.14 nm at different peak fluences (interaction of molybdenum thin film with ultra-short pulsed laser)

| Peak fluence (Jcm^{-2}) | Background (I_0) (A.U.) | FWHM (Γ) (nm) | Area under the curve (A) (A.U.) | Height (H) (A.U.) |
|---|---|--|--|--------------------------|
| 0 | NA | NA | NA | NA |
| 12.69 | 1180.77 | 0.52 | 1201.59 | 1960.01 |

| | | | | |
|-------|---------|------|----------|----------|
| 14.09 | 1484.41 | 0.38 | 1965.78 | 3144.03 |
| 15.51 | 1639.59 | 0.36 | 2948.23 | 5256.99 |
| 16.92 | 2082.52 | 0.36 | 2333.93 | 6094.81 |
| 18.33 | 1843.64 | 0.38 | 4550.39 | 7447.00 |
| 19.74 | 1795.20 | 0.40 | 6149.38 | 9847.96 |
| 21.15 | 1826.60 | 0.41 | 7186.60 | 11424.76 |
| 22.53 | 2200.45 | 0.38 | 8002.67 | 13551.81 |
| 23.96 | 2339.53 | 0.37 | 9745.79 | 16823 |
| 25.38 | 2709.86 | 0.36 | 10572.80 | 18613.95 |
| 26.78 | 2202.37 | 0.44 | 13783.31 | 20074.89 |

Spectral lines: Interaction of nanosecond laser pulse with molybdenum thin film

Table A.11: Variation of the background intensity, height, FWHM and area under the fitted Lorentzian curve centred at 553.31 nm at different peak fluences (interaction of molybdenum thin film with short pulsed laser)

| Peak fluence (Jcm⁻²) | Background (I₀) (A.U.) | FWHM (Γ) (nm) | Area under the curve (A) (A.U.) | Height (H) (A.U.) |
|--|--|--|--|--|
| 0 | NA | NA | NA | NA |
| 6.50 | 697.56 | 0.34 | 1886.97 | 3573.62 |
| 8.81 | 1134.19 | 0.29 | 2002.76 | 4369.74 |
| 10.04 | 1605.20 | 0.18 | 1682.13 | 5953.60 |
| 12.16 | 1771.22 | 0.28 | 2744.84 | 6221.44 |
| 13.46 | 1030.62 | 0.32 | 3893.89 | 7821.71 |
| 14.67 | 1347.01 | 0.31 | 4665.75 | 9695.94 |
| 15.43 | 1644.80 | 0.26 | 5657.82 | 13747.69 |

Table A.12: Variation of the background intensity, height, FWHM and area under the fitted Lorentzian curve centred at 557.04 nm at different peak fluences (interaction of molybdenum thin film with short pulsed laser)

| Peak fluence (Jcm^{-2}) | Background (I_0) (A.U.) | FWHM (Γ) (nm) | Area under the curve (A) (A.U.) | Height (H) (A.U.) |
|---|---|--|--|----------------------------------|
| 0 | NA | NA | NA | NA |
| 6.50 | 994.47 | 0.19 | 792.78 | 2648.73 |
| 8.81 | 907.51 | 0.24 | 1324.14 | 3581.34 |
| 10.04 | 809.26 | 0.29 | 1874.25 | 4166.99 |
| 12.16 | 1375.05 | 0.21 | 1710.92 | 5180.91 |
| 13.46 | 1235.40 | 0.30 | 2260.95 | 4855.87 |
| 14.67 | 1306.20 | 0.21 | 2638.10 | 8076.91 |
| 15.43 | 1658.22 | 0.25 | 3677.60 | 9453.19 |

Table A.13: Variation of the background intensity, height, FWHM and area under the fitted Lorentzian curve centred at 563.23 nm at different peak fluences (interaction of molybdenum thin film with short pulsed laser)

| Peak fluence (Jcm^{-2}) | Background (I_0) (A.U.) | FWHM (Γ) (nm) | Area under the curve (A) (A.U.) | Height (H) (A.U.) |
|---|---|--|--|----------------------------------|
| 0 | NA | NA | NA | NA |
| 6.50 | 906.24 | 0.27 | 1708.22 | 3997.39 |
| 8.81 | 1175.80 | 0.29 | 1952.92 | 4342.42 |
| 10.04 | 1243.68 | 0.32 | 698.06 | 1386.19 |
| 12.16 | 1657.22 | 0.21 | 383.94 | 1191.57 |
| 13.46 | 1604.63 | 0.25 | 818.19 | 2096.05 |
| 14.67 | 1840.29 | 0.21 | 645.69 | 1976.62 |
| 15.43 | 2133.42 | 0.21 | 916.50 | 2791.43 |

Table A.14: Variation of the background intensity, height, FWHM and area under the fitted Lorentzian curve centred at 568.91 nm at different peak fluences (interaction of molybdenum thin film with short pulsed laser)

| Peak fluence (Jcm^{-2}) | Background (I_0) (A.U.) | FWHM (Γ) (nm) | Area under the curve (A) (A.U.) | Height (H) (A.U.) |
|---|---|--|--|----------------------------------|
| 0 | NA | NA | NA | NA |
| 6.50 | 1317.44 | 0.22 | 559.18 | 1607.44 |
| 8.81 | 1186.55 | 0.27 | 521.22 | 1242.48 |
| 10.04 | 1569.23 | 0.20 | 783.26 | 2466.34 |
| 12.16 | 1810.05 | 0.21 | 860.87 | 2589.07 |
| 13.46 | 1364.73 | 0.40 | 1556.34 | 2461.63 |
| 14.67 | 1787.97 | 0.29 | 1650.54 | 3607.01 |
| 15.43 | 1916.55 | 0.25 | 2003.66 | 5136.51 |

Table A.15: Variation of the background intensity, height, FWHM and area under the fitted Lorentzian curve centred at 575.14 nm at different peak fluences (interaction of molybdenum thin film with short pulsed laser)

| Peak fluence (Jcm^{-2}) | Background (I_0) (A.U.) | FWHM (Γ) (nm) | Area under the curve (A) (A.U.) | Height (H) (A.U.) |
|---|---|--|--|----------------------------------|
| 0 | NA | NA | NA | NA |
| 6.50 | 906.24 | 0.27 | 1708.22 | 3997.39 |
| 8.81 | 1175.80 | 0.29 | 1952.92 | 4342.42 |
| 10.04 | 1302.08 | 0.23 | 800.85 | 2265.54 |
| 12.16 | 1761.03 | 0.11 | 428.30 | 2571.16 |
| 13.46 | 1705.47 | 0.30 | 918.13 | 1953.21 |
| 14.67 | 1705.82 | 0.26 | 1060.18 | 2585.30 |
| 15.43 | 2072.41 | 0.28 | 1628.18 | 3722.91 |

Publications and other outputs

Publications

1. Farid, Nazar; O'Connor, Gerard; Dasgupta, Pinaki, *Onset and evolution of LIPSS on ITO thin films for clean ablation using a repetitively pulsed picosecond laser at low fluence*, **Journal of Physics D** (2018) (communicated)
2. **Das Gupta, Pinaki**; O'Connor, Gerard, *Comparison of ablation mechanisms at low fluence for ultrashort and short-pulse laser exposure of very thin molybdenum films on glass*, **Applied Optics** (2016) **55** (9), 2117-2125

Patent

1. Dasgupta, P., Farid, N., Chan, H., Milne, H. & O'Connor, G. M., *Method of Processing of a Target Material*, **GB patent application 1714802.4**, 14th September 2017.

Conference presentations

1. Farid, N., Dasgupta, P., Chan, H., Milne, H. & O'Connor, G. M., 'Non-thermal selective patterning of ITO thin film by 10 ps laser' **CLEO, Munich, 2017**.
2. Farid, N, Gupta, P. D. & O'Connor, G. M., 'Real-time monitoring and controlled selective ablation based on optical emission spectroscopy technique' (Conference Presentation) **SPIE LASE, San Francisco, 2017**.
3. Gupta, P. D., Farid, N & O'Connor, 'Selective structuring of molybdenum-aluminium-molybdenum multilayered thin film using short and ultra-short laser', **ALT, Galway, 2016**.
4. Gupta, P. D. & O'Connor, 'Molybdenum film ablation by ultra-short (fs) and short pulse (ns) laser', **Photonics Ireland, Cork, 2015**.
5. Gupta, P. D. & O'Connor, 'Femtosecond laser ablation of molybdenum', **EMRS, Lille, France 2014**.
6. Gupta, P. D. & O'Connor, 'High speed tilted plane technique to investigate dependence of threshold fluence for ablation', **Photonics Ireland, Belfast, 2013**.
7. Gupta, P. D. & O'Connor, 'Laser ablation of very thin films', **IOP Ireland Spring meeting, Galway 2013**.

References

1. M. Key, "Laboratory production of X-ray lasers," *Nature* **316**, 314-319 (1985).
2. A. Chodos, "Einstein Predicts Stimulated Emission" (AMERICAN PHYSICAL SOCIETY), retrieved March 22, 2017, <https://www.aps.org/publications/apsnews/200508/history.cfm>.
3. A. Pais, *Subtle is the Lord: The Science and the Life of Albert Einstein: The Science and the Life of Albert Einstein* (Oxford University Press, USA, 1982).
4. K. Thyagarajan and A. Ghatak, *Lasers: fundamentals and applications* (Springer Science & Business Media, 2010).
5. G. Friedman, "Inventing the light fantastic: Ted Maiman and the world's first laser" (SPIE, 2007), retrieved March 22, 2017, <http://spie.org/newsroom/maiman-oer>.
6. W. T. Silfvast, *Laser fundamentals* (Cambridge University Press New York, 1996), Vol. 459.
7. T. Fan and R. Byer, "Modeling and CW operation of a quasi-three-level 946 nm Nd: YAG laser," *IEEE Journal of Quantum Electronics* **23**, 605-612 (1987).
8. T. H. Maiman, "Stimulated optical radiation in ruby," (1960).
9. F. B. Früngel, *Optical Pulses-Lasers-Measuring Techniques* (Academic Press, 2014).
10. M. Rodahl, F. Höök, A. Krozer, P. Brzezinski, and B. Kasemo, "Quartz crystal microbalance setup for frequency and Q-factor measurements in gaseous and liquid environments," *Review of Scientific Instruments* **66**, 3924-3930 (1995).
11. C. McDonnell, D. Milne, C. Prieto, H. Chan, D. Rostohar, and G. O'Connor, "Laser patterning of very thin indium tin oxide thin films on PET substrates," *Applied Surface Science* **359**, 567-575 (2015).
12. O. Svelto and D. C. Hanna, *Principles of lasers* (Springer, 1976).
13. W. G. Wagner and B. A. Lengyel, "Evolution of the giant pulse in a laser," *Journal of Applied Physics* **34**, 2040-2046 (1963).
14. U. Morgner, F. Kärtner, S.-H. Cho, Y. Chen, H. A. Haus, J. G. Fujimoto, E. P. Ippen, V. Scheuer, G. Angelow, and T. Tschudi, "Sub-two-cycle pulses from a Kerr-lens mode-locked Ti: sapphire laser," *Optics letters* **24**, 411-413 (1999).
15. D. H. Sutter, G. Steinmeyer, L. Gallmann, N. Matuschek, F. Morier-Genoud, U. Keller, V. Scheuer, G. Angelow, and T. Tschudi, "Semiconductor saturable-absorber mirror-assisted Kerr-lens mode-locked Ti: sapphire laser producing pulses in the two-cycle regime," *Optics letters* **24**, 631-633 (1999).
16. G. H. New, "Theory of passive mode-locking in giant pulse lasers," *Proceedings of the IEEE* **67**, 380-396 (1979).
17. H. Haus, "A theory of forced mode locking," *IEEE Journal of Quantum Electronics* **11**, 323-330 (1975).
18. D. Kuizenga and A. Siegman, "FM and AM mode locking of the homogeneous laser-Part I: Theory," *IEEE Journal of Quantum Electronics* **6**, 694-708 (1970).
19. D. Kuizenga and A. Siegman, "FM and AM mode locking of the homogeneous laser-Part II: Experimental results in a Nd: YAG laser with internal FM modulation," *IEEE Journal of Quantum Electronics* **6**, 709-715 (1970).
20. S. Somekh and A. Yariv, "Phase matching by periodic modulation of the nonlinear optical properties," *Optics Communications* **6**, 301-304 (1972).
21. H. A. Haus, "Theory of mode locking with a fast saturable absorber," *Journal of Applied Physics* **46**, 3049-3058 (1975).

22. T. Brabec, C. Spielmann, P. Curley, and F. Krausz, "Kerr lens mode locking," *Optics letters* **17**, 1292-1294 (1992).
23. E. P. Ippen, H. A. Haus, and L. Liu, "Additive pulse mode locking," *JOSA B* **6**, 1736-1745 (1989).
24. D. Strickland and G. Mourou, "Compression of amplified chirped optical pulses," *Optics communications* **56**, 219-221 (1985).
25. M. Pessot, P. Maine, and G. Mourou, "1000 times expansion/compression of optical pulses for chirped pulse amplification," *Optics communications* **62**, 419-421 (1987).
26. C. Barty, T. Guo, C. Le Blanc, F. Raksi, C. Rose-Petruck, J. Squier, K. Wilson, V. Yakovlev, and K. Yamakawa, "Generation of 18-fs, multiterawatt pulses by regenerative pulse shaping and chirped-pulse amplification," *Optics letters* **21**, 668-670 (1996).
27. P. Maine, D. Strickland, P. Bado, M. Pessot, and G. Mourou, "Generation of ultrahigh peak power pulses by chirped pulse amplification," *IEEE Journal of Quantum electronics* **24**, 398-403 (1988).
28. F. Röser, T. Eidam, J. Rothhardt, O. Schmidt, D. N. Schimpf, J. Limpert, and A. Tünnermann, "Millijoule pulse energy high repetition rate femtosecond fiber chirped-pulse amplification system," *Optics Letters* **32**, 3495-3497 (2007).
29. D. W. Bäuerle, *Laser processing and chemistry* (Springer Science & Business Media, 2011).
30. M. Bass, *Laser materials processing* (Elsevier, 2012), Vol. 3.
31. W. Duley, *Laser processing and analysis of materials* (Springer Science & Business Media, 2012).
32. W. Duley, "Laser Processing of Semiconductors," in *Laser Processing and Analysis of Materials* (Springer, 1983), pp. 177-194.
33. W. Brown, "Laser processing of semiconductors," *Laser Materials Processing* **3**, 337 (2012).
34. D.-L. KWONG, "LASER PROCESSING OF SEMICONDUCTORS," (Rice University, 1982).
35. B. Chichkov, C. Momma, S. Nolte, F. Von Alvensleben, and A. Tünnermann, "Femtosecond, picosecond and nanosecond laser ablation of solids," *Applied Physics A* **63**, 109-115 (1996).
36. E. G. Gamaly, A. V. Rode, B. Luther-Davies, and V. T. Tikhonchuk, "Ablation of solids by femtosecond lasers: Ablation mechanism and ablation thresholds for metals and dielectrics," *Physics of plasmas* **9**, 949-957 (2002).
37. N. Haustrup, "Wavelength dependence of femtosecond laser ablation of thin gold films," (National University of Ireland, Galway, Galway, 2014).
38. R. W. Boyd, *Nonlinear optics* (Academic press, 2003).
39. A. Sabbah and D. M. Riffe, "Femtosecond pump-probe reflectivity study of silicon carrier dynamics," *Physical Review B* **66**, 165217 (2002).
40. P. M. Norris, A. P. Caffrey, R. J. Stevens, J. M. Klopff, J. T. McLeskey Jr, and A. N. Smith, "Femtosecond pump-probe nondestructive examination of materials," *Review of scientific instruments* **74**, 400-406 (2003).
41. A. Vorobyev and C. Guo, "Enhanced absorptance of gold following multipulse femtosecond laser ablation," *PHYSICAL REVIEW-SERIES B-* **72**, 195422 (2005).
42. A. Vorobyev, V. Kuzmichev, N. Kokody, P. Kohns, J. Dai, and C. Guo, "Residual thermal effects in Al following single ns-and fs-laser pulse ablation," *Applied Physics A* **82**, 357-362 (2006).
43. M. Shirk and P. Molian, "A review of ultrashort pulsed laser ablation of materials," *Journal of Laser Applications* **10**, 18-28 (1998).

44. L. Jiang and H.-L. Tsai, "Improved two-temperature model and its application in ultrashort laser heating of metal films," *Journal of heat transfer* **127**, 1167-1173 (2005).
45. M. Domke, J. Sotrop, S. Rapp, M. Börger, D. Felsl, and H. P. Huber, "Transient temperature modeling and shock wave observation in confined laser ablation of thin molybdenum films," in *SPIE LASE*, (International Society for Optics and Photonics, 2013), 86111B-86111B-86115.
46. D. Swinehart, "The beer-lambert law," *Journal of chemical education* **39**, 333 (1962).
47. P. Soukiassian, R. Riwan, J. Lecante, E. Wimmer, S. Chubb, and A. J. Freeman, "Adsorbate-induced shifts of electronic surface states: Cs on the (100) faces of tungsten, molybdenum, and tantalum," *Physical Review B* **31**, 4911 (1985).
48. A. Mooradian, "Photoluminescence of metals," *Physical Review Letters* **22**, 185 (1969).
49. R. Schoenlein, W. Lin, J. Fujimoto, and G. Eesley, "Femtosecond studies of nonequilibrium electronic processes in metals," *Physical Review Letters* **58**, 1680 (1987).
50. J. Jasapara, A. Nampoothiri, W. Rudolph, D. Ristau, and K. Starke, "Femtosecond laser pulse induced breakdown in dielectric thin films," *Physical Review B* **63**, 045117 (2001).
51. R. R. Gattass and E. Mazur, "Femtosecond laser micromachining in transparent materials," *Nature photonics* **2**, 219-225 (2008).
52. D. Rayner, A. Naumov, and P. Corkum, "Ultrashort pulse non-linear optical absorption in transparent media," *Optics express* **13**, 3208-3217 (2005).
53. J. Bechtel and W. L. Smith, "Two-photon absorption in semiconductors with picosecond laser pulses," *Physical Review B* **13**, 3515 (1976).
54. X. Liu, D. Du, and G. Mourou, "Laser ablation and micromachining with ultrashort laser pulses," *Quantum Electronics, IEEE Journal of* **33**, 1706-1716 (1997).
55. M. M. Kirillova, Nomerova.Lv, and M. M. Noskov, "Optical Properties of Molybdenum Single Crystals," *Sov Phys JETP-USSR* **33**, 1210+ (1971).
56. T. Bigioni, R. Whetten, and Ö. Dag, "Near-infrared luminescence from small gold nanocrystals," *The Journal of Physical Chemistry B* **104**, 6983-6986 (2000).
57. S. Link, A. Beeby, S. FitzGerald, M. A. El-Sayed, T. G. Schaaff, and R. L. Whetten, "Visible to infrared luminescence from a 28-atom gold cluster," *The Journal of Physical Chemistry B* **106**, 3410-3415 (2002).
58. M. V. Shugaev, C. Wu, O. Armbruster, A. Naghilou, N. Brouwer, D. S. Ivanov, T. J.-Y. Derrien, N. M. Bulgakova, W. Kautek, and B. Rethfeld, "Fundamentals of ultrafast laser-material interaction," *MRS Bulletin* **41**, 960-968 (2016).
59. J. Liu, J. De Groot, J. Matte, T. Johnston, and R. Drake, "Measurements of inverse bremsstrahlung absorption and non-Maxwellian electron velocity distributions," *Physical review letters* **72**, 2717 (1994).
60. L. Schlessinger and J. Wright, "Inverse-bremsstrahlung absorption rate in an intense laser field," *Physical Review A* **20**, 1934 (1979).
61. C. Phipps, *Laser ablation and its applications* (Springer, 2007), Vol. 129.
62. C. Momma, B. N. Chichkov, S. Nolte, F. von Alvensleben, A. Tünnermann, H. Welling, and B. Wellegehausen, "Short-pulse laser ablation of solid targets," *Optics communications* **129**, 134-142 (1996).
63. B. Rethfeld, K. Sokolowski-Tinten, D. Von Der Linde, and S. Anisimov, "Timescales in the response of materials to femtosecond laser excitation," *Applied Physics A* **79**, 767-769 (2004).
64. B. H. Christensen, K. Vestentoft, and P. Balling, "Short-pulse ablation rates and the two-temperature model," *Applied Surface Science* **253**, 6347-6352 (2007).
65. S. Anisimov, B. Kapeliovich, and T. Perelman, "Electron emission from metal surfaces exposed to ultrashort laser pulses," *Zh. Eksp. Teor. Fiz* **66**, 375-377 (1974).

66. T. Qiu and C. Tien, "Short-pulse laser heating on metals," *International Journal of Heat and Mass Transfer* **35**, 719-726 (1992).
67. S.-S. Wellershoff, J. Hohlfeld, J. Güdde, and E. Matthias, "The role of electron–phonon coupling in femtosecond laser damage of metals," *Applied Physics A* **69**, S99-S107 (1999).
68. Y. Ren, J. Chen, and Y. Zhang, "Modeling of ultrafast phase changes in metal films induced by an ultrashort laser pulse using a semi-classical two-temperature model," *International Journal of Heat and Mass Transfer* **55**, 1620-1627 (2012).
69. M. Colina, C. Molpeceres, M. Morales, F. Allens-Perkins, G. Guadaño, and J. Ocaña, "Laser ablation modelling of aluminium, silver and crystalline silicon for applications in photovoltaic technologies," *Surface Engineering* **27**, 414-423 (2011).
70. Z. Lin and L. V. Zhigilei, "Thermal excitation of d band electrons in Au: implications for laser-induced phase transformations," in *High-Power Laser Ablation 2006*, (International Society for Optics and Photonics, 2006), 62610U-62610U-62614.
71. A. N. Smith and P. M. Norris, "Numerical solution for the diffusion of high intensity, ultrashort laser pulses within metal films," *laser* **510**, 4 (1998).
72. I. Mazin and V. Antropov, "Electronic structure, electron–phonon coupling, and multiband effects in MgB₂," *Physica C: Superconductivity* **385**, 49-65 (2003).
73. G. Grimvall, *The electron-phonon interaction in metals* (North-Holland Amsterdam, 1981), Vol. 8.
74. C. K. Poole, H. A. Farach, and R. J. Creswick, *Handbook of superconductivity* (Academic Press, 1999).
75. M. Kagnov, I. Lifshitz, and M. Tanatarov, "Relaxation between electrons and crystalline lattices," *Soviet Physics JETP* **4**, 173-178 (1957).
76. R. Fardel, M. Nagel, T. Lippert, F. Nösch, A. Wokaun, and B. S. Lukyanchuk, "Influence of thermal diffusion on the laser ablation of thin polymer films," *Applied Physics A* **90**, 661-667 (2008).
77. D. Bauerle, *Laser Processing and Chemistry*, 4th ed. (Springer, 1986).
78. H. S. Carslaw and J. C. Jaeger, *Heat conduction in Solids* (Oxford Science, 1989).
79. D. Sowdari and P. Majumdar, "Finite element analysis of laser irradiated metal heating and melting processes," *Optics & Laser Technology* **42**, 855-865.
80. X. Xu, "Phase explosion and its time lag in nanosecond laser ablation," *Applied Surface Science* **197–198**, 61-66 (2002).
81. T. Q. Qiu and C. L. Tien, "Femtosecond laser heating of multi-layer metals—I. Analysis," *International Journal of Heat and Mass Transfer* **37**, 2789-2797 (1994).
82. D. Koutsoyiannis, "Clausius–Clapeyron equation and saturation vapour pressure: simple theory reconciled with practice," *European Journal of physics* **33**, 295 (2012).
83. B. J. Garrison and R. Srinivasan, "Laser ablation of organic polymers: microscopic models for photochemical and thermal processes," *Journal of Applied Physics* **57**, 2909-2914 (1985).
84. A. Welch, M. Motamedi, S. Rastegar, G. L. LeCarpentier, and D. Jansen, "Laser thermal ablation," *Photochemistry and photobiology* **53**, 815-823 (1991).
85. E. Matthias, M. Reichling, J. Siegel, O. Käding, S. Petzoldt, H. Skurk, P. Bizenberger, and E. Neske, "The influence of thermal diffusion on laser ablation of metal films," *Applied Physics A* **58**, 129-136 (1994).
86. H. Dachraoui, W. Husinsky, and G. Betz, "Ultra-short laser ablation of metals and semiconductors: Evidence of ultra-fast Coulomb explosion," *Applied Physics A: Materials Science and Processing* **83**, 333-336 (2006).
87. F. Ladieu, P. Martin, and S. Guizard, "Measuring thermal effects in femtosecond laser-induced breakdown of dielectrics," *Applied Physics Letters* **81**, 957-959 (2002).

88. N. M. Bulgakova and A. V. Bulgakov, "Pulsed laser ablation of solids: transition from normal vaporization to phase explosion," *Applied Physics A* **73**, 199-208 (2001).
89. E. Glezer, Y. Siegal, L. Huang, and E. Mazur, "Behavior of χ (2) during a laser-induced phase transition in GaAs," *Physical Review B* **51**, 9589 (1995).
90. A. Miotello and R. Kelly, "Laser-induced phase explosion: New physical problems when a condensed phase approaches the thermodynamic critical temperature," *Applied Physics A: Materials Science and Processing* **69**, S67-S73 (1999).
91. M. Toulemonde, C. Dufour, A. Meftah, and E. Paumier, "Transient thermal processes in heavy ion irradiation of crystalline inorganic insulators," *Nuclear Instruments and Methods in Physics Research Section B: Beam Interactions with Materials and Atoms* **166**, 903-912 (2000).
92. I. Zinovik and A. Povitsky, "Dynamics of multiple plumes in laser ablation: Modeling of the shielding effect," *Journal of Applied Physics* **100**(2006).
93. J. König, S. Nolte, and A. Tünnermann, "Plasma evolution during metal ablation with ultrashort laser pulses," *Optics Express* **13**, 10597-10607 (2005).
94. K. Sokolowski-Tinten, J. Bialkowski, A. Cavalleri, D. von der Linde, A. Oparin, J. Meyer-ter-Vehn, and S. Anisimov, "Transient states of matter during short pulse laser ablation," *Physical Review Letters* **81**, 224 (1998).
95. R. Stoian, A. Rosenfeld, D. Ashkenasi, I. Hertel, N. Bulgakova, and E. Campbell, "Surface charging and impulsive ion ejection during ultrashort pulsed laser ablation," *Physical review letters* **88**, 097603 (2002).
96. W. G. Roeterdink, L. B. F. Jurlink, O. P. H. Vaughan, J. Dura Diez, M. Bonn, and A. W. Kleyn, "Coulomb explosion in femtosecond laser ablation of Si(111)," *Applied Physics Letters* **82**, 4190-4192 (2003).
97. H.-P. Cheng and J. Gillaspay, "Nanoscale modification of silicon surfaces via Coulomb explosion," *Physical Review B* **55**, 2628 (1997).
98. L. Jiang and H. Tsai, "Femtosecond laser ablation: challenges and opportunities," in *NSF Workshop on Unsolved Problems and Research Needs in Thermal Aspects of Material Removal Processes, Stillwater, OK*, 2003), 1-15.
99. H. Dachraoui and W. Husinsky, "Fast electronic and thermal processes in femtosecond laser ablation of Au," *Applied physics letters* **89**, 104102 (2006).
100. S. Besner, A. V. Kabashin, and M. Meunier, "Fragmentation of colloidal nanoparticles by femtosecond laser-induced supercontinuum generation," *Applied physics letters* **89**, 233122 (2006).
101. N. Haustrup and G. O'Connor, "The influence of thin film grain size on the size of nanoparticles generated during UV femtosecond laser ablation of thin gold films," *Applied Surface Science* **278**, 86-91 (2013).
102. E. G. Gamaly, *Femtosecond Laser-Matter Interaction: Theory, Experiments and Applications* (CRC Press, 2011).
103. N. M. Bulgakova, R. Stoian, A. Rosenfeld, I. V. Hertel, and E. E. Campbell, "Fast electronic transport and Coulomb Explosion in materials irradiated with ultrashort laser pulses," in *Laser ablation and its applications* (Springer, 2007), pp. 17-36.
104. S. S. Harilal, J. R. Freeman, P. K. Diwakar, and A. Hassanein, "Femtosecond laser ablation: Fundamentals and applications," in *Laser-Induced Breakdown Spectroscopy* (Springer, 2014), pp. 143-166.
105. Z. Toth, B. Hopp, T. Szoerenyi, Z. Bor, E. A. Shakhno, and V. P. Veiko, "Pulsed laser ablation mechanisms of thin metal films," in *Industrial Lasers and Inspection (EUROPTO Series)*, (International Society for Optics and Photonics, 1999), 18-26.

106. J. P. McDonald, V. R. Mistry, K. E. Ray, S. M. Yalisove, J. A. Nees, and N. R. Moody, "Femtosecond-laser-induced delamination and blister formation in thermal oxide films on silicon (100)," (2006).
107. L. V. Zhigilei, Z. Lin, and D. S. Ivanov, "Atomistic modeling of short pulse laser ablation of metals: connections between melting, spallation, and phase explosion[†]," *The Journal of Physical Chemistry C* **113**, 11892-11906 (2009).
108. B. J. Demaske, V. V. Zhakhovsky, N. A. Inogamov, and I. I. Oleynik, "Ablation and spallation of gold films irradiated by ultrashort laser pulses," *Physical Review B* **82**, 064113 (2010).
109. C. Cheng and X. Xu, "Non-Equilibrium Thermodynamics and Formation of Nanoparticles in Femtosecond Laser Ablation," in *ASME 2004 International Mechanical Engineering Congress and Exposition*, (American Society of Mechanical Engineers, 2004), 541-546.
110. L. V. Zhigilei, Z. Lin, D. S. Ivanov, E. Leveugle, W. H. Duff, D. Thomas, C. Sevilla, and S. J. Guy, "Atomic/molecular-level simulations of laser-materials interactions," in *Laser-Surface Interactions for New Materials Production* (Springer, 2010), pp. 43-79.
111. M. Tanski, M. Kocik, R. Barbucha, K. Garasz, and J. Mizeraczyk, "Time-resolved observation of the ablation plasma plume dynamics during nanosecond laser micromachining," in *Photonics and Optoelectronics (SOPO), 2012 Symposium on*, (IEEE, 2012), 1-4.
112. Z. Zhang and G. Gogos, "Effects of Laser Intensity and Ambient Conditions on the Laser Induced Plume," in *ASME 2004 International Mechanical Engineering Congress and Exposition*, (American Society of Mechanical Engineers, 2004), 483-489.
113. S. Harilal, T. Sizyuk, A. Hassanein, D. Campos, P. Hough, and V. Sizyuk, "The effect of excitation wavelength on dynamics of laser-produced tin plasma," *Journal of Applied Physics* **109**, 063306 (2011).
114. S. Harilal, G. Miloshevsky, T. Sizyuk, and A. Hassanein, "Effects of excitation laser wavelength on Ly- α and He- α line emission from nitrogen plasmas," *Physics of Plasmas* (1994-present) **20**, 013105 (2013).
115. N. Farid, C. Li, H. Wang, and H. Ding, "Laser-induced breakdown spectroscopic characterization of tungsten plasma using the first, second, and third harmonics of an Nd:YAG laser," *Journal of Nuclear Materials* **433**, 80-85 (2013).
116. A. V. Gusarov, A. G. Gnedovets, and I. Smurov, "Gas dynamics of laser ablation: influence of ambient atmosphere," *Journal of Applied Physics* **88**, 4352-4364 (2000).
117. S. Harilal, B. O'Shay, Y. Tao, and M. S. Tillack, "Ambient gas effects on the dynamics of laser-produced tin plume expansion," *Journal of Applied Physics* **99**, 083303 (2006).
118. A. Bogaerts, Z. Chen, and D. Bleiner, "Laser ablation of copper in different background gases: comparative study by numerical modeling and experiments," *Journal of Analytical Atomic Spectrometry* **21**, 384-395 (2006).
119. S. Amoroso, A. Sambri, and X. Wang, "Propagation dynamics of a LaMnO₃ laser ablation plume in an oxygen atmosphere," *Journal of applied physics* **100**, 013302 (2006).
120. H. Furusawa, T. Sakka, and Y. H. Ogata, "Characterization of ablated species in laser-induced plasma plume," *Journal of applied physics* **96**, 975-982 (2004).
121. S. Harilal, C. Bindhu, V. Nampoory, and C. Vallabhan, "Influence of ambient gas on the temperature and density of laser produced carbon plasma," *Applied physics letters* **72**, 167-169 (1998).
122. N. Farid, S. Harilal, H. Ding, and A. Hassanein, "Dynamics of ultrafast laser plasma expansion in the presence of an ambient," *Applied Physics Letters* **103**, 191112 (2013).

123. W. Wei, J. Wu, X. Li, S. Jia, and A. Qiu, "Study of nanosecond laser-produced plasmas in atmosphere by spatially resolved optical emission spectroscopy," *Journal of Applied Physics* **114**, 113304 (2013).
124. A. De Giacomo, M. Dell'Aglio, R. Gaudiuso, S. Amoroso, and O. De Pascale, "Effects of the background environment on formation, evolution and emission spectra of laser-induced plasmas," *Spectrochimica Acta Part B: Atomic Spectroscopy* **78**, 1-19 (2012).
125. M. Cirisan, J. Jouvard, L. Lavis, L. Hallo, and R. Oltra, "Laser plasma plume structure and dynamics in the ambient air: The early stage of expansion," *Journal of applied physics* **109**, 103301 (2011).
126. S. Mahmood, R. S. Rawat, M. Darby, M. Zakauallah, S. V. Springham, T. Tan, and P. Lee, "On the plume splitting of pulsed laser ablated Fe and Al plasmas," *Physics of Plasmas (1994-present)* **17**, 103105 (2010).
127. S. Mehrabian, M. Aghaei, and S. Tavassoli, "Effect of background gas pressure and laser pulse intensity on laser induced plasma radiation of copper samples," *Physics of Plasmas (1994-present)* **17**, 043301 (2010).
128. N. Farid, H. Wang, C. Li, X. Wu, H. Y. Oderji, H. Ding, and G.-N. Luo, "Effect of background gases at reduced pressures on the laser treated surface morphology, spectral emission and characteristics parameters of laser produced Mo plasmas," *Journal of Nuclear Materials* **438**, 183-189 (2013).
129. W. Sdorra and K. Niemax, "Basic investigations for laser microanalysis: III. Application of different buffer gases for laser-produced sample plumes," *Microchimica Acta* **107**, 319-327 (1992).
130. H. O. Jeschke, M. E. Garcia, and K. Bennemann, "Theory for the ultrafast ablation of graphite films," *Physical review letters* **87**, 015003 (2001).
131. B. C. Stuart, M. D. Feit, S. Herman, A. Rubenchik, B. Shore, and M. Perry, "Nanosecond-to-femtosecond laser-induced breakdown in dielectrics," *Physical Review B* **53**, 1749 (1996).
132. P. Mannion, J. Magee, E. Coyne, and G. M. O'Connor, "Ablation thresholds in ultrafast laser micromachining of common metals in air," in *Opto Ireland*, (International Society for Optics and Photonics, 2003), 470-478.
133. M. Lenzner, J. Krüger, S. Sartania, Z. Cheng, C. Spielmann, G. Mourou, W. Kautek, and F. Krausz, "Femtosecond optical breakdown in dielectrics," *Physical Review Letters* **80**, 4076 (1998).
134. M. Li, S. Menon, J. P. Nibarger, and G. N. Gibson, "Ultrafast electron dynamics in femtosecond optical breakdown of dielectrics," *Physical review letters* **82**, 2394 (1999).
135. D. Ristau, X. Dang, and J. Ebert, "Interface and bulk absorption of oxide layers and correlation to damage threshold at 1.06 μm ," in *Laser Induced Damage in Optical Materials: 1984* (ASTM International, 1986).
136. S. Akhtar, D. Ristau, and J. Ebert, "Thermal Conductivity of Dielectric Films and Correlation to Damage Threshold at 1064nm," in *Laser Induced Damage in Optical Materials: 1986* (ASTM International, 1988).
137. M. R. Lange, J. K. McIver, and A. H. Guenther, "Pulsed laser damage in thin film coatings: fluorides and oxides," *Thin Solid Films* **125**, 143-155 (1985).
138. J. Andrew, P. Dyer, R. Greenough, and P. Key, "Metal film removal and patterning using a XeCl laser," *Applied physics letters* **43**, 1076-1078 (1983).
139. J. O. Porteus, D. L. Decker, W. N. Faith, D. J. Grandjean, S. C. Seitel, and M. Soileau, "Pulsed laser-induced melting of precision diamond-machined Cu, Ag, and Au at infrared wavelengths," *Quantum Electronics, IEEE Journal of* **17**, 2078-2085 (1981).
140. Y. Jee, M. F. Becker, and R. M. Walser, "Laser-induced damage on single-crystal metal surfaces," *JOSA B* **5**, 648-659 (1988).

141. O. Lyngnes, A. Ode, and D. C. Ness, "Anti-reflection coating damage threshold dependence on substrate material," in *Laser Damage Symposium XLI: Annual Symposium on Optical Materials for High Power Lasers*, (International Society for Optics and Photonics, 2009), 75040E-75040E-75049.
142. D. Nieto, J. Arines, and M. T. Flores-Arias, "Fluence ablation threshold dependence on tin impurities in commercial soda-lime glass," *Applied optics* **53**, 5416-5420 (2014).
143. J. Hermann, M. Benfarah, S. Bruneau, E. Axente, G. Coustillier, T. Itina, J. Guillemoles, and P. Alloncle, "Comparative investigation of solar cell thin film processing using nanosecond and femtosecond lasers," *Journal of Physics D: Applied Physics* **39**, 453 (2006).
144. M. Merisalo and T. Paakkari, "Debye-Waller factor and Debye temperature for Fe, Mo, Ta, and W," *Materials Research Bulletin* **8**, 195-199 (1973).
145. J. Hohlfeld, S.-S. Wellershoff, J. Gdde, U. Conrad, V. Jhnke, and E. Matthias, "Electron and lattice dynamics following optical excitation of metals," *Chemical Physics* **251**, 237-258 (2000).
146. J. A. Shields, "Applications of Molybdenum Metal and its Alloys" (International Molybdenum Association (IOMA), London, UK), retrieved 2013, http://www.imoa.info/download_files/molybdenum/Applications_Mo_Metal.pdf.
147. C. Y. Ho, R. W. Powell, and P. E. Liley, "Thermal conductivity of the elements," *Journal of Physical and Chemical Reference Data* **1**, 279-421 (1972).
148. E. D. Palik, *Handbook of optical constants of solids* (Academic press, 1998), Vol. 3.
149. J. Chen and J. Beraun, "Modelling of ultrashort laser ablation of gold films in vacuum," *Journal of Optics A: Pure and Applied Optics* **5**, 168 (2003).
150. Z. L. Leonid V. Zhigilei, "Electron-Phonon Coupling and Electron Heat Capacity in Metals at High Electron Temperatures" (9th September), retrieved 9th September, 2015, <http://www.faculty.virginia.edu/CompMat/electron-phonon-coupling/>.
151. Z. Lin, L. V. Zhigilei, and V. Celli, "Electron-phonon coupling and electron heat capacity of metals under conditions of strong electron-phonon nonequilibrium," *Physical Review B* **77**, 075133 (2008).
152. H.-M. Wu, S.-C. Liang, Y.-L. Lin, C.-Y. Ni, H.-Y. Bor, D.-C. Tsai, and F.-S. Shieu, "Structure and electrical properties of Mo back contact for Cu (In, Ga) Se 2 solar cells," *Vacuum* **86**, 1916-1919 (2012).
153. V. P. Singh, J. C. McClure, G. Lush, W. Wang, X. Wang, G. Thompson, and E. Clark, "Thin film CdTe-CdS heterojunction solar cells on lightweight metal substrates," *Solar energy materials and solar cells* **59**, 145-161 (1999).
154. J. Drayton, A. Vasko, A. Gupta, and A. Compaan, "Magnetron sputtered CdTe solar cells on flexible substrates," in *Photovoltaic Specialists Conference, 2005. Conference Record of the Thirty-first IEEE*, (IEEE, 2005), 406-409.
155. F. H. Karg, "Development and manufacturing of CIS thin film solar modules," *Solar Energy Materials and Solar Cells* **66**, 645-653 (2001).
156. S. Zhang, *Organic nanostructured thin film devices and coatings for clean energy* (CRC Press, 2010).
157. S. Zoppel, H. Huber, and G. A. Reider, "Selective ablation of thin Mo and TCO films with femtosecond laser pulses for structuring thin film solar cells," *Applied Physics A* **89**, 161-163 (2007).
158. L. Stolt, J. Hedstrm, J. Kessler, M. Ruckh, K. O. Velthaus, and H. W. Schock, "ZnO/CdS/CuInSe2 thin-film solar cells with improved performance," *Applied Physics Letters* **62**, 597-599 (1993).
159. T. Dalibor, S. Jost, H. Vogt, R. Brenning, A. Hei, S. Visbeck, T. Happ, J. Palm, A. Avelln, and T. Niesen, "Advanced CIGSSe device for module efficiencies above 15%,"

- in *Proceedings of the 25th European Photovoltaic Solar Energy Conference, Valencia*, 2010), 2854-2857.
160. G. Heise, M. Englmaier, C. Hellwig, T. Kuznicki, S. Sarrach, and H. P. Huber, "Laser ablation of thin molybdenum films on transparent substrates at low fluences," *Applied Physics A* **102**, 173-178 (2011).
 161. R. Le Harzic, N. Huot, E. Audouard, C. Jonin, P. Laporte, S. Valette, A. Fraczkiewicz, and R. Fortunier, "Comparison of heat-affected zones due to nanosecond and femtosecond laser pulses using transmission electronic microscopy," *Applied Physics Letters* **80**, 3886-3888 (2002).
 162. S. Preuss, A. Demchuk, and M. Stuke, "Sub-picosecond UV laser ablation of metals," *Applied Physics A* **61**, 33-37 (1995).
 163. M. Domke, L. Nobile, S. Rapp, S. Eiselen, J. Sotrup, H. P. Huber, and M. Schmidt, "Understanding Thin Film Laser Ablation: The Role of the Effective Penetration Depth and the Film Thickness," *Physics Procedia* **56**, 1007-1014 (2014).
 164. J. Kim and S. Na, "Metal thin film ablation with femtosecond pulsed laser," *Optics & Laser Technology* **39**, 1443-1448 (2007).
 165. S. Döring, S. Richter, A. Tünnermann, and S. Nolte, "Influence of pulse duration on the hole formation during short and ultrashort pulse laser deep drilling," in *SPIE LASE*, (International Society for Optics and Photonics, 2012), 824717-824717-824719.
 166. J. Hermann, M. Benfarah, G. Coustillier, S. Bruneau, E. Axente, J.-F. Guillemoles, M. Sentis, P. Alloncle, and T. Itina, "Selective ablation of thin films with short and ultrashort laser pulses," *Applied Surface Science* **252**, 4814-4818 (2006).
 167. P. D. Gupta and G. M. O'Connor, "Comparison of ablation mechanisms at low fluence for ultrashort and short-pulse laser exposure of very thin molybdenum films on glass," *Applied Optics* **55**, 2117-2125 (2016).
 168. D. Bartl, A. Michalowski, M. Hafner, A. Letsch, S. Nolte, and A. Tünnermann, "Time-resolved study of back side ablated molybdenum thin films by ultrashort laser pulses," *Applied Physics A* **110**, 227-233 (2013).
 169. G. Heise, M. Domke, J. Konrad, S. Sarrach, J. Sotrup, and H. P. Huber, "Laser lift-off initiated by direct induced ablation of different metal thin films with ultra-short laser pulses," *Journal of Physics D: Applied Physics* **45**, 315303 (2012).
 170. H. P. Huber, M. Englmaier, C. Hellwig, A. Heiss, T. Kuznicki, M. Kemnitzer, H. Vogt, R. Brenning, and J. Palm, "High speed structuring of CIS thin-film solar cells with picosecond laser ablation," in *SPIE LASE: Lasers and Applications in Science and Engineering*, (International Society for Optics and Photonics, 2009), 72030R-72030R-72039.
 171. M. Domke, S. Rapp, M. Schmidt, and H. P. Huber, "Ultra-fast movies of thin-film laser ablation," *Applied Physics A* **109**, 409-420 (2012).
 172. J. Wang, R. L. Weaver, and N. R. Sottos, "A parametric study of laser induced thin film spallation," *Experimental Mechanics* **42**, 74-83 (2002).
 173. D. S. Ivanov, B. Rethfeld, G. M. O'Connor, T. J. Glynn, A. N. Volkov, and L. V. Zhigilei, "The mechanism of nanobump formation in femtosecond pulse laser nanostructuring of thin metal films," *Applied Physics A* **92**, 791-796 (2008).
 174. E. Leveugle, D. Ivanov, and L. Zhigilei, "Photomechanical spallation of molecular and metal targets: molecular dynamics study," *Applied Physics A* **79**, 1643-1655 (2004).
 175. L. V. Zhigilei and B. J. Garrison, "Microscopic mechanisms of laser ablation of organic solids in the thermal and stress confinement irradiation regimes," *Journal of Applied Physics* **88**, 1281-1298 (2000).
 176. D. Kim, M. Ye, and C. Grigoropoulos, "Pulsed laser-induced ablation of absorbing liquids and acoustic-transient generation," *Applied Physics A* **67**, 169-181 (1998).

177. K. Seshan, *Handbook of thin film deposition* (William Andrew, 2012).
178. S.-Y. Lin, Y.-C. Chen, C.-M. Wang, P.-T. Hsieh, and S.-C. Shih, "Post-annealing effect upon optical properties of electron beam evaporated molybdenum oxide thin films," *Applied Surface Science* **255**, 3868-3874 (2009).
179. M. Bereznaï, Z. Toth, A. Caricato, M. Fernandez, A. Luches, G. Majni, P. Mengucci, P. Nagy, A. Juhasz, and L. Nanai, "Reactive pulsed laser deposition of thin molybdenum- and tungsten-nitride films," *Thin Solid Films* **473**, 16-23 (2005).
180. J. A. Thornton and D. W. Hoffman, "Internal stresses in titanium, nickel, molybdenum, and tantalum films deposited by cylindrical magnetron sputtering," *Journal of Vacuum Science and Technology* **14**, 164-168 (1977).
181. P. Kelly and R. Arnell, "Magnetron sputtering: a review of recent developments and applications," *Vacuum* **56**, 159-172 (2000).
182. S. Rossnagel, S. W. Sproul, and K. Legg, "Opportunities for Innovation Advanced Surface Engineering," (Technomic Publishing Co, Switzerland, 1995).
183. C. McDaniel, "Physical and bio cellular response of laser induced periodic surface structures formed using a femtosecond laser on a platinum alloy," (National university of Ireland, Galway, Galway, 2016).
184. B. E. Saleh, M. C. Teich, and B. E. Saleh, *Fundamentals of photonics* (Wiley New York, 1991), Vol. 22.
185. L. C. Andrews and R. L. Phillips, *Laser beam propagation through random media* (SPIE press Bellingham, WA, 2005), Vol. 52.
186. G. Bain, "Integrating Sphere Diffuse Reflectance Technology for Use with UV-Visible Spectrophotometry," Thermo Fisher Scientific, Madison, Wisconsin (2007).
187. J. Liu, "Simple technique for measurements of pulsed Gaussian-beam spot sizes," *Optics letters* **7**, 196-198 (1982).
188. H. Jianqiang, L. Xinxin, B. Haifei, W. Yuelin, L. Bin, and G. Xiaohong, "High-yield fabrication of AFM probes with simultaneous formation of both nano-tips and cantilever," in *Sensors, 2005 IEEE*, (2005), 4 pp.
189. B. Cappella and G. Dietler, "Force-distance curves by atomic force microscopy," *Surface science reports* **34**, 1-104 (1999).
190. U. Manual, *ICCD Detectors* (Andor Technology, United Kingdom, 2003).
191. J. Sotrop, A. Kersch, M. Domke, G. Heise, and H. P. Huber, "Numerical simulation of ultrafast expansion as the driving mechanism for confined laser ablation with ultra-short laser pulses," *Applied Physics A* **113**, 397-411 (2013).
192. D. R. Lide, *CRC handbook of chemistry and physics* (CRC press, 2004), Vol. 85.
193. U. T. F. P. AG, "Indium Tin Oxide for Evaporation", retrieved http://www.thinfilmproducts.umicore.com/Products/TechnicalData/show_ito_evaporation.pdf.
194. C. McDonnell, "Pulsed laser material interaction with thin indium tin oxide films," (National university of Ireland, Galway, Galway, 2015).
195. D. Hohnholz, K. H. Schweikart, and M. Hanack, "A simple method for the subdivision of ITO glass substrates," *Advanced Materials* **11**, 646-649 (1999).
196. D. Thuau, I. Koymen, and R. Cheung, "A microstructure for thermal conductivity measurement of conductive thin films," *Microelectronic Engineering* **88**, 2408-2412 (2011).
197. Y. Y. Sun, L. Zheng, L. M. Song, Q. R. Jia, and S. B. Liu, "Research on the Thermal Effect of Long Pulse Laser Irradiation BK7 Glass," *Applied Mechanics and Materials* **347**, 1123-1126 (2013).

198. J. Bovatsek, A. Tamhankar, R. Patel, N. M. Bulgakova, and J. r. Bonse, "Effects of pulse duration on the ns-laser pulse induced removal of thin film materials used in photovoltaics," in 2009), 720116-720116-720113.
199. W. D. Callister and D. G. Rethwisch, *Materials science and engineering: an introduction* (Wiley New York, 2007), Vol. 7.
200. "Schott N-BK7 Glass", retrieved 15 November, 2016, <http://www.matweb.com/search/datasheet.aspx?matguid=a8c2d05c7a6244399bbc2e15c0438cb9&ckck=1>.
201. J. P. Waldron and D. W. Juenker, "Optical Properties of Clean Molybdenum," *J Opt Soc Am* **54**, 204-& (1964).
202. Y. P. Udoyev, M. L. Kapitsa, and Kozyakov.Ns, "Optical Properties of Tungsten and Molybdenum," *Phys Metals Metallog* **31**, 229-& (1971).
203. "BK-7 OPTICAL GLASS", retrieved 28th November, 2016, <http://www.glassdynamicsllc.com/BK7%20Material%20Data%20Sheet.htm>.
204. A. Nasekovskii, "Temperature dependence of the thermal-expansion coefficient of certain polycrystalline materials," *Soviet Physics Journal* **12**, 45-48 (1969).
205. W. Whaling and J. W. Brault, "Comprehensive Transition-Probabilities in Mo-I," *Phys Scripta* **38**, 707-718 (1988).
206. W. Meggers, C. Corliss, and B. Scribner, "Tables of Spectral-Line Intensities, Part I–Arranged by Elements, Part II–Arranged by Wavelengths," *Natl. Bur. Stand. Monograph* **145**, 600pp (1975).
207. J. E. Sansonetti and W. C. Martin, "Handbook of basic atomic spectroscopic data," *Journal of Physical and Chemical Reference Data* **34**, 1559-2259 (2005).
208. D. M. Rayner, S. Mitchell, O. Bourne, and P. A. Hackett, "First-ionization potential of niobium and molybdenum by double-resonance, field-ionization spectroscopy," *JOSA B* **4**, 900-905 (1987).
209. C. Sikström, H. Pihlemark, H. Nilsson, U. Litzén, S. Johansson, Z. Li, and H. Lundberg, "Experimental Mo II oscillator strengths," *Journal of Physics B: Atomic, Molecular and Optical Physics* **34**, 477 (2001).
210. M. Thiagarajan and S. Thompson, "Optical breakdown threshold investigation of 1064 nm laser induced air plasmas," *Journal of Applied Physics* **111**(2012).
211. D. W. Hahn and N. Omenetto, "Laser-induced breakdown spectroscopy (LIBS), part I: review of basic diagnostics and plasma–particle interactions: still-challenging issues within the analytical plasma community," *Applied spectroscopy* **64**, 335A-366A (2010).
212. G. Cristoforetti, A. De Giacomo, M. Dell'Aglio, S. Legnaioli, E. Tognoni, V. Palleschi, and N. Omenetto, "Local thermodynamic equilibrium in laser-induced breakdown spectroscopy: beyond the McWhirter criterion," *Spectrochimica Acta Part B: Atomic Spectroscopy* **65**, 86-95 (2010).
213. D. W. Hahn and N. Omenetto, "Laser-induced breakdown spectroscopy (LIBS), part II: review of instrumental and methodological approaches to material analysis and applications to different fields," *Applied spectroscopy* **66**, 347-419 (2012).
214. V. Unnikrishnan, K. Alti, V. Kartha, C. Santhosh, G. Gupta, and B. Suri, "Measurements of plasma temperature and electron density in laser-induced copper plasma by time-resolved spectroscopy of neutral atom and ion emissions," *Pramana J. Phys* **74**, 983-993 (2010).
215. N. Konjević, "Plasma broadening and shifting of non-hydrogenic spectral lines: present status and applications," *Physics reports* **316**, 339-401 (1999).
216. N. M. Shaikh, B. Rashid, S. Hafeez, Y. Jamil, and M. Baig, "Measurement of electron density and temperature of a laser-induced zinc plasma," *Journal of Physics D: Applied Physics* **39**, 1384 (2006).

217. M. Taschuk, Y. Godwal, Y. Tsui, R. Fedosejevs, M. Tripathi, and B. Kearton, "Absolute characterization of laser-induced breakdown spectroscopy detection systems," *Spectrochimica Acta Part B: Atomic Spectroscopy* **63**, 525-535 (2008).
218. C. J. Sansonetti, M. L. Salit, and J. Reader, "Wavelengths of spectral lines in mercury pencil lamps," *Applied optics* **35**, 74-77 (1996).
219. M. Fryling, C. J. Frank, and R. L. McCreery, "Intensity calibration and sensitivity comparisons for CCD/Raman spectrometers," *Applied spectroscopy* **47**, 1965-1974 (1993).
220. C.-H. Tseng, J. F. Ford, C. K. Mann, and T. J. Vickers, "Wavelength calibration of a multichannel spectrometer," *Applied spectroscopy* **47**, 1808-1813 (1993).
221. P. Yaroshchuk, D. Body, R. J. S. Morrison, and B. L. Chadwick, "A semi-quantitative standard-less analysis method for laser-induced breakdown spectroscopy," *Spectrochimica Acta B* **61**, 200-209 (2006).
222. R. DeWames, J. Pasko, E. Yao, A. Vanderwyck, and G. Williams, "Dark current generation mechanisms and spectral noise current in long-wavelength infrared photodiodes," *Journal of Vacuum Science & Technology A: Vacuum, Surfaces, and Films* **6**, 2655-2663 (1988).
223. D. D. Kelson, "Optimal techniques in two-dimensional spectroscopy: Background subtraction for the 21st century," *Publications of the Astronomical Society of the Pacific* **115**, 688 (2003).
224. A. Kramida, Y. Ralchenko, and J. Reader, "NIST Atomic Spectra Database (Gaithersburg, MD: National Institute of Standards and Technology)(Ver. 5.3)," (2013).
225. Y. Deguchi, *Industrial applications of laser diagnostics* (CRC Press, 2011).
226. L. J. Radziemski and D. A. Cremers, "Laser-induced plasmas and applications," (1989).
227. S. S. Harilal, C. V. Bindhu, M. S. Tillack, F. Najmabadi, and A. C. Gaeris, "Internal structure and expansion dynamics of laser ablation plumes into ambient gases," *Journal of Applied Physics* **93**, 2380-2388 (2003).
228. S. Amoroso, R. Bruzzese, N. Spinelli, and R. Velotta, "Characterization of laser-ablation plasmas," *Journal of Physics B: Atomic, Molecular and Optical Physics* **32**, R131 (1999).
229. H. Griem, *Spectral line broadening by plasmas* (Elsevier, 2012).
230. H. R. Griem, *Principles of plasma spectroscopy* (Cambridge University Press, 2005), Vol. 2.
231. R. E. Russo, X. L. Mao, J. J. Gonzalez, and S. S. Mao, "Femtosecond laser ablation ICP-MS," *Journal of Analytical Atomic Spectrometry* **17**, 1072-1075 (2002).
232. C. Aragón and J. A. Aguilera, "Characterization of laser induced plasmas by optical emission spectroscopy: A review of experiments and methods," *Spectrochimica Acta Part B: Atomic Spectroscopy* **63**, 893-916 (2008).
233. R. Elton and H. Griem, "Measurement of Stark Profiles of the Lyman- α and Lyman- β Lines of Hydrogen in an Electromagnetic Shock Tube," *Physical Review* **135**, A1550 (1964).
234. R. Al-Wazzan, C. Lewis, and T. Morrow, "A technique for mapping three-dimensional number densities of species in laser produced plumes," *Review of scientific instruments* **67**, 85-88 (1996).
235. C. J. Foot, *Atomic physics* (Oxford University Press, 2005), Vol. 7.
236. J. Aguilera, C. Aragón, and F. Penalba, "Plasma shielding effect in laser ablation of metallic samples and its influence on LIBS analysis," *Applied surface science* **127**, 309-314 (1998).
237. M. A. Ismail, H. Imam, A. Elhassan, W. T. Youniss, and M. A. Harith, "LIBS limit of detection and plasma parameters of some elements in two different metallic matrices," *Journal of Analytical Atomic Spectrometry* **19**, 489-494 (2004).

238. J. Wu, X. Li, W. Wei, S. Jia, and A. Qiu, "Understanding plume splitting of laser ablated plasma: A view from ion distribution dynamics," *Physics of Plasmas* **20**, 113512 (2013).
239. T. A. Labutin, V. N. Lednev, A. A. Ilyin, and A. M. Popov, "Femtosecond laser-induced breakdown spectroscopy," *Journal of Analytical Atomic Spectrometry* **31**, 90-118 (2016).
240. X. Wang, D. M. Riffe, Y.-S. Lee, and M. Downer, "Time-resolved electron-temperature measurement in a highly excited gold target using femtosecond thermionic emission," *Physical Review B* **50**, 8016 (1994).
241. E. Logothetis and P. Hartman, "Laser-induced electron emission from solids: many-photon photoelectric effects and thermionic emission," *Physical Review* **187**, 460 (1969).
242. S. Coulombe and J.-L. Meunier, "Thermo-field emission: a comparative study," *Journal of physics D: Applied physics* **30**, 776 (1997).
243. K. Yamada, K. Miyajima, and F. Mafuné, "Thermionic emission of electrons from gold nanoparticles by nanosecond pulse-laser excitation of interband," *The Journal of Physical Chemistry C* **111**, 11246-11251 (2007).
244. I. Petroff and C. Viswanathan, "Calculation of the photoelectric emission from tungsten, tantalum, and molybdenum," *Physical Review B* **4**, 799 (1971).
245. V. L. Moruzzi, J. F. Janak, and A. R. Williams, *Calculated electronic properties of metals* (Elsevier, 2013).
246. A. Zunger, G. Kerker, and M. L. Cohen, "Calculation of the electronic properties of Mo in a first-principles nonlocal-pseudopotential approach," *Physical Review B* **20**, 581 (1979).
247. N. Bacalis, K. Blathras, P. Thomaides, and D. Papaconstantopoulos, "Various approximations made in augmented-plane-wave calculations," *Physical Review B* **32**, 4849 (1985).
248. A. R. Jani, G. S. Tripathi, N. E. Brener, and J. Callaway, "Band-Structure and Related Properties of Molybdenum," *Physical Review B* **40**, 1593-1602 (1989).
249. E. Black, D. W. Lynch, and C. Olson, "Optical properties (0.1-25 eV) of Nb-Mo and other Nb-based alloys," *Physical Review B* **16**, 2337 (1977).
250. M. KffiiLLOVA, L. Nomerovannaya, and M. Noskov, "Optical properties of molybdenum single crystals," *Soviet Physics JETP* **33**(1971).
251. J. J. Friel, *X-ray and image analysis in electron microscopy* (Princeton Gamma-Tech, Incorporated, 1994).
252. L. Kocsis, P. Herman, and A. Eke, "The modified Beer-Lambert law revisited," *Physics in medicine and biology* **51**, N91 (2006).
253. R. Wood and G. Giles, "Macroscopic theory of pulsed-laser annealing. I. Thermal transport and melting," *Physical Review B* **23**, 2923 (1981).
254. J. Poate, *Laser annealing of semiconductors* (Elsevier, 2012).
255. T. Sameshima, S. Usui, and M. Sekiya, "XeCl Excimer laser annealing used in the fabrication of poly-Si TFT's," *IEEE Electron Device Letters* **7**, 276-278 (1986).
256. B. Stritzker, A. Pospieszczyk, and J. Tagle, "Measurement of lattice temperature of silicon during pulsed laser annealing," *Physical Review Letters* **47**, 356 (1981).
257. H. Lee, S. Hong, J. Kwon, Y. D. Suh, J. Lee, H. Moon, J. Yeo, and S. H. Ko, "All-solid-state flexible supercapacitors by fast laser annealing of printed metal nanoparticle layers," *Journal of Materials Chemistry A* **3**, 8339-8345 (2015).
258. E. Seebauer and C. Allen, "Estimating surface diffusion coefficients," *Progress in surface science* **49**, 265-330 (1995).
259. G. Ehrlich, "Direct observations of the surface diffusion of atoms and clusters," *Surface Science* **246**, 1-12 (1991).
260. J. Lander and J. Morrison, "Surface reactions of silicon with aluminum and with indium," *Surface Science* **2**, 553-565 (1964).

261. E. Riedo, E. Gnecco, R. Bennewitz, E. Meyer, and H. Brune, "Interaction potential and hopping dynamics governing sliding friction," *Physical review letters* **91**, 084502 (2003).
262. J. Choi, K. Nielsch, M. Reiche, R. Wehrspohn, and U. Gösele, "Fabrication of monodomain alumina pore arrays with an interpore distance smaller than the lattice constant of the imprint stamp," *Journal of Vacuum Science & Technology B* **21**, 763-766 (2003).